Giant Planets Transiting Giant Stars

A DISSERTATION SUBMITTED TO THE GRADUATE DIVISION OF THE UNIVERSITY OF HAWAIʻI AT MĀNOA IN PARTIAL FULFILLMENT OF THE REQUIREMENTS FOR THE DEGREE OF

DOCTOR OF PHILOSOPHY

IN

ASTRONOMY

August 2019

By
Samuel Kai Grunblatt

Dissertation Committee:

Daniel Huber, Chairperson
Eric J. Gaidos
Andrew W. Howard
Christoph J. Baranec
Rolf-Peter Kudritzki
Jonathan P. Williams

To I. Piehler, H. Grunblatt, and H. and E. Blake

Acknowledgements

As my six years as a graduate student in Hawaii draws to a close, I’m grateful to a wide range of individuals who have made this thesis possible. Without a broad network of support and enthusiasm for my research, obtaining this degree would not have been possible. A famous scientist once said, ”If I have seen further it is by standing on the shoulders of Giants.” Though my achievements certainly pale in comparison, the sentiment rings true to my work. Thank you to all of you who helped me get to this point–it wouldn’t have happened without you.

First, I’d like to acknowledge the support of the US taxpayers. Without the funding that all of us provide, the NASA and NSF funds used to pay my salary would not be available. I’d also like to thank the citizens of the state of Hawaii. Your (retroactive) choice to allow scientific research at the summit of Maunakea was essential to the success of this research. Given the very significant cultural role and reverence that the summit of Maunakea has always had within the indigenous Hawai‘ian community, I am very grateful to have been given the opportunity to use this unique place to best further exoplanet and astronomical studies for the common good.

Next, I’d like to thank my advisors. I’m incredibly honored to be the first graduating Ph.D. student of Dr. Daniel Huber. I will be forever grateful for running into you at the IAU meeting in 2015, where you offered a thesis project to me in a 15 minute conversation in the lobby. You took a potentially life-changing risk on me, and then never hesitated to answer my questions or make yourself available to me when I needed it most. More importantly, you’ve shown me how to be an outstanding scientist yet a well-balanced person at the same time.

But I’ve been lucky enough to have many other great mentors throughout my scientific career. I’d also like to thank Eric Gaidos, for similarly taking a leap of faith to become the chair of my thesis committee before ever having worked with me. Your intellectual curiosity inspires me every time I come into contact with it. Andrew Howard generously gave me the first taste of publishable-quality research, and continues to inspire my interest in exoplanets and attention to detail. Stuart Jefferies taught me the beauty and importance of being able to explain difficult concepts in approachable terms. Rolf Kudritzki made the value of this even clearer in my most memorable class as a graduate student.

Before I arrived in Hawaii, there were many others who helped me onto the proper path. Joe Patterson–thanks for being more than happy to help out an eager undergrad, and keeping his astronomy enthusiasm alive and well throughout those four years. Your lack of hesitation to get me involved in observing has played a huge role in my life since then. Thanks to Chryssa Kouvelioutou and Jochen Greiner, for taking the time to give me my first tastes of doing research at an institute, and giving me the confidence in my research I needed to continue. Thanks to Dr. Fred Chromey for taking the time to teach a high schooler how to do astronomy research and use IRAF even when he had nothing to gain from it. Thanks to Mr. Kirk Reinhardt for believing in the potential of Kingston High School students and always giving us access to the tools we needed to succeed. And lastly, thanks to Dr. Norbert Magnussen for inspiring and encouraging me to become an astrophysicist almost twenty years ago.

I'd also like to thank all of my fellow students for their support along the way. Thanks to all of the UH IfA incoming grad classes of 2012, 2013, and 2014 for collaborating with me on homeworks and commiserating when things got tougher than anything I had seen in undergrad. A special thanks to my former housemates, Conor and Max, for driving me insane and later keeping me sane as we all faced this new challenge together. And of course to my apartment mate of the past four years, Travis–your patience is a thing of legend, and your friendship is something I'll treasure for the rest of my life. Thanks for all the great memories and conversations, scientific and otherwise. And to my own student, Stephanie: mentoring you over the past two years has taught me so much, and your success and drive inspires me every day. I'm so proud of what you've accomplished, and I can't wait to see where you're headed next.

And finally, I'd like to thank my loving family. Whether it was the ridiculously large body of knowledge of Dad's or the unrivaled work ethic of Mom that inspired me to make this choice, you have both supported me 100% without ever giving it a second thought. You gave me the self-confidence, ambition, and downright desire to make this happen. Thanks to my sister Eva, for being one of my closest friends and the best sister I could ever hope for. I'd also like to thank my grandmothers, Inge Piehler and Hilda Grunblatt, and my "adopted" grandparents Helen and Ed Blake for always

believing in me and making me into the person I am now. I know that you'd be here supporting me every chance you got if you were still here today, and for that I can never thank you enough.

Abstract

Every Sun-like star will eventually evolve into a red giant, a transition which can profoundly affect the evolution of a surrounding planetary system. The timescale of dynamical planet evolution and orbital decay has important implications for planetary habitability, as well as post-main sequence star and planet interaction, evolution and internal structure. In this thesis, I investigate the population of giant planets transiting low luminosity red giant branch stars observed by the NASA *K2* mission. I report the discovery of two new planets orbiting evolved stars, and confirm the existence of a third, doubling the number of evolved ($R_* > 3.5\ R_\odot$, $T_{\rm eff} < T_{\rm eff,\odot}$) stars with known transiting planets. By developing new tools to mitigate stellar variability in evolved star light curves, I robustly measure the planetary radii of these systems. I find that all of these planets are inflated, the first evidence that planets may be inflated directly by an increase in incident stellar radiation, and thus comprise a previously unknown class of re-inflated planets. I also obtain radial velocity measurements of planets orbiting evolved stars to constrain their orbital properties and the efficiency of re-inflation. I find that close-in giant planets orbiting evolved stars display a preference for moderately eccentric orbits, a previously predicted outcome of late-stage planetary system evolution. Finally, I perform a comprehensive planet occurrence study using all oscillating low luminosity red giant branch stars observed in the first 16 campaigns of *K2*. I measure stellar masses and radii to 6% precision or better using asteroseismology, and find a comparable fraction of close-in giant planets around evolved stars as main sequence stars. A higher fraction of inflated close-in gas giants is also found around evolved stars. These discoveries imply that planet engulfment happens more slowly than previously predicted, and that the effects of stellar evolution on the occurrence of close-in planets larger than Jupiter is not significant until stars have begun ascending substantially up the red giant branch ($\gtrsim$ 6 $R_\odot$). Further surveys of these stars by the NASA *TESS* mission will reveal the dependence of late-stage planetary evolution on star and planet properties.

Table of Contents

List of Tables

List of Figures

Chapter 1

Introduction

For millenia, our species has wondered whether there are places other than Earth where life could exist. Over a span of less than a generation, this question has transitioned from a hypothetical argument limited by a lack of evidence for planets outside our own solar system into a concrete scientific field of study, with over 4,000 examples known to date. Understanding the distribution of exoplanets, planets outside our solar system, is essential to arrive at an answer to this question.

Over the relatively short history of exoplanet science, we have determined that planets orbit a majority of stars in our Galaxy (Mayor et al. 2011), and that planets and/or planetesimals surround all types of stars in our Galaxy (Wolszczan & Frail 1992; Mayor & Queloz 1995; Marois et al. 2008; Lillo-Box et al. 2014; Vanderburg et al. 2015; Anglada-Escudé et al. 2016; Gaudi et al. 2017). For my thesis, I have focused on understanding the planet population of stars beginning to ascend the red giant branch, an evolutionary state lasting ∼10% of a star's lifetime. These systems represent both a significant fraction of planetary systems in our Galaxy today, as well as the future state of our own Solar System.

The structure of this thesis is as follows. In Chapter 2 we discuss the discovery and confirmation of K2-97b, the first planet found by our survey, and discuss its implications for understanding the planet inflation mechanism(s). We use asteroseismology to derive precise stellar parameters, and Gaussian process analysis to mitigate the effect of stellar variability when measuring planet transit parameters. In Chapter 3 we introduce K2-132b, the second re-inflated planet found by our survey, and further develop our Gaussian process model such that it accounts for both stellar granulation and oscillations, and thus can be used to perform asteroseismology entirely in the time domain. We use this improved model to measure precise star and planet parameters and place additional constraints on the mechanism and efficiency of planet inflation. In Chapter 4 we investigate the orbital eccentricity distribution of the population of giant planets orbiting red giant stars, and compare it to the giant planet eccentricity distribution of the population of main sequence stars. In Chapter 5, we perform asteroseismology of our full *K2* target sample, and then use the stellar parameters thereby determined to calculate planet occurrence for the entire sample, as a function of planet radius, stellar radius, and orbital period. We then compare this planet occurrence rate to main sequence stars, and conclude that orbital evolution of planets is not occurring as quickly around evolved stars as was inferred previously. In Chapter 6, we discuss ongoing projects to calibrate effective temperature and radius relations based on stellar luminosities for red giant stars, and understand the variability of evolved stars in radial velocity measurements. Finally, in Chapter 7, we state our conclusions, and discuss the feasibility of extending the study of transiting planets around evolved stars with *TESS*.

1.1 Exoplanet Demographics

1.1.1 Exoplanet surveys: a recent history

Though philosophers predicted the existence of other worlds thousands of years ago, techniques for detecting them only became available in the past century. Two potential methods of detecting planets were suggested by Struve (1952): measuring the spectroscopic signature produced by the cyclical wobble of the host star being pulled by a planet in orbit around the star, and measuring the periodic dimming of a star as a planet passes between the star and us once per orbit.

The former method is commonly referred to as the radial velocity (RV) technique. By measuring the line-of-sight velocity of the star K, the mass ratio of a planet to a star can be inferred using the following equation:

$$K = \left(\frac{2\pi G}{P}\right)^{1/3} \frac{M_p \sin i}{M_*^{2/3}} \frac{1}{\sqrt{1-e^2}} \tag{1.1}$$

where M_p and M_* are the masses of the planet and host star, P is the orbital period, e is the orbit eccentricity and i is the orbit inclination. Additionally, if a planet passes between us and its host star once per orbit, the star will periodically be dimmed by the fraction of the stellar disk blocked:

$$\frac{\Delta F}{F} \propto \left(\frac{R_p}{R_*}\right)^2 \tag{1.2}$$

where R_p and R_* are the planet and stellar radius, respectively. The vast majority of planets discovered to date have been found using these two methods. As both methods require determining planet properties relative to stellar properties, accurate stellar characterization is key to determining proper planet population characteristics.

Latham et al. (1989) reported the first detection of a planetary mass object orbiting HD 114762 using the RV method. Three years later, Wolszczan & Frail (1992) made the first unambiguous detection of planet-mass objects outside of the Solar System. Mayor & Queloz (1995) reported the discovery of 51 Pegasi b, a Jupiter-mass planet orbiting a main sequence star. This spawned the era of RV planet searches, with planet totals reaching twelve by the year 2000 and reaching 100 less than a decade later (Han et al. 2014).

Though the RV method has been a longer history of success, transiting planet discoveries currently dominate the majority of planet discovered to date. Charbonneau et al. (2000) and Henry et al. (2000) reported the first discovery of a transiting exoplanet, HD209458b. This planet was found to be larger than giant planet models predicted was possible, spurring investigation into planet inflation (Burrows et al. 2000; Bodenheimer et al. 2001). However, the noise limitations of the atmosphere severely limited the precision of transit observations from the ground, and thus space observations were needed to enable detections of large numbers of planets using this method.

The *Kepler* and *CoRoT* space telescopes were both approved for planet transit observations in the early 2000s, with *CoRoT* launching in 2006, and *Kepler* in 2009 (Auvergne et al. 2009; Borucki et al. 2010). In this thesis, we have chosen to focus on *Kepler* as it is responsible for all light curves analyzed in this study. For four years starting in December 2009, the *Kepler* telescope measured precise brightnesses of >150,000 stars in a 10 × 10 degree field of view in the constellation Cygnus every 30 minutes. This mission discovered thousands of transiting planets and revolutionized the field of exoplanet science.

In the 21st century, exoplanet science has moved from an era of individual detection to a study of populations. Instead of focusing on individual planet studies, populations of planets were studied. The occurrence of planets,

$$f_{\mathrm{pl}} = \frac{N_p}{N_*}, \tag{1.3}$$

where N_p represents a total number of planets around a population of N_* stars, could be inferred for the first time using various planet populations. It is important to note that this fraction is *different* from the fraction of stars that host planets, as many stars host more than one planet.

Marcy et al. (2005) used the early detections of hot Jupiters in order to estimate an occurrence rate of 1.2 ± 0.1 %. Cumming et al. (2008) determined that ≈ 10% of Sun-like stars have a giant planet with an orbital period less than 5.5 years. Following these RV studies, *Kepler* results were able to extend these population studies from hundreds to thousands of planets, and were tremendously successful in accomplishing the mission goal of determining the frequency of planets around Sun-like stars. Howard et al. (2012) used *Kepler* mission light curves of 58,041 stars with 1,235 planet candidates to estimate the distribution of planets as a function of planet radius, orbital period, and stellar effective temperature for orbital periods less than 50 days and planet radii greater than 2 $R_\oplus$. They found that the distribution of planet radii can be described as a power law, with smaller, sub-Neptune-sized planets being significantly more common than Jupiters. Later studies of planet occurrence confirmed this result (Fressin et al. 2013).

Petigura et al. (2013) extended this study in the planet radius dimension to determine the fraction of Earth-like planets expected around Sun-like stars, and found that 22 ± 8 % of Sun-like stars host 1-4 $R_\oplus$ planets receiving 0.25-4 $F_\oplus$, one of the goals of the *Kepler* mission. Additional ground-based spectroscopic followup of these transiting planetary systems revealed additional structure in the radius distribution of planets (Fulton et al. 2017). This gap is predicted to be due to the photoevaporation of planetary atmospheres during the first hundred million years of stellar evolution, when the flux on a planet from high-energy photons is orders of magnitude higher than during its main sequence lifetime (Owen & Wu 2017). This was the first direct evidence of stellar evolution impacting the observed planet population.

However, the focus of the *Kepler* prime mission on main sequence systems left evolved stars relatively unexplored. A handful of planet detections around evolved stars by *Kepler* (Huber et al. 2013a; Lillo-Box et al. 2014; Campante et al. 2015) motivated a more targeted search of evolved stars to understand the correlation between planetary properties and late-stage stellar evolution. A larger sample of gas giant planets at 0.1–0.3 AU orbits around evolved stars is essential to understanding the correlation between planet inflation and stellar irradiation (Lopez & Fortney 2016). An understanding of the orbits of planets around evolved stars can constrain tidal circularization and inspiral timescales for all planetary systems, and its correlation with stellar radius (Villaver et al. 2014). A larger, well-characterized population of planets around evolved stars allows direct comparison to main sequence systems, revealing how the last 10% of a star's life can sculpt planetary environments in unique ways (Jones et al. 2016). A survey of giant stars by a mission like *Kepler* can reveal a population of planets within $\lesssim$ 0.3 AU, where earlier RV planet surveys of evolved stars were not sensitive.

1.1.2 The K2 Mission

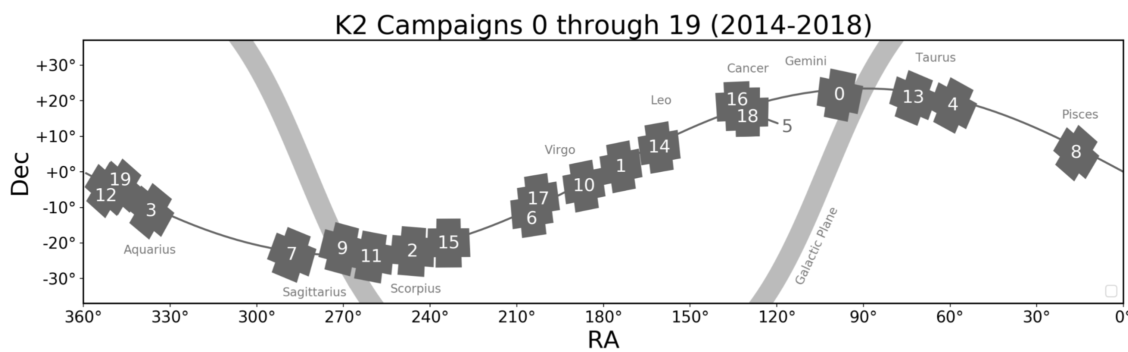

Figure 1.1 Fields of view observed by the *K2* mission, displayed in right ascension and declination. Taken from `https://keplerscience.arc.nasa.gov/` on 06-08-19. All fields lie along the ecliptic plane (black curve).

In May 2013, the second of four reaction wheels responsible for maintaining the pointing of the *Kepler* spacecraft broke, making a continuation of the *Kepler* prime mission impossible. However, ingenuity among the *Ball Aerospace* and *Kepler* engineers led to a new mission similar to the *Kepler* prime mission, in which the *Kepler* telescope would observe a different field along the ecliptic plane every ≈80 days, its pointing balanced in two dimensions by its remaining function reaction wheels and in the third dimension by the pressure due to the Sun's radiation and particle expulsion (Figure 1.1). The constantly changing field made rapid target selection essential, causing the *K2* mission targets to be chosen entirely by the scientific community. This allowed for systematic targeting of evolved stars for transit surveys for the first time.

The *K2* extension to the *Kepler* prime mission opened target selection to the wider astronomical community, extending transiting exoplanet studies to a much wider range of host stars (see Figure 1.2). The large numbers of targets acquired by the *Kepler* and *K2* missions has allowed the first comparable estimates of planet occurrence as a function of stellar type (e.g., van Sluijs & Van Eylen 2018).

For this work, we have chosen to focus on low-luminosity red giant branch (LLRGB) stars. These stars have evolved significantly from their main sequence states, but are not so evolved that *K2* photometric precision is insufficient to detect transiting planets smaller than Jupiter. In addition, low- and intermediate-mass star evolutionary tracks converge during the LLRGB phase, potentially allowing more unbiased comparison between planet populations as a function of stellar mass (Johnson et al. 2010a). By using the *K2* mission to search for transits around a representative population of low-luminosity red giant branch stars, we can understand how the evolution of main sequence, Sun-like stars into red giants affects planet stability and evolution, and place additional limits on the timescale for habitability of a planetary system.

The *K2* mission has already resulted in hundreds of planet discoveries (Mayo et al. 2018), many of which have been around stars which would not have been targeted by the *Kepler* prime mission (e.g., Vanderburg et al. 2015). These studies, along with the previous analysis of the *Kepler* prime mission, is allowing for new estimates of planet occurrence at different stages of planetary system evolution. *Kepler* and *K2* surveys of young stars have begun to uncover evolutionary trends at the earliest stages of planet evolution (Gaidos et al. 2016; Mann et al. 2017). In contrast, this thesis explores the other end of planetary lifetimes, and how late-stage stellar evolution can disrupt and potentially destroy planets.

1.1.3 Planets around evolved stars

RV surveys

Following the discovery of a number of planets around Sun-like stars via radial velocity (RV) surveys, the field of exoplanets moved toward trying to understand the occurrence of planets as a function of stellar mass. However, massive main sequence stars were not amenable to RV studies due to their rapid rotation. Thus, RV surveys of massive stars were limited to evolved stars, around which a number of new planets were found (Sato et al. 2005; Johnson et al. 2007, 2010a). These studies

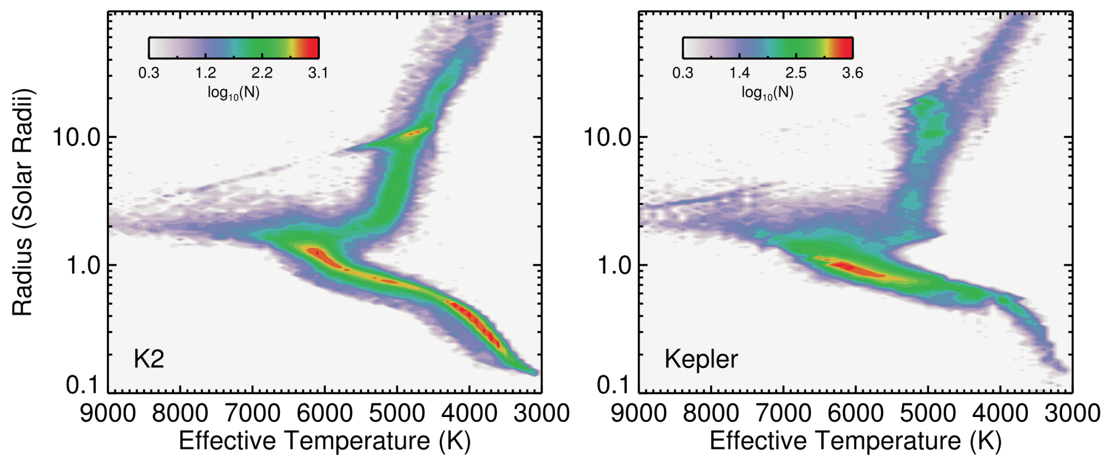

Figure 1.2 Stellar radius versus effective temperature for stars observed by the *K2* (left) and *Kepler* (right) missions. Color indicates the density of stars at any given point on the figure. While the *Kepler* prime mission was heavily focused on main sequence stars similar to the Sun, *K2* observed a higher fraction of cooler stars, both red dwarfs and red giant stars. Taken from Huber et al. (2016).

revealed a correlation between stellar mass and planet occurrence: more massive stars are more likely to host planets. However, this population of evolved stars could not be directly compared to solar mass, main sequence stars, due to the additional confounding effects of mass and metallicity bias present in the evolved planet host sample. Moreover, uncertainties in stellar mass determination for these stars from isochrone fitting made determining the relation between stellar mass and planet occurrence more difficult and heavily debated (Johnson et al. 2010a; Lloyd 2011, 2013; Ghezzi & Johnson 2015).

However, though these surveys were relatively successful at finding planets on $\sim$1 AU orbits around evolved stars, they appeared to find a much smaller fraction of planets at orbits < 0.5 AU (Bowler et al. 2010; Jones et al. 2016). Despite the decades-long baseline of many RV campaigns, only one planet had been discovered via the RV method around evolved stars at periods less than 80 days at the start of this project (Johnson et al. 2010b, see Figure 1.3). Two additional RV planets have been discovered around evolved stars at periods less than 80 days since the start of this survey, but this is still less than half the number of transiting planets known around evolved stars to date (Niedzielski et al. 2016; Takarada et al. 2018). It has been suggested that this dearth of planets at short orbital periods around evolved stars could be a consequence of stellar evolution (Villaver & Livio 2009; Jones et al. 2017). However, both the bias of RV surveys toward bright, low-activity stars

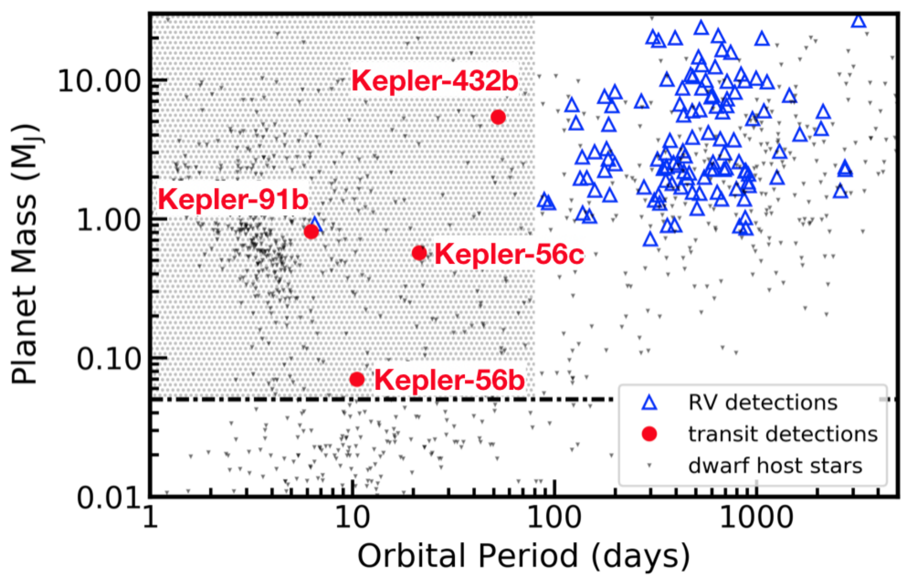

Figure 1.3 Planet mass versus orbital period for the main sequence and evolved star populations known at the start of this thesis. Planets orbiting evolved stars ($R_* > 3.5\ R_\odot$, $T_{\mathrm{eff},*} < T_{\mathrm{eff},\odot}$) are designated in color, with blue triangles representing planets found using the radial velocity method, and red circles representing planets found via the transit method. All three transiting planetary systems were discovered by *Kepler*. Planets known orbiting main sequence stars are shown as black dots. The shaded region roughly corresponds to the region of sensitivity of past and current photometric searches for planet transits.

and the observation strategy could affect the detection of close-in planets. In addition, a number of planets confirmed around evolved stars using RV methods at orbital distances >0.5 AU are now being retracted as false positive detections attributed to long period stellar variability (Delgado Mena et al. 2018). Thus, a direct determination of planet occurrence around evolved stars using only RV measurements was not possible.

Transit discoveries

The launch of *Kepler* started a new era for the study of exoplanets, making transit studies possible for a large number of host stars. Though the mission was largely focused on main sequence stars, the first planets known to be transiting evolved stars were serendipitously discovered by *Kepler* (Huber et al. 2013a; Lillo-Box et al. 2014; Campante et al. 2015, , see Figure 1.3). Thanks to the discovery of these systems, investigation of the effect of late stage stellar evolution on planet radius was made possible for the first time. The *K2* mission allowed for the first targeted survey of evolved stars in order to search for transiting planets, and has resulted in the detection of three planets orbiting evolved stars to date (Chapter 2, Chapter 3, Chapter 5, Mayo et al. 2018). These handful of transiting planets, along with a larger population of RV planets at longer periods, allow for a more complete understanding of the planet population of evolved stars (Jones et al. 2016, Chapter 4). The *TESS* mission is currently taking similar data of the entire sky, predicted to result in hundreds of more transiting planet detections around evolved stars over the next 5 years (Barclay et al. 2018).

Investigating Hot Jupiter Inflation

Though relatively uncommon, Jupiter-sized planets on short-period orbits have been instrumental in pioneering new studies into our understanding of the demographics of exoplanets. The first planet confirmed around a Sun-like star was such a Hot Jupiter (Mayor & Queloz 1995), leading to larger and larger surveys of nearby stars to find previously unknown planets. Due to the large size and small orbital separation of these planets, hot Jupiters produce relatively large signals in transit and radial velocity studies (Marcy & Butler 1996), and thus represent both a large fraction of the first planets confirmed outside of our solar system, as well as some of the best targets for detailed studies to understand planet formation and evolution (Bodenheimer et al. 2001; Fortney et al. 2007). One of the longest-standing unanswered questions about planet evolution is the mechanism(s) responsible for hot Jupiter inflation, which has been debated for over 20 years in the literature (Guillot et al. 1996; Burrows et al. 2000; Lopez & Fortney 2016). Studying inflated hot Jupiters around evolved stars, such as low-luminosity red giant branch stars, is key to determining what stellar evolutionary effects are related to planet inflation.

Planetary Archaeology

Looking for planets around evolved stars, or at least the subset of evolved stars around which planet transits are detectable, is imperative to understand the distribution of planets around our Galaxy. Due to Malmquist bias (Malmquist 1922), giant stars at relatively larger distances will be overrepresented in magnitude-limited surveys. As two of the top five most distant planets detected by *K2* listed in the NASA Exoplanet Archive to date are orbiting stars included in our LLRGB survey (Akeson et al. 2013; Gaia Collaboration et al. 2018, , Chapters 3–5), this suggests studies of planets found transiting similar stars will allow the development of comparative planetary archaeology. Though limited to the faintest and nearest giant stars, this planetary archaeology can be conducted

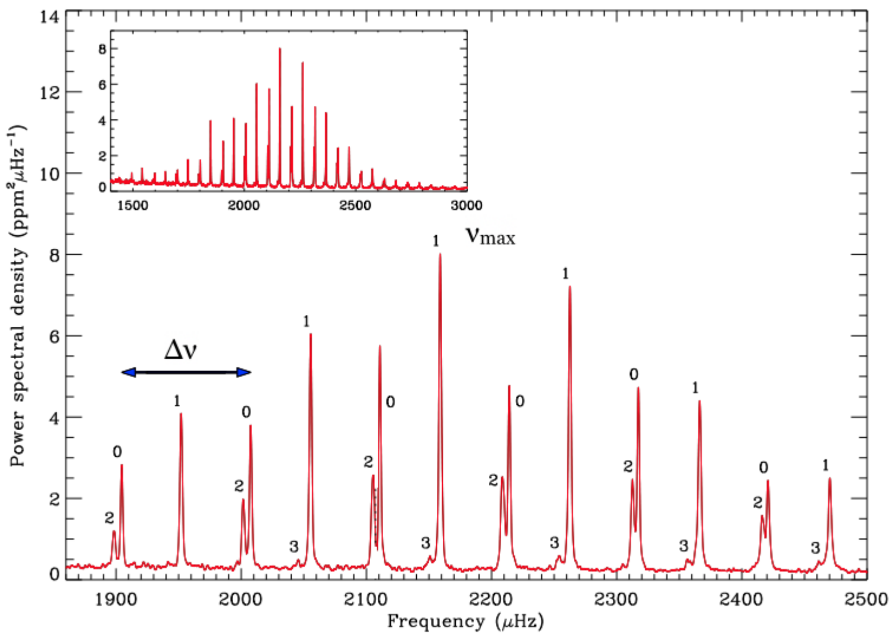

Figure 1.4 Power spectral density as a function of frequency in the light curve of 16 Cyg A, a nearby G-type main sequence star observed by *Kepler*. The inset illustrates a wider range of frequencies where the full range of oscillations can be seen. In the main plot, $\nu_{\rm max}$, the frequency of maximum power, and $\Delta\nu$, the regular frequency spacing between different radial orders of oscillations, have been labeled. Numbers correspond to the different modes of oscillation (0: radial, 1: dipole, 2: quadrupole, 3: octupole). Multiple radial orders of each mode can be seen, separated by $\Delta\nu$. Modified from Chaplin & Miglio (2013).

with targets $\gtrsim$1 kiloparsec away from Earth (Chapters 3–5 **?**). Planets detected around these evolved stars will teach us about the spatial variation of the exoplanet distribution at the largest possible scales within our Galaxy. Thus, understanding how evolved systems correlate to main sequence systems will be crucial to infer the main sequence distribution of planets as a function of spatial location in our Galaxy.

1.2 Asteroseismology

Waves traveling through a physical medium can move transversely, as gravity waves, or longitudinally, as pressure waves. In a homologous physical medium such as a star, waves can propagate transversely as gravity waves or g-modes, where the restoring force is governed by buoyancy, or longitudinally as pressure waves or p-modes, where pressure gradients provide the restoring force. Below the acoustic cutoff frequency of a star, these waves can resonate at the stellar surface, providing direct information about internal structure from surface observations.

Turbulence, driven by convection at or near the surface of a star, will stochastically drive p-mode oscillations at the surface of that star while damping those oscillations internally (Houdek et al. 1999). These oscillations can be described as a series of spherical harmonics of radial order n, angular degree l, and azimuthal order m. For the Sun, a wide range of radial orders and angular degrees can be used to infer the subsurface structure of localized features, such as sunspots or coronal mass ejections, as well as global properties like the average stellar surface gravity, density, rotation period and age. In other stars, however, the effects of geometrical cancellation make the observation of high angular degrees impossible, and thus only the modes of low angular degree can be used, limiting analysis to the global properties of the star. Asteroseismology is the study of relating these observed oscillations to the physical properties of the star Christensen-Dalsgaard & Frandsen (1983).

Using photometric light curves with cadences of minutes to hours, such as those produced by *Kepler* and *K2*, we can measure stellar oscillations to sufficient precision to constrain fundamental stellar properties more precisely than current leading spectroscopic methods. This has been used to greatly refine the parameters of known planet hosting systems, and uncover and confirm new features in the known planet population (Huber et al. 2013a; Lundkvist et al. 2016; Van Eylen et al. 2018). Given the relatively lower frequency and higher amplitude of red giant oscillations, the 30-minute cadence data of *Kepler* and *K2* has been particularly beneficial for red giant asteroseismology, leading to multiple surveys of these stars with the *Kepler* telescope (Stello et al. 2013, 2017; Yu et al. 2018; Hon et al. 2018, Chapter 5).

Figure 1.4 shows the power spectral density of a Sun-like star exhibiting solar-like oscillations observed by *Kepler*. Multiple radial orders of oscillation are visible, with digits 0-3 highlighting the radial, dipole, quadrupole, and octopole oscillation modes respectively. The regular frequency spacing between two adjacent modes of the same angular degree is known as $\Delta\nu$, and is directly proportional to the square root of the average stellar density, expected to scale as follows (Ulrich 1986; Brown et al. 1991):

$$\Delta\nu = \frac{(M/M_{\odot})^{1/2}}{(R/R_{\odot})^{3/2}} \Delta\nu_{\odot}. \tag{1.4}$$

In addition, the inset in Figure 1.4 reveals the full range of frequencies over which stellar oscillations can be seen. This range of frequencies can be approximated by a Gaussian envelope with a central peak very near the frequency of maximum oscillation power. The frequency at the central peak of this Gaussian envelope is known as $\nu_{\rm max}$, and has been observed to be closely correlated with the acoustic cutoff frequency $\nu_{\rm ac}$ of a star (Brown et al. 1991; Kjeldsen & Bedding 1995). Thus, $\nu_{\rm max}$ is indirectly proportional to the surface gravity and effective temperature of a star:

$$\frac{\nu_{\rm max}}{\nu_{\rm max,\odot}} = \frac{g}{g_\odot}\left(\frac{T_{\rm eff}}{T_{\rm eff,\odot}}\right)^{-1/2} \tag{1.5}$$

Both $\Delta\nu$ and $\nu_{\rm max}$ have been labeled in Figure 1.4. We rearrange the above equations to solve for stellar mass and radius:

$$\frac{M}{\mathrm{M}_\odot} \approx \left(\frac{\nu_{\rm max}}{\nu_{\rm max,\odot}}\right)^3 \left(\frac{\Delta\nu}{f_{\Delta\nu}\Delta\nu_\odot}\right)^{-4} \left(\frac{T_{\rm eff}}{T_{\rm eff,\odot}}\right)^{1.5} \tag{1.6}$$

$$\frac{R}{\mathrm{R}_\odot} \approx \left(\frac{\nu_{\rm max}}{\nu_{\rm max,\odot}}\right) \left(\frac{\Delta\nu}{f_{\Delta\nu}\Delta\nu_\odot}\right)^{-2} \left(\frac{T_{\rm eff}}{T_{\rm eff,\odot}}\right)^{0.5}. \tag{1.7}$$

We adopt solar reference values of $\nu_{\rm max,\odot} = 3090$ μHz, $\Delta\nu_\odot = 135.1$ μHz and $T_{\rm eff,\odot} = 5777$ K as given in the literature (Huber et al. 2011).

A more detailed exploration of stellar oscillation modes observed by *Kepler* can reveal the age, rotation, and inclination properties of a star as well (Huber et al. 2013b). However, given the shorter time baseline of *K2* light curves, such detailed analysis was more difficult. Thus the asteroseismic analysis considered for this thesis project is limited to the use of the above quantities and equations. We performed ensemble asteroseismology on thousands of LLRGB stars to determine precise stellar radii and masses, and thus determine planet occurrence accurately for red giant stars (see Chapter 5 for more details).

1.3 Gaussian Process Analysis

Gaussian process (GP) regression is a nonparametric method to describe a dataset by evaluating correlations between n data points through a covariance kernel. This kernel describes the relationship of each point in the dataset to each other point, and can be expressed as an $n \times n$ matrix (subsequently referred to as the covariance matrix). The kernel is a function of hyperparameters. More complicated kernels can have more hyperparameters that characterize different qualities of the correlations in the data, such as various periods, characteristic amplitudes and length scales, etc.

Gaussian process regression is widely used in the field of machine learning (Neal 1997; Herbrich et al. 2003; Quiñonero-Candela & Rasmussen 2005; Wang et al. 2008). Gibson et al. (2012) introduced the technique to the field of exoplanets through analysis of transmission spectroscopy to model correlated noise in the instrumental systematics of HST/NICMOS. Haywood et al. (2014) have demonstrated the technique of GP modeling of RV and photometric signals for the CoRoT-7 planetary system, first modeling the photometry with a GP and then using the photometric GP hyperparameters to train the initial RV GP hyperparameters. This study demonstrated that in the case of CoRoT-7b, parametric stellar activity models gave incorrect planet properties and uncertainties. Thus, it is important to test many time series techniques, and further explore the novel application of GPs in stellar variability analysis.

Finding the best GP regression requires choosing a kernel and initial hyperparameters, evaluating the likelihood of those hyperparameter values, and then iterating through parameter space until the most likely values are found. The squared exponential kernel, for example, defines a covariance matrix through an operator,

$$\Sigma_{ij} = k(t_i, t_j) = h^2 \exp\left[- \left(\frac{t_i - t_j}{\lambda} \right)^2 \right], \tag{1.8}$$

where h is the covariance amplitude, and λ the covariance length scale. The amplitude observed is described by h, while λ is a characteristic timescale over which the data is going to be correlated. This kernel function can be used to describe correlated noise, such as stellar variability, and thus by identifying the best fit kernel function hyperparameters, we can model this variability robustly and obtain more accurate transit depths for red giant stars (see Chapter 2).

In addition, more complex Gaussian process kernels can be used to describe periodic and quasiperiodic variability. These models are important for describing other variations of stellar variability, such as rotation, particularly in systems where planetary periods are easily distinguished from stellar rotation timescales. Quasiperiodic models have been shown to be effective at describing stellar activity observed in RV measurements, allowing the recovery of a much smaller amplitude

Table 1.1. Gaussian Process Kernel Options

Name	Mathematical expression	Hyperparameters[a]	Comments
Squared exponential	$h^2 \exp\left[-\left(\frac{t_i - t_j}{\lambda}\right)^2\right]$	h, λ	h amplitude,
			λ a characteristic timescale
Periodic	$h^2 \exp\left[-\frac{\sin^2[\pi(t_i - t_j)/\theta]}{2w^2}\right]$	h, θ, w	θ equivalent to $\mathrm{P_{rot}}$,
			w similar to above λ expressed as a fraction of θ
Quasi-Periodic	$h^2 \exp\left[-\frac{\sin^2[\pi(t_i - t_j)/\theta]}{2w^2} - \left(\frac{t_i - t_j}{\lambda}\right)^2\right]$	h, θ, w, λ	w coherence of periodic variation
			λ timescale of aperiodic variation

Note. — The name of kernel functions and hyperparameters in Table 1.1 are taken from Rasmussen (2006).

[a]Each kernel $\mathbf{\Sigma_{ij}}$ can be modified to include an additional hyperparameter, a white noise term σ^2 by adding one in quadrature: $\mathbf{\Sigma_{ij}} = \mathbf{\Sigma_{ij}} + \sigma^2 \mathbf{I}_i$.

planetary signal underneath (Grunblatt et al. 2015). We discuss the quasiperiodic kernel and other simple GP kernels and the inferred physical meaning of their hyperparameters in Table 1.1.

Approximations to the covariance matrix used in GP analysis can vastly expand the speed of the GP calculation, opening the door to a much wider range of potential kernel models. Approximating the covariance matrix as a tridiagonal matrix allows us to treat stellar variability as a simple damped harmonic oscillator (Foreman-Mackey et al. 2017). As stellar oscillations can be described as damped harmonic oscillations, asteroseismic models can be generated from simple harmonic oscillator GP regressions of oscillating star data. These models can then be combined with planet transit models to simultaneously characterize stellar and planet parameters, and provide comparable transit depth precision to the simpler kernel functions, as we demonstrate in Chapter 3. We use this asteroseismic GP model to marginalize over stellar variability when measuring transit depths in Chapters 3 and 5.

The logarithm of the posterior likelihood of the GP regression is calculated as

$$\log[\mathcal{L}(\mathbf{r})] = -\frac{1}{2}\mathbf{r}^{\mathrm{T}}\mathbf{\Sigma}^{-1}\mathbf{r} - \frac{1}{2}\log|\mathbf{\Sigma}| - \frac{n}{2}\log(2\pi), \tag{1.9}$$

where $\mathbf{r}$ is the vector of residuals after removal of the (optional) mean function, $\mathbf{\Sigma}$ is the covariance matrix, and n the number of data points. A prior term, $\mathcal{L}_{\mathrm{prior}}$, can be added to the likelihood to account for any priors placed on the hyperparameters. This likelihood calculation can be used to

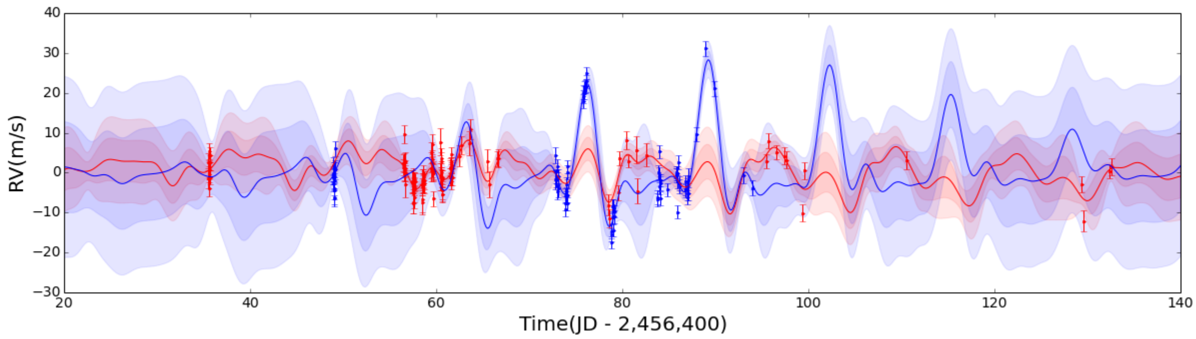

Figure 1.5 Radial velocity signal of Kepler-78 as a function of time, measured by Keck/HIRES (blue) and TNG/HARPS-N (red). A quasiperiodic Gaussian process model has been used to describe both datasets. By treating the quasiperiodic, longer-period stellar activity signal as a Gaussian process, the signal can be removed to reveal the signal of Kepler-78b, a lava world in an 8-hour orbit, at one-tenth the RV amplitude. Taken from Grunblatt et al. (2015).

identify the best fit GP hyperparameters. For a more complete description of Gaussian process regression and posterior likelihood evaluation, see Rasmussen (2006).

Chapter 2

K2-97b: A (Re-?)Inflated Planet Orbiting a Red Giant Star

This chapter has been published previously in the *Astronomical Journal* (Grunblatt, S., Huber, D., Gaidos, E. et al, 2016, AJ 152, 185).

2.1 Introduction

The first measurements of the radius of a planet outside our solar system were reported by Charbonneau et al. (2000) and Henry et al. (2000). These groundbreaking measurements also revealed a mystery in exoplanet science: the planet radius was considerably larger than expected from planet models (Burrows et al. 1997; Bodenheimer et al. 2001; Guillot & Showman 2002). Further transit studies of giant planets in short period orbits revealed similarly enlarged planets (Collier Cameron et al. 1999; Hebb et al. 2009). Although very young ($<$ 10 Myr) planets are expected to have large radii ($>$1.2 R_J) due to heat from formation, this cannot explain the dozens of known planets with radii $>$1.2 R_J orbiting several billion year old stars (Guillot & Gautier 2014). Moreover, a correlation has been observed between incident stellar radiation and planetary radius inflation (Burrows et al. 2000; Laughlin et al. 2011; Lopez & Fortney 2016).

Several potential mechanisms for planet inflation have been suggested (Baraffe et al. 2014), but these mechanisms can generally be placed into two broad classes. In the first class, $\lesssim$1% of the stellar irradiance is deposited into the planet's interior, causing the planet to heat and expand (Batygin & Stevenson 2010). In the second class, the planet retains its initial heat from formation and remains inflated due to stalled contraction (Chabrier & Baraffe 2007; Wu & Lithwick 2013). A planet with an orbital period of ~10-30 days would be too cool to be inflated around a solar-type main sequence star, but would experience irradiation >500 times the flux on Earth for more than 100 Myr while its host star evolves onto the red giant branch. Thus, the discovery of an inflated planet in this period range around an evolved star would indicate that inflation is a response to high stellar irradiation, whereas a population of exclusively non-inflated gas giant planets would suggest that inflation is governed more strongly by delayed cooling (Lopez & Fortney 2016).

Searches for planets around evolved stars may also provide clues to understanding the occurrence of planets around stars more massive than the Sun. Massive stars have been observed to produce more giant planets than small stars (Johnson & Apps 2009; Gaidos et al. 2013), suggesting that these stars have more planet-forming material than small stars (Andrews et al. 2013). However, the larger radii of these stars make planet transit signals smaller. More importantly, the fast rotation and relatively few absorption lines of main sequence, intermediate-mass ($\geq$1.5 $M_\odot$) stars made planet detection using radial velocities difficult before the *Kepler* era. However, these F- and A-type stars evolve into G- and K-type giants with deeper absorption lines and slower rotation rates, allowing precise radial velocity measurement. Early radial velocity surveys to investigate planet occurrence as a function of stellar mass included evolved stars (Johnson et al. 2007a), and indicated a strong correlation between planet occurrence and stellar mass. However, this correlation is heavily debated, as the short lives and intrinsic rarity of these stars result in systematic uncertainties on host star masses derived from stellar models (Lloyd 2011; Schlaufman & Winn 2013; Lloyd 2013; Johnson et al. 2013, 2014; Ghezzi & Johnson 2015).

To answer the questions of giant planet occurrence and inflation, we have begun a search for transiting planets orbiting giant stars with the NASA K2 Mission (Howell et al. 2014; Huber et al. 2015). By targeting low-luminosity red-giant branch (RGB) stars which oscillate with frequencies detectable with K2's long-cadence data, stellar radius and mass can be precisely determined using asteroseismology for stars around which giant planet transits are detectable. This precision is crucial to investigate the mechanisms for planet inflation and the dependence of planet occurrence on stellar mass. Here, we present the discovery and characterization of the first planet from our survey.

2.2 Observations

2.2.1 K2 Photometry

In the K2 extension to the NASA *Kepler* mission, multiple fields along the ecliptic are observed almost continuously for approximately 80 days (Howell et al. 2014). EPIC 211351816 (now known as K2-97) was selected for observation as a part of K2 Guest Observer Proposal GO5089 (PI: Huber) and observed in Campaign 5 of K2 during the first half of 2015. As the *Kepler* telescope now has unstable pointing due to the failure of two of its reaction wheels, it is necessary to correct for the pointing-dependent error in the flux received per pixel. We produced a lightcurve by simultaneously fitting thruster systematics, low frequency variability, and planet transits with a Levenberg-Marquardt minimization algorithm, using a modified version of the pipeline from Vanderburg et al. (2016).

We also analyzed the PDC-MAP light curve provided by the K2 Science Office (Stumpe et al. 2012; Smith et al. 2012) as well as the detrended lightcurves created with the methods of Vanderburg et al. (2016), Petigura (2015), and Aigrain et al. (2016). The use of different lightcurves resulted in statistically significant differences in the transit depth, illustrating the additional systematic uncertainties introduced by lightcurve reductions (see § 5.1 for more details). However, the results from all lightcurves analyzed were broadly consistent with the modified Vanderburg et al. (2016) results (see Discussion). Figure 5.5 shows our adopted lightcurve for K2-97.

2.2.2 Imaging with Keck/NIRC2 AO

Natural guide-star adaptive optics (AO) images of K2-97 were obtained through the broad K$'$ filter ($\lambda_{\rm center}$ = 2.124 μm) with the Near-Infrared Camera (NIRC2) at the Keck-2 telescope on Mauna Kea during the nights of UT 19 March and 12 May 2016. The narrow camera (pixel scale 0.01”) was used for both sets of observations. No additional sources were detected within $\sim$3” of the star. The contrast ratio of the detection limit is more than 7 magnitudes at 0.5”; brighter objects could be detected to within 0.15” of the star.

2.2.3 Spectroscopy with UH88/SNIFS, IRTF/SpeX, and Keck/HIRES

We obtained a high resolution, high signal-to-noise spectrum of K2-97 using the High Resolution Echelle Spectrometer (HIRES) on the 10 meter Keck-I telescope at Mauna Kea Observatory on the

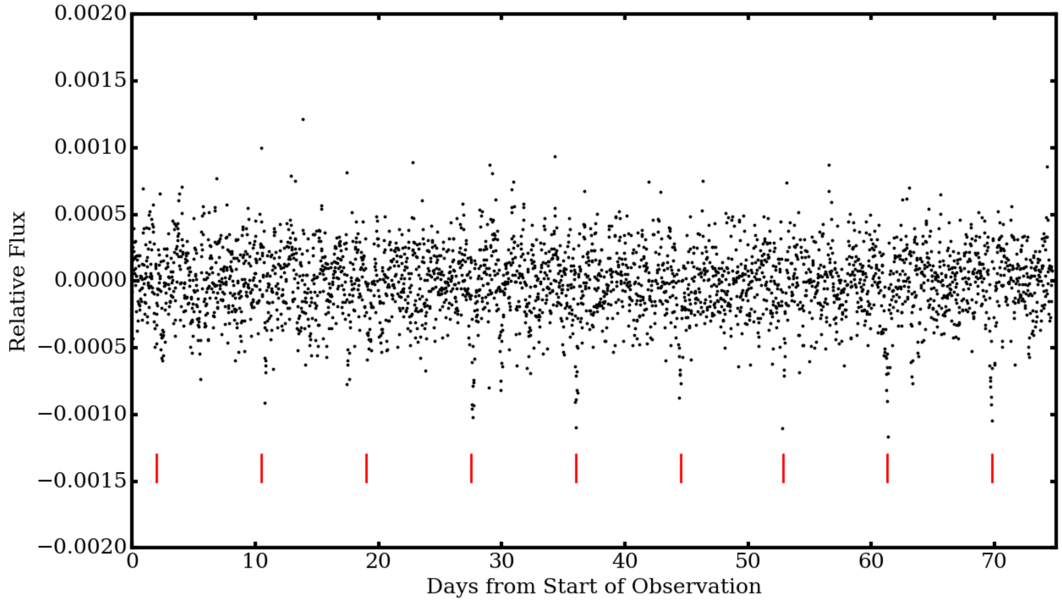

Figure 2.1 Detrended K2 lightcurve of K2-97. This lightcurve was produced using a modified method of the pipeline presented in Vanderburg et al. (2016), where both instrument systematics and the planet transit were modeled simultaneously to prevent transit dilution. The lightcurve has been normalized as well as unity subtracted. Individual transits are visible by eye, and are denoted by red fiducial marks.

Big Island of Hawaii. HIRES provides spectral resolution of roughly 100,000 in a wavelength range of 0.3 to 1.0 microns (Vogt et al. 1994). We also obtained medium-resolution optical and infrared spectra using the Supernova Integrated Field Spectrograph (SNIFS) on the 2.2 meter University of Hawaii telescope and SpeX on the 3 meter Infrared Telescope Facility (IRTF), providing spectral resolution of 1000–2000 over a wavelength range from 0.3 to 5.5 microns (Lantz et al. 2004; Rayner et al. 2003).

We joined and flux calibrated the SNIFS and SpeX spectra following the method outlined in Mann et al. (2015). We first downloaded photometry from the Two-Micron All-Sky Survey (2MASS, Skrutskie et al. 2006), AAVSO All-Sky Photometric Survey (APASS, Henden et al. 2012), and The Wide-field Infrared Survey Explorer (WISE, Wright et al. 2010). The spectrum and all photometry were converted to physical fluxes using the appropriate zero-points and filter profiles (Cohen et al. 2003; Jarrett et al. 2011; Mann & von Braun 2015). We scaled the optical and NIR spectra to match the photometry and each other in overlapping regions (0.8-0.95 μm), accounting for correlated errors in the flux calibration. Regions of high telluric contamination or missing from our spectrum (e.g., beyond 2.4 μm) were replaced with a best-fit atmospheric model from the BT-SETTL grid (Allard et al. 2011, 2013). The final calibrated and combined spectrum is shown in Figure 2.2.

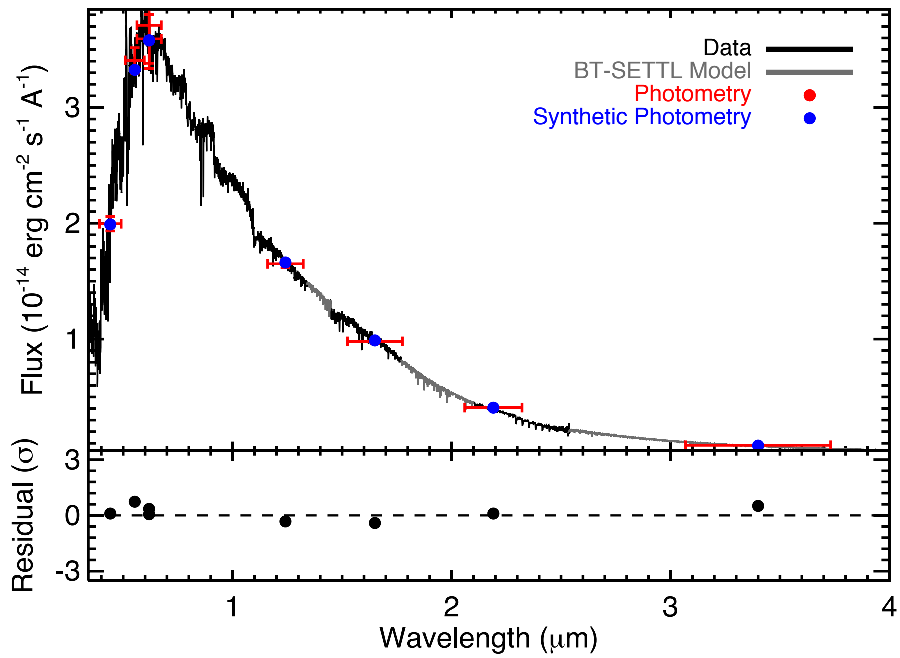

Figure 2.2 Flux calibrated optical and NIR spectrum of EPIC 211351816. Photometry is shown in red, with the horizontal error bars representing the effective width of the filter. Synthetic photometry derived from the spectrum is shown in blue. We replaced regions of high telluric absorption and those outside the range of our empirical spectra with an atmospheric model, which we show in grey. The spectrum and photometry shown here have not been corrected for reddening. The bottom panel shows the residual (photometry-synthetic) in units of standard deviations.

2.2.4 Radial Velocity Measurements

Radial velocity measurements were obtained between January 27 and May 16, 2016 using the High Resolution Echelle Spectrometer (HIRES) on the Keck-I Telescope at the Mauna Kea Observatory in Hawaii and the Levy spectrometer on the Automated Planet Finder (APF) telescope at Lick Observatory in California. The specific measurements are listed in Table 3.1. The nine spectra observed were obtained using an iodine cell. Measurements with the Keck telescope achieved a precision of greater than 1 m s^{-1}, whereas the APF measurements have measurement uncertainties of $\sim$30 m s^{-1}. We collected three measurements with Keck/HIRES and six with APF.

The Levy Spectrograph is a high-resolution slit-fed optical echelle spectrograph mounted at one of the two Nasmyth foci of the APF designed specifically for the detection and characterization of

Table 2.1. Radial Velocities

BJD-2440000	RV (m s^{-1})	Prec. (m s^{-1})	Tel./inst. used
17414.927751	14.84	0.68	Keck/HIRES
17422.855362	-17.18	0.72	Keck/HIRES
17439.964043	1.92	0.82	Keck/HIRES
17495.743272	-2	24	APF/Levy
17498.729824	-30	27	APF/Levy
17505.670536	-84	39	APF/Levy
17507.723056	27	30	APF/Levy
17524.687701	0	32	APF/Levy
17525.686520	67	30	APF/Levy

Note. — The precisions listed here are instrumental only, and do not take into account the uncertainty introduced by stellar jitter. For evolved stars, radial velocity jitter on relevant timescales is typically ∼5 m s^{-1} (see text).

exoplanets (Burt et al. 2014; Fulton et al. 2015). Each spectrum covers a continuous wavelength range from 3740 to 9700 Å. We observed EPIC 211351816 using a 1.0” wide decker for an approximate spectral resolution of R = 100,000. Starlight passed through a cell of gaseous iodine which serves as a simultaneous calibration source for the instrumental PSF and wavelength reference. We measured relative RVs using a Doppler pipeline descended from the iodine technique in Butler et al. (1996). We forward-modeled 848 segments of each spectrum between 5000 and 6200 Å. The model consists of a stellar template spectrum, an ultra high-resolution Fourier transform spectrum of the iodine absorption of the Levy cell, a spatially variable PSF, a wavelength solution, and RV. Traditionally, a high signal-to-noise iodine-free observation of the same star is deconvolved with the instrumental PSF and used as the stellar template in the forward modeling process. However, in this case the star is too faint to collect the signal-to-noise needed for reliable deconvolution in a reasonable amount of time on the APF. Instead, we simulated this observation by using the SpecMatch software (Petigura 2015) to construct a synthetic template from the Coelho (2014) models and best-fit stellar parameters.

2.3 Host Star Characteristics

2.3.1 Spectroscopic Analysis

In order to obtain precise values for the stellar parameters, we collected a moderate signal-to-noise iodine-free observation using the HIRES spectrograph on the Keck I telescope (Vogt et al. 1994).

We measured the effective temperature ($T_{\rm eff}$), surface gravity ($\log g$), iron abundance ([Fe/H]), and rotational velocity of the star using the tools available in the SpecMatch software package (Petigura 2015). We first corrected the observed wavelengths to be in the observers rest frame by cross-correlating a solar model with the observed spectrum. Then we fit for $T_{\rm eff}$, $\log g$, [Fe/H], $v\sin i$, and the instrumental PSF using the underlying Bayesian differential-evolution Markov Chain Monte Carlo machinery of ExoPy (Fulton et al. 2013). At each step in the MCMC chains, a synthetic spectrum is created by interpolating the Coelho (2014) grid of stellar models for a set of $T_{\rm eff}$, $\log g$, and [Fe/H] values and solar alpha abundance. We convolved this synthetic spectrum with a rotational plus macroturbulence broadening kernel using the prescriptions of Valenti & Fischer (2005) and Hirano et al. (2011). Finally, we performed another convolution with a Gaussian kernel to account for the instrumental PSF, and compared the synthetic spectrum with the observed spectrum to assess the goodness of fit. The priors are uniform in $T_{\rm eff}$, $\log g$, and [Fe/H] but we assign a Gaussian prior to the instrumental PSF that encompasses the typical variability in the PSF width caused by seeing changes and guiding errors. Five echelle orders of the spectrum were fit separately and the resulting posterior distributions were combined before taking the median values for each parameter. Parameter uncertainties were estimated as the scatter in spectroscopic parameters given by SpecMatch relative to the values for 352 stars in the in Valenti & Fischer (2005) sample and 76 stars in the Huber et al. (2013a) asteroseismic sample. Systematic trends in SpecMatch values as a function of $T_{\rm eff}$, $\log g$, and [Fe/H] relative to these benchmark samples were fit for and removed in the final quoted parameter values. Initial fits to the stellar spectrum for $T_{\rm eff}$, $\log g$, [Fe/H], and $v\sin i$ were made without asteroseismic constraints, and were found to be in good agreement with the asteroseismic quantities. A prior was applied to the value for $\log g$ based on the asteroseismic estimate of 3.26 ± 0.015 (see Section 3.2), which resulted in convergence to the values listed in Table 4.1.

2.3.2 Asteroseismology

Stellar oscillations are a powerful tool to determine precise fundamental properties of exoplanet host stars (e.g Christensen-Dalsgaard et al. 2010; Gilliland et al. 2011; Huber et al. 2013a). The top panel of Figure 3.3 shows the power spectrum calculated from the K2 data after removing the transits from the light curve. We detect a strong power excess with regularly spaced peaks near $\sim 220\,\mu$Hz (75 minutes), typical for an oscillating low-luminosity red giant star.

The power excess can be characterized by the frequency of maximum power ($\nu_{\rm max}$) and the average separation of modes with the same spherical degree and consecutive radial order ($\Delta\nu$). To measure $\nu_{\rm max}$ and $\Delta\nu$ we analyzed the K2SC lightcurve of this system (Aigrain et al. 2016) using the method of Huber et al. (2009), which corrects the background granulation noise by fitting a 2-component Harvey model (Harvey 1985) in the frequency domain. The frequency of maximum power was then measured from the peak of the heavily smoothed, background-corrected power spectrum, and $\Delta\nu$ was measured using an autocorrelation of the power spectrum. We calculated uncertainties using 1000 Monte Carlo simulations as described in Huber et al. (2011), yielding $\nu_{\rm max} = 223.7 \pm 5.4$ μHz and $\Delta\nu = 16.83 \pm 0.17$ μHz.

The bottom panel of Figure 3.3 shows an échelle diagram, which stacks radial orders on top of each other, showing the asymptotic spacing of oscillation modes with the same spherical degree l. The échelle diagram of K2-97 shows the characteristic signature of nearly vertically aligned quadrupole ($l = 2$) and radial ($l = 0$) modes, while the dipole modes ($l = 1$) show a more complex distribution due to the coupling of pressure modes with gravity mode in the core (known as mixed modes, e.g. Dziembowski et al. 2001; Montalbán et al. 2010; Bedding et al. 2010). The position of the $l = 0$ ridge agrees with the expected value for a low-luminosity RGB star (Huber et al. 2010; Corsaro et al. 2012).

To estimate stellar properties from $\nu_{\rm max}$ and $\Delta\nu$, we use the scaling relations of Brown et al. (1991); Kjeldsen & Bedding (1995):

$$\frac{\Delta\nu}{\Delta\nu_\odot} \approx f_{\Delta\nu} \left(\frac{\rho}{\rho_\odot}\right)^{0.5} , \tag{2.1}$$

$$\frac{\nu_{\rm max}}{\nu_{\rm max,\odot}} \approx \frac{g}{{\rm g}_\odot} \left(\frac{T_{\rm eff}}{T_{\rm eff,\odot}}\right)^{-0.5} . \tag{2.2}$$

Equations (1) and (2) can be rearranged to solve for mass and radius:

$$\frac{M}{{\rm M}_\odot} \approx \left(\frac{\nu_{\rm max}}{\nu_{\rm max,\odot}}\right)^{3} \left(\frac{\Delta\nu}{f_{\Delta\nu}\Delta\nu_\odot}\right)^{-4} \left(\frac{T_{\rm eff}}{T_{\rm eff,\odot}}\right)^{1.5} \tag{2.3}$$

$$\frac{R}{{\rm R}_\odot} \approx \left(\frac{\nu_{\rm max}}{\nu_{\rm max,\odot}}\right) \left(\frac{\Delta\nu}{f_{\Delta\nu}\Delta\nu_\odot}\right)^{-2} \left(\frac{T_{\rm eff}}{T_{\rm eff,\odot}}\right)^{0.5} . \tag{2.4}$$

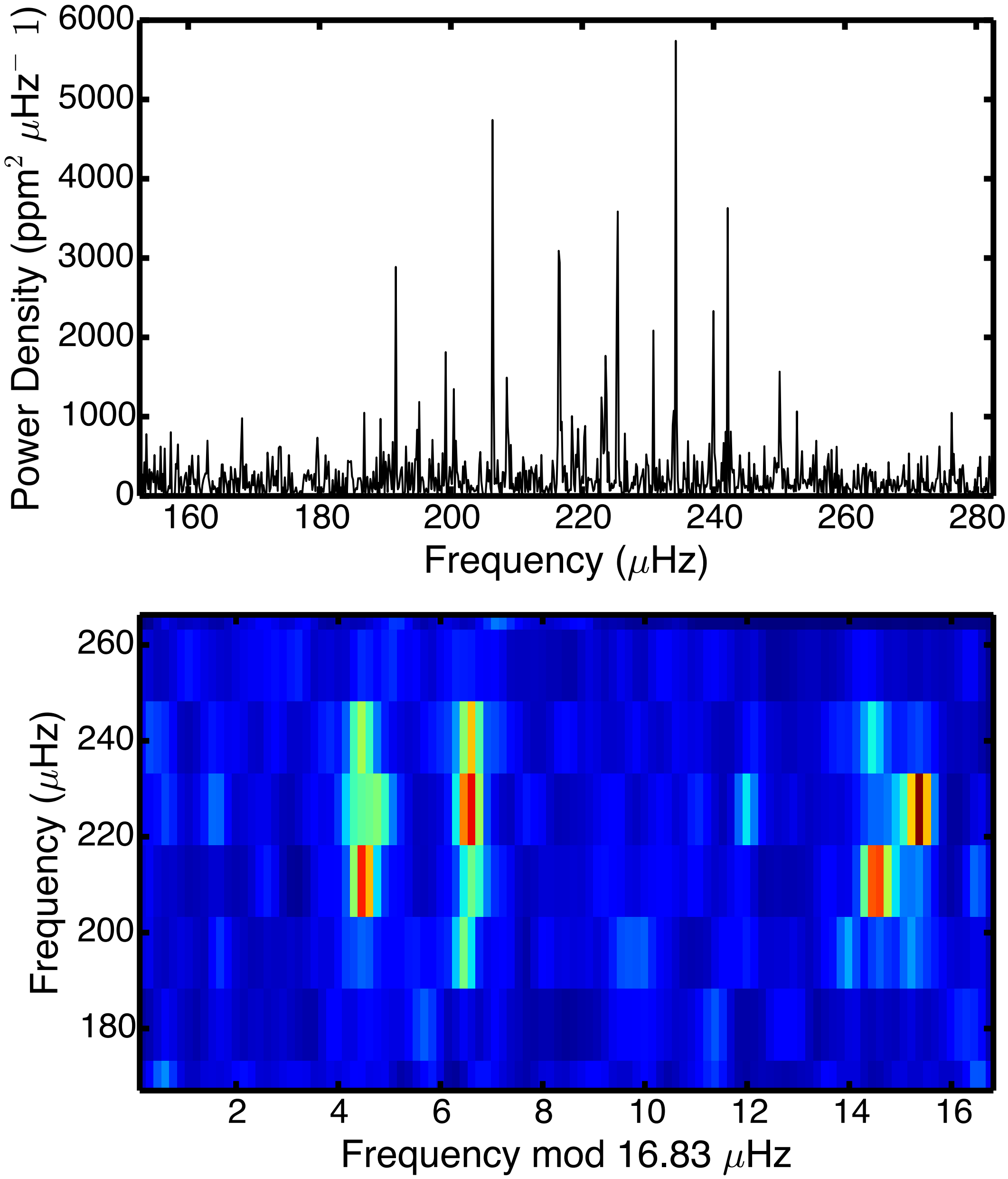

Figure 2.3 Top panel: Power spectrum of the K2 time series centered on the frequency region with detected oscillations. Bottom panel: Echelle diagram of the granulation background-corrected power spectrum using $\Delta\nu = 16.83\mu\,$Hz. Oscillation modes with $l = 0, 2$ (left) and $l = 1$ (right) are visible. Note that dipole mode series is more complex due to the presence of mixed modes.

Table 2.2. Stellar and Planetary Properties

Property	Value	Source
ID	K2-97, EPIC 211351816, 2MASS 08310308+1050513	Huber et al. (2016)
Kepler Magnitude	12.409	Huber et al. (2016)
T_{eff}	4790 ± 90 K	spectroscopy
$V sin(i)$	2.8 ± 1.6 km s^{-1}	spectroscopy
[Fe/H]	+0.42 ± 0.08	spectroscopy
Stellar Mass, M_{star}	1.16 ± 0.12 $M_\odot$	asteroseismology
Stellar Radius, R_{star}	4.20 ± 0.14 $R_\odot$	asteroseismology
Density, ρ_*	0.0222 ± 0.0004 g cm^{-3}	asteroseismology
log g	3.26 ± 0.01	asteroseismology
Age	7.8 ± 2 Gyr	isochrones
Planet Radius, R_p	1.31 ± 0.11 R_J	asteroseismology, GP+transit model
Orbital Period P_{orb}	8.4061 ± 0.0015 days	GP+transit model
Planet Mass, M_p	1.10 ± 0.11 M_J	asteroseismology, RV model

Our adopted solar reference values are $\nu_{\max,\odot} = 3090\,\mu$Hz and $\Delta\nu_\odot = 135.1\,\mu$Hz (Huber et al. 2011), as well as $T_{\text{eff},\odot} = 5777$ K.

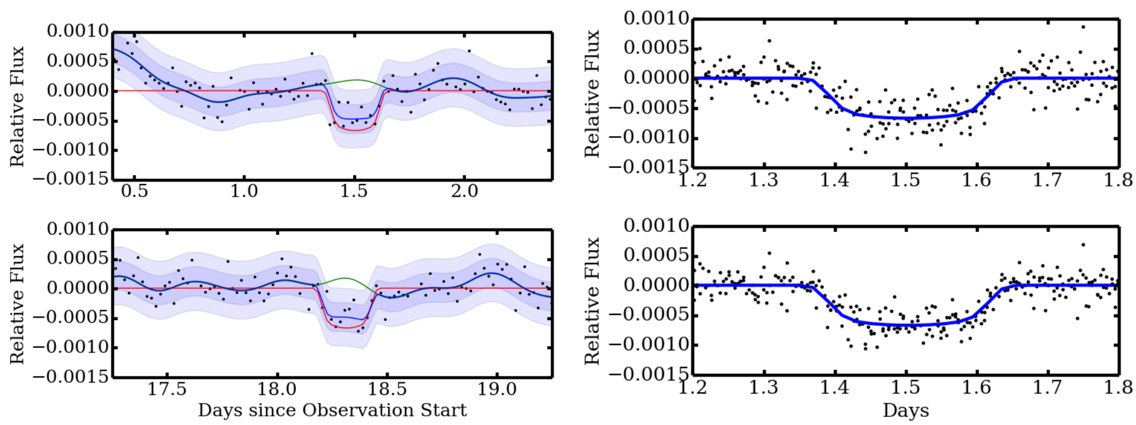

Figure 2.4 Left: Two examples of transits in the EPIC 211351816 lightcurve. Detrended K2 observations of K2-97 are shown as black dots. The best fit transit model has been plotted in red. The best-fit Gaussian process estimation to the residual lightcurve with transits subtracted is shown in green. The best-fit combined transit + GP model is shown in blue, with 1 and 2 σ errors given by the blue contours. The calculation of the relevant values is described in Section 4.1. Top Right: The lightcurve folded at the orbital period of the planet. The best fit transit model has been overplotted in dark blue. Bottom right: The lightcurve folded at the orbital period of the planet, after the best-fit GP model has been subtracted. The decrease in scatter is clearly visible.

Equations (1)–(4) are not exact, particularly for stars that are significantly more evolved than the Sun. Empirical tests using interferometry and open clusters and individual frequency modeling have illustrated that the relations typically hold to ∼5% in radius and ∼10% in mass. Comparisons to model frequencies have also demonstrated that the $\Delta\nu$ scaling relation shows systematic deviations of up to a few percent as a function of T_{eff} and [Fe/H] (White et al. 2011). We accounted for this through the correction factor $f_{\Delta\nu}$ in Equations (1)–(4), which we determined by iterating the spectroscopic $T_{\rm eff}$ and [Fe/H] as well as the asteroseismic mass and $\log g$ using the model grid by Sharma et al. (2016). The converged correction factor was $f_{\Delta\nu} = 0.994$, and our final adopted values for the stellar radius, mass, $\log g$ and density are listed in Table 4.1.

To estimate a stellar age, which cannot be derived from scaling relations alone, we used evolutionary tracks from Bressan et al. (2012). Matching the asteroseismic radius to an isochrone with the best-fit asteroseismic mass and [Fe/H] = +0.42 dex from spectroscopy (see Table 3.3) yielded ~7.8 ± 2 Gyr. An independent analysis using the BAyesian STellar Algorithm (BASTA), which is based a grid of BaSTI models and has been applied to model several dozen Kepler exoplanet host stars (Silva Aguirre et al. 2015), yielded strongly consistent results. The stellar age can be constrained more precisely by modeling individual asteroseismic frequencies, but such modeling is beyond the scope of this paper.

A model-independent estimate of the distance was found using the bolometric flux of $3.579 \pm 0.086 \times 10^{-13}$ W m^{-2} (uncorrected for extinction) computed from the flux-calibrated spectrum (§ 2.3), the temperature from the high-resolution spectroscopic analysis (§ 3.1), a reddening value of $E(B-V) = 0.039$ based on the maps of Schlafly & Finkbeiner (2011) and the extinction law of Fitzpatrick (1999). The estimated distance is 763 ± 42 pc, placing the star 350 pc above the galactic plane ($b = 27$ deg). The location well above the plane is consistent with the locations of other RGB stars (Casagrande et al. 2016) and justifies our use of the ∞ value for reddening.

2.4 Lightcurve Analysis and Planetary Parameters

2.4.1 Gaussian process transit model

The transit of K2-97b was first identified by applying the box least-squares algorithm of Kovács et al. (2002) to all targets in our K2 Campaign 5 program. The transits are sufficiently deep to be spotted by eye (see Figure 5.5) and the combined signal to noise is greater than 20, well above commonly adopted thresholds for significant transit events. The transit event was also identified in the planet candidate paper of Pope et al. (2016).

Evolved stars show correlated stellar noise on timescales of hours to weeks due to stellar granulation (Mathur et al. 2012), leading to significant biases in transit parameter estimation (Carter & Winn 2009; Barclay et al. 2015). To account for this, we used Gaussian process estimation, which has been successfully applied to remove correlated noise in transmission spectroscopy, Kepler lightcurves, and radial velocity data in the past (Gibson et al. 2012; Dawson et al. 2014; Haywood et al. 2014; Barclay et al. 2015; Grunblatt et al. 2015). This is accomplished by describing the covariance of the time-series data as an N×N matrix $\mathbf{\Sigma}$ where

$$\Sigma_{ij} = \sigma_i^2 \delta_{ij} + k(t_i, t_j) \tag{2.5}$$

where σ_i is the observational uncertainty, δ_{ij} is the Kronecker delta, and $k(t_i, t_j)$ is the so-called covariance kernel function that quantifies the correlations between data points. The simplest and most commonly used kernel function, the squared-exponential or radial basis function kernel, can be expressed as

$$k(t_i, t_j) = h^2 \exp\left[- \left(\frac{t_i - t_j}{\lambda} \right)^2 \right] \tag{2.6}$$

where the covariance amplitude h is measured in flux units and the length scale λ is measured in days (Rasmussen 2006). Previous transit studies have used the squared exponential kernel to remove correlated noise without removing the transit signal (Barclay et al. 2015).

To analyze the lightcurves, initial parameter guesses are selected for the kernel function, and then a likelihood of the residuals defined by the kernel function parameters is calculated, where the residuals are equivalent to the lightcurve with a Mandel-Agol transit model subtracted from it (Mandel & Agol 2002). The logarithm of the posterior likelihood of our model is given as

$$\log[\mathcal{L}(\mathbf{r})] = -\frac{1}{2}\mathbf{r}^{\mathrm{T}}\mathbf{\Sigma}^{-1}\mathbf{r} - \frac{1}{2}\log|\mathbf{\Sigma}| - \frac{n}{2}\log(2\pi), \tag{2.7}$$

where $\mathbf{r}$ is the vector of residuals of the data after removal of the mean function (in our case, $\mathbf{r}$ is the lightcurve signal minus the transit model), and n the number of data points.

The GP kernel function and transit model parameters are then fit as free parameters via Markov chain Monte Carlo (MCMC) exploration of parameter space using the Python software package `emcee` (Foreman-Mackey et al. 2013). The `emcee` package contains an Affine-invariant MCMC Ensemble sampler, which determines the maximum likelihood parameters through an iterative exploration of parameter space. We draw the planet radius from this MCMC exploration of parameter space, with 1-σ error corresponding to 68% confidence intervals in the MCMC distributions of all free parameters. Along with the planet-to-star radius ratio, the impact parameter,

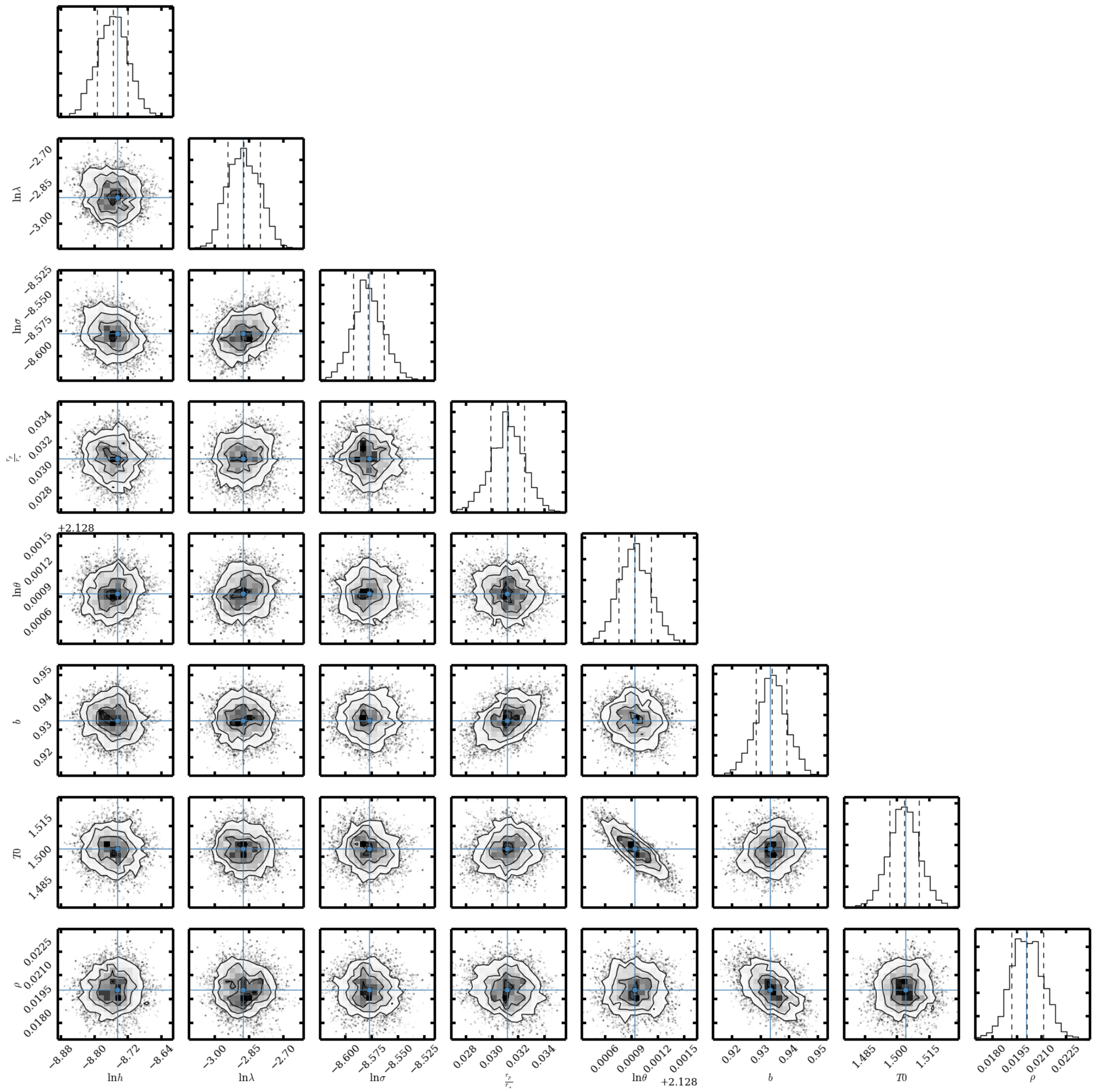

Figure 2.5 Posterior distributions and correlations between all pairs of parameters in our lightcurve MCMC model. Parameters include transit model parameters, squared exponential Gaussian process kernel parameters, and a stellar jitter term. Posterior distributions for each individual parameter are given along the diagonal. 2D contour plots show the correlations between individual parameter pairs. Blue lines correspond to median values. Dotted lines correspond to mean values and standard deviations from the mean. We find that our estimation of the transit depth is not strongly correlated with the other parameters in our model.

period, and ephemeris of transit were fit simultaneously with the Gaussian process kernel parameters and a photometric jitter term. Limb darkening parameters were fixed to the Claret & Bloemen (2011) stellar atmosphere model grid values closest to the measured temperature, surface gravity, and metallicity of the host star. Initial parameter values and priors were determined via a least

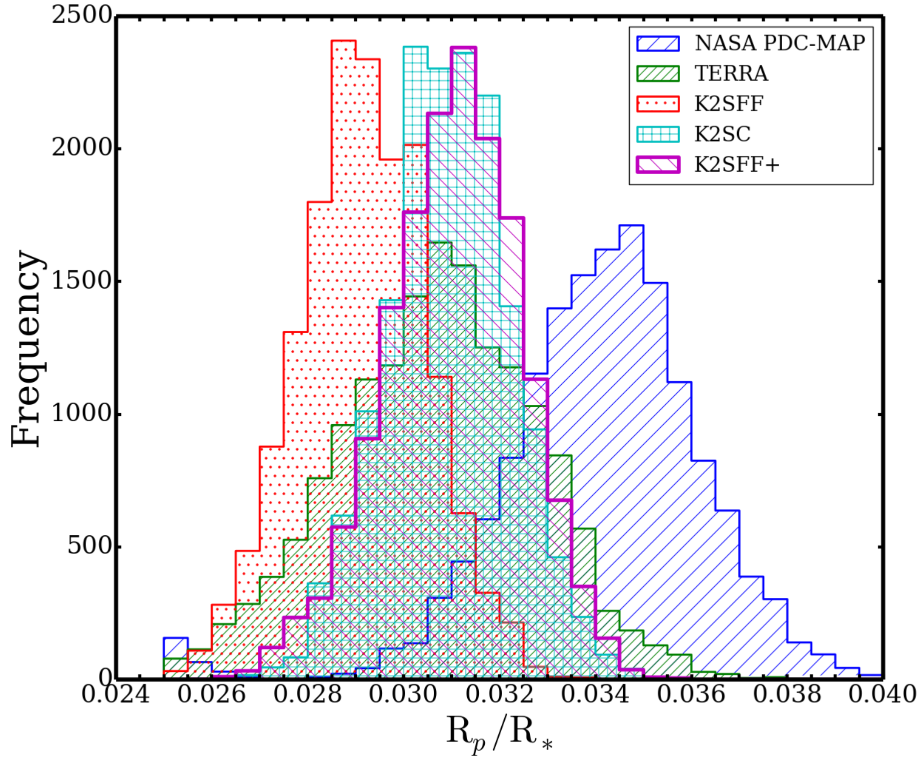

Figure 2.6 Recovered star-to-planet ratios for the K2-97b event using lightcurves produced with five different detrending algorithms. We find that the K2SFF lightcurve created with the algorithm of Vanderburg et al. (2016) produces the smallest planet to star ratios on average, while the NASA PDC-MAP lightcurve produces a planet to star ratio considerably larger than the other detrending algorithms. We choose the lightcurve where transits and instrumental effects were fit simultaneously for subsequent analysis, as a transit injection/recovery test comparing this K2SFF+ method and the standard K2SFF method revealed that transit depths were diluted by the standard K2SFF detrending but retained by the simultaneous K2SFF detrending and transit fit method.

squares transit fit using `ktransit` (Barclay 2015). The results and priors for this simultaneous parameter fitting are listed in Table 3.3 and parameter distributions are given in Figure 3.8.

To ensure our results were replicable, we performed a second MCMC analysis of the system using additional model parameters using a method very similar to that applied to Kepler-91 by Barclay et al. (2015). Mean stellar density, photometric zeropoint, two limb darkening parameters, radial velocity zero point, two Gaussian process hyperparameters, time of mid-transit, orbital period, impact parameter, the scaled planet radius, two eccentricity vectors ($e \sin \omega$ and $e \cos \omega$), radial velocity semi-amplitude, secondary eclipse depth, amplitude of ellipsoidal variations, amplitude of reflected light from the planet, and two uncertainty parameters added in quadrature with the reported uncertainties on radial velocity and photometric data were included in this secondary

Table 2.3. Posterior Probabilities from Lightcurve and Radial Velocity MCMC Modeling

Parameter	Median	84.1%	15.9 %	Prior
ρ (g cm^{-3})	0.020	+0.001	-0.001	$\mathcal{N}$(0.02; 0.001)
T_0 (BKJD)	2309.072	+0.007	-0.007	$\mathcal{U}$(1.3; 2.5)
$P_{\rm orb}$ (days)	8.4062	+0.0015	-0.0015	$\mathcal{U}$(8.3; 8.5)
b	0.933	+0.006	-0.007	$\mathcal{U}$(0.0, 1.0 + R_p/R_*)
R_p/R_*	0.0311	+0.0013	-0.0015	$\mathcal{U}$(0.0, 0.5)
K (m s^{-1})	103	+8	-8	
$T_{0,\rm RV}$ (BKJD)	2583.808	+0.007	-0.007	$\mathcal{U}$(0.0, $P_{\rm orb}$)
ln$f$	-3.8	+2.8	-3.9	$\mathcal{U}$(-10, 10)
$h_{\rm GP}$ (ppm)	157	+5	-5	$\mathcal{U}$(exp(-12, 0))
$\lambda_{\rm GP}$ (days)	0.057	+0.005	-0.004	$\mathcal{U}$(exp(-10, 10))
$\sigma_{\rm GP}$ (ppm)	189	+4	-4	$\mathcal{U}$(exp(-20, 0))

Note. — $\mathcal{N}$ indicates a normal distribution with mean and standard deviation given respectively. $\mathcal{U}$ indicates a uniform distribution between the two given boundaries. Ephemerides were fit relative to the first measurement in the sample and then later converted to Barycentric *Kepler* Julian Date (BKJD). Transit limb darkening parameters γ_1 and γ_2 were fixed to 0.6505 and 0.1041, respectively.

model. The priors on these parameters were uniform except for a Gaussian prior based on the asteroseismic value of the mean stellar density, priors that kept the two limb darkening parameters physical (Burke 2008) plus Gaussian priors with means taken from Claret & Bloemen (2011) and a standard deviation of 0.4, a prior of $1/e$ on the eccentricity to avoid biasing this value high (Eastman et al. 2012) and an additional prior that took the form of a Beta function with parameters determined by Van Eylen & Albrecht (2015). Additionally, we sampled the logarithm of the Gaussian process hyperparameters, RV semi-amplitude, secondary eclipse depth, ellipsoidal variations, reflected light, and two uncertainty parameters. We ran the MCMC algorithm using 600 walkers and 20,000 steps yielding 12 million samples. We found posteriors on the scaled planet radius of $0.0296^{+0.0035}_{-0.0024}$ and an impact parameter of $0.921^{+0.023}_{-0.032}$, strongly consistent with our earlier study. A secondary eclipse, ellipsoidal variations and any reflected light from the planet were not detected. We found an eccentricity of a few percent, marginally inconsistent with zero.

2.4.2 Radial Velocity Analysis: Planetary Confirmation and False Positive Assessment

We modeled the APF and Keck radial velocity measurements of the planet with a Keplerian orbital model. Assuming K2-97b would produce the dominant signal in the radial velocity measurements, we assume a circular orbit for the planet and fit the data with a sinusoid with a period set to the orbital period obtained from the transit fitting. Using a Markov chain Monte Carlo method, best-fit values were determined for the phase and amplitude of the radial velocity variations. We applied a velocity shift of 23 m s^{-1} to the APF measurements relative to the Keck measurements, and additionally fit for a non-zero offset to the resultant sinusoid to account for the different RV zero points of the two instruments. The mass of the planet was then estimated from the Doppler amplitude. The best fit RV model and relative measurement values are shown in Figure 3.9. As subgiant and giant stars are known to have an additional 4-6 m s^{-1} of velocity scatter due to stellar jitter (Johnson et al. 2007b), we adopted a value of 5 m s^{-1} and add it to our measurement errors in quadrature.

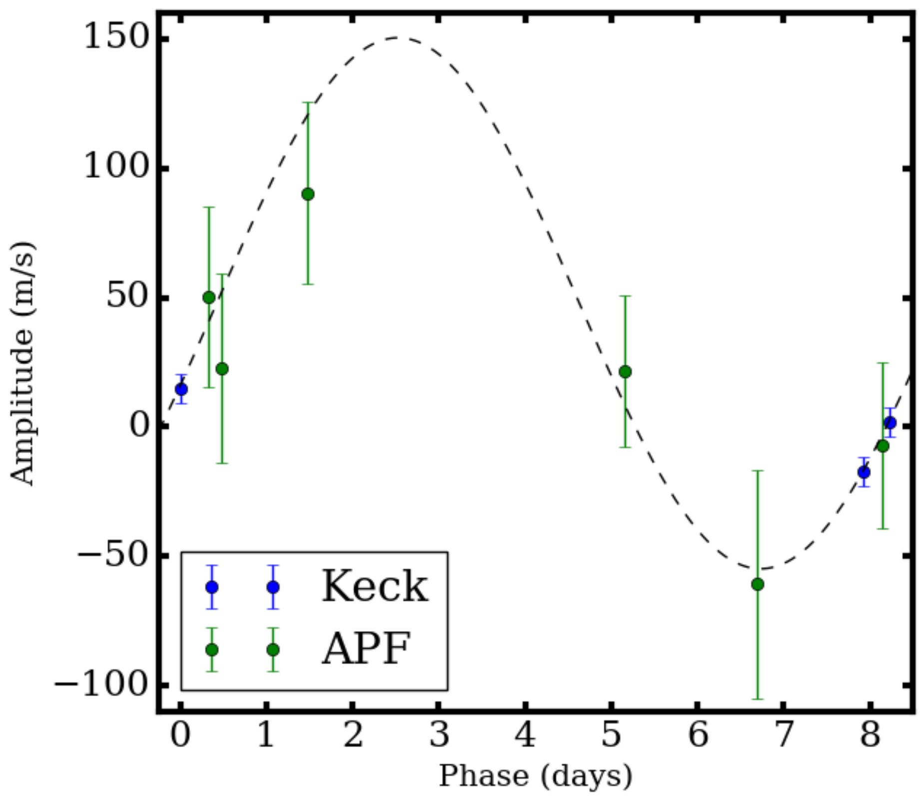

Figure 2.7 Radial velocity measurements of the system, phase-folded at the known orbital period. The initial measurements obtained with Keck/HIRES are shown in blue and have errors which are smaller than the markers in the plot. The remaining green measurements were taken with the Levy spectrometer on the Automated Planet Finder telescope. The dashed gray curve corresponds to a one-planet Keplerian orbit fit to the data. The best fit Keplerian orbital parameters were found using `emcee`. A stellar jitter term of 5 m s^{-1} was added in quadrature to make measurement errors more robust.

The *Kepler* pixels span 4" on the sky, and thus background eclipsing binaries (EBs) can often cause false positive transit signals (Jenkins et al. 2010; Batalha et al. 2010; Everett et al. 2015). In addition, the K2 lightcurve was constructed using an aperture that is 7 pixels or 28" across, exacerbating the possibility of a false positive. As the maximum transit depth of an EB is 50%, such a system would have to be at least as bright as Kepler magnitude (K_P) $\approx$ 19 to mimic a transit. To identify potential culprits, we searched the photometry database of the Sloan Digital Sky Survey (Data Release 9) for sources within 30" of K2-97. We identified only a single source (SDSS J083104.13+105112.9) of interest. It has an estimated $K_P = 19.05$, yet is well outside the photometric aperture and the small fraction of light scattered into the aperture by the *Kepler* point response function ensures it could not have produced the transit signal. No sources were detected in our Keck 2-NIRC 2 AO imaging down to $K' = 15.5 - 18$ (0.2-2"), corresponding to $K_P > 19$ for M dwarf stars that are the most likely components of faint background EBs.

To calculate a false positive probability for the background EB scenario, we followed the method of Gaidos et al. (2016). This discrete (Monte Carlo) Bayesian calculation uses a synthetic population generated by the TRILEGAL galactic stellar population model as priors (v. 1.6; Vanhollebeke et al. 2009) for 10 square degrees at the location of K2-97 on the sky. Likelihoods are calculated by imposing constraints on stellar density from the transit duration and orbital period, and on brightness from the non-detections in the SDSS and NIRC2 images, requiring that the diluted eclipse depth is at least equal to the transit depth. We found that the false positive probability for this scenario is effectively zero, as no star from the simulated background population can simultaneously satisfy the stellar magnitude and density constraints. Background stars are either too faint to produce the transit or are ruled out by our high-resolution imaging, and the long transit duration implies a stellar density that is too low for dwarf stars[1]. Low stellar density precludes a companion dwarf EB as the source of the signal; evolved companions are ruled out by our AO imaging to within 0.2" and stellar counterparts within ~ 1 AU are ruled out by the absence of a drift in our radial velocity data.

[1]Long transit durations can occur at the apoapsis of highly eccentric orbits, but such orbits would have been circularized by the ~7 Gyr age of this system.

2.5 Discussion

2.5.1 Is EPIC 211351816.01 Inflated?

We have described the discovery and characterization of a Jupiter-mass planet on an 8.4-day orbit around a red giant branch star. This object joins a sample of only five other known transiting planets hosted by highly evolved stars (Huber et al. 2013b; Lillo-Box et al. 2014; Barclay et al. 2015; Quinn et al. 2015; Ciceri et al. 2015; Van Eylen et al. 2016). The high metallicity of the host star is also characteristic of the close-in gas giant planet population, suggesting that this system may be simply a successor to such "hot Jupiter" systems.

As the stellar radius of K2-97 has been determined to 3% precision through asteroseismology, the dominant uncertainty in planet radius for this system comes from the transit depth. We compared the star-to-planet radius ratio (R_p/R_*) for this system using lightcurves produced by the PDC-MAP pipeline (Stumpe et al. 2012; Smith et al. 2012), the K2 "self flat field" (K2SFF) pipeline (Vanderburg et al. 2016) as well as a modified version of the Vanderburg et al. (2016) pipeline which simultaneously fit thruster systematics, low frequency variability, and planet transits with a Levenberg-Marquardt minimization algorithm, the K2SC pipeline (Aigrain et al. 2016), and the TERRA pipeline (Petigura et al. 2013). We find that measured transit depths varies by over 30% between the different systematic detrending pipelines we tested. We plot the spread in recovered star-to-planet radius ratios in Figure 2.6.

To investigate the differences in R_p/R_* recovered from lightcurves produced from different pipelines, we injected transits modeled from those in the K2-97 system into lightcurves (with systematics) of 50 stars classified as low-luminosity red giants from our K2 Campaign 5 target list. These lightcurves were then detrended using both the standard K2SFF method of Vanderburg et al. (2016) as well as the modified method which detrended instrumental noise and fit the planet transit simultaneously (hereby referred to as K2SFF+). The transit depths in both sets of processed lightcurves were then fit using a box least squares search (Kovács et al. 2002) and a Mandel-Agol transit model (Mandel & Agol 2002; Barclay 2015). This transit injection/recovery test revealed that the transit depth was retained with some scatter when both the transit and systematics were fit simultaneously, but when the systematics were fit and removed with the nominal Vanderburg et al. (2016) method, transit depths were reduced by 13% and the planet's radius was underestimated by 8% on average.

We report results from the K2SFF+ lightcurve as it was demonstrated to preserve transit depth through our transit injection/recovery tests, and its measured transit depth is strongly consistent with transit depths measured from two independently detrended lightcurves. We add an additional 5% error in planet radius to account for the uncertainty in transit fitting seen in the injection/recovery tests. Current and future studies with injection/recovery tests similar to those performed for Kepler (Petigura et al. 2013; Christiansen et al. 2015) will help resolve this discrepancy between accuracy and precision in measuring transit depths with K2.

2.5.2 Planet Inflation Scenarios

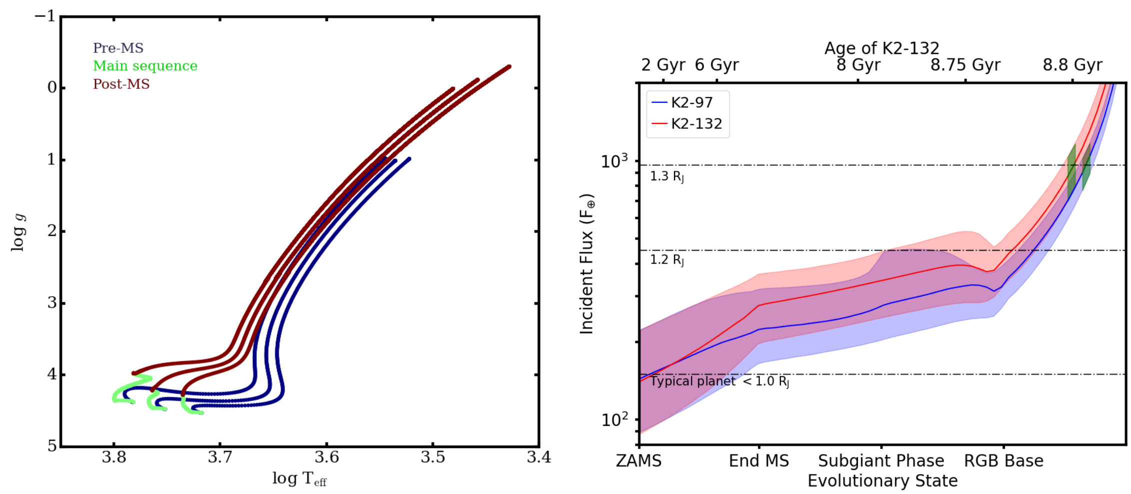

Figure 2.8 Left: Surface gravity versus effective temperature for 1.0 (rightmost), 1.15, and 1.3 $M_\odot$ (leftmost) Parsec evolutionary tracks with [Fe/H] = 0.60, +0.42, and 0.34 dex, respectively. Note that the choice of mass and metallicity correspond to lower and upper bounds for the stellar characteristics of K2-97. Blue, green, and red correspond to pre-main sequence, main sequence, and red giant branch stages of stellar evolution. Right: Change in incident flux on K2-97b over time for the models shown in the left panel. The current incident flux on the planet, assuming a stellar radius constrained by asteroseismic measurement, is denoted by dark green. The point at which the planet will be engulfed is denoted in orange, and tidally disrupted noted in yellow (see §5.3). The gray dotted line corresponds to the inflation threshold as cited by Lopez & Fortney (2016).

We can test planet inflation mechanisms by examining the response of planets to increasing irradiation as the host star leaves the main sequence. In particular, planets with orbital periods of <30 days will experience levels of irradiation comparable to typical hot Jupiters for more than 100 Myr. Following the nomenclature of Lopez & Fortney (2016), if the inflation mechanism requires direct heating and thus falls into Class I, the planet's radius should enter a re-inflated state around

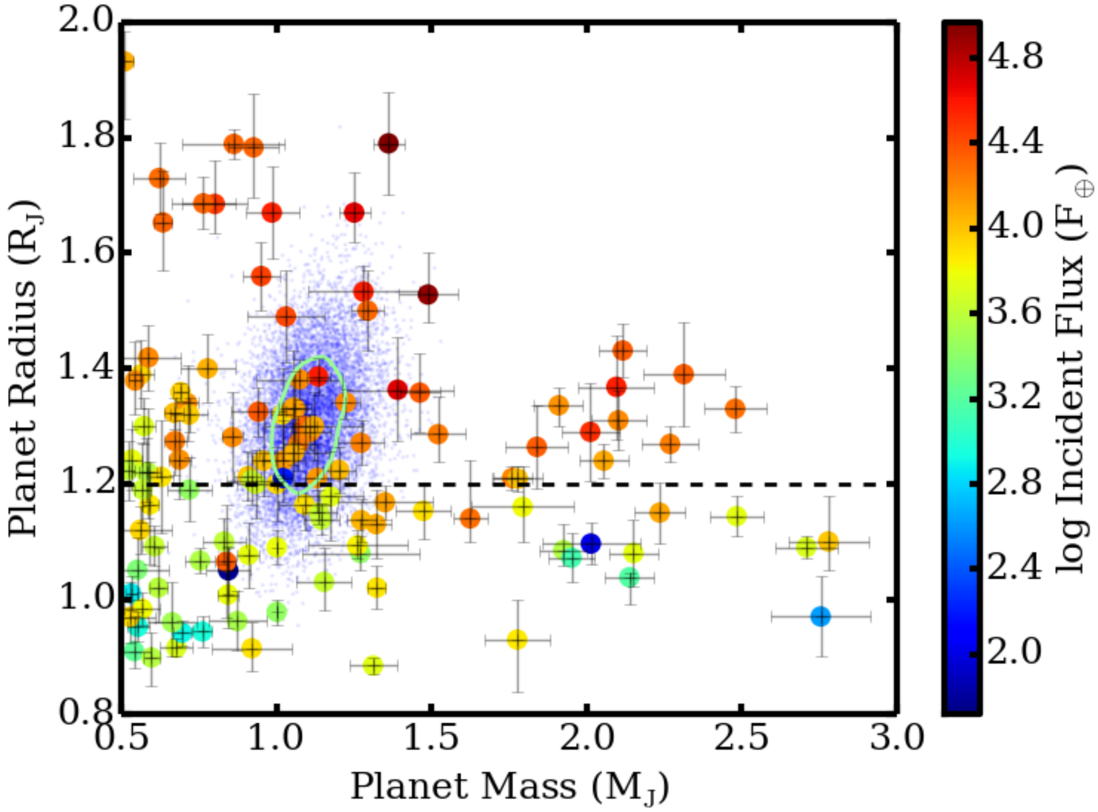

Figure 2.9 Planet mass versus radius in units of Jupiter mass and radius for well characterized planets with errors of less than 0.1 Jupiter radii and 0.2 Jupiter masses. The dotted line shows the approximate threshold of planet inflation, as given by Lopez & Fortney (2016). Color shows the logarithm of the incident flux in units of Earth fluxes. K2-97b is shown as the cloud of points near 1.25 R_J and 1.1 M_J, with 1-σ errors shown by the teal contour. The color of points in the cloud correspond to the incident flux K2-97b received on the main sequence, which is clearly uncharacteristic of the known, well-characterized inflated planets, suggestive of a non-inflated past. The color of the contour indicates its current incident flux. Planet characteristics have been taken from the Exoplanet Orbit Database and the Exoplanet Data Explorer at exoplanets.org.

a post-main sequence star. However, if the inflation mechanism falls into Class II, requiring delayed cooling, there should be no effect on planet radius as a star enters the red giant phase, and re-inflation will not occur. K2-97b provides a valuable test for the re-inflation hypothesis, as it is inflated now but orbits at a distance such that it may not have received irradiation above the inflation threshold for its entire existence.

To estimate the change in stellar irradiation over time, we use the Parsec evolutionary tracks (Bressan et al. 2012) with the host star mass and metallicity derived in §3.2. Figure 3.11 shows an HR diagram and incident flux evolution for models with masses of 1.0, 1.15 and 1.3 $M_\odot$ from the

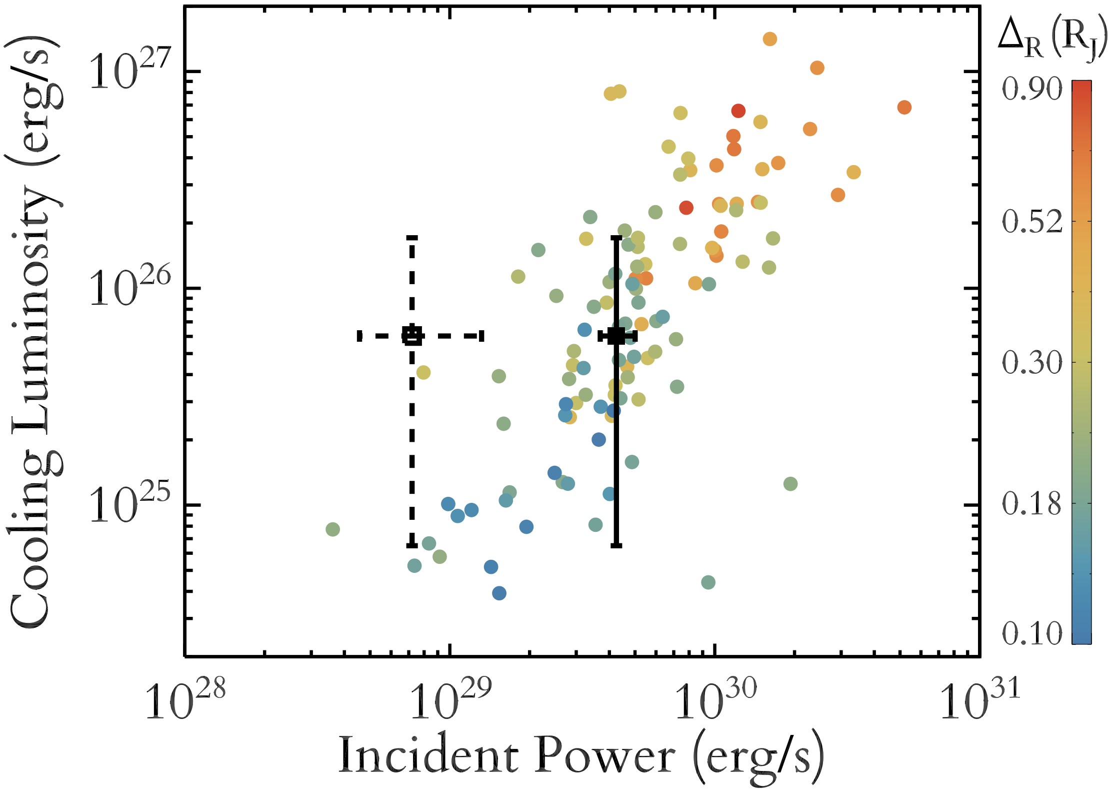

Figure 2.10 Steady-state cooling luminosity, or the power the planet must emit to retain its measured radius, as a function of incident power, with radius anomaly, or the difference in radius between measured and predicted planet size indicated in color. Predicted planet sizes have been calculated assuming a planet of pure H/He using the models of Lopez & Fortney (2016). The filled square with solid error bars shows K2-97b at its current incident flux, whereas the open square with dashed error bars show the planet at its main sequence incident flux. The current cooling luminosity of the planet is characteristic of the inflated planet population around main sequence stars, suggesting that the physical mechanism inflating this planet is the same. However, the planet would be inflated to an uncharacteristically high degree if it were to maintain its current radius around a main sequence star. The planet seen nearest to this case on the plot is WASP-67b, a young, 0.47 M_J planet, whose significantly lower mass allows it to be more easily inflated. Inflating the more massive K2-97b to the same degree as WASP-67b should require an incident power higher than the K2-97b receives now.

pre-main sequence to the tip of the red giant branch. We used metallicities of 0.6, 0.42 and 0.34 dex for the 1.0, 1.15 and 1.3 $M_\odot$ models, respectively, which results in overestimated limits given that metal-poor stars are hotter than metal-rich stars for a fixed mass. We also denote an inflation threshold of 2×10^8 erg s^{-1} cm^{-2} ($\sim$150 $F_\oplus$) following Demory & Seager (2011) and Miller & Fortney (2011), who note that this corresponds to an equilibrium temperature of 990 K assuming a Bond albedo of 0.1, comparable to the temperature at which Ohmic heating may become important

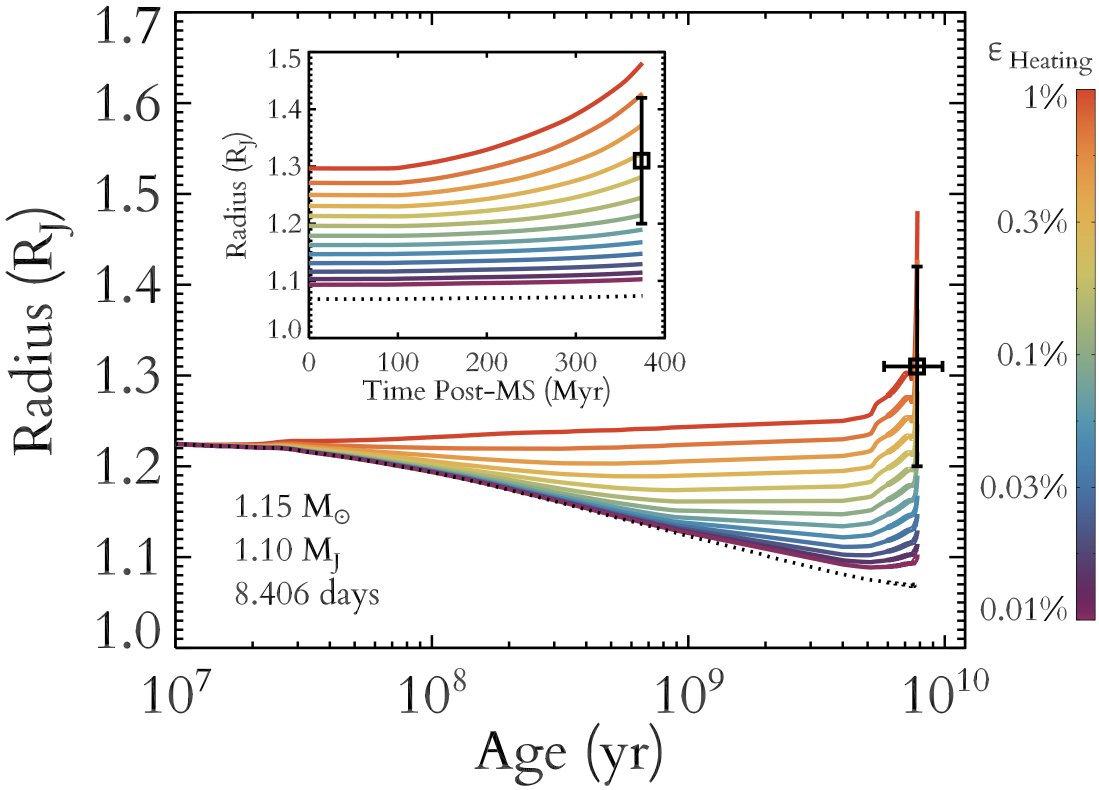

Figure 2.11 Planetary radius as a function of time, shown for various potential heating efficiencies. We assume the best-fit values for the stellar mass and the planetary mass and radius, and a planetary composition of a H/He envelope surrounding a 20 $M_\oplus$ core of heavier elements. The dotted line corresponds to a scenario with no planetary heating. The inset shows the post-main sequence evolution at a finer time resolution. The measured planet radius is consistent with heating efficiencies of 0.1 to 0.5%, and inconsistent with the class II, delayed cooling scenario.

(Batygin et al. 2011). None of the 38 transiting giant planets with insolations below this threshold known to date appear to be inflated (Thorngren et al. 2015).

Figure 3.11 demonstrates that the incident flux of this planet may have been above the 150 $F_\oplus$ threshold for inflation throughout its main sequence life. However, it is also possible that the planet experienced a flux below this threshold, depending on the exact mass and metallicity of the star. To estimate the main-sequence incident flux level quantitatively, we performed Monte Carlo simulations by interpolating the evolutionary tracks to randomly sampled values of stellar mass and metallicity as measured for K2-97 and calculated the average incident flux on the main sequence. The resulting distribution yielded an average main sequence flux of 170^{+140}_{-60} $F_\oplus$. We also estimated the incident flux evolution using a different set of evolutionary tracks from the MIST database (Choi et al. 2016), which yielded consistent results. Our analysis demonstrates that EPIC 211351816.01 received a main-sequence incident flux which is close to the inflation threshold, but lower than the typical incident flux for planets with a comparable radius. This suggests that additional inflation occurred after the star evolved off the main sequence.

We illustrate the current constraints on the mass and radius of K2-97b in Figure 2.9 relative to other known, well-characterized giant planets. The dotted line denotes the empirical threshold for planet inflation put forth by Miller & Fortney (2011). Colors correspond to the incident fluxes on these planets, except in the case of K2-97b where we have also indicated the incident flux the planet would have received on the main sequence to illustrate how uncharacteristic of the inflated planet population it would have been at that time.

Furthermore, the energetics of K2-97b indicate that if it was inflated to its current radius while its host star was on the main sequence, the planet would be an outlier within the inflated planet population, with internal heating over an order of magnitude higher than would be expected. We illustrate this in Figure 2.10, where we plot the intrinsic cooling luminosity predicted by the models of Lopez & Fortney (2016) against incident flux for the known inflated planet population. The radius anomaly, or difference in measured and predicted planet size, is indicated by color. The filled square corresponds to K2-97b today, showing clear agreement with the rest of the inflated planet population energetically. However, the open square with dashed error bars corresponds to the incident flux on the planet when its host star was on the main sequence. The only planet energetically comparable to this scenario is WASP-67b, a planet with less than half the mass around a young star (Hellier et al. 2012). As lower mass planets are easier to inflate, and young planets may still be inflated from their initial formation, it would be very surprising to find a Jupiter-mass, middle-aged planet with similar energetic qualities. This, along with the empirical evidence for the energetic boundary of inflation of 2×10^8 erg s^{-1} established by Miller & Fortney (2011), suggest that K2-97b was not inflated when its host star was on the main sequence.

Assuming that the inflation of the planet was due to the deposition of flux into the planet interior, we can use the model of Lopez & Fortney (2016) to estimate the heating efficiency needed to reproduce the current radius of K2-97b. Figure 3.12 shows the radius evolution of K2-97b as a function of age, given a range of heating efficiencies, a planetary structure of a H/He envelope with a 20 $M_{\oplus}$ core of heavier elements, and a 1.15 Msun, [Fe/H] = + 0.42 dex model for the star. The scenario with no additional interior heating is shown by the dotted line. The planet is consistent with heating efficiencies of $\sim$ 0.3%, and inconsistent with a class II scenario with no additional heating at late times. This suggests K2-97b may be the first re-inflated planet discovered.

Further studies of giant planets around evolved stars will be necessary to confirm this hypothesis. Gas planets at a slightly larger orbital period ($\sim$10–30 days) around a similar star would experience fluxes well below the empirical inflation threshold during the main sequence and would thus provide a clearer picture of the inflation mechanism. Although planets inflated by mechanisms more heavily dependent on factors other than incident flux, such as metallicity, have not been observed around main sequence stars, these factors could potentially delay contraction at orbital distances beyond the nominal inflation boundary, and thus we cannot completely rule out the possibility that such effects may also be responsible for the inflation of this planet (Chabrier & Baraffe 2007).

2.5.3 Planetary Engulfment

The expansion of a star in the red giant phase can extend to AU scales, eventually engulfing any short-period planets. We calculate that K2-97b will be engulfed when its host star reaches a radius of $\sim$18 $R_\odot$. This provides a conservative upper limit for the remaining lifetime of the planet of $\sim$200 Myr.

The scarcity of short-period planets orbiting giant stars has been suggested to be a result of tidally-driven orbital decay (Schlaufman & Winn 2013). We can estimate the timescale of orbital decay due to tides following the prescription of Schlaufman & Winn (2013):

$$t = 10 \text{ Gyr } \frac{Q_*/k_*}{10^6} \left(\frac{M_*}{\mathrm{M}_\odot}\right)^{1/2} \left(\frac{M_p}{\mathrm{M}_{\mathrm{Jup}}}\right)^{-1} \times \left(\frac{R_*}{\mathrm{R}_\odot}\right)^{-5} \left(\frac{a}{0.06\mathrm{AU}}\right)^{-13/2} \tag{2.8}$$

Here, Q_* is the tidal quality factor of the star, and k_* its tidal Love number. These values are highly uncertain, but making the usual assumption of $Q_*/k_* = 10^6$ (Schlaufman & Winn 2013) the decay time is $\approx$ 60 Myr. If, however, $Q_*/k_* = 10^2$, as Schlaufman & Winn (2013) suggest may be the case for sub-giant stars, then $t \approx$ 6,000 yr. This indicates that such a low value for Q_*/k_* is implausible. Consequently, the discovery of K2-97b along with other planets around evolved such as K2-39b (Van Eylen et al. 2016) and Kepler-91b (Barclay et al. 2015) suggests that observation bias may contribute to the relative paucity of planets detected on short-period orbits around giant stars.

2.6 Conclusions

We report the discovery of a transiting planet with R = 1.31 ± 0.11 R_J and M = 1.10 ± 0.11 M_J around the low luminosity giant star K2-97. We use a Gaussian process to estimate the correlated noise in the lightcurve to quantify and remove potential correlations between planetary and noise properties. We also tested five different lightcurves produced by independent systematic detrending methods to account for inconsistencies in the treatment of K2 data and derive an accurate transit depth and planet radius. We performed an iterative spectroscopic and asteroseismic study of the host star EPIC 211351816 to precisely determine its stellar parameters and evolutionary history.

We determine that, assuming a stable planetary orbit for the range of acceptable stellar parameters, K2-97b requires approximately 0.3% of the current incident stellar flux to be deposited into the planet's deep convective interior to explain its radius. The measured planet radius is inconsistent with most inflation scenarios without current heating of the planet's interior. This suggests planet inflation may be a direct response to stellar irradiation rather than an effect of delayed planet cooling after formation, and K2-97b is a strong candidate for the first known re-inflated planet.

Further studies of planets around evolved stars are essential to confirm the planet re-inflation hypothesis. Planets may be inflated beyond the nominal inflation regime by methods that are more strongly dependent on other factors, such as atmospheric metallicity, than incident flux. An inflated planet observed around a giant star with an orbital period of $\sim$20 days would have been outside the inflated planet regime when its host star was on the main sequence, and thus finding such a planet could provide more insight into the re-inflation hypothesis. Using a Gaussian process to characterize stellar noise seen in the lightcurve may allow for the discovery of smaller planets than previously possible around giant stars. Other Gaussian process kernels, or fitting additional transit parameters such as limb darkening coefficients, could provide additional insight. Further study on this particular system, such as a more detailed asteroseismic analysis to determine a more precise age, will provide deeper insight into the evolutionary history of this system and the inflation history of hot Jupiters as a whole. This discovery also motivates new theoretical work exploring exactly how different inflationary heating mechanisms respond to post main sequence changes in irradiation.

Chapter 3

Seeing double with K2: Testing Re-inflation with Two Remarkably Similar Planets Around Red Giant Branch Stars

This chapter has been previously published in the *Astronomical Journal* (Grunblatt, S., Huber, D., Gaidos, E. et al, 2017, AJ 154, 254).

3.1 Introduction

Since the first measurement of planet radii outside our solar system (Charbonneau et al. 2000; Henry et al. 2000), it has been known that gas giant planets with equilibrium temperatures greater than 1000 K tend to have radii larger than model predictions (Burrows et al. 1997; Bodenheimer et al. 2001; Guillot & Showman 2002). Moreover, a correlation has been observed between incident stellar radiation and planetary radius inflation (Burrows et al. 2000; Laughlin et al. 2011; Lopez & Fortney 2016). The diversity of mechanisms proposed to explain the inflation of giant planets (Baraffe et al. 2014) can be split into two general classes: mechanisms where stellar irradiation is deposited directly into the planet's deep interior, driving adiabatic heating of the planet and thus inflating its radius (Class I; e.g., Bodenheimer et al. 2001; Batygin & Stevenson 2010; Ginzburg & Sari 2016), and mechanisms where no energy is deposited into the deep planetary interior and the inflationary mechanism simply acts to slow the radiative cooling of the planet's atmosphere, preventing it from losing its initial heat and thus radius inflation from its formation (Class II; e.g., Burrows et al. 2000;

Chabrier & Baraffe 2007; Wu & Lithwick 2013). These mechanism classes can be distinguished by measuring the radii of planets that have recently experienced a large changes in irradiation, such as planets orbiting red giant stars at 10-30 day orbital periods (Lopez & Fortney 2016). To quantify the distinction between mechanism classes, we require that planets (1) approach or cross the empirical planet inflation threshold of 2×10^8 erg s^{-1} cm^{-2} ($\approx$150 $F_\oplus$ Demory & Seager 2011)) after reaching the zero age main sequence, and (2) experience a change in incident flux large enough that the planet radius would increase significantly, assuming it followed the trend between incident flux and planet radius found by Laughlin et al. (2011). If such planets are currently inflated, heat from irradiation must have been deposited directly into the planet interior, indicating that Class I mechanisms must be at play, whereas if these planets are not inflated, no energy has been transferred from the planet surface into its deep interior, and thus Class II mechanisms are favored. By constraining the efficiency of heat transfer to inflated planets orbiting evolved host stars, we can distinguish the efficiency of these two classes of inflation mechanisms (Ginzburg & Sari 2016; Lopez & Fortney 2016).

To constrain the properties of giant planet inflation, we search for transiting giant planets orbiting low-luminosity red giant branch (LLRGB) stars with the NASA *K2* Mission (Howell et al. 2014; Huber 2016). These stars are large enough that we can detect their oscillations to perform asteroseismology but small enough that gas giant planet transits are still detectable in *K2* long-cadence data. Close-in planets in these systems have experienced significant changes in irradiation over time. The first planet discovered by our survey, K2-97b, was published by Grunblatt et al. (2016, hereafter referred to as G16). Using a combination of asteroseismology, transit analysis, and radial velocity measurements, G16 measured the mass and radius of this planet to be 1.10 $\pm$ 0.12 M_J and 1.31 $\pm$ 0.11 R_J, respectively. This implied a direct heating efficiency of 0.1%–0.5%, suggesting that the planet radius was directly influenced by the increase in irradiation caused by the host-star evolution.

Here, we present additional radial velocity data that revise the mass of K2-97 to 0.48 $\pm$ 0.07 M_J, as well as the discovery of the second planet in our survey, K2-132b, with a radius of 1.30 $\pm$ 0.07 R_J and mass of 0.49 $\pm$ 0.06 M_J. These planets currently receive incident fluxes between 700 and 1100 $F_\oplus$, but previously received fluxes between 100 and 350 $F_\oplus$ when the host stars were on the main sequence. Quantifying the incident flux evolution of these systems allows us to estimate the planetary heating efficiency and distinguish between planetary inflation mechanisms.

3.2 Observations

3.2.1 K2 Photometry

In the *K2* extension to the NASA *Kepler* mission, multiple fields along the ecliptic are observed almost continuously for approximately 80 days (Howell et al. 2014). EPIC 211351816 (now known as K2-97; G16) was selected for observation as a part of *K2* Guest Observer Proposal GO5089 (PI: Huber) and observed in Campaign 5 of *K2* during the first half of 2015. EPIC 228754001 (now known as K2-132) was selected and observed in Campaign 10 of *K2* as part of *K2* Guest Observer Proposal GO10036 (PI: Huber) in the second half of 2016. As the *Kepler* telescope now has unstable pointing due to the failure of two of its reaction wheels, it is necessary to correct for the pointing-dependent error in the flux received per pixel. We produced a lightcurve by simultaneously fitting thruster systematics, low frequency variability, and planet transits with a Levenberg-Marquardt minimization algorithm, using a modified version of the pipeline from Vanderburg et al. (2016). These lightcurves were then normalized and smoothed with a 75 hr median filter, and points deviating from the mean by more than 5σ were removed. By performing a box least-squares transit search for transits with 5- to 40-day orbital periods and 3–30 hr transit durations on these lightcurves using the algorithm of Kovács et al. (2002), we identified transits of $\approx$500 and $\approx$1000 ppm, respectively. Using the techniques of G16 and those described in §4.1, we determined the transits came from an object which was planetary in nature. Figure 5.5 shows our adopted lightcurves for K2-97 and K2-132.

3.2.2 Imaging with Keck/NIRC2 AO

To check for potential blended background stars, we obtained natural guide-star adaptive optics (AO) images of K2-132 through the broad K' filter ($\lambda_{\mathrm{center}} = 2.124\ \mu$m) with the Near-Infrared Camera (NIRC2) at the Keck-2 telescope on Maunakea during the night of UT 25 January 2017. The narrow camera (pixel scale 0.01") was used for all sets of observations. No additional sources were detected within $\sim$3" of the star. The contrast ratio of the detection limit is more than 7 magnitudes at 0.5"; brighter objects could be detected to within 0.15" of the star. These data were collected to quantify the possibility of potential false positive scenarios in these systems, and the relevant analysis is described in §4.2. Previous analysis by G16 of NIRC2 AO images of K2-97 reached effectively identical conclusions.

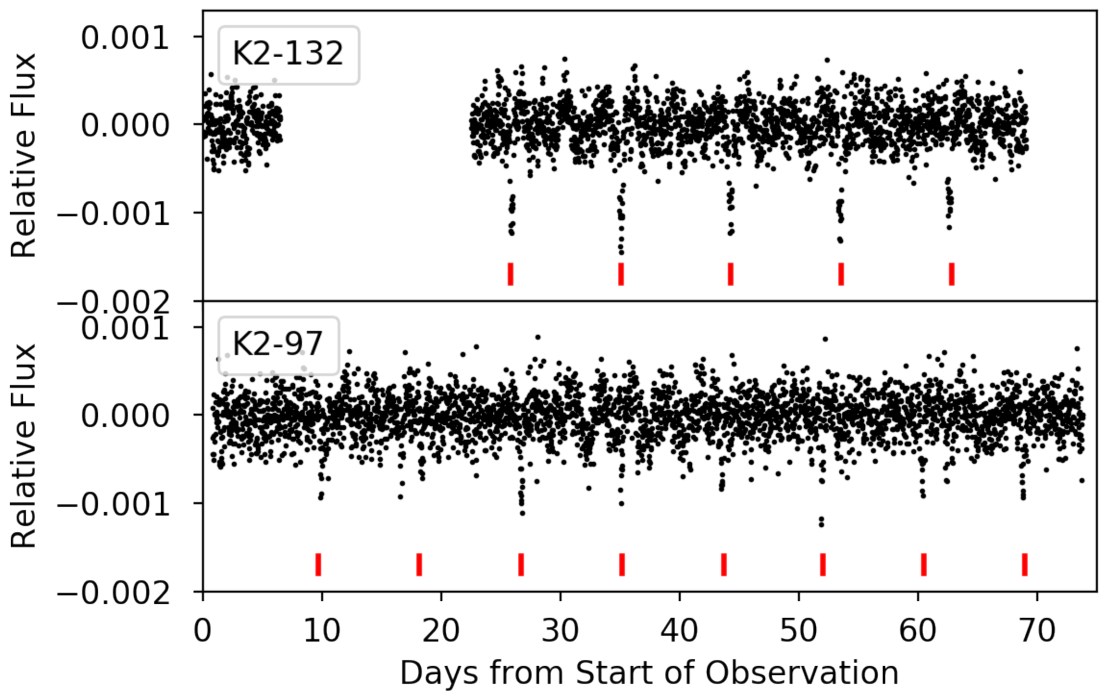

Figure 3.1 Detrended K2 lightcurves of K2-97 (bottom) and K2-132 (top). These lightcurves were produced using a modified method of the pipeline presented in Vanderburg et al. (2016), where both instrument systematics and the planet transit were modeled simultaneously to prevent transit dilution. The lightcurve has been normalized and median filtered as well as unity subtracted. Individual transits are visible by eye, and are denoted by red fiducial marks.

Images were processed using a custom Python pipeline that linearized, dark-subtracted, flattened, sky-subtracted, and co-added the images (Metchev & Hillenbrand 2009). A cutout ∼3.0" across, centered on the star, was made and inserted back into the processed image as a simulated companion. A contrast curve was generated by decreasing the brightness and angular separation of the simulated companion with respect to the primary, until the limits of detection (3.0σ) were reached. Figure 3.2 plots the contrast ratio for detection as a function of distance from the source K2-132.

3.2.3 High-Resolution Spectroscopy and Radial Velocity Measurements with Keck/HIRES

We obtained a high-resolution, high signal-to-noise spectrum of K2-97 and K2-132 using the High Resolution Echelle Spectrometer (HIRES) on the 10 meter Keck-I telescope at Mauna Kea Observatory on the Big Island of Hawaii. HIRES provides spectral resolution of roughly 65,000 in

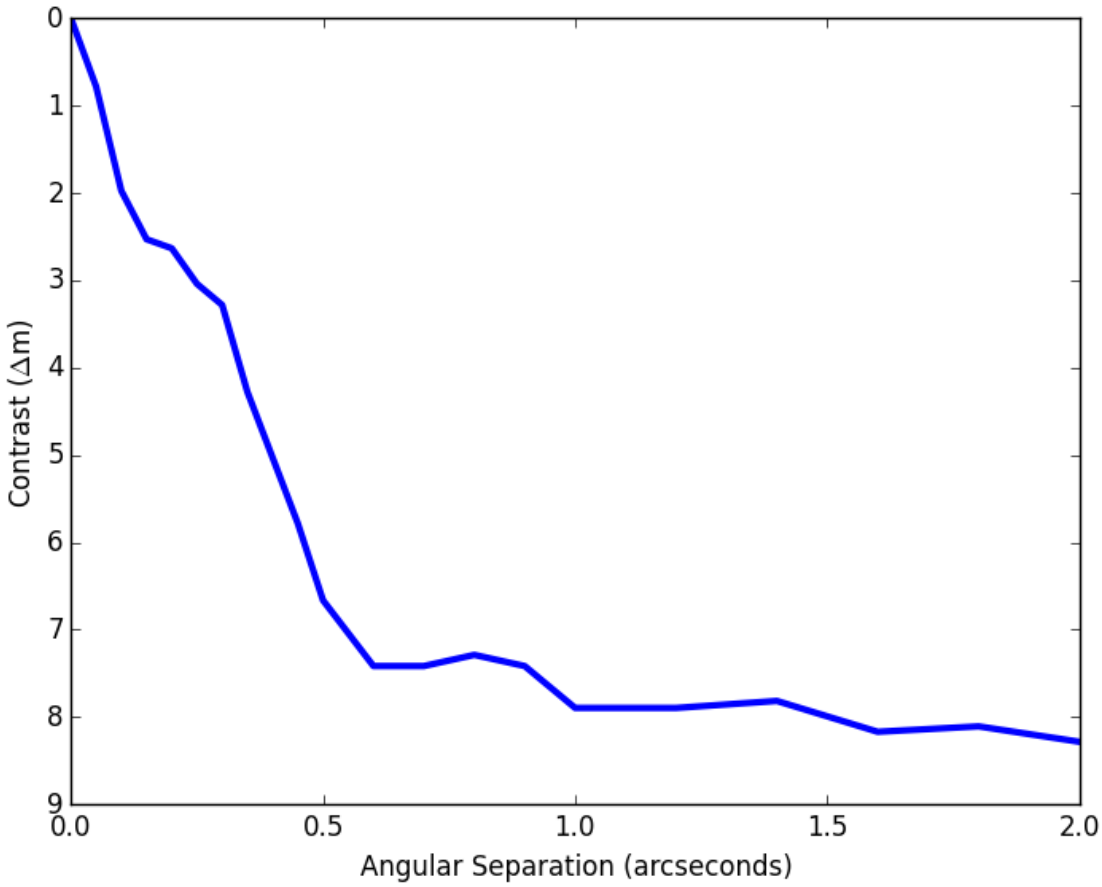

Figure 3.2 Contrast in differential K' magnitude as a function of angular separation from K2-132. No companions were detected within 3" of the source. G16 found effectively identical results for K2-97.

a wavelength range of 4500 to 6200 Å (Vogt et al. 1994), and has been used to both characterize over 1000 *Kepler* planet host stars (Petigura et al. 2017) as well as confirm and provide precise parameters of over 2000 *Kepler* planets (Fulton et al. 2017; Johnson et al. 2017). Our spectra were analyzed using the software package SpecMatch (Petigura 2015) following the procedure outlined in G16.

Radial velocity (RV) measurements were obtained between January 27, 2016 and April 10, 2017 using the High Resolution Echelle Spectrometer (HIRES) on the Keck-I Telescope at the Mauna Kea Observatory in Hawaii. Individual measurements are listed in Table 3.1 and shown in Figure 3.9. All RV spectra were obtained through an iodine gas cell. We collected three measurements of K2-97 with Keck/HIRES in 2016, and seven additional measurements in 2017. All eleven measurements

Table 3.1. Radial Velocities

Star	BJD-2440000	RV (m s^{-1})	Prec. (m s^{-1})
K2-97	17414.927751	-4.91	1.79
K2-97	17422.855362	-38.94	1.72
K2-97	17439.964043	-17.95	2.22
K2-97	17774.905553	-44.03	1.85
K2-97	17790.840786	-50.74	1.77
K2-97	17802.819367	7.96	1.76
K2-97	17803.836621	38.90	1.64
K2-97	17830.802784	32.84	1.77
K2-97	17853.790069	23.05	1.78
K2-97	17854.774479	46.68	1.85
K2-132	17748.099507	-30.32	1.95
K2-132	17764.115738	25.80	1.66
K2-132	17766.139232	-40.85	1.96
K2-132	17776.065142	-26.91	1.54
K2-132	17789.093812	26.09	1.74
K2-132	17790.091515	45.40	1.68
K2-132	17791.071462	46.31	1.85
K2-132	17794.992775	-22.43	1.88
K2-132	17803.927316	-37.99	1.91
K2-132	17830.066681	-34.92	1.83
K2-132	17854.937650	50.42	1.78

Note. — The precisions listed here are instrumental only, and do not take into account the uncertainty introduced by stellar jitter. For moderately evolved stars like K2-97 and K2-132, radial velocity jitter on relevant timescales can reach $\gtrsim$10 m s^{-1} (see G16 and §4.2 for more details).

of K2-132 were taken between December 2016 and April 2017. Fits to the radial velocity data were made using the publicly available software package `RadVel` (Fulton & Petigura 2017) and confirmed through independent analysis presented in §4.2. We adopted the same method for radial velocity analysis as described in G16 (Butler et al. 1996).

3.3 Host Star Characteristics

3.3.1 Spectroscopic Analysis

In order to obtain precise values for the effective temperature and metallicity of the star, we used the software package SpecMatch (Petigura 2015) and adopted the spectroscopic analysis method described in G16 for both stars. SpecMatch searches a grid of synthetic model spectra from Coelho et al. (2005) to find the best-fit values for $T_{\rm eff}$, $\log g$, [Fe/H], mass and radius of the star. We report the effective temperature $T_{\rm eff}$ and metallicity [Fe/H] from the SpecMatch analysis here. We also note that the $\log g_{\rm spec} = 3.19 \pm 0.07$ value from the spectroscopic analysis is fully consistent with the

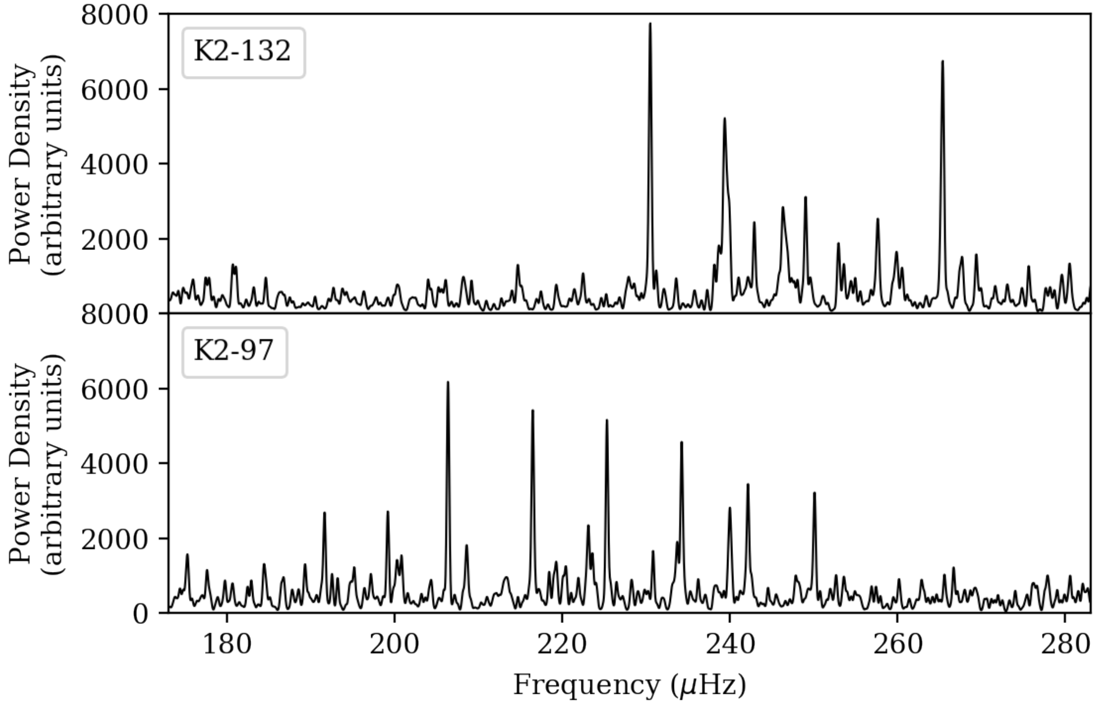

Figure 3.3 Power density of K2-132 (top) and K2-97 (bottom) estimated from *K2* lightcurves, centered on the frequency range where stellar oscillations can be detected for low luminosity red giant branch (LLRGB) stars. In both cases, stellar oscillations are clearly visible. Note that the power excess of K2-132 does not display a typical Gaussian solar-like oscillation profile due to its proximity to the *K2* long-cadence Nyquist frequency (283 μHz).

asteroseismic determination of $\log g_{\rm AS} = 3.26 \pm 0.008$ (see next Section for details), so no iteration was needed to recalculate $T_{\rm eff}$ and metallicity once asteroseismic parameters had been determined.

3.3.2 Asteroseismology

Stellar oscillations are stochastically excited and damped at characteristic frequencies due to turbulence from convection in the outer layers of the star. The characteristic oscillation timescales or frequencies are determined by the internal structure of the star. By measuring the peak frequency of power excess ($\nu_{\rm max}$) and frequency spacing between individual radial orders of oscillation ($\Delta\nu$), the stellar mass, radius, and density can all be determined to 10% precision or better.

Similar to G16, we employed asteroseismology using *K2* long-cadence data by measuring stellar oscillation frequencies to determine precise fundamental properties of the evolved host star K2-132. Figure 3.3 compares the power spectra of K2-97 and K2-132. Compared to the power excess of

K2-97 near $\approx 220\,\mu$Hz (75 minutes), K2-132 oscillates with higher frequencies near $\approx 250\,\mu$Hz (65 minutes), indicative of a smaller, less evolved RGB star.

Figure 3.3 also shows that the power excess of K2-132 is less broad and triangular than K2-97. This is most likely due to the proximity of the power excess to the long-cadence Nyquist frequency (283.24 μHz), causing an attenuation of the oscillation amplitude due to aliasing effects. The proximity to the Nyquist frequency also implies that the real power excess could lie either below or above the Nyquist frequency (Chaplin et al. 2014; Yu et al. 2016). To discern between these scenarios, we applied the method of Yu et al. (2016) to distinguish the real power excess from its aliased counterpart. Based on the power-law relation determined by Yu et al. (2016), $\Delta\nu = 0.262 \times 0.770\nu_{\rm max}$, as well as a consistent measurement of $\Delta\nu = 18.46 \pm 0.26\ \mu$Hz both above and below the Nyquist frequency, we find $\nu_{\rm max} = 245.65 \pm 3.51\mu$Hz, suggesting the true oscillations lie below the Nyquist frequency. To validate this conclusion, we also constructed the global oscillation pattern via the ε-$\Delta\nu$ relation (Stello et al. 2016) for the given $\Delta\nu$ value and found the power excess below the Nyquist frequency demonstrates the expected frequency phase shift ε and matches the expected frequency pattern more precisely. The collapsed échelle diagram generated from the Huber et al. (2009) pipeline indicates the total power of the $l = 2$ modes is smaller than that for the $l = 0$ modes, which also suggests the real power excess is below the Nyquist frequency (Yu et al. 2016). Independent asteroseismic analyses using both a separate pipeline for asteroseismic value estimation as well as using lightcurves detrended using different methods recovered asteroseismic parameters in good agreement with the values shown here (North et al. 2017). In addition, the asteroseismic analyses of G16 also strongly agree with our results for K2-97.

To estimate stellar properties from $\nu_{\rm max}$ and $\Delta\nu$, we use the asteroseismic scaling relations of Brown et al. (1991); Kjeldsen & Bedding (1995):

$$\frac{\Delta\nu}{\Delta\nu_\odot} \approx f_{\Delta\nu}\left(\frac{\rho}{\rho_\odot}\right)^{0.5}, \tag{3.1}$$

$$\frac{\nu_{\rm max}}{\nu_{\rm max,\odot}} \approx \frac{g}{g_\odot}\left(\frac{T_{\rm eff}}{T_{\rm eff,\odot}}\right)^{-0.5}. \tag{3.2}$$

Equations (1) and (2) can be rearranged to solve for mass and radius:

Table 3.2. Stellar and Planetary Properties for K2-97 and K2-132

Property	K2-97	K2-132	Source
Kepler Magnitude	12.41	11.65	Huber et al. (2016)
Temperature $T_{\rm eff}$	4790 ± 90 K	4840 ± 90 K	spectroscopy
Metallicity [Fe/H]	+0.42 ± 0.08	-0.01 ± 0.08	spectroscopy
Stellar Mass, $M_{\rm star}$	1.16 ± 0.12 $M_\odot$	1.08 ± 0.08 $M_\odot$	asteroseismology
Stellar Radius, $R_{\rm star}$	4.20 ± 0.14 $R_\odot$	3.85 ± 0.13 $R_\odot$	asteroseismology
Density, ρ_*	0.0222 ± 0.0004 g cm^{-3}	0.0264 ± 0.0008 g cm^{-3}	asteroseismology
log g	3.26 ± 0.01	3.297 ± 0.007	asteroseismology
Age	$7.6\ ^{+5.5}_{-2.3}$ Gyr	$8.5\ ^{+4.5}_{-2.8}$ Gyr	isochrones
Planet Radius, R_p	1.31 ± 0.11 R_J	1.30 ± 0.07 R_J	GP+transit model
Orbital Period $P_{\rm orb}$	8.4061 ± 0.0015 days	9.1751 ± 0.0025 days	GP+transit model
Planet Mass, M_p	0.48 ± 0.07 M_J	0.49 ± 0.06 M_J	RV model

Note. — All values for the K2-97 system have been taken from G16, with the exception of the system age, which was recalculated for this publication. See §5.1 for a discussion of the system age calculations.

$$\frac{\mathrm{M}}{\mathrm{M}_\odot} \approx \left(\frac{\nu_{\rm max}}{\nu_{\rm max,\odot}}\right)^3 \left(\frac{\Delta\nu}{f_{\Delta\nu}\Delta\nu_\odot}\right)^{-4} \left(\frac{T_{\rm eff}}{T_{\rm eff,\odot}}\right)^{1.5} \tag{3.3}$$

$$\frac{\mathrm{R}}{\mathrm{R}_\odot} \approx \left(\frac{\nu_{\rm max}}{\nu_{\rm max,\odot}}\right) \left(\frac{\Delta\nu}{f_{\Delta\nu}\Delta\nu_\odot}\right)^{-2} \left(\frac{T_{\rm eff}}{T_{\rm eff,\odot}}\right)^{0.5}. \tag{3.4}$$

Our adopted solar reference values are $\nu_{\rm max,\odot} = 3090\,\mu$Hz and $\Delta\nu_\odot = 135.1\,\mu$Hz (Huber et al. 2011a), as well as $T_{\rm eff,\odot} = 5777$ K.

It has been shown that asteroseismically-determined masses are systematically larger than masses determined using other methods, particularly for the most evolved stars (Sharma et al. 2016). To address this, we also adopt a correction factor of $f_{\Delta\nu} = 0.994$ for K2-97 from G16 and calculate a correction factor $f_{\Delta\nu} = 0.998$ for K2-132 following the procedure of Sharma et al. (2016). Our final adopted values for the stellar radius, mass, log g and densities of K2-97 and K2-132 are calculated using these modified asteroseismic scaling relations, and are listed in Table 4.1.

3.4 Lightcurve Analysis and Planetary Parameters

3.4.1 Gaussian process transit models

The transits of K2-97b and K2-132.01 were first identified using the box least-squares procedure described in G16 and §2.1 (Kovács et al. 2002). The detrended lightcurves, phase folded at the

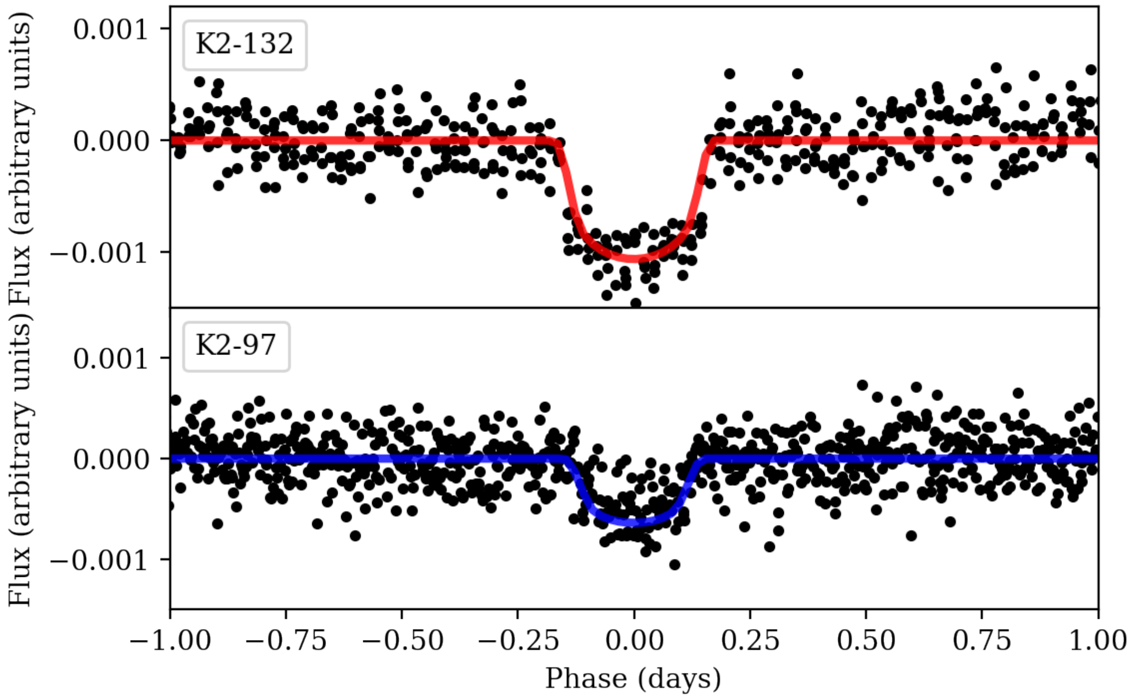

Figure 3.4 Detrended *K2* lightcurves of K2-132 (top) and K2-97 (bottom), folded at the observed transit period. Preliminary transit fit parameters were established through a box least squares search (Kovács et al. 2002); our final pure transit models (Mandel & Agol 2002) are shown as solid lines.

period detected by the box least-squares search and fit with best-fit transit models, are shown in Figure 3.4.

Evolved stars display correlated stellar variation on timescales of hours to weeks due to stellar granulation and oscillation (Mathur et al. 2012), leading to systematic errors in transit parameter estimation (Carter & Winn 2009; Barclay et al. 2015). Thus, a stochastically-driven and damped simple harmonic oscillator can be used to both describe the stellar oscillation and granulation noise in a lightcurve as well as characterize the fundamental physical properties of the star.

In G16, we used a squared exponential Gaussian process estimation model to remove stellar variability in the K2 lightcurve and measure the transit depth of K2-97b precisely. Here, we used a Gaussian process estimation kernel that assumes stellar variability can be described by a stochastically-driven damped simple harmonic oscillator, modified from the method of G16. We also present results using the previously tested squared exponential Gaussian process kernel, which has been successfully applied to remove correlated noise in various one dimensional datasets in the

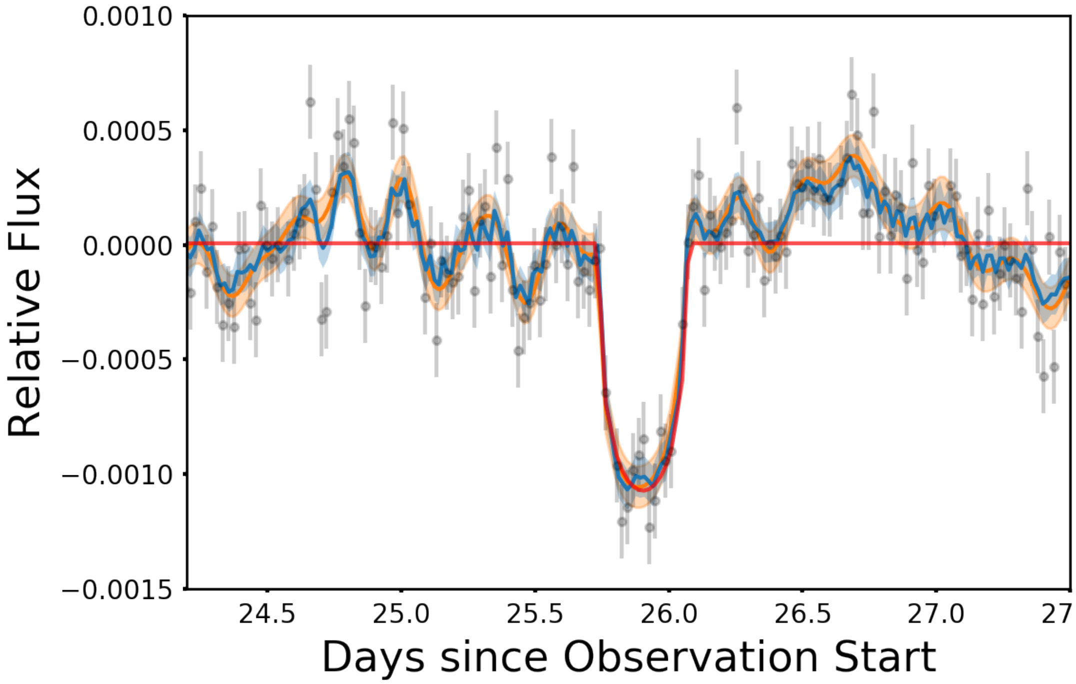

Figure 3.5 Illustration of a transit in the K2-132 lightcurve. The best-fit transit model is shown in red. A combined best-fit transit + squared exponential Gaussian process (SE GP) model is shown in orange, with 1-σ model uncertainties shown by the orange shaded region. A combined best-fit transit + simple harmonic oscillator Gaussian process (SHO GP) model is shown with 1-σ uncertainties in blue. In addition to having a smaller uncertainties than the SE GP model, the SHO GP model also captures variations on different timescales more accurately, and is physically motivated by the oscillation signal of the star.

past (Gibson et al. 2012; Dawson et al. 2014; Haywood et al. 2014; Barclay et al. 2015; Grunblatt et al. 2015, 2016).

We describe the covariance of the time-series data as an N×N matrix $\mathbf{\Sigma}$ where

$$\Sigma_{ij} = \sigma_i^2 \delta_{ij} + k(\tau_{ij}) \tag{3.5}$$

where σ_i is the observational uncertainty, δ_{ij} is the Kronecker delta, and $k(\tau_{ij})$ is the so-called covariance kernel function that quantifies the correlations between times t_i and t_j (Rasmussen 2006).

Following Foreman-Mackey et al. (2017), the kernel function we use can be expressed as

$$k(\tau_{ij}) = \sum_{n=1}^{N} [a_n \exp(-c_n \tau_{ij}) \cos(d_n \tau_{ij}) + b_n \exp(-c_n \tau_{ij}) \cos(d_n \tau_{ij})] \tag{3.6}$$

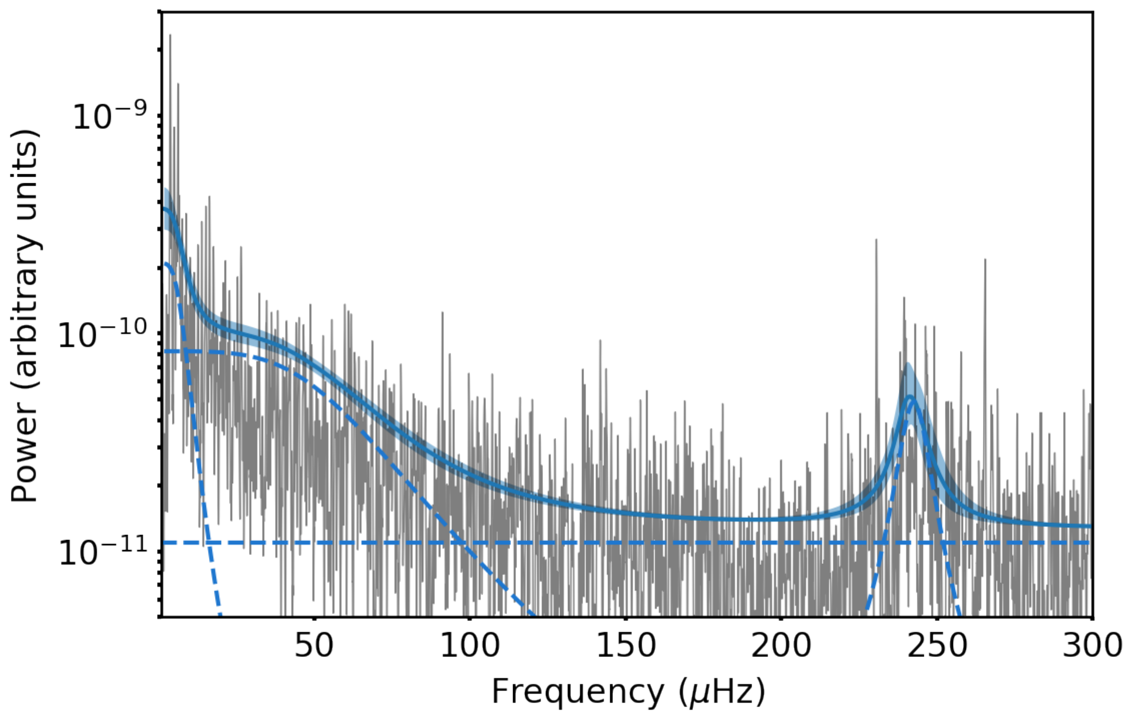

Figure 3.6 The power spectrum of the K2-132 lightcurve (gray) overlaid with the simple harmonic oscillator Gaussian process model (solid blue line). Uncertainties in the model are given by the blue contours. The individual component terms of the Gaussian process model are shown by dotted lines. The two low Q components account for the granulation noise signal at low frequencies. The high Q component traces the envelope of stellar oscillation signal and allows us to estimate the frequency of maximum power of the stellar oscillations, and thus determine $\nu_{\max}$ from the time domain.

where a_n, b_n, c_n and d_n are a set of constants that define the nth term in our kernel function. We then redefine these constants a_n, b_n, c_n and d_n as simple harmonic oscillator components Q_n, $\omega_{0,n}$ and $S_{0,n}$ such that

$$k(\tau_{ij}) = S_0\omega_0 Q e^{-\frac{\omega_0\tau_{ij}}{2Q}} \times \begin{cases} \cosh(\eta\omega_0\tau_{ij}) + \frac{1}{2\eta Q}\sinh(\eta\omega_0\tau_{ij}), & 0 < Q < 1/2 \\ 2(1+\omega_0\tau_{ij}), & Q = 1/2 \\ \cos(\eta\omega_0\tau_{ij}) + \frac{1}{2\eta Q}\sin(\eta\omega_0\tau_{ij}), & 1/2 < Q, \end{cases} \tag{3.7}$$

where Q_n represents the quality factor or damping coefficient of the nth simple harmonic oscillator, $\omega_{0,n}$ represents the resonant frequency of the nth simple harmonic oscillator, $S_{0,n}$ is proportional to the power at $\omega = \omega_{0,n}$, and $\eta = \sqrt{1-(4Q^2)^{-1}}$. We find that we can describe the stellar variability seen in our data as a sum of three simple harmonic oscillator components, similar to

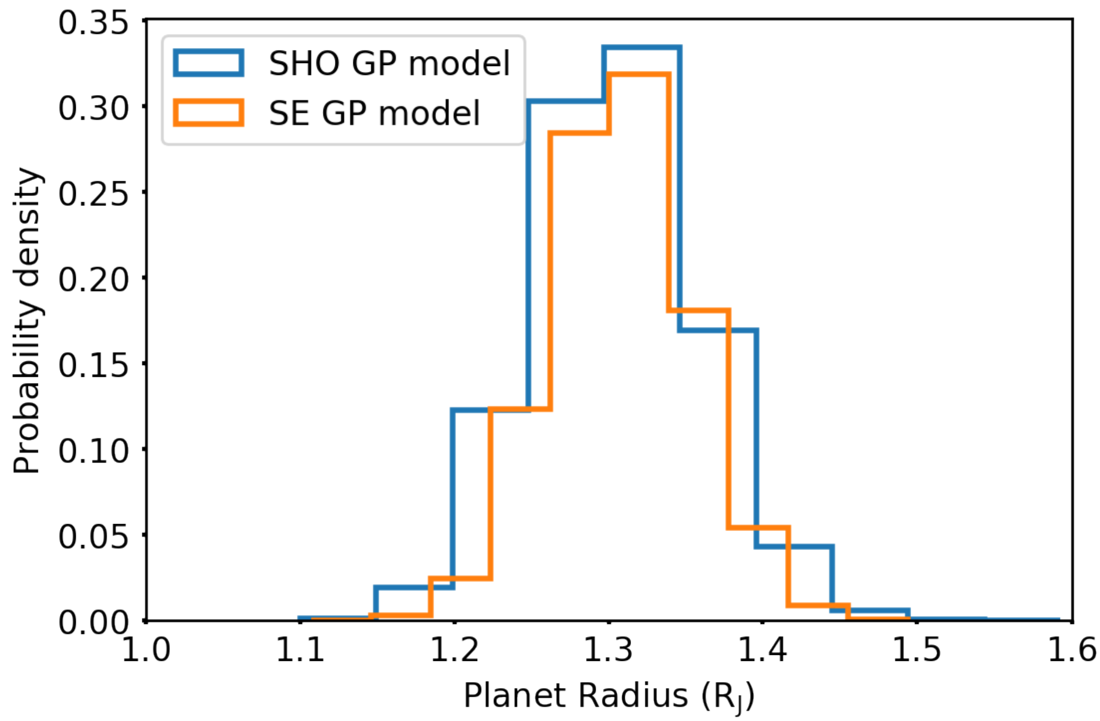

Figure 3.7 Posterior distributions of planet radius based on our stellar parameters derived from asteroseismology and transit depth measured in our transit + squared exponential Gaussian process model (SE GP model, orange) and our transit + simple harmonic oscillator Gaussian process model (SHO GP model, blue) for K2-132.01. Parameters differ between the two models, but both provide estimates of R_p/R_* which can be converted into planet radius and directly compared. We find that our squared exponential (SE) GP model strongly agrees with our simple harmonic oscillator (SHO) GP model.

many asteroseismic models used to describe stellar oscillations (eg., Huber et al. 2009). This allows us to create a physically motivated model of stellar variability from which we can produce rigorous probabilistic measurements of asteroseismic quantities using only time domain information.

Our simple harmonic oscillator Gaussian process model consists of three main components: two $Q = 1/\sqrt{2}$ terms, which are commonly used to model granulation in asteroseismic analyses (Harvey 1985; Huber et al. 2009; Kallinger et al. 2014), and one $Q \gg 1$ term, which has been shown to describe stellar oscillations effectively (Foreman-Mackey et al. 2017), to describe the envelope of stellar oscillation signal. The resonant frequency ω_0 of this component of is thus an independent estimate of $\nu_{\max}$, and we compare our asteroseismic $\nu_{\max}$ measurement made from analysis in the frequency domain to the $\nu_{\max}$ we generate here through a pure time domain analysis. We find good agreement between our independent estimates of $\nu_{\max}$ for K2-132 using both traditional asteroseismic

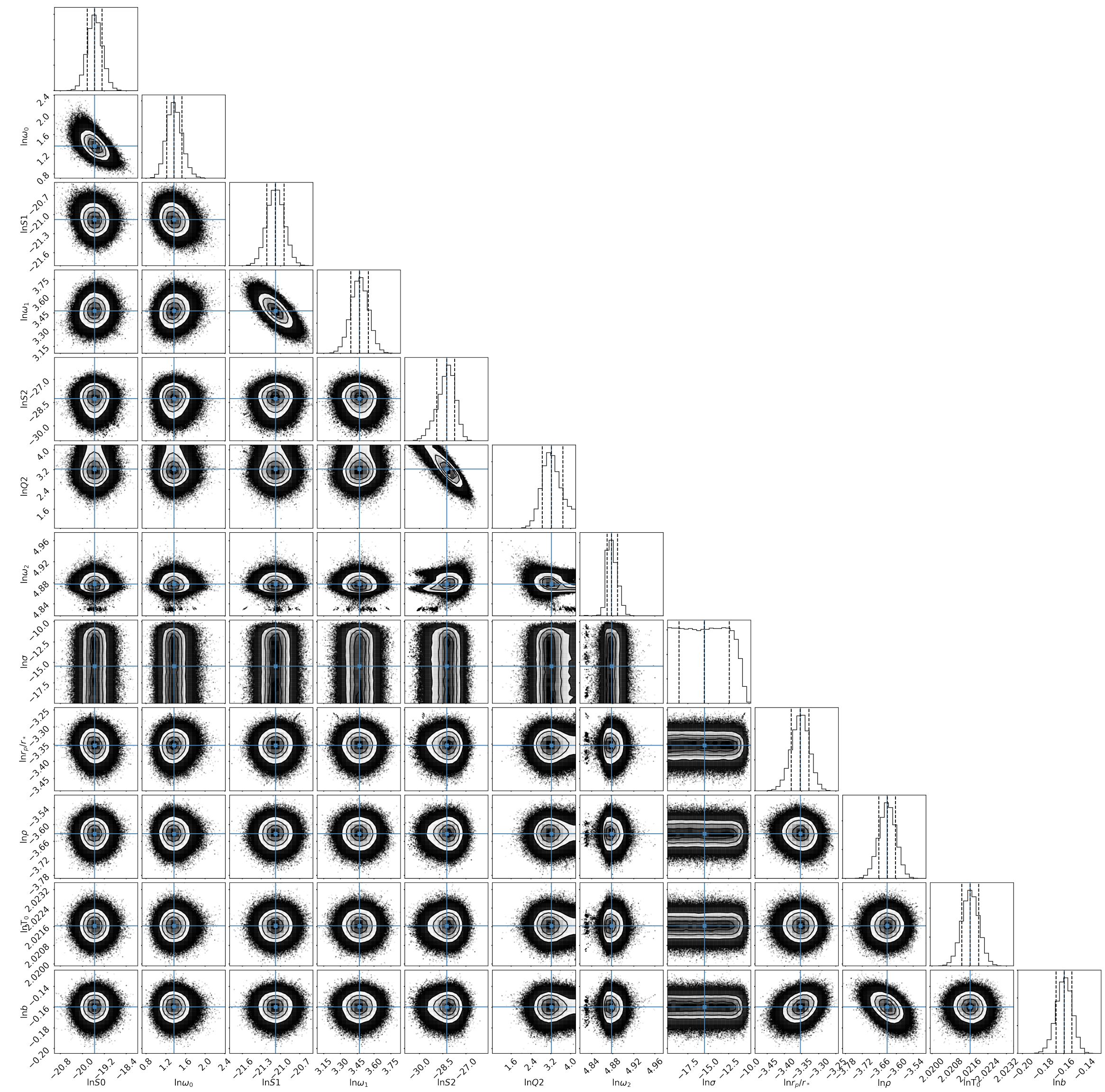

Figure 3.8 Posterior distributions for the complete transit + GP model of K2-132. The first 8 parameters are part of the GP model, whereas the last 4 are components of the transit model. Individual parameter posterior distributions are shown along the diagonal, while correlations between two parameters are shown as the off-diagonal, two-dimensional distributions. Median values are indicated by the blue lines; dotted lines indicate 1-σ uncertainties. Priors are discussed in further detail within the text.

analysis methods ($\nu_{\max} = 245.65 \pm 3.51$ μHz) and our simple harmonic oscillator Gaussian process model estimate ($\nu_{\max,\mathrm{GP}} = 241.8 \pm 1.9$ μHz).

Following the procedure of G16, we incorporate a transit model with initial parameters determined by the box least-squares analysis as the mean function from which residuals and the

Gaussian process kernel parameters are estimated. By exploring probability space through an MCMC routine where a likelihood for the combined transit and variability model is calculated repeatedly, we simultaneously optimize both the stellar variability and transit parameters. The logarithm of the posterior likelihood of our model is given as

$$\log[\mathcal{L}(\mathbf{r})] = -\frac{1}{2}\mathbf{r}^{\mathrm{T}}\mathbf{\Sigma}^{-1}\mathbf{r} - \frac{1}{2}\log|\mathbf{\Sigma}| - \frac{n}{2}\log(2\pi), \tag{3.8}$$

where $\mathbf{r}$ is the vector of residuals of the data after removal of the mean function (in our case, $\mathbf{r}$ is the lightcurve signal minus the transit model), and n the number of data points.

We repeat this process using both the new simple harmonic oscillator Gaussian process estimator as well as the squared exponential Gaussian process estimator. We illustrate our transit + GP models and uncertainties in the time domain in Figure 3.5, as well as our simple harmonic oscillator GP model in the frequency domain in Figure 3.6. We find that our simple harmonic oscillator Gaussian process estimation is able to capture variation on a wider range of timescales than the squared exponential Gaussian process estimation, and also features smaller uncertainty distributions in the time domain. In addition, the simple harmonic oscillator model exploits the tridiagonal structure of a covariance matrix generated by a mixture of exponentials such that it scales linearly, rather than cubicly, with the size of the input dataset. This means the squared exponential Gaussian process estimation takes over an order of magnitude more time to generate for the entire lightcurve than the simple harmonic oscillator model despite having less than half the number of parameters. Furthermore, the squared exponential estimate provides a poor estimate of the appearance of the data in the frequency domain, whereas the simple harmonic oscillator estimate is able to reproduce both an estimate of the granulation background as well as the stellar oscillation signal, two of the strongest features of the stellar signal in the frequency domain. The similarity between the simple harmonic oscillator estimate and the power spectral density estimate from the lightcurve is particularly remarkable considering all fitting was done using time domain information, suggesting that this simple harmonic oscillator estimation technique may be a valuable prototype for designing a technique to perform ensemble asteroseismology using only time domain information (Brewer & Stello 2009; Foreman-Mackey et al. 2017).

Due to the benefits from employing the simple harmonic oscillator Gaussian process estimation technique to extract the planet to star radius ratio, we choose to use the results from this model as our accepted values for calculating planet radius. We show the best-fit results for selected parameters of interest in Table 3.3. The posterior distributions of the planet radius estimated with both methods are shown in Figure 3.7, illustrating that planet radius estimates by both Gaussian process techniques are in very good agreement.

Figure 3.8 illustrates the parameter distributions for the full transit+GP model. All parameters are sampled in logarithmic space. The first nine parameters are simple harmonic oscillator components terms of the model, as well as the white noise σ. The last four parameters of the model are transit parameters R_p/R_*, stellar density ρ, phase parameter T_0, and impact parameter b, . Correlations between b and R_p/R_* can be seen. Uniform box priors were placed on all GP parameters to ensure physical values. In addition, $\ln\omega_{0,0}$ has a strict lower bound of 1.1 as the data quality at frequencies lower than 3 μHz is too poor to warrant modeling. $\ln Q_2$ has a strict upper bound of 4.2 to ensure that the envelope of stellar oscillations is modeled as opposed to individual frequencies of stellar oscillation (which correspond to higher Q values), and $\omega_{0,2}$ has bounds of 200 and 280 μHz to ensure that the excess modeled corresponds to the asteroseismic excess determined previously. The lower bound of the white noise parameter $\ln\sigma$ posterior distribution is also set by a uniform box prior, as the median absolute deviation of the lightcurve (162 ppm, not a variable in our model) is sufficient to capture the uncorrelated variability in our data and thus any additional white noise below this level is equally likely given this dataset. A Gaussian prior has been placed on ρ according to its asteroseismic determination in §3.2. Eccentricity is fixed to zero for our transit model, based on arguments explained in §5.3.

In addition, the quadratic limb darkening parameters γ_1 and γ_2 in our transit model were fixed to the (Claret & Bloemen 2011) stellar atmosphere model grid values of 0.6505 and 0.1041, respectively. These values correspond to the stellar model atmosphere closest to the measured temperature, surface gravity, and metallicity of the host star. As Barclay et al. (2015) demonstrate that limb darkening parameters are poorly constrained by the transits of a giant planet orbiting a giant star with 4 years of *Kepler* photometry, our much smaller sample of transits, all of which are polluted by stellar variability, would not be sufficient to constrain limb darkening.

In order to evaluate parameter convergence, the Gelman-Rubin statistic was calculated for each parameter distribution and forced to reach 1.01 or smaller (Gelman & Rubin 1992). In order to achieve this, 30 Monte Carlo Markov Chains with 50,000 steps each were used to produce parameter distributions.

3.4.2 Radial Velocity Analysis, Planetary Confirmation, and False Positive Assessment

We modeled the Keck/HIRES RV measurements of K2-97 and K2-132 following the method of G16, with slight modifications. Similarly to G16, we produced an initial fit for the systems using the publicly available Python package `RadVel` (Fulton & Petigura 2017), and then fit the data independently as a Keplerian system with amplitude K, phase ϕ, white noise σ, and radial velocity zeropoint z, and a period θ predetermined and fixed from the transit analysis.

We assume the eccentricity of the planet is fixed to zero in our transit and radial velocity analysis based on dynamical arguments presented in §5.3. Nevertheless, the data is not sufficient to precisely constrain the eccentricity of this system. Jones et al. (2017) explore the possibilities of eccentricity in this system in further detail.

Due to the relatively high degree of scatter within our radial velocity measurements, and the known increase in radial velocity scatter due to stellar jitter as stars evolve up the red giant branch (Huber et al. 2011b), we fit for the astrophysical white noise error and add it to our radial velocity measurement errors in quadrature, finding typical errors of 10–15 m s^{-1}. Non-transiting planets orbiting at different orbital periods may also add additional uncertainty to our measurements. We have probed modestly for these planets by collecting radial velocity measurements spanning multiple orbital periods of the transiting planet in both systems, confirming that the dominant periodic radial velocity signal coincides with the transit events. Median values and uncertainties on Keplerian model parameters were determined using Monte Carlo Markov Chain analysis powered by `emcee` (Foreman-Mackey et al. 2013). We illustrate the radial velocity measurements of both systems as well as the best-fit Keplerian models in Figure 3.9.

Figure 3.10 illustrates the posterior distributions for the RV model amplitude K, phase ϕ, zeropoint z, and uncorrelated uncertainty σ. In order to evaluate parameter convergence, the Gelman-Rubin statistic was calculated for each parameter distribution and forced to reach 1.01 or smaller (Gelman & Rubin 1992). In order to achieve this, 30 Monte Carlo Markov Chains with 50,000 steps each were used to produce parameter distributions.

The initial confirmation of the K2-97b system included the three earliest Keck/HIRES measurements shown here as well as radial velocities measured by the Automated Planet Finder (APF) Levy Spectrometer at the Lick Observatory in California. Due to the relatively large uncertainties on the APF measurements, the earlier mass estimates were dominated by the Keck/HIRES data. However, the small number of Keck/HIRES measurements spanned less than 10% of the entire orbit. This limited coverage, as well as an overly conservative estimate of stellar jitter, resulted in an overestimate of the mass of K2-97b in G16. The additional coverage by Keck/HIRES since the publication of G16 has negated the issues brought by the relatively large uncertainties of the APF measurements, and effectively expanded the radial velocity phase coverage to >50%. This revealed that the previous characterization of stellar jitter was an underestimate and the planet mass was significantly lower than estimated in G16.

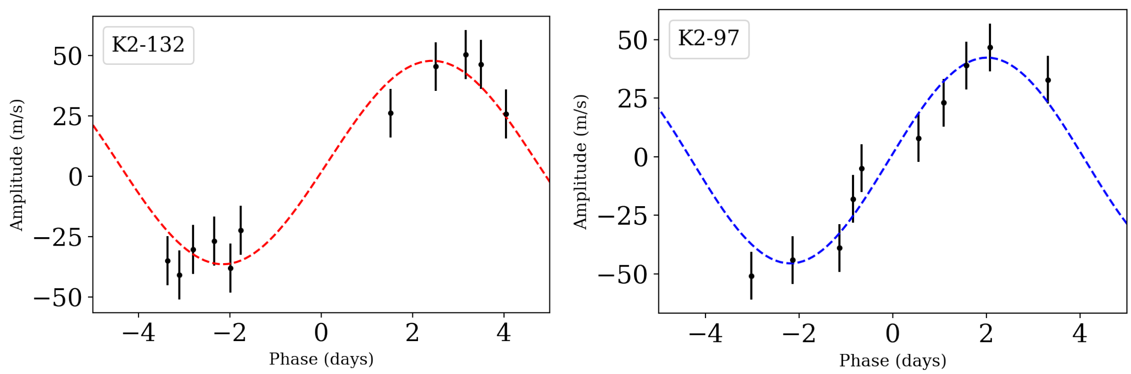

Figure 3.9 Black points show Keck/HIRES radial velocity measurements of the K2-97b and K2-132.01 systems, phase-folded at their orbital periods derived from lightcurve analysis. Errors correspond to the measurement errors of the instrument added in quadrature to the measured astrophysical jitter. The dashed colored curves correspond to the one-planet Keplerian orbit fit to the data, using the median value of the posterior distribution for each fitted Keplerian orbital parameter. Parameter posterior distributions were determined through MCMC analysis with `emcee`.

We quantitatively evaluated false positive scenarios for K2-132b as in G16 and more thoroughly described in Gaidos et al. (2016), using our adaptive optics (AO) imaging and lack of a long-term trend in our radial velocity measurements of K2-132 to rule out a background eclipsing binaries or hierarchical triple (companion eclipsing binary). We reject these scenarios because the nearly 8 hr transit duration is much too long compared to that expected for an eclipsing binary with the same period, provided that the system is not highly eccentric ($e > 0.3$), and our radial velocity measurements rule out a scenario involving two stellar mass objects. Preliminary evidence from our radial velocity data also suggests that an eccentricity of $e > 0.3$ is unlikely for this system, but a full exploration of eccentricity scenarios is beyond the scope of this article (see §5.3 for more details). Furthermore, a background evolved star that was unresolved by our AO imaging is too unlikely

Table 3.3. Posterior Probabilities from Lightcurve and Radial Velocity MCMC Modeling of K2-132

Parameter	Posterior Value	Prior
ρ (g cm^{-3})	$0.0264^{+0.0008}_{-0.0007}$	$\mathcal{N}(0.0264;\ 0.0008)$
T_0 (BJD-2454833)	$2757.1491^{+0.008}_{-0.009}$	$\mathcal{U}(5.5;\ 9.5)$
$P_{\rm orb}$ (days)	$9.1751^{+0.0023}_{-0.0027}$	$\mathcal{U}(9.0;\ 9.4)$
b	$0.848^{+0.007}_{-0.008}$	$\mathcal{U}(0.0,\ 1.0 + R_p/R_*)$
R_p/R_*	$0.0325^{+0.0014}_{-0.0011}$	$\mathcal{U}(0.0,\ 0.5)$
$\nu_{\rm max,GP}$ (μHz)	$241.8^{+1.9}_{-1.9}$	$\mathcal{U}(120,\ 280))$
K (m s^{-1})	$42.1^{+4.3}_{-4.2}$	
$T_{0,\rm RV}$ (BKJD % $P_{\rm orb}$)	$3.57^{+0.19}_{-0.19}$	$\mathcal{U}(0.0,\ P_{\rm orb})$
$\sigma_{\rm RV}$ (m s^{-1})	$11.5^{+4.1}_{-2.6}$	$\mathcal{U}(0,\ 100)$

Note. — $\mathcal{N}$ indicates a normal distribution with mean and standard deviation given respectively. $\mathcal{U}$ indicates a uniform distribution between the two given boundaries. Ephemerides were fit relative to the first measurement in the sample and then later converted to Barycentric *Kepler* Julian Date (BKJD).

$\ll 2 \times 10^{-7}$ and the dilution too high by the foreground (target) star to explain the signal. Evolved companions are ruled out by our AO imaging to within 0.2" and stellar counterparts within ~ 1 AU are ruled out by the absence of an RV drift.

We cannot rule out companions that could cause a small systematic error in planet radius due to dilution of the transit signal. However, to change the planet radius by one standard error the *minimum* contrast ratio in the *Kepler* bandpass must be 0.1. If the star is cooler than K2-132 (likely, since a hotter, more massive star would be more evolved) then the contrast in the K-band of our NIRC2 imaging would be even higher. We can rule out all such stars exterior to 0.15 arcsec (~ 50 AU) of the primary; absence of a significant drift in the Doppler data or a second set of lines in the HIRES spectrum rules out stellar companions within about 1 AU. Regardless, transit dilution by an unresolved companion would mean that the planet is actually *larger* than we estimate and inflation even more likely.

3.5 Constraining Planet Inflation Scenarios

3.5.1 Irradiation Histories of K2-97b and K2-132.01

Planets with orbital periods of <30 days will experience levels of irradiation comparable to typical hot Jupiters for more than 100 Myr during post-main sequence evolution. Thus, we can test planet inflation mechanisms by examining how planets respond to increasing irradiation as the host star

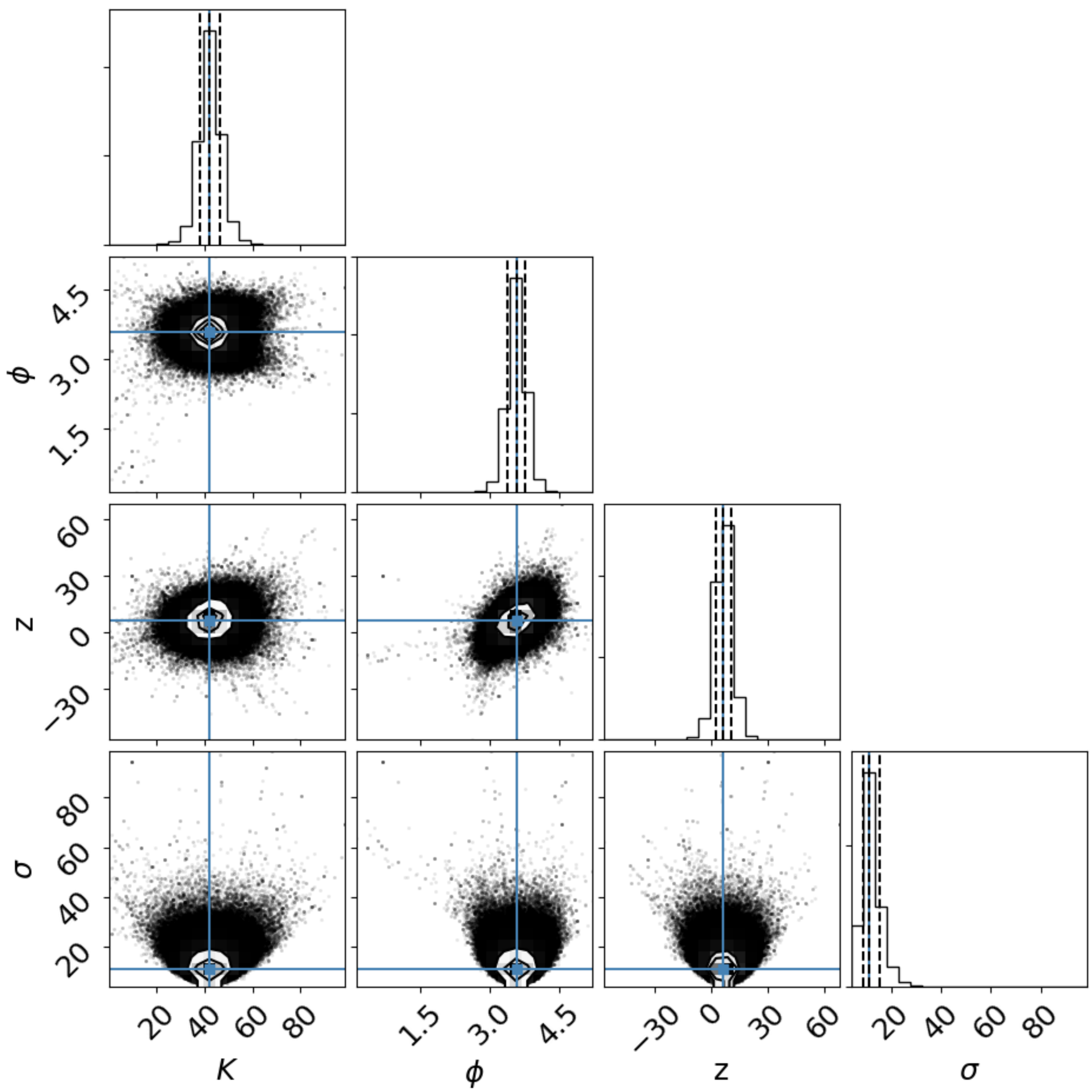

Figure 3.10 Posterior distributions for the complete RV model of K2-132.01. Individual parameter posterior distributions are shown along the diagonal, while correlations between two parameters are shown as the off-diagonal, two-dimensional distributions. Median values are indicated by the blue lines; dotted lines indicate 1-σ uncertainties.

leaves the main sequence. Following the nomenclature of Lopez & Fortney (2016), if the inflation mechanism requires direct heating and thus falls into Class I, the planet's radius should increase around a post-main sequence star. However, if the inflation mechanism falls into Class II, requiring delayed cooling, there should be no effect on planet radius as a star enters the red giant phase, and re-inflation will not occur. As K2-97b and K2-132.01 are inflated now but may not have

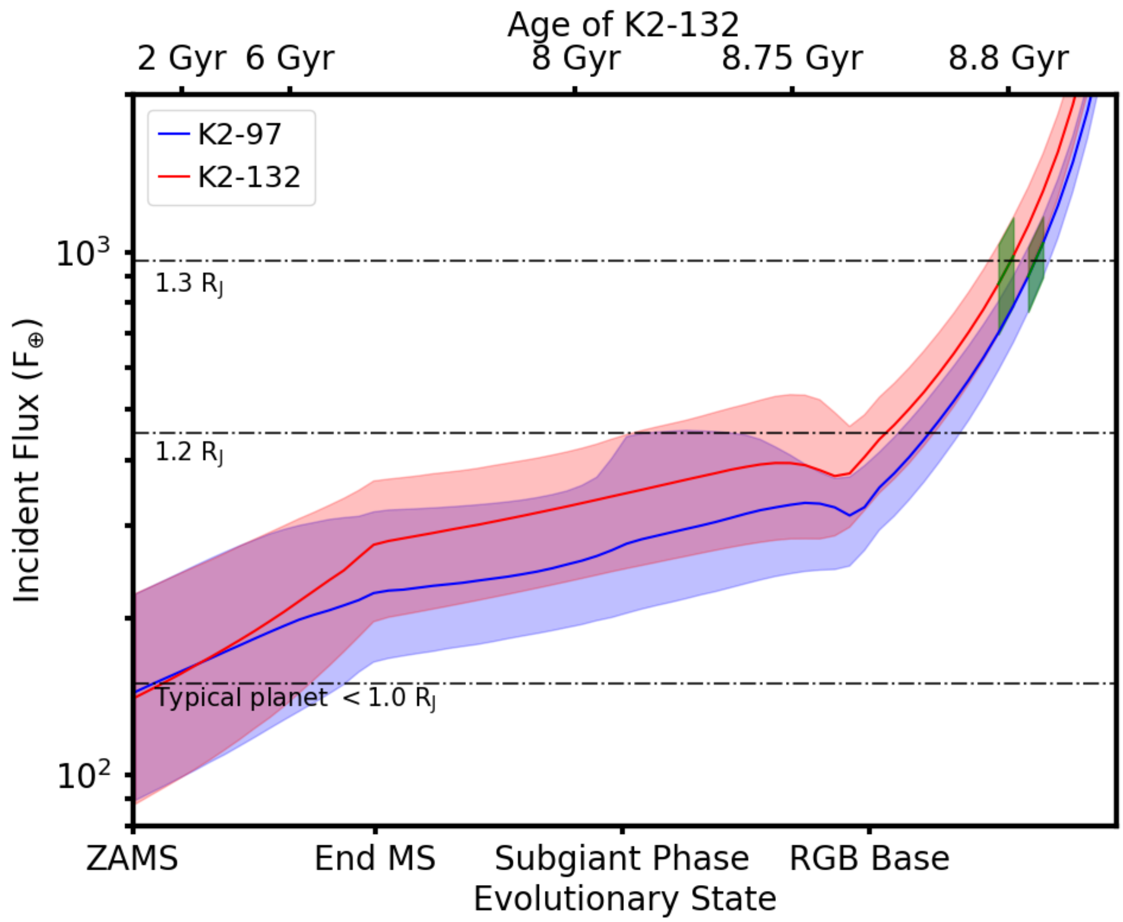

Figure 3.11 Incident flux as a function of evolutionary state for K2-97b and K2-132.01. The current incident flux on the planets is denoted in green. Solid blue and red lines and shaded areas show the median and 1-σ confidence interval considering uncertainties in stellar mass and metallicity. The black dashed lines correspond to the median incident fluxes for known populations of hot gas giant planets of different radii (Demory & Seager 2011, NASA Exoplanet Archive, 9/14/2017). The top axis shows representative ages for the best-fit stellar parameters of K2-132.

received irradiation significantly above the inflation threshold on the main sequence, they provide valuable tests for the re-inflation hypothesis. Furthermore, these systems can be used to constrain the mechanisms of heat transfer and dissipation within planets (e.g., Tremblin et al. 2017).

To trace the incident flux history of both planets we used a grid of Parsec v2.1 evolutionary tracks (Bressan et al. 2012) with metallicities ranging from [Fe/H] $= -0.18$ to 0.6 dex and masses ranging from $0.8 - 1.8 M_\odot$. Compared to G16, we used an improved Monte-Carlo sampling scheme by interpolating evolutionary tracks to a given mass and metallicity following normal distributions with the values given in Table 4.1, and tracing the incident flux across equal evolutionary states

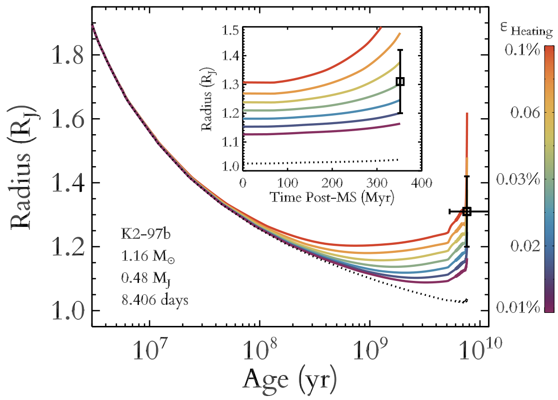

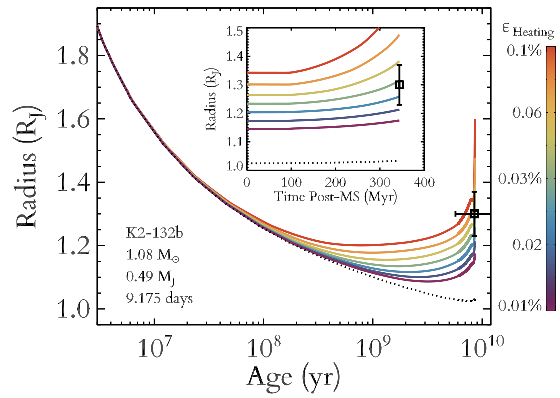

Figure 3.12 Planetary radius as a function of time for K2-97b (left) and K2-132.01 (right), shown for various different values of heating efficiency. We assume the best-fit values for the stellar mass and the planetary mass and radius, and a planetary composition of a H/He envelope surrounding a 10 $M_\oplus$ core of heavier elements. The dotted line corresponds to a scenario with no planetary heating. The inset shows the post-main sequence evolution at a finer time resolution. The measured planet radii are consistent with a heating efficiency of $0.03\%^{+0.04\%}_{-0.02\%}$ and $0.03\%^{+0.3\%}_{-0.1\%}$, respectively.

as indicated by the "phase" parameter in Parsec models. We performed 1000 iterations for each system, and the resulting probability distributions are shown as a function of evolutionary state in Figure 3.11. We note that each evolutionary state corresponds to a different age depending on stellar mass and metallicity. Representative ages for the best-fit stellar parameters of K2-132 are given on the upper x-axis. Current incident flux and age ranges for the planets were determined by restricting models to within 1-σ of the measured temperature and radius of each system (Table 4.1).

Figure 3.11 demonstrates that both planets lie near the Demory & Seager (2011) empirical threshold for inflated planets at the zero age main sequence. Planets below this threshold have typical planet radii below 1.0 R_J. Just after the end of their main sequence lifetimes, the irradiance on these planets reached the median incident flux on a typical 1.2 R_J planet determined by the median incident flux values for confirmed planets listed in the NASA Exoplanet Archive with radii consistent with 1.2 R_J.As the maximum radius of H/He planets determined by structural evolutionary models has been found to be 1.2 R_J, we treat this as the maximum size at which planets could be considered "uninflated," providing a more conservative incident flux boundary range for inflation than the lower limit established by Demory & Seager (2011) or the Laughlin et al. (2011) planetary effective temperature-radius anomaly models. Now that the host stars have evolved off the main sequence, these planets have reached incident flux values typical for 1.3 R_J planets. The median incident

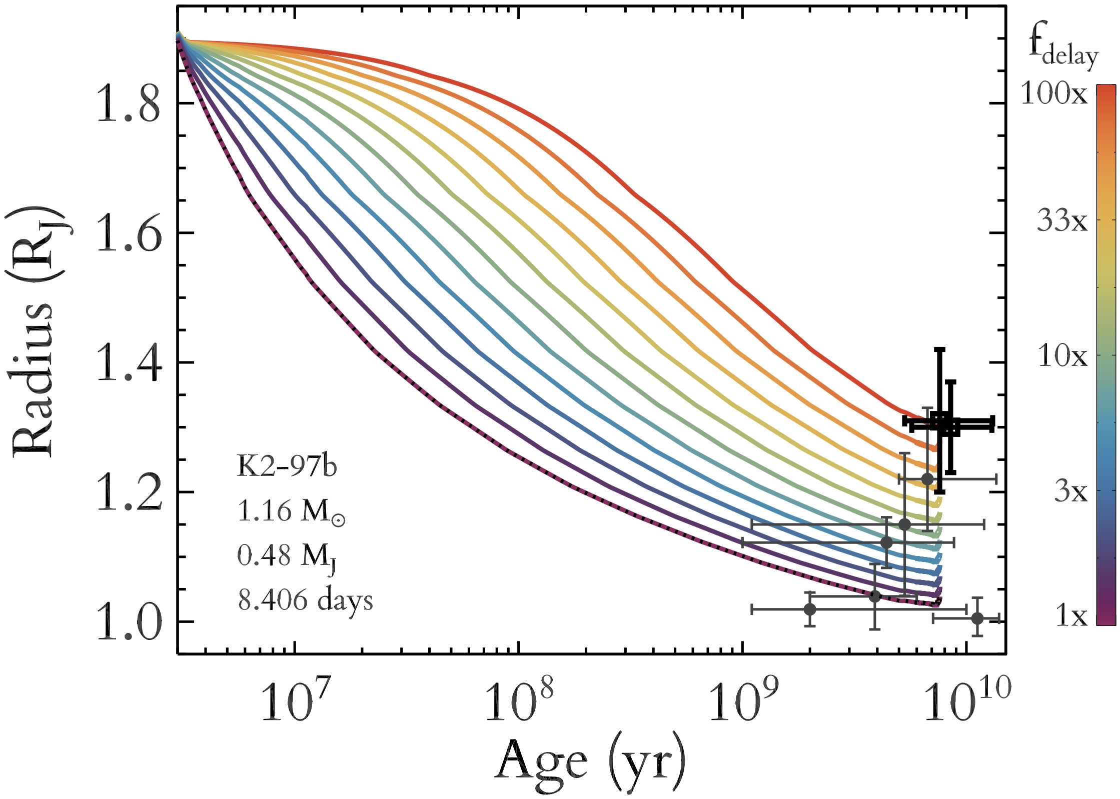

Figure 3.13 Planetary radius as a function of time for K2-97b and K2-132.01 (bold), as well other similar mass planets with similar main sequence fluxes orbiting main sequence stars. Colored tracks represent scenarios where planets begin at an initial radius of 1.85 R_J and then contract according to the Kelvin-Helmholtz timescale delayed by the factor given by the color of the track. All main sequence planets seem to lie on tracks that would favor different delayed cooling factors than the post-main sequence planets studied here.

flux for 1.3 R_J planets was determined from a sample of confirmed planets taken from the NASA Exoplanet Archive (accessed 9/14/2017).

The average main sequence fluxes of K2-97b and K2-132.01 are 170^{+140}_{-60} $F_\oplus$ and 190^{+150}_{-80} $F_\oplus$, respectively. These values are more than 4.5-σ from the median fluxes of well-characterized 1.3 R_J planets. However, the current incident fluxes of 900±200 $F_\oplus$ on these planets, shown in green on Figure 3.11, is strongly consistent with the observed incident flux range of 1.3 R_J planets, suggesting that the radii of these planets is tied closely to their current irradiation. Despite the fact that the planets crossed the empirical threshold for inflation relatively early on in their lifetimes if at all, the planets did not receive sufficient flux to display significant radius anomalies or be inflated to their observed sizes until post-main sequence evolution.

Though the current incident fluxes of the planets in this study lie much closer to the median value for 1.3 R_J planets, it is important to note that their incident flux is also consistent with the 1.2 R_J planet population, as the standard deviation in both planet populations is $\gtrsim$500 $F_\oplus$. This is to be expected, as the vast majority of confirmed planet radii are not measured to within 10% or less, and thus the 1.2 R_J and 1.3 R_J planet populations are not distinct.

3.5.2 Comparing Re-Inflation and Delayed Cooling Models

Figure 3.12 illustrates Class I models for the radius evolution of K2-97b and K2-132.01, assuming the best-fit values for planet mass, radius, and orbital period. Each of these models assumes a constant planetary heating efficiency, defined to be the fraction of energy a planet receives from its host star that is deposited into the planetary interior, causing adiabatic heating and inflation of the planet. The colors of the various planetary evolution curves correspond to different planetary heating efficiencies ranging from 0.01% to 0.1%, assuming a planet with the best-fit planet mass at a constant orbital distance from a star with the best-fit stellar mass calculated here. The incident flux on the planet is then calculated as a function of time using the MESA stellar evolutionary tracks (Choi et al. 2016). From this, the planet radius is calculated by convolving the Kelvin-Helmholtz cooling time with planetary heating at a consistent efficiency with respect to the incident stellar flux over the lifetime of the system. The black dotted lines correspond to planetary evolution with no external heat source. Post main sequence evolution is shown with higher time resolution in the insets. Based on the calculated planet radii, we estimate a heating efficiency of $0.03\%^{+0.04\%}_{-0.02\%}$ for K2-97b and $0.03\%^{+0.03\%}_{-0.01\%}$ for K2-132.01. Uncertainties on the heating efficiency were calculated by running additional models for each system with both masses and radii lowered/raised by one standard deviation. As planet mass and radius uncertainties are not perfectly correlated, using such a method to calculate planetary heating efficiency should provide conservative errors.

Based on these two particular planets, the heating efficiency of gas giant planets via post-main sequence evolution of their host stars is strongly consistent between both planets but smaller than theories predict (Lopez & Fortney 2016), and disagrees with the previous estimate of planetary heating efficiency of 0.1%–0.5% made by G16. This disagreement stems from the overestimate of the mass of K2-97b in the previous study. As the radii of lower density planets are more sensitive to heating and cooling effects than those of higher density, the required heating to inflate a 1.1 M_J planet to 1.3 R_J is significantly larger than the heating necessary to inflate a 0.5 M_J planet to the same size. These new estimates of planet heating efficiency tentatively suggest that if planetary re-inflation occurred in these systems, the process is not as efficient as previous studies suggested (Lopez & Fortney 2016).

Slowed planetary cooling cannot be entirely ruled out as the cause for large planet radii, as the planets are not larger than they would have been during their pre-main sequence formation. Figure 3.13 illustrates the various delayed cooling tracks that could potentially produce these planets. Different colored curves correspond to cooling models where the Kelvin-Helmholtz cooling time is increased by a constant factor. K2-97b and K2-132.01 are shown in bold, whereas planets with masses of 0.4–0.6 M_J, incident fluxes of 100–300 $F_\oplus$, and host stars smaller than $2R_\odot$ (to ensure that they have not begun RGB evolution) are shown in gray (specifically these planets are K2-30b, Kepler-422b, OGLE-TR-111b, WASP-11b, WASP-34b, and WASP-42b). It can be seen that the main sequence planets have systematically smaller radii, and thus suggest delayed cooling rates that are significantly different from those which would be inferred from the planets in this study. The required cooling delay factor for the post-main sequence planets studied here is 20–250, significantly more than the factor of ∼1–10 for main sequence cases. Delayed cooling models predict a decrease in planet radius with age, which strongly disagrees with the data shown here. Re-inflation models predict the opposite. Thus, we conclude that Class I re-inflation mechanisms are more statistically relevant than Class II mechanisms in the evolution of K2-97b and K2-132.01, and thus stellar irradiation is likely to be the direct cause of warm and hot Jupiter inflation.

Furthermore, the assumption of a $10M_\oplus$ core is low compared to the inferred core masses of cooler non-inflated giants. Using the planet-core mass relationship of Thorngren et al. (2015), we predict core masses of $\approx$37 $M_\oplus$ for both K2-97b and K2-132.01. These higher core masses would significantly increase the required heating efficiencies to $0.10\%^{+0.09\%}_{-0.05\%}$ for K2-97b and $0.14\%^{+0.07\%}_{-0.04\%}$ for K2-132.01, or delayed cooling factors of 300–3000× for these planets. Though these values suggest better agreement with previous results (e.g., G16), we report the conservative outcomes assuming 10 M⊕ cores to place a lower limit on the efficiency of planetary heating.

3.5.3 Eccentricity Effects

Jones et al. (2017) independently report a non-zero eccentricity for K2-132.01 based on the HIRES data presented here and additional RV measurements obtained with other instruments. Since transit parameters are often degenerate, an inaccurate eccentricity could result in an inaccurate planet radius (e.g. Eastman et al. 2013) and thus potentially affect our conclusions regarding planet re-inflation.

A non-circular orbit would be surprising given the expected tidal circularization timescale for such planets. Our estimated planet parameters suggest a timescale of $\tau_e \sim 6$ Gyr using the relation of Gu et al. (2003) and assuming a tidal quality factor $Q_p \approx 10^6$, comparable to Jupiter (Ogilvie & Lin 2004; Wu 2005). This suggests that the orbit of this planet should have been circularized before post-main sequence evolution, as long as no other companion could have dynamically excited the system. However, these timescale estimates are very sensitive to planet density and tidal quality factor, and adjusting these parameters within errors can result in estimates of $\tau_e < 1$ Gyr as well as $\tau_e > 10$ Gyr. Thus, we cannot rule out a non-zero eccentricity for this system based on tidal circularization timescale arguments alone.

We also used the relations of Bodenheimer et al. (2001) to determine the tidal circularization energy and thus tidal radius inflation that would expected for this system. We find that the tidal inflation should be negligible for this system even for a potentially high eccentricity. Thus, if this planet were to be on an eccentric orbit, we should still be able to distinguish between tidal and irradiative planet inflation.

We attempted to model the eccentricity of this system and obtained results which were consistent with our circular model. However, these tests resulted in non-convergent posterior chains, and thus we cannot rule out a non-negligible eccentricity for this system. Additional RV measurements should help to constrain the eccentricity of this system, and clarify if and how eccentricity affects the planet radius presented here.

3.5.4 Selection Effects and the Similarity of Planet Parameters

K2-97 and K2-132 are remarkably similar: the stellar radii and masses and planet radii, masses, and orbital periods agree within 10%. This begs the question: is it only coincidence that these systems are so similar, is it the product of convergent planetary evolution, or is it the result of survey bias or selection effect? Here, we investigate the last possibility.

Two effects modulate the intrinsic distribution of planets as a function of mass M, radius R, and orbital period P to produce the observed occurrence in a survey of evolved stars: the detection of the planet by transit, and the lifetime of planets against orbital decay due to tides raised on large, low-density host stars. A deficit of giant planets close to evolved stars (Kunitomo et al.

2011) as well as the peculiar characteristics of some RGB stars (rapid rotation, magnetic fields, and lithium abundance) have been explained as the result of orbital decay and ingestion of giant planets (Carlberg et al. 2009; Privitera et al. 2016a,b; Aguilera-Gómez et al. 2016a,b).

The volume V over which planets of radius R_p and orbital period P can be detected transiting a star of mass and radius M_* and R_* is (see Appendix):

$$V \sim R_p^{\frac{3}{(1-\alpha)}} P^{-1} R_*^{-\frac{3(3\alpha-1)}{2(1-\alpha)}} M_*^{-\frac{1}{2}}, \tag{3.9}$$

. where α is the power-law index relating RMS photometric error to number of observations ($\alpha = 1/2$ for uncorrelated white noise). The lifetime of a planet against orbital decay due to tides raised on the star, in the limit that the decay time is short compared to the RGB lifetime, is

$$\tau_{\rm tide} \approx 4.1 \left(\frac{M_P}{M_J}\right)^{-1} P_{\rm days}^{\frac{13}{3}} \frac{Q'_*}{2\times 10^5} \left(\frac{M_*}{M_\odot}\right)^{\frac{5}{3}} \left(\frac{R_*}{R_\odot}\right)^{-5} \text{Myr}, \tag{3.10}$$

. where Q'_* is a modified tidal quality factor (see Appendix).

The bias effect B is the product $V \cdot \tau_{\rm tide}$ which then scales as:

$$B \propto R_p^{\frac{3}{(1-\alpha)}} M_P^{-1} P^{\frac{10}{3}} M_*^{\frac{7}{6}} R_*^{-\frac{7-\alpha}{2(1-\alpha)}}. \tag{3.11}$$

This formulation ignores the possibility of Roche-lobe overflow and mass exchange between the planet and the star (e.g., Jackson et al. 2017, and references therein). Roche-lobe overflow of the planet will occur only when $a \lesssim 2.0R_*(\rho_*/\rho_p)^{1/3}$ (Rappaport et al. 2013) and since ρ_p is at least an order of magnitude larger than ρ_* on the RGB, overflow never occurs before the planet is engulfed. In fact, the planet may accrete mass from the star before engulfment but this only hastens its demise.

Our survey is biased towards planets with large radii (easier to detect) but against planets with large masses (shorter lifetime). Contours of constant bias in a mass-radius diagram describe the relation $R_P \propto M_P^{(1-\alpha)/3}$. If the power-law index of the planetary mass-radius relation is *steeper* than the critical value $(1-\alpha)/3$ then larger planets are favored; if it is shallower than smaller planets are favored. A maximum in B occurs where the index breaks, i.e. at a "knee" in the mass-radius relation. For $\alpha = 1/2$ the critical value of the power-law index is 1/6, i.e. well below the values inferred for rocky planets or "ice giants" like Neptune. Chen & Kipping (2017) inferred a break at $0.41 \pm 0.06M_J$ where the index falls from 0.59 to -0.04, reflecting the onset of support by electron degeneracy in gas giant planets. Bashi et al. (2017) found a similar transition of 0.55 to 0.01 at $0.39 \pm 0.02 M_J$. Since the power-law index of B is bounded by 0 and 1/3, the location of B is independent of α, but the magnitude of the bias does increase with α. This is illustrated in Fig. 3.14, where B (normalized by the maximum value) is calculated for planets following the Chen & Kipping (2017) mass-radius relation and with $\alpha = 1/2$ (pure Poisson noise) and $\alpha = 0.7$ (finite correlated noise).

For periods less than a critical value P_* (see Appendix), where

$$P_* = 0.63 \left(M_P \tau_{\rm RGB} M_*^{-1} \rho_i^{-5/3} \right)^{3/13} \text{ days}, \tag{3.12}$$

where M_P is in Jupiter masses, $\tau_{\rm RGB}$ is in Myr, and M_* and ρ_i are in solar units, the decay time is shorter than the RGB lifetime and Eqn. 3.12 holds. Using the stellar evolution models of Pols et al. (1998) for a solar-like metallicity, we find $P_* \approx 5-6$ days, roughly independent of M_* over the range 0.9–1.6$M_\odot$, and only weakly dependent on M_P. For planets with $P > P_*$, including K2-97b and K2-132.01, planet lifetime is governed by the RGB evolution time rather than orbital decay time, and detection bias dominates.

The survey bias for P can be seen in Eqn. 3.11 where B increases rapidly with P to P_*, at which point $\tau_{\rm tide}$ becomes comparable to $\tau_{\rm RGB}$ and Eqn. 3.11 no longer applies. Beyond that point, survey bias is governed by detection bias, which *decreases* with P (Eqn. 3.9). Thus B has a maximum at $P = 5-6$ days, weakly dependent on planet mass and Q_*. This potentially can explain Kepler-91b (6.25 days), but perhaps not K2-97b or K2-132.01.

Since P_* is weakly M_P-dependent, survey bias at $P = P_*$ is also dependent on both R_P and M_P. Substituting Eqn. 3.12 into Eqn. 3.11 yields $B \propto R_P^{3/(1-\alpha)} M_P^{-3/13}$. Interestingly, this mass dependence, combined with the slightly negative mass-radius power-law index for giant planets due to electron degeneracy pressure, is enough to produce a peak in B, again at the $0.4M_J$ transition. Explanation of the similarities of the K2-97b and K2-132.01 systems by survey bias, however, might require an anomalously low value of Q'_*, inconsistent with constraints from binary stars and analyses of other planetary systems (see discussion in Patra et al. 2017), as well as the theoretical expectation that dissipation on the RGB is weaker because of the small core mass and radius (e.g., Gallet et al. 2017).

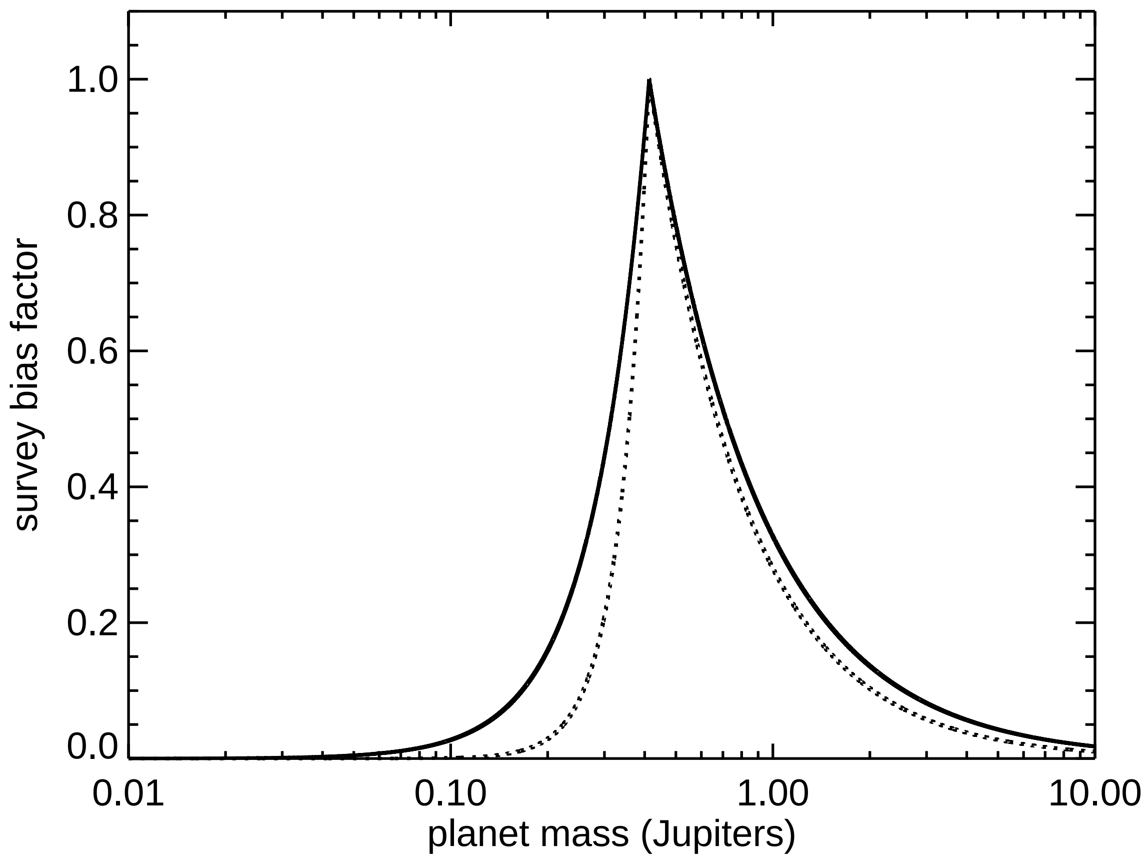

Figure 3.14 Survey bias factor B as a function of planet mass for planets around evolved stars, calculated using Eqn. 3.11 and the Chen & Kipping (2017) planet mass-radius relation, and assuming the orbital decay time is much shorter than the stellar evolution time. The solid lines is for pure "white" (Poisson) noise ($\alpha = 0.5$) while the dashed line is for the case of "red" (correlated) noise ($\alpha = 0.7$). Detection of planets of $0.4M_J$ mass is strongly favored: smaller planets are more difficult to detect while more massive planets do not survive long enough.

Alternatively, we note that our selection criterion criterion of detectable stellar oscillations imposes a lower limit on R_* of about $3R_\odot$. This means that that effective initial stellar density in our sample ρ_i is several times smaller, which increase P_* by a factor of ~ 1.5, making it consistent with the orbits of K2-97b and K2-132.01. In future work we will perform a more rigorous treatment of bias using the actual stars in our survey and their properties using asteroseismology, spectroscopy, and forthcoming *Gaia* parallaxes.

3.6 Conclusions

We report the discovery of a transiting planet with R = 1.30 ± 0.07 R_J and M = 0.49 ± 0.06 M_J around the low luminosity giant star K2-132, and revise our earlier mass estimate of K2-97b. We use a simple harmonic oscillator Gaussian process model to estimate the correlated noise in the lightcurve to quantify and remove potential correlations between planetary and stellar properties, and measure asteroseismic quantities of the star using only time domain information. We also performed spectroscopic, traditional asteroseismic, and imaging studies of the host stars K2-97 and K2-132 to precisely determine stellar parameters and evolutionary history and rule out false positive scenarios. We find that both systems have effectively null false positive probabilities. We also find that the masses, radii, and orbital periods of these systems are similar to within 10%, possibly due to a selection bias toward larger yet less massive planets.

We determine that K2-97b and K2-132.01 require approximately 0.03% of the current incident stellar flux to be deposited into the planets' deep convective interior to explain their radii. This suggests planet inflation is a direct response to stellar irradiation rather than an effect of delayed planet cooling after formation, especially for inflated planets seen in evolved systems. However, stellar irradiation may not be as efficient a mechanism for planet inflation as indicated by Grunblatt et al. (2016), due to the previously overestimated mass of K2-97b driven by the limited phase coverage of the original Keck/HIRES radial velocity measurements.

Further studies of planets around evolved stars are essential to confirm the planet re-inflation hypothesis. Planets may be inflated by methods that are more strongly dependent on other factors such as atmospheric metallicity than incident flux. An inflated planet on a 20 day orbit around a giant star would have been definitively outside the inflated planet regime when its host star was on the main sequence, and thus finding such a planet could more definitively test the re-inflation hypothesis. Similarly, a similar planet at a similar orbital period around a more evolved star will be inflated to a higher degree (assuming a constant heating efficiency for all planets). Thus, discovering such a planet would provide more conclusive evidence regarding these phenomena. Heating efficiency may also vary between planets, dependent on composition and other environmental factors. Continued research of planets orbiting subgiant stars and planet candidates around larger, more evolved stars should provide a more conclusive view of planet re-inflation.

The NASA TESS Mission (Sullivan et al. 2015) will observe over 90% of the sky with similar cadence and precision as the K2 Mission for 30 days or more. This data will be sufficient to identify additional planets in ∼10 day orbital periods around over an order of magnitude more evolved stars, including oscillating red giants (Campante et al. 2016). This dataset should be sufficient to constrain the heating efficiency of gas-giant planets to the precision necessary to effectively distinguish between delayed cooling and direct re-inflationary scenarios. It will also greatly enhance our ability to estimate planet occurrence around LLRGB stars and perhaps help determine the longevity of our own planetary system.

3.6.1 Survey Bias for Star and Planet Properties

Following Gaudi et al. (2005), we estimated the distance d to which systems can be detected, but we modify the calculation to account for coherent ("red") noise from stellar granulation and noise due to drift of the spacecraft and stellar image on the *K2* CCDs, whereby the RMS noise increases faster than the the square root of the number of measurements n, or the signal-to-noise decreases more slowly than $n^{-1/2}$. We parameterize this by the index α, where the RMS noise scales as n^{α}. In a magnitude-limited survey of stars of a monotonic color (i.e. bolometric correction) and fixed solid angle, the volume V that can observed to a distance d and hence the number of systems in a survey goes as d^3. This scales as[1]:

$$V \propto R_p^{\frac{3}{(1-\alpha)}} P^{-1} R_*^{-\frac{3\alpha}{1-\alpha}} \rho_*^{-\frac{1}{2}}. \tag{3.13}$$

For the case of $\alpha = 1/2$ (white noise) we recover the original scaling of Gaudi et al. (2005):

$$V \propto R_p^6 R_*^{-\frac{3}{1-\alpha}} P^{-1} \rho_*^{-\frac{1}{2}}. \tag{3.14}$$

Since stars on the RGB differ far more in radius than they do in mass, we re-express ρ_* in Eqn. 3.9 terms of M_* and R_*:

$$V \sim R_p^{\frac{3}{(1-\alpha)}} P^{-1} R_*^{-\frac{3(3\alpha-1)}{2(1-\alpha)}} M_*^{-\frac{1}{2}} \tag{3.15}$$

[1]This assumes that d does not extend outside the galactic disk over a significant portion of the survey.

We also consider the lifetime of a planet against orbital decay due to the tides it raises on the slowly-rotating star. This is expressed as (e.g., Patra et al. 2017):

$$\frac{dP}{dt} = -\frac{27\pi}{2Q'_*}\frac{M_P}{M_*}\left(\frac{3\pi}{G\rho_*}\right)^{\frac{5}{3}} P^{-\frac{10}{3}}, \tag{3.16}$$

where Q'_* is a modified tidal dissipation factor that includes the Love number, M_* and ρ_* the stellar mass and mean density, and G is the gravitational constant.

If a planet's orbit decays on a time scale that is short compared to any evolution of the host star on the RGB (i.e. R_* is constant) and mass loss is negligible (i.e. M_* is constant) then integrating Eqn. 3.16 yields the decay lifetime $\tau_{\rm tide}$:

$$\tau_{\rm tide} \approx 4.1 \left(\frac{M_P}{M_J}\right)^{-1} P_{\rm dy}^{\frac{13}{3}} \frac{Q'_*}{2\times 10^5}\left(\frac{M_*}{M_\odot}\right)^{\frac{5}{3}}\left(\frac{R_*}{R_\odot}\right)^{-5} \text{Myr}, \tag{3.17}$$

where stellar values are those at the base of the RGB.

For sufficiently low M_P or large P the orbital decay time becomes comparable to the timescale of evolution of the host star on the RGB. R_* increases, decreasing the volume over which the planet could be detected (Eqn. 3.9), and shortens the lifetime (Eqn. 3.10). Rather than $V\tau_{\rm tide}$, we must evaluate

$$B \propto \int_0^{\tau_{\rm tide}} dt\, V(t). \tag{3.18}$$

To model the density evolution on the RGB during H-shell burning we adopt a helium core-mass evolution equation:

$$\frac{dM_c}{dt} = -\frac{L}{X\xi}, \tag{3.19}$$

where L is the luminosity, X is the mixing ratio of H fuel (≈ 0.7) and ξ the energy release for H-burning. We use the core mass-luminosity relation of Refsdal & Weigert (1970):

$$\frac{L}{L_\odot} \approx 200\left(\frac{M_c}{M_0}\right)^{\beta} \tag{3.20}$$

where $M_0 = 0.3 M_\odot$ is a reference core mass and $\beta = 7.6$. Assuming a constant $T_{\rm eff}$ so that $L_* \propto R_*^2$ and neglecting mass loss on the RGB, the density evolves as;

$$R_* = R_i \left[1 - \frac{L_0\,(\beta-1)}{M_0 X \xi} \left(\frac{M_i}{M_0} \right)^{\beta-1} \right]^{\frac{-\beta}{2(\beta-1)}}, \tag{3.21}$$

where ρ_i and M_i are the initial stellar density and core mass on the RGB. This can be re-written in terms of the duration of the RGB phase $\tau_{\rm RGB}$ and the final core mass M_f at the tip of the RGB when the helium flash occurs:

$$R_*(t) = R_i \left[1 + \frac{t}{\tau_{\rm RGB}} \left[1 - \left(\frac{M_i}{M_f} \right)^{\beta-1} \right] \right]^{\frac{-\beta}{2(\beta-1)}} \tag{3.22}$$

By the time the helium flash occurs, the radius of the star has evolved considerably, i.e. $R_f/R_i = (M_f/M_i)^{\beta/2}$. For a solar-mass star, $M_f/M_i \approx 4$ (Pols et al. 1998) and stars at the RGB tip will have enlarged by over two orders of magnitude relative to the end of the main sequence, while $\tau_{\rm tide}$ will have fallen by a factor of 10^{11} (Eqn. 3.10). We assume that the no planet of interest survives that long, i.e. $\tau_{\rm tide}$ never approaches $\tau_{\rm RGB}$. Moreover, even giant planets will not be detected by transit because R_P/R_* will be too small, and we neglect the mass term in Eqn. 3.22:

$$R_*(t) \approx R_i \left(1 - \frac{t}{\tau_{\rm RGB}} \right)^{\frac{-\beta}{2(\beta-1)}} \tag{3.23}$$

To obtain a scaling relation for $\tau_{\rm tide}$ we substitute Eqn. 3.22 into Eqn. 3.16 to and integrate to obtain $P(t)$, then evaluate the time-dependent factors in Eqn. 3.18. Substituting $x = 1 - t/\tau_{\rm RGB}$, B scales as

$$\begin{aligned} B \;\propto\; & R_p^{\frac{3}{1-\alpha}} M_*^{-\frac{1}{2}} \tau_{\rm RGB} \\ & \times \int_{x_{\rm min}}^{1} dx\; \left[1 - A \left(x^{-\frac{3\beta+2}{2(\beta-1)}} - 1 \right) \right]^{-\frac{3}{13}} x^{\frac{3\beta(3\alpha-1)}{4(1-\alpha)(\beta-1)}}, \end{aligned} \tag{3.24}$$

where

$$A = \frac{117\pi}{Q_*} \frac{\beta-1}{3\beta+2} \frac{M_P}{M_*} \left(\frac{3\pi}{G\rho_i} \right)^{5/3} \frac{\tau_{\rm RGB}}{P_0^{13/3}}, \tag{3.25}$$

and

$$x_{\rm min} = \left(1 + A^{-1} \right)^{-\frac{2(\beta-1)}{3\beta+2}}. \tag{3.26}$$

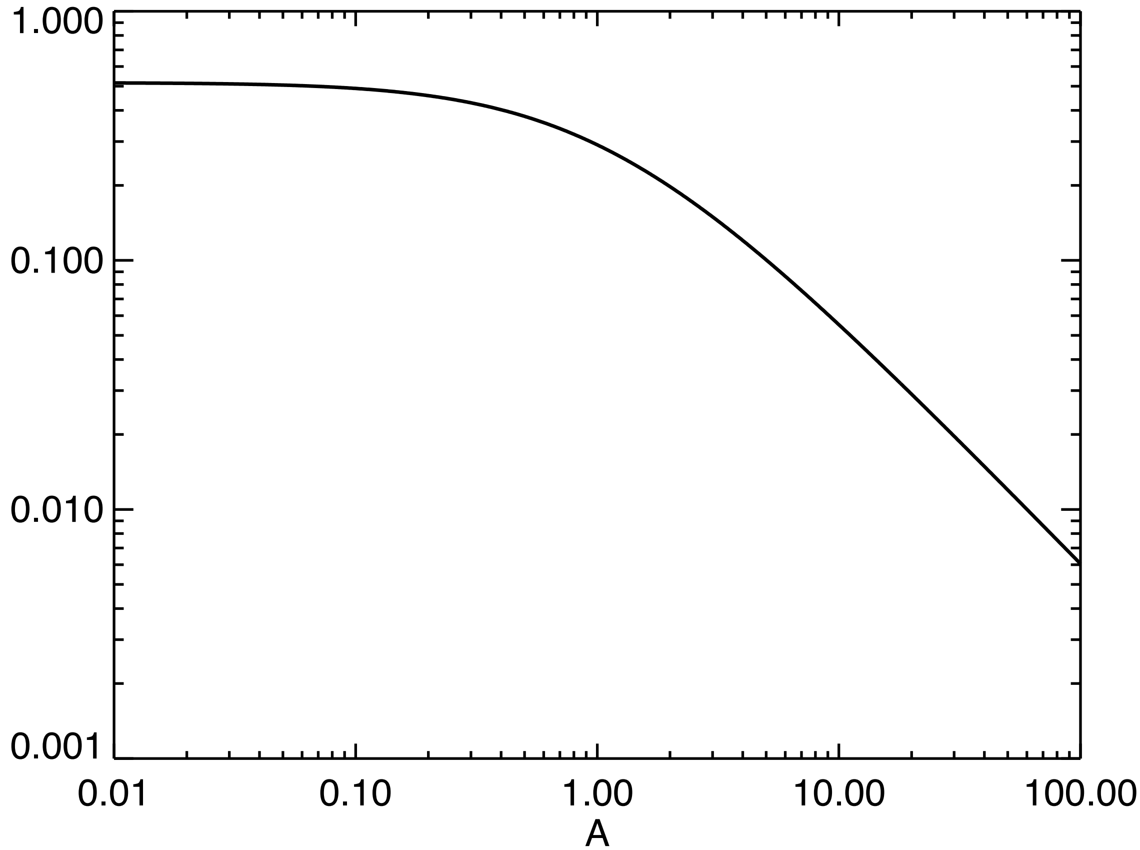

Figure 3.15 Survey bias factor B as a function of A (Eqn. 3.25), which contains the dependencies on M_P, P, and R_*, and accounts for simultaneous orbital decay and evolution of the host star along the RGB. In the regime where $A \gg 1$ (orbital decay faster than stellar evolution), $B \propto 1/A$ and Eqn. 3.11 is recovered. If $A \ll 1$, B is independent of A and dependent only on R_P.

Figure 3.15 plots B as a function of A for $\beta = 7.6$ and $\alpha = 1/2$. It shows that if $A \gg 1$ (rapid tidal evolution) then $B \propto A^{-1}$ and hence $B \propto R_P^{3/(1-\alpha)} M_p^{-1}$, as in Eqn. 3.11 and thus detection of transition objects at the electron degeneracy threshold is favored. However, if $A \ll 1$ then B is independent of A and hence M_P and P (but not R_P). Detection of gas giants, particularly inflated planets with the largest radii, is then favored. For the same values of α and β and $Q_* = 2 \times 10^5$, the condition for $A = 1$ becomes a critical value for period

$$P_* = 0.63 \left(M_P \tau_{\mathrm{RGB}} M_*^{-1} \rho_i^{-5/3} \right)^{3/13} \text{ days}, \tag{3.27}$$

where M_P in Jupiter masses, τ_{RGB} is in Myr, and M_* and ρ_i are in solar units.

Chapter 4

Do close-in giant planets orbiting evolved stars prefer eccentric orbits?

This chapter has been previously published in the *Astrophysical Journal Letters* (Grunblatt, S., Huber, D., Gaidos, E. et al, 2018, ApJL, 861, 5).

4.1 Introduction

The NASA *Kepler* mission has discovered thousands of extrasolar planets, allowing populations of planets orbiting different types of stars to be compared (Howard et al. 2012; Petigura et al. 2013; Dressing & Charbonneau 2015; Santerne et al. 2016; Fulton et al. 2017; van Sluijs & Van Eylen 2018). However, the population of planets around evolved stars remained poorly described because so few have been discovered to date, particularly at orbital distances of 0.5 AU or less (Sato et al. 2005; Johnson et al. 2010; Lillo-Box et al. 2014; Barclay et al. 2015; Jones et al. 2016).

It has been suggested that the planet population of evolved stars should look quite different from their main sequence counterparts due to dynamical interactions driven by stellar evolution (Veras 2016). Accelerated angular momentum exchange should cause the planet to spiral in to the host star (Zahn 1977; Hut 1981; MacLeod et al. 2018). This results in a scenario where orbital decay happens faster than circularization, producing a population of transient, moderately eccentric close-in planets around evolved stars that are not seen around main sequence stars (Villaver & Livio 2009; Villaver et al. 2014). The increase in planetary heating from both elevated stellar irradiation and tides raised on the planet will likely also cause inflation of these planets at late times (Bodenheimer et al. 2001; Lopez & Fortney 2016).

Two well-characterized, close-in inflated giant planets orbiting moderately evolved, or low-luminosity red giant branch stars, K2-97b and K2-132b, were recently discovered by the *K2* extension to the *Kepler* mission (Grunblatt et al. 2016, 2017). Here, we report new radial velocity (RV) measurements of these planets, as well as RV measurements of a previously validated planet orbiting an evolved star observed by the original *Kepler* mission, Kepler-643 (Huber et al. 2013; Morton et al. 2016). These measurements allow us to constrain the orbital eccentricities of these planets, which motivate an investigation of the orbital eccentricities of the population of planets around giant stars compared to dwarf stars.

Table 4.1. Close-In Giant Planets Orbiting Giant Stars

Name	Mass	Radius	Semi. Axis	Ecc.	Stellar Mass	Stellar Radius	Reference
K2-132b	0.49 ± 0.06 M_J	1.30 ± 0.07 R_J	0.086 AU	0.36 ± 0.06	1.08 ± 0.08 $M_\odot$	3.85 ± 0.13 $R_\odot$	1, this work
K2-97b	0.48 ± 0.07 M_J	1.31 ± 0.11 R_J	0.081 AU	0.22 ± 0.08	1.16 ± 0.12 $M_\odot$	4.20 ± 0.14 $R_\odot$	1, this work
K2-39b	0.125 ± 0.014 M_J	0.51 ± 0.06 R_J	0.057 AU	0.15 ± 0.08	1.19 ± 0.08 $M_\odot$	2.93 ± 0.21 $R_\odot$	2
Kepler-643b	1.01 ± 0.20 M_J	1.14 ± 0.05 R_J	0.126 AU	0.37 ± 0.06	1.15 ± 0.12 $M_\odot$	2.69 ± 0.11 $R_\odot$	3, 4, this work
Kepler-91b	0.81 ± 0.18 M_J	1.37 ± 0.07 R_J	0.073 AU	$0.04^{+0.06}_{-0.02}$	1.31 ± 0.1 $M_\odot$	6.30 ± 0.16 $R_\odot$	5
HD 102956b	0.96 ± 0.05 M_J	non-transiting	0.081 AU	0.05 ± 0.03	1.70 ± 0.11 $M_\odot$	4.4 ± 0.1 $R_\odot$	6
TYC3667...b	5.4 ± 0.4 M_J	non-transiting	0.21 AU	$0.04^{+0.04}_{-0.02}$	1.87 ± 0.17 $M_\odot$	6.26 ± 0.86 $R_\odot$	7

Note. — Reference key: 1. Grunblatt et al. (2017), 2. Petigura et al. (2017), 3. Huber et al. (2013), 4. Morton et al. (2016), 5. Barclay et al. (2015), 6. Johnson et al. (2010), 7. Niedzielski et al. (2016).

4.2 Observations

RV measurements of K2-97, K2-132, and Kepler-643 were obtained between 2016 January 27 and 2018 February 1 using the High Resolution Echelle Spectrometer (HIRES) on the Keck-I Telescope at the Maunakea Observatory in Hawaii. Individual measurements and orbit solutions are shown in Figure 1. All RV spectra were obtained through an iodine gas cell. In order to constrain orbital parameters, we fit the radial velocity data using the publicly available software package `RadVel` (Fulton et al. 2018). The orbital period of the planets were fixed to published values from transit measurements (Morton et al. 2016; Grunblatt et al. 2017), while we fit for the semi-amplitude, phase,and modified eccentricity parameters of the orbit (Eastman et al. 2013). We also fit for an RV jitter term for our measurements and obtained a value between 5-10 m s^{-1} for all systems studied here. We adopted the same method for determining RVs as described in Butler et al. (1996).

Since RV measurements are not usually taken at regular time intervals, data sampling is often uneven and thus introduces orbital parameter biases, potentially inflating eccentricities beyond their true value (Eastman et al. 2013). To ensure that our measured eccentricities are robust, we produced 100 artificial RV datasets of circular orbits for each system, with equivalent orbital periods, semi-amplitudes, and random scatter as measured in our real data, taken at the same times as our real measurements. We then recovered an orbit from each artificial dataset using the same techniques given for our real RV data. We find that the distribution of eccentricities recovered from fitting the artificial datasets is consistent with zero in all cases. For all best fit orbit solutions for the simulated, e=0 orbit generated data, we do not recover an eccentricity of greater than 0.1. We therefore conclude that the eccentricities found by our analysis are not due to sparse sampling of our RV measurements.

4.3 Eccentricity Distributions Around Evolved Stars

Figure 2 illustrates the population of known giant planets with published eccentricities orbiting giant stars as well as the equivalent planet population orbiting dwarfs in the orbital period and eccentricity plane (left) and the a/R$_*$ and eccentricity plane (right). Planets are designated as giants if $R_p >$ 0.4 $R_{\rm J}$. 419 dwarf star systems and 136 giant star systems with constrained eccentricities listed in the NASA Exoplanet Archive are included in our figure (Akeson et al. 2013). Transiting systems are shown as filled circles, while non-transiting systems are shown as empty circles. For non-transiting

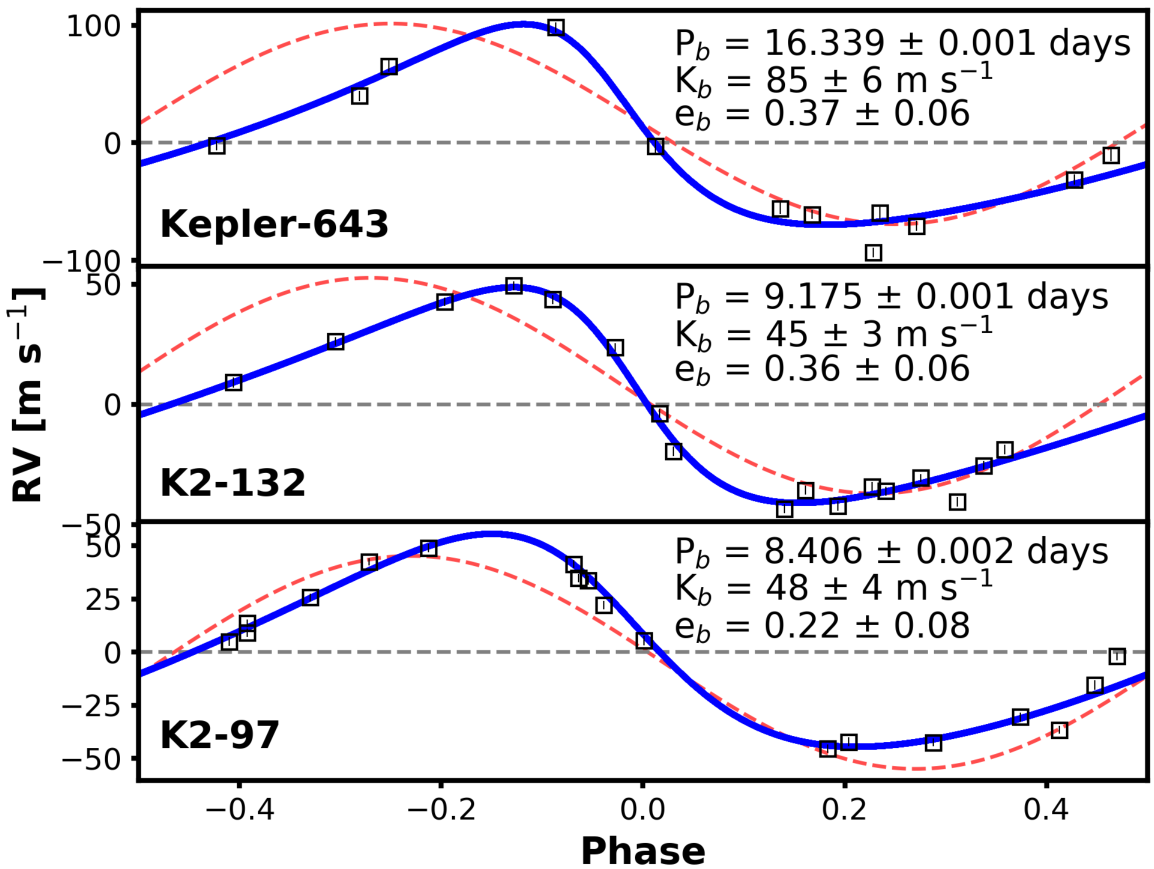

Figure 4.1 Keck/HIRES radial velocity observations of Kepler-643 (top), K2-132 (center) and K2-97 (bottom), three systems where close-in giant planets orbit evolved stars. All orbits display moderate eccentricities between 0.2 and 0.4. The planets appear to follow a trend, where those on longer orbits are more eccentric than those orbiting their host star more closely. Circular orbits are shown as red dotted lines for reference.

systems, planet radii were estimated using the mass-radius relations of Chen & Kipping (2017). Distinctions as giant or dwarf star systems were made using the physically motivated boundaries in effective temperature and surface gravity described in Huber et al. (2016). Stellar parameters have been taken from the NASA Exoplanet Archive, and individual sources for all known close-in giant planets with published eccentricities orbiting giant stars are listed in Table 1. Our new RV measurements give tentative evidence that the dwarf and giant system eccentricity distributions are inconsistent at periods $\lesssim$ 50 days and $a/\mathrm{R}_* \lesssim 10$.

Figure 3 illustrates the cumulative distributions of eccentricities for various different planetary system samples analyzed here. When considering planets of all sizes, close-in planets show a tendency for low eccentricities. However, this preference is not as strong when considering only giant planets,

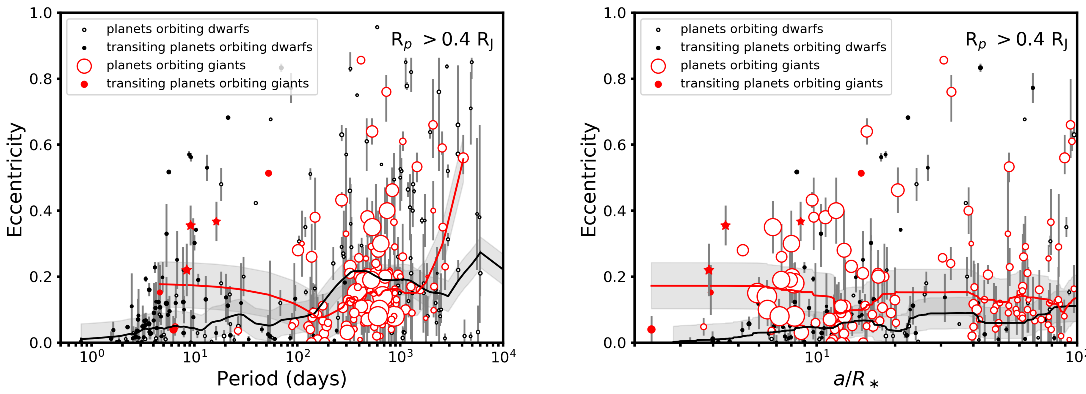

Figure 4.2 Left: Orbital period versus eccentricity for all giant (>0.4 R_J) planets with published eccentricities orbiting giant and dwarf stars. Stellar radius scales with the size of the points; planets orbiting giant stars are shown in red, while planets orbiting dwarfs are shown in black. The systems with eccentricities measured in this study are highlighted as red stars. A locally weighted regression of the eccentricities of are shown by the solid black and red lines for the dwarf and giant star populations, respectively. Right: Same as left, except with a/R_* on the x-axis.

likely due to trends related to planet multiplicity (Van Eylen & Albrecht 2015; Xie et al. 2016). Remarkably, comparing the population of giant planets orbiting at $\lesssim$ 50 day orbital periods as well as all known planets around giant stars (red lines) to the equivalent planet population orbiting dwarf stars (black lines) illustrates a stronger preference for moderate eccentricities in giant star systems than is seen in dwarf star systems.

To evaluate the significance of the difference between the dwarf and giant star planet populations, we compared the median eccentricities for both populations (see Figures 2 and 3). We restrict our analysis to giant ($> 0.4\ R_J$) planets with orbital periods between 4.5 and 30 days and published eccentricity constraints. This ensures that all planets compared here could have been detected around both dwarf and low-luminosity red giant branch stars observed by *K2*. Furthermore, this sample includes the closest-in known transiting planets orbiting evolved stars while rejecting the shortest period dwarf system planets, which likely would be engulfed by evolved stars due to their large sizes. It also minimizes biases due to planets found in surveys which were particularly well-suited to discovering short-period giant planets on circular orbits around dwarf stars (*e.g.*, WASP, Pollacco et al. 2006). Planets with published upper limits on eccentricity are treated as having circular orbits with error distributions that reach the listed upper limit at a 1-σ confidence interval.

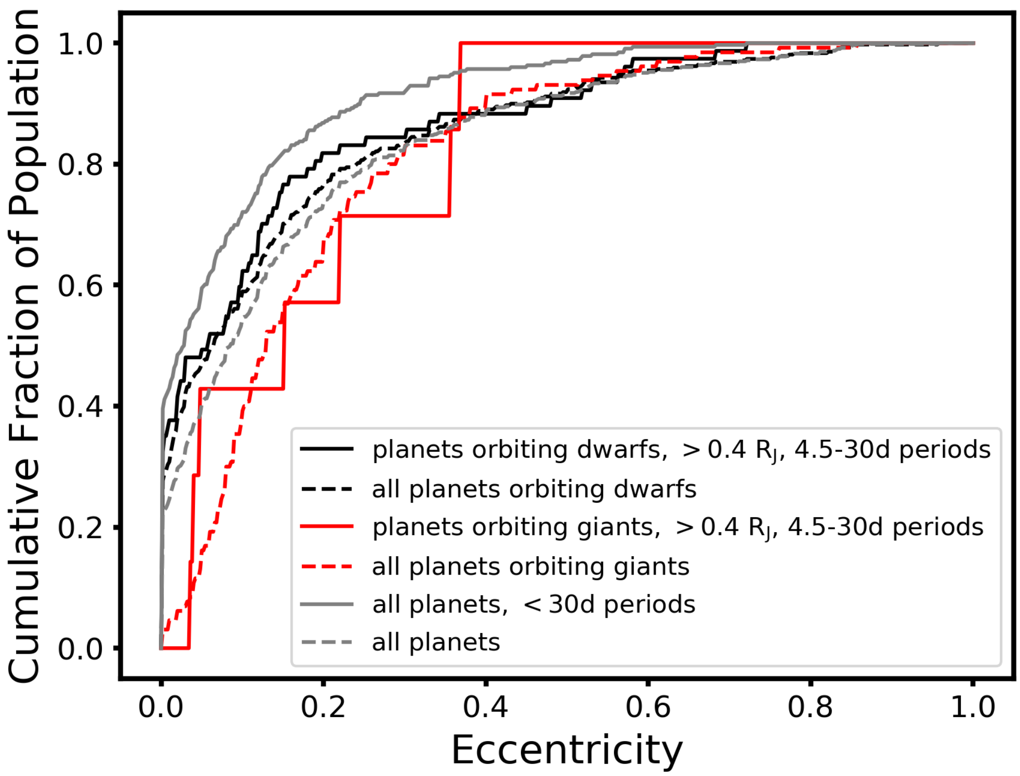

Figure 4.3 Cumulative eccentricity distributions of different populations of planets. Planets orbiting giant stars (red lines), particularly at periods of 30 days or less, display a preference for moderate eccentricities not seen in dwarf star systems (black lines).

We find a median eccentricity of $0.152^{+0.077}_{-0.042}$ for close-in giant planets orbiting evolved stars, and a median eccentricity of $0.056^{+0.022}_{-0.006}$ for close-in giant planets orbiting dwarfs.

We also tested the sensitivity of these values to increasing the planet radius cut to $> 0.8\ R_{\rm J}$, as well as adjusting the inner period bound between 3-8 days, and the outer period bound between 25-80 days. We find that our statistics are only significantly affected by changing the inner period bound, driven by the small number of close-in planets known orbiting evolved stars. Thus, we choose bounds to include all known close-in planets orbiting evolved stars while minimizing the number of close-in planets around dwarf stars without an evolved counterpart population.

To further quantify the significance of the eccentricity dichotomy between the populations of giant planets orbiting dwarf and giant stars, we calculate the Anderson-Darling statistic, which is more robust to different-sized and small number distributions than similar tests such as the Kolmogorov-Smirnov statistic (Simpson 1951; Stephens 1974). We find that both samples are drawn from the same parent population in 6.3% or fewer of cases. Adjusting our planet radius and period cuts, we find that both samples are drawn from the same parent population in 3.8%–15.4% or fewer of cases for all tested samples. This range is dominated by stochastic variation due to the small sample of evolved systems.

As an additional test, we performed a Monte Carlo simulation in which we drew an equal number of eccentricity values from the eccentricity distributions of our bias-resistant sample of close-in giant planets orbiting dwarf stars and giant stars in 4.5-30 days. We find that after repeating this process one million times, the random sample of planets drawn from the dwarf star sample has a similar or higher median eccentricity than the planets orbiting giant stars in 5.7% of cases, with a range of 4.1% to 16.7% for all period and radius ranges tested. We also performed the same test for the population of all close-in planets known around dwarf and giant stars, as well as all planets known around dwarf and giant stars, and find that the dwarf star sample has a similar or higher median eccentricity in 0.34% and 10.6% of cases, respectively.

Thus, based on our statistical tests, we conclude that close-in, evolved star system planets display different eccentricity characteristics than close-in dwarf star system planets at a 1- to 2-σ level. We note that this is a conservative estimate, as many early literature estimates of eccentricities for both types of systems may be biased toward higher eccentricities due to mischaracterization of systematic and astrophysical uncertainties (Eastman et al. 2013). More recent RV studies, using newer analysis packages such as `RadVel`, account for this artificial bias. Reanalysis of RV measurements used to constrain the population of planetary eccentricities could remove this bias, but is beyond the scope of this Letter.

4.4 Discussion

The formation of close-in giant planets is commonly explained by three different hypotheses: *in situ* formation, disk migration, and tidal migration (see Dawson & Johnson (2018) for a recent review). Populations of eccentric giant planets are generally viewed as evidence for tidal migration, as they cannot be explained by the other two prevailing mechanisms. Although these planets support tidal migration theory for close-in giant planet formation, we assert that unlike those around dwarf stars, these close-in giant planets are actively undergoing tidal migration, sped up by the late stage evolution of their host stars. An observed correlation between stellar host evolutionary state and long-period, planetary companions to close-in giant planet systems supports this (Lillo-Box et al. 2016).

Models of the dynamical evolution of close-in giant planets can be strongly affected by the evolution of the host star (Villaver & Livio 2009; Villaver et al. 2014). The timescale of this dynamical evolution is defined by the tidal interactions between the planet and its host star. Following the reasoning of Villaver et al. (2014), the eccentricity evolution of a planetary orbit will be dominated by planetary tides driving orbit circularization on the main sequence, and stellar tides driving tidal inspiral on the red giant branch. For example, assuming $Q_p = Q_* \sim 10^6$, and using the equilibrium tide formulations of Patra et al. (2017) derived from Goldreich & Soter (1966), the timescale for orbit circularization for K2-97b is $\sim$5 Gyr, while the tidal inspiral timescale is $\lesssim$2 Gyr. This suggests orbital decay is driven more rapidly than eccentricity evolution as the stellar radius increases, producing a population of transient planets displaying moderate eccentricities at close-in orbits around evolved stars. Though these tidal timescale formulae do not account for planetary or stellar rotation or dynamical tides, these results are consistent with our observations.

Villaver et al. (2014) also predict that more massive systems evolve more quickly toward lower eccentricities and semimajor axes. This is also tentatively supported by observations, as the most massive hosts in our sample also have the lowest eccentricity orbits (see Table 1). However, a larger sample of systems is needed to confirm this. Correlations between planet and star mass and composition and planetary orbital evolution have not yet been fully explored.

Tidal interaction and migration has long been thought to cause radius inflation in gas-giant planets (Bodenheimer et al. 2001; Storch et al. 2014). Increased irradiation due to stellar evolution is also thought to be a source of planetary heating (Lopez & Fortney 2016). Two of the close-in evolved planets with new RV measurements presented here, K2-97b and K2-132b, show signs of being significantly inflated relative to similar planets seen orbiting main sequence stars (Grunblatt et al. 2017).

To evaluate the dominant radius inflation mechanism for these planets, we follow the prescription for tidal heating given by Miller et al. (2009) and Dobbs-Dixon et al. (2004), and assume synchronous rotation of the planet and tidal quality factors $Q_p = 10^4$ and $Q_* = 10^6$, within an order of magnitude of observed and model constraints (Patra et al. 2017; Gallet et al. 2017). We find that if the planets are actively circularizing, tidal evolution driven by the star can dominate planetary heating by an order of magnitude over irradiative mechanisms. Furthermore, tidal resonance locking may also greatly enhance tidal heating rates (Fuller 2017). Thus, planet radius inflation for these systems may be driven solely by tidal processes.

However, a Q_p value of 10^4 and $Q_* = 10^6$ would suggest the orbit circularization timescale is significantly shorter than the orbital decay timescale. In contrast, the observed eccentricities of these planet orbits suggests that orbit circularization and orbital decay are happening on similar timescales, implying $Q_* \sim Q_p$. This disagrees with predictions of Q_* for evolved stars (Gallet et al. 2017). Furthermore, rotation and/or dynamical tides can drastically change these timescales and may even increase orbital eccentricity over time (Hut 1981; Fuller 2017). Determining the orbital evolution of evolved systems and causes of late stage planet inflation will require more in-depth characterization of the combined effect of increased irradiation and tidal energy dissipation on a larger sample of planets.

4.5 Summary and Outlook

The NASA *Kepler* and *K2* Missions have recently revealed a population of giant planets at small orbital separations around evolved stars. Here, we report radial velocity observations which show that a majority of these planets display moderate eccentricities, indicating a different evolutionary state for planets around giant stars than those orbiting main sequence stars. This late stage evolution is likely driven by the increase in size of the stellar radius and convective envelope, strongly increasing the angular momentum exchange between the star and the planet, causing the planet to circularize its orbit and spiral into the host star. These two components of orbital evolution must happen on timescales similar enough such that these migrating giant planets with moderate eccentricities appear to be relatively common around evolved stars (Villaver et al. 2014). These planets will thus allow constraints on the determination of the tidal quality factors Q_p and Q_*. Continued follow-up of low-luminosity red giant branch stars will allow estimation of close-in planetary occurrence around evolved stars (Grunblatt et al. 2018, *in prep.*), which will further constrain our understanding of planetary evolution and dynamical interactions within planetary systems.

Additional eccentricity constraints and more systems are needed in order to confirm the tentative result presented here. The NASA *TESS* Mission, launched earlier this year, will observe two orders of magnitude as many evolved stars as *Kepler* and *K2*, likely resulting in over 100 planet detections around evolved stars (Sullivan et al. 2015; Campante et al. 2016; Barclay et al. 2018). This detection of additional planets orbiting evolved stars will outline the diversity of all such systems, and the likelihood and timescale of planetary system disruption via stellar tides. With this information, we can investigate how quickly planets undergo orbital evolution around low-luminosity red giant branch stars, and at what point planets can no longer survive around giant stars, significantly distinguishing these systems from planet populations of main sequence stars.

Chapter 5

Giant planet occurrence within 0.2 AU of low-luminosity red giant branch stars with K2

This chapter has been submitted and favorably reviewed for publication in the *Astronomical Journal* (Grunblatt, S., Huber, D., Gaidos, E. et al, 2019, ApJ, under review).

5.1 Introduction

As a star like our Sun ages, changes in stellar luminosity, composition and structure can induce changes in orbiting planets (Villaver et al. 2014; Veras 2016). The increase in stellar irradiation during the red giant phase of stellar evolution may lead to planet inflation (Guillot et al. 1996; Lopez & Fortney 2016). Tides in both the star and the planet can also affect planet interiors, causing inflation and disruption of their magnetic dynamo (Bodenheimer et al. 2001; Driscoll & Barnes 2015). However, despite being relatively luminous, and thus overrepresented in magnitude-limited surveys (Malmquist 1922), the variability of evolved stars makes it difficult to detect transiting planets around them (Sliski & Kipping 2014). Therefore even though these systems hold many insights into the nature of planet inflation, migration and evolution, transiting planet surveys have largely avoided these stars.

Previous searches for planets around evolved stars utilized radial velocity measurements (Hatzes et al. 2000; Sato et al. 2005; Reffert et al. 2015). Despite the relatively long history of planet searches around evolved stars, no planets were found interior to 0.5 AU around such stars, suggestive of intrinsic differences between the main sequence and evolved system populations (Johnson et al.

2010; Jones et al. 2016). The recent explosion in planet discoveries around Sun-like and smaller stars fueled by transit surveys has been accompanied by only a handful of planet transit detections around evolved stars (Lillo-Box et al. 2014; Barclay et al. 2015; Van Eylen et al. 2016; Grunblatt et al. 2016, 2017). To determine whether the relatively small number of planets known around evolved stars is due to small survey size, planet detection difficulties unique to evolved stars, or an intrinsic lack of planets, a systematic transit survey of evolved stars is needed.

Here, we investigate over 10 000 stars observed by the *K2* mission to estimate planet occurrence around low-luminosity red giant branch stars. Searching for planet transits around these moderately evolved stars captures the intrinsic photometric variability due to the oscillations of these stars as well. These oscillations can be used to measure stellar densities and surface gravities through asteroseismic methods, which we use to calculate planet occurrence statistics with more precision than current spectroscopic techniques would allow (Huber et al. 2013; Petigura et al. 2017). We restrict our sample to 2476 of these stars whose radii are large enough for precise characterization with asteroseismology but are also small enough to allow planet transit detection. We use this sample to determine planet occurrence for our evolved stars, which we compare to planet occurrence estimates around main sequence stars.

5.2 Target Selection

The targets for our study were chosen as follows:

1. 10 444 initial targets observed for this study were selected by the Giants Orbiting Giants *K2* Guest Observer campaigns (GO4089, GO5089, GO6084, GO7084, GO8036, GO10036, GO11048, GO12048, GO13048, GO14004, GO15004, GO16004, PI: D. Huber). These stars were identified as having temperatures between 4500 and 5500 K, surface gravities of 2.9 > log g > 3.5, and magnitudes of $K_p < 15$ as compiled in the Ecliptic Plane Input Catalog (EPIC; Perryman et al. 1997; Gaia Collaboration et al. 2018; Majewski et al. 2017; Kunder et al. 2017; Cui et al. 2012; Huber et al. 2016) to increase the likelihood that stellar oscillations would be detectable by *K2* (Chaplin et al. 2014; Stello et al. 2015).

2. 458 additional stars observed serendipitously as part of the *K2* Galactic Archaeology Program (GAP, Stello et al. 2017) were identified as potential LLRGB stars using stellar radii determined

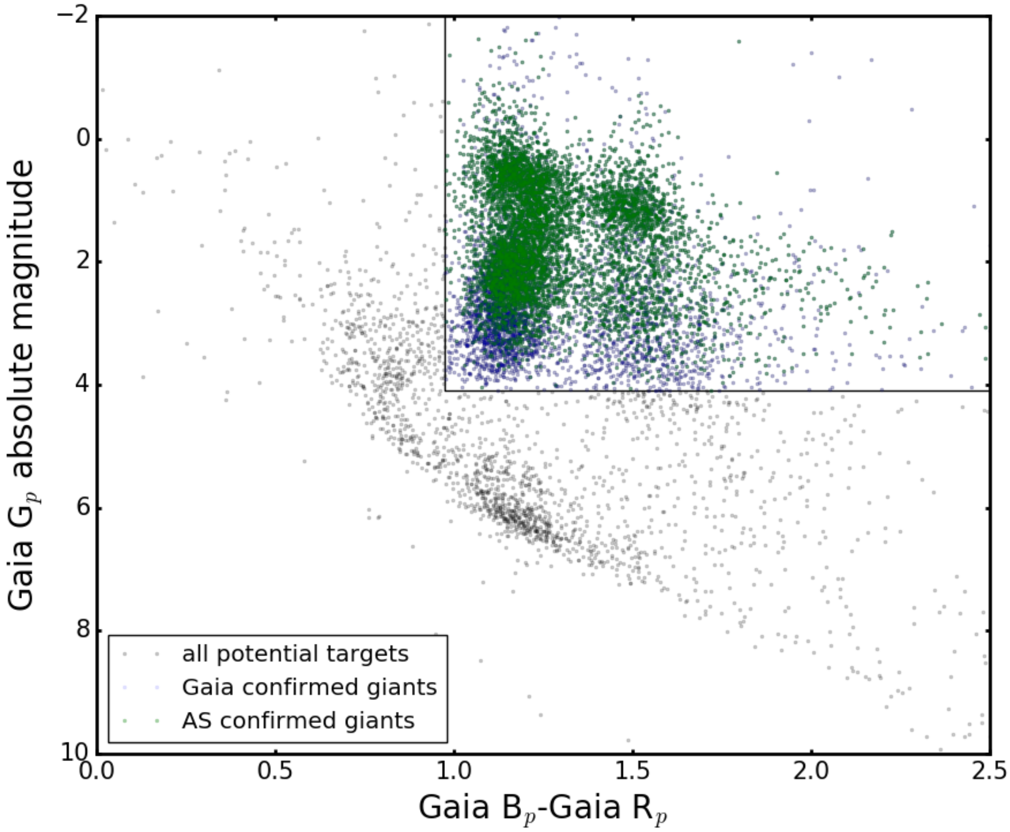

Figure 5.1 Color-magnitude diagram made using *Gaia* Data Release 2 data. We restrict our asteroseismic analysis to those stars with colors and magnitudes consistent with giant stars (colored points, above and right of black lines). Targets detected as oscillating giants by multiple asteroseismic pipelines are shown in green.

using EPIC parameters (Huber et al. 2016). Including these stars with EPIC radii between 3 and 10 $R_\odot$ increases our target sample to a total of 10902 stars (Figure 5.1).

3. After *Gaia* Data Release 2 became available last year (Gaia Collaboration et al. 2018), stars with absolute magnitudes *Gaia G* magnitude > 4.1 and *Gaia* B_p-R_p < 0.9 and > 3.0 were excluded from our study, leaving 8933 potential oscillating red giant stars (blue and green points, upper right of Figure 5.1).

4. Multiple asteroseismic pipelines were then used to ensure that oscillations could be detected unambiguously and could be used to accurately characterize the host star (Huber et al. 2009a; Hon et al. 2018, Zinn et al., *in prep.*), leaving 6330 oscillating stars in the sample (green

points in Figures 5.1 and 5.2). We then performed additional vetting based on the quality of the observed oscillations and stellar parameters determined therewith (see Figure 5.2, Section 3.1).

5.3 Asteroseismology

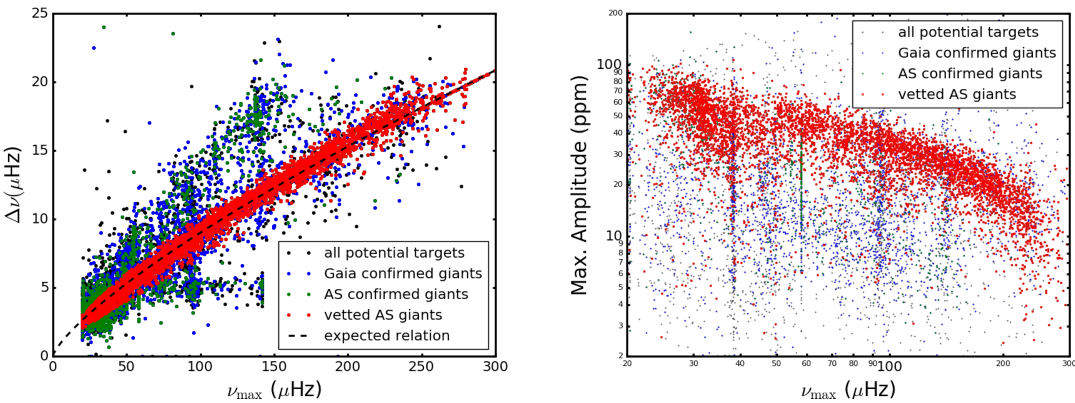

Figure 5.2 Left: Frequency of maximum oscillation power $\nu_{\rm max}$ versus large frequency separation $\Delta\nu$. Asteroseismic oscillating giants passing all of our quality cuts are shown in red, while rejected stars are plotted in blue, black and green. The dotted line corresponds to the previously published power-law relation between $\nu_{\rm max}$ and $\Delta\nu$ (Stello et al. 2009; Yu et al. 2018). Right: Maximum oscillation amplitude in ppm versus frequency of maximum oscillation power $\nu_{\rm max}$. Helium-burning stars in the red clump can be seen as an increase in amplitude dispersion between 20 and 40 μHz.

5.3.1 Data Analysis

Asteroseismology is the study of relating observed oscillations to the physical properties of a star (Christensen-Dalsgaard & Frandsen 1983). These oscillations can be seen in the power spectra of stellar light curves. Numerous analysis packages have been developed to derive stellar properties accurately and precisely from asteroseismic oscillation signals, by analysis of power spectra of oscillating stars (Huber et al. 2009b; Hon et al. 2018). In order to accurately and precisely determine the stellar radii and masses of all the stars in our sample, we produce power density spectra of all of our targets from their *K2* lightcurves created with the K2SFF algorithm (Vanderburg & Johnson 2014).

Known *K2* lightcurve features, such as those produced by the firing of thrusters to keep the spacecraft pointing accurate every 6 hours, can mimic an asteroseismic signal. In addition, astrophysical false positive signals can also be produced by eclipsing binary systems or classical pulsators such as RR Lyrae variables. To exclude these unwanted signals from our analysis, we median filter our light curves with a 3-day window in addition to the initial detrending done by the NASA and K2SFF teams (Smith et al. 2012; Vanderburg & Johnson 2014). We also exclude data within 1 day of any gap in data acquisition within a campaign, as well as within 1 day of the start and end of each campaign to remove spurious signals near stellar oscillation or transit timescales.

In order to determine whether oscillations were present in a particular stellar light curve, we use deep learning-based classification to detect oscillations from 2-dimensional images of power spectral density plots of *K2* light curves following the method of Hon et al. (2018). This technique is trained using *Kepler* data curated by asteroseismic experts to assign a probability p that a star is or is not oscillating. Though Hon et al. (2018) achieved an accuracy over 98% on their test sample using a threshold probability of $p_{\mathrm{thres}} > 0.58$, we adopt a more conservative threshold of $p_{\mathrm{thres}} > 0.95$ in our final analysis to ensure minimal contamination by false positives in our dataset. We also apply the Bayesian classification scheme of Zinn et al. (*in prep.*) to our light curve data to classify the star as oscillating or not. We find that our classification of asteroseismically oscillating stars agree between these asteroseismic pipelines in more than 99% of cases.

We then perform an asteroseismic analysis on all power spectra that pass the filters above, calculating the best-fit frequency of maximum power (ν_{max}) and regular frequency spacing ($\Delta\nu$) between sequential radial oscillation modes using the Huber et al. (2009a) pipeline, which has been well established for the asteroseismic analysis of *Kepler* and *K2* photometry (Huber et al. 2011, 2013; Stello et al. 2017). We calculate uncertainties for our asteroseismic quantities using a Monte Carlo method, producing 100 realizations of each asteroseismic fit and using the standard deviation of the sample of asteroseismic fits for each star to determine parameter errors as described in Huber et al. (2011). We then use these ν_{max} and $\Delta\nu$ errors to determine errors on stellar mass and radius. We cross check our ν_{max} results with two other asteroseismic pipelines (Hon et al. 2018, Zinn et al., *in prep.*) and find that our ν_{max} estimates agree within 1% on average, and more than 95% of stars designated as oscillating have ν_{max} values that agree to within 5%. We reject all stars which do not meet these requirements, resulting in a sample of 6330 oscillating stars (green points in Figures 5.1 and 5.2).

We remove additional poor asteroseismic detections by excluding stars which have a measured ν_{max} above 285 μHz, below 20μHz, or within 0.05 μHz of 58.05 μHz due to an observed nonphysical pileup of $\nu_{\rm max}$ values observed at this frequency. Visual inspection of stars showing $\nu_{\rm max}$ values within this range reveal stellar power spectra polluted by a periodic signal not linked to stellar oscillation, and thus these stars are excluded from our subsequent analysis. In addition, we reject stars whose $\nu_{\rm max}$ and $\Delta\nu$ values disagree with the empirical relation derived by Yu et al. (2018) (given in the following paragraph) by more than 20%. This leaves us with a vetted asteroseismic sample of 5227 oscillating stars (red points in Figure 5.2).

The left panel of Figure 5.2 illustrates the relation between $\nu_{\rm max}$ and $\Delta\nu$ for stars in our target sample including both the stars which pass our asteroseismic vetting (red) as well as those which do not (green), including those designated as dwarfs by *Gaia* photometry (black) and those without consistent oscillations found by multiple asteroseismic pipelines (blue). The right panel gives the correlation between maximum oscillation amplitude and $\nu_{\rm max}$ for all stars in our target sample. We highlight the Yu et al. (2018) relation determined between $\nu_{\rm max}$ and $\Delta\nu$ from a sample of 16094 *Kepler* red giants,

$$\Delta\nu = \alpha(\nu_{\rm max})^{\beta}, \tag{5.1}$$

where $\alpha = 0.267$ and $\beta = 0.764$. We also note the pile up of measured $\nu_{\rm max}$ values at the known *K2* thruster firing frequency of 47 μHz and its multiples. However, stars with measured $\nu_{\rm max}$ values near these thruster harmonics do not seem to be preferred by our three tested pipelines, and thus we do not mask these stars from our analysis. We also note that $\nu_{\rm max}$ values near 283 μHz calculated by our pipelines tend to be inaccurate due to the reflection of both sub- and super-Nyquist oscillation peaks about the Nyquist frequency, causing an artificial oscillation peak at the Nyquist frequency for stars oscillating slightly above or below this value (Yu et al. 2016). However, since $\Delta\nu$ is still well-constrained for these stars, we use the derived relation of Yu et al. (2018) to estimate $\nu_{\rm max}$ analytically for all stars with $\nu_{\rm max} > 280$ μHz, which we then use to derive stellar masses and radii. We note that this relation assumes a fixed mass for these stars, but as we are investigating planet occurrence as a function of stellar radius and not stellar mass in this sample, the inaccuracy of these stellar masses will not influence our planet occurrence results.

Table 5.1. Asteroseismic Parameters

EPIC ID	$\nu_{\rm max}$ (μHz)	$\Delta\nu$ (μHz)	Stellar Radius ($R_\odot$)	Stellar Mass ($M_\odot$)	$T_{\rm eff}$[a]
201091253	116.9 ± 0.4	10.39 ± 0.09	5.66 ± 0.21	1.11 ± 0.04	4916
201092039	160.1 ± 1.7	13.87 ± 0.17	4.37 ± 0.18	0.90 ± 0.03	4946
201102783	60.2 ± 0.7	6.23 ± 0.05	7.78 ± 0.09	1.07 ± 0.03	4794
201106507	190.6 ± 1.1	15.86 ± 0.10	4.07 ± 0.06	0.95 ± 0.03	5377
201114106	220.3 ± 7.9	17.69 ± 0.15	3.77 ± 0.18	0.95 ± 0.09	5068
201134999	83.2 ± 1.5	8.25 ± 0.15	6.86 ± 0.39	1.19 ± 0.06	5100
201145260	132.8 ± 1.2	11.75 ± 0.11	5.07 ± 0.12	1.03 ± 0.03	5070
201145884	126.7 ± 0.8	10.99 ± 0.16	5.56 ± 0.36	1.17 ± 0.12	4961
201161185	70.8 ± 1.5	7.91 ± 0.11	6.28 ± 0.12	0.84 ± 0.03	4915
201195238	64.1 ± 0.6	6.61 ± 0.05	7.83 ± 0.12	1.19 ± 0.03	5000
etc.					

[a]Uncertainties on $T_{\rm eff}$ are 94 K for all stars in our sample, based on the González Hernández & Bonifacio (2009) color-$T_{\rm eff}$ relation used in this analysis.

Note. — The expanded version of this table has been made available in Appendix A. We include parameters for all 2476 stars selected for our occurrence analysis.

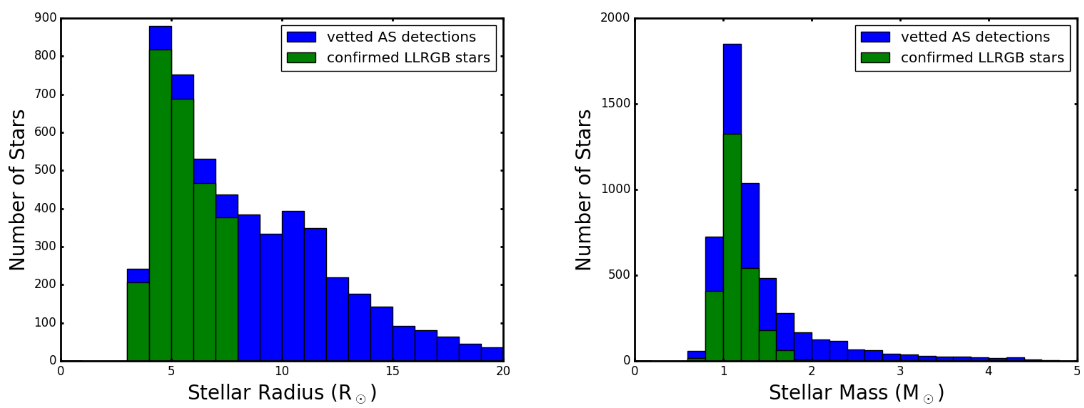

Figure 5.3 Asteroseismic radius (left) and mass (right) distribution of our target sample. Stars which pass our asteroseismic vetting (§3.1) are shown in blue. 2476 stars shown in green have radii < 8 $R_\odot$, and pass our quality cuts into our defined range of low-luminosity red giant branch (LLRGB) stars.

5.3.2 Stellar Radius Determination

To estimate stellar masses and radii from our measured $\nu_{\rm max}$ and $\Delta\nu$ values which passed our asteroseismic vetting (Figure 5.2, red points), we use the asteroseismic scaling relations of Brown et al. (1991) and Kjeldsen & Bedding (1995):

$$\frac{\Delta\nu}{\Delta\nu_\odot} \approx f_{\Delta\nu}\left(\frac{\rho}{\rho_\odot}\right)^{0.5}, \tag{5.2}$$

$$\frac{\nu_{\rm max}}{\nu_{\rm max,\odot}} \approx \frac{g}{\rm g_\odot} \left(\frac{T_{\rm eff}}{T_{\rm eff,\odot}}\right)^{-0.5} . \tag{5.3}$$

where $f_{\Delta\nu}$ is the correction factor suggested by Sharma et al. (2016) to account for known deviations from the previously established asteroseismic scaling relation. Equations (1) and (2) can be rearranged to solve for mass and radius:

$$\frac{M}{\rm M_\odot} \approx \left(\frac{\nu_{\rm max}}{\nu_{\rm max,\odot}}\right)^3 \left(\frac{\Delta\nu}{f_{\Delta\nu}\Delta\nu_\odot}\right)^{-4} \left(\frac{T_{\rm eff}}{T_{\rm eff,\odot}}\right)^{1.5} \tag{5.4}$$

$$\frac{R}{\rm R_\odot} \approx \left(\frac{\nu_{\rm max}}{\nu_{\rm max,\odot}}\right) \left(\frac{\Delta\nu}{f_{\Delta\nu}\Delta\nu_\odot}\right)^{-2} \left(\frac{T_{\rm eff}}{T_{\rm eff,\odot}}\right)^{0.5} . \tag{5.5}$$

We combine our $\nu_{\rm max}$ and $\Delta\nu$ values calculated via the Huber et al. (2009a) pipeline with stellar temperatures calculated using the direct method of `isoclassify` (Huber et al. 2017). We used J and K photometry available from the EPIC along with the reddening map of Bovy et al. (2016) to determine empirical effective temperatures for our sample with the $J-K$ color relation of González Hernández & Bonifacio (2009). Our adopted solar reference values are $\nu_{\rm max,\odot} = 3090$ μHz, $\Delta\nu_\odot = 135.1\,\mu$Hz, and $T_{\rm eff,\odot} = 5777\,$K (Huber et al. 2011). We calculate our final reported stellar masses and radii using the package `asfgrid` (Sharma et al. 2016). As our stars have effective temperatures between 4500 and 5500 K, typical asteroseismic correction factor $f_{\Delta\nu}$ values for all of the stars in our analysis are between 0.98 and 1.02 (Sharma et al. 2016). We apply this correction factor along with asteroseismic $\nu_{\rm max}$ and $\Delta\nu$ values to determine masses and radii in our sample.

Yu et al. (2018) illustrated that fewer than 1% of asteroseismically confirmed red giant stars smaller than 8 $\rm R_\odot$ have already completed an ascent of the red giant branch, and begun helium burning. Thus, we reject stars larger than 8 $\rm R_\odot$ in order to avoid targeting these "red clump" stars, which have undergone significantly more evolution than LLRGB stars. We also reject all stars with asteroseismic mass measurement errors greater than 10% or asteroseismic radius errors larger than 5%, leaving us with a sample of 2476 LLRGB stars with radii between 3.5 and 8 $\rm R_\odot$. We list our asteroseismic frequency parameters and errors and derived asteroseismic masses and radii in Table 5.1. We recover a median radius uncertainty of 3.2% and mass uncertainty of 5.0% for our full asteroseismic sample, and 2.2% in radius and 3.7% in mass for our LLRGB sample of 2476 stars.

Figure 5.3 illustrates the distribution of masses and radii for all 5227 asteroseismically vetted stars in our target sample, highlighting our LLRGB star subsample in green.

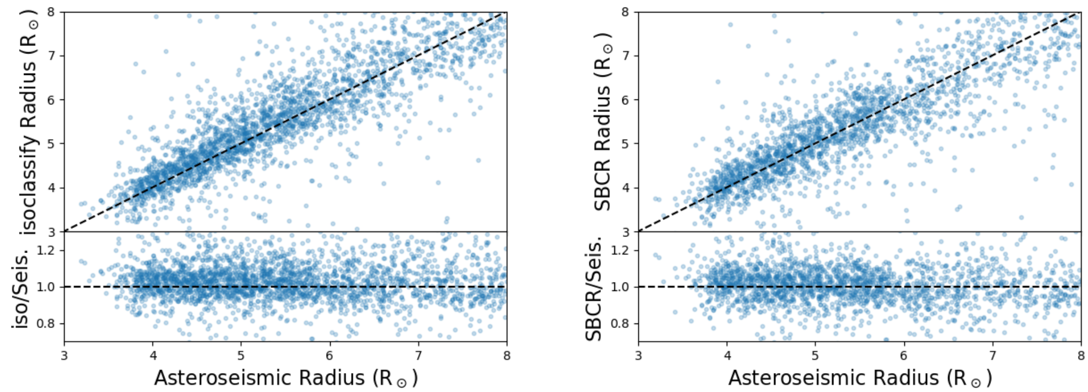

Figure 5.4 Comparison of stellar radii determined through parallax and asteroseismic methods. Left: Radii determined using `isoclassify` with JHK photometry and *Gaia* DR2 parallaxes are compared against our asteroseismic estimates. Right: A surface brightness–color relation from Graczyk et al. (2018) and reddening maps of Bovy et al. (2016) have been used to calculate stellar radii, which are then compared against our asteroseismic radii. The scatter in radius determination is larger than the typical offset between parallax-dependent and asteroseismic methods.

5.3.3 Cross-Validation with Independent Radius Estimates

In order to ensure our asteroseismic results are robust, we use *Gaia* DR2 parallax measurements to determine stellar radii independently and validate our results (Gaia Collaboration et al. 2018). We calculate radii using *Gaia* parallaxes with two different methods. First, we combine previously determined JHK magnitudes with the combined reddening map of Bovy et al. (2016) to calculate stellar temperatures using the relation of González Hernández & Bonifacio (2009) and stellar radii via the Stefan–Boltzmann relation using the `isoclassify` package (Boltzmann 1884; Huber et al. 2017). We list our effective temperatures calculated with `isoclassify` in Table 5.1.

We also compute stellar radii for our sample using the surface brightness-color relation of Graczyk et al. (2018). Surface brightness relations are calibrated using directly measured angular diameters from interferometry (Kervella & Fouqué 2008; Boyajian et al. 2014) and have been applied to measure precise distances to nearby galaxies many times in the literature (e.g., Kudritzki et al. 2014). For our study, dereddened $V - K$ colors were calculated using the reddening maps of Bovy et al. (2016) for 2MASS K magnitudes and CTIO V magnitudes, applied to the 2MASS K and APASS V magnitudes for these stars. These dereddened colors were then converted into angular diameters, which were then combined with *Gaia* parallaxes to determine stellar radii using the relations found in Graczyk et al. (2018).

Figure 5.4 highlights the differences in radius between our asteroseismically determined and parallax-derived radii. We find good agreement between the three sets of stellar radii, with a standard deviation of 10% for both parallax-driven radius determination methods, and a median offset between asteroseismic radii and radii determined with *Gaia* parallaxes of 3%.

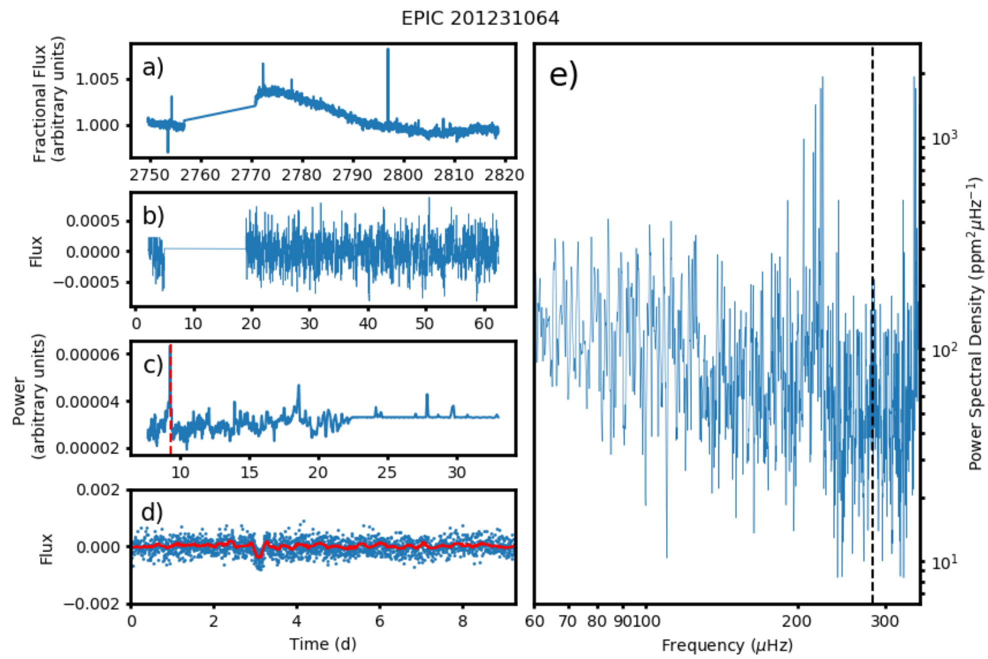

Figure 5.5 Light curve and power spectral density of K2-161, a member of our LLRGB catalog. The raw K2SFF light curve is shown in panel a), whereas a 3-day smoothed version is in panel b) directly underneath. Panel c) displays the power measured by a box least-squares (BLS) search as a function of period, where the red line indicates the best-fit period for that light curve. Panel d) displays the smoothed light curve folded at the best fit period identified by the BLS. The x-axis corresponds to units of time in days for all four panels. Here, the transit of K2-161 b is clearly visible. Panel e), on the right, shows the power spectral density of the light curve. The dotted vertical line highlights the Nyquist frequency for typical *K2* data. Stellar oscillations are visible above the granulation signal around 220 μHz and are mirrored above the Nyquist frequency.

Table 5.2. Planets Around LLRGB Stars Found By *K2*

Name	Planet Radius (R_J)	Orbital Period (days)	Stellar Mass ($M_\odot$)	Stellar Radius ($R_\odot$)	Source
K2-97b	1.3 ± 0.11	8.406 ± 0.0015	1.16 ± 0.12	4.2 ± 0.2	Grunblatt et al. (2017)
K2-132b	1.3 ± 0.10	9.175 ± 0.0015	1.08 ± 0.12	3.8 ± 0.2	Grunblatt et al. (2017)
K2-161b	$1.45\ ^{+0.16}_{-0.14}$ [a]	9.283 ± 0.002	1.09 ± 0.10	4.12 ± 0.14[a]	this work

[a]Revised from Mayo et al. (2018).

5.4 Planetary Analysis

5.4.1 Planet Sample and Reanalysis of K2-161

The planets included in our sample are K2-97, K2-132, and K2-161 (Grunblatt et al. 2016, 2017; Mayo et al. 2018). All three planets are warm ($> 150\ F_\oplus$) gas giants larger than Jupiter. The planet host stars are all both the Giants Orbiting Giants Program and *K2* Galactic Archaeology Program targets. For all systems, stellar parameters have been determined through both spectroscopy and asteroseismology as described in the above publications. Planet parameters have been determined through a box least squares search as described in the following subsection and subsequent transit modeling of the *K2* light curves as described in Grunblatt et al. (2017) and Mayo et al. (2018). We list the parameters of the planetary systems in Table 5.2.

K2-161 b, also known as EPIC 201231064.01, was originally validated by Mayo et al. (2018) as a 0.5 ± 0.1 R_J planet orbiting a 2.6 ± 0.3 $R_\odot$ star, with stellar parameters determined by applying the Stellar Parameter Classification (SPC) tool (Buchhave et al. 2012) to TRES spectra. We note that of all the systems validated by the Mayo et al. (2018) study, this particular star had the lowest surface gravity of any validated host star in their sample.

As K2-161 was also a target of our Giants Orbiting Giants *K2* Guest Observer campaign GO10036, we follow the procedure of Grunblatt et al. (2017) using asteroseismology to analyze both the light curve and the frequency spectrum of the light curve of this target (see Figure 5.5). We identify an asteroseismic power excess (Figure 5.5e), and using equations (4) and (5) determine a stellar mass of 1.09 ± 0.10 $M_\odot$ and radius of 4.12 ± 0.14 $R_\odot$. Though the stellar mass determinations between the asteroseismic and spectral analysis are in good agreement (the spectral analysis of Mayo et al. (2018) gives a mass of $0.99^{+0.08}_{-0.06}\ M_\odot$), the spectroscopic and asteroseismic stellar radius determinations disagree at the 3.5-σ level. To resolve this discrepancy, we have also determined the

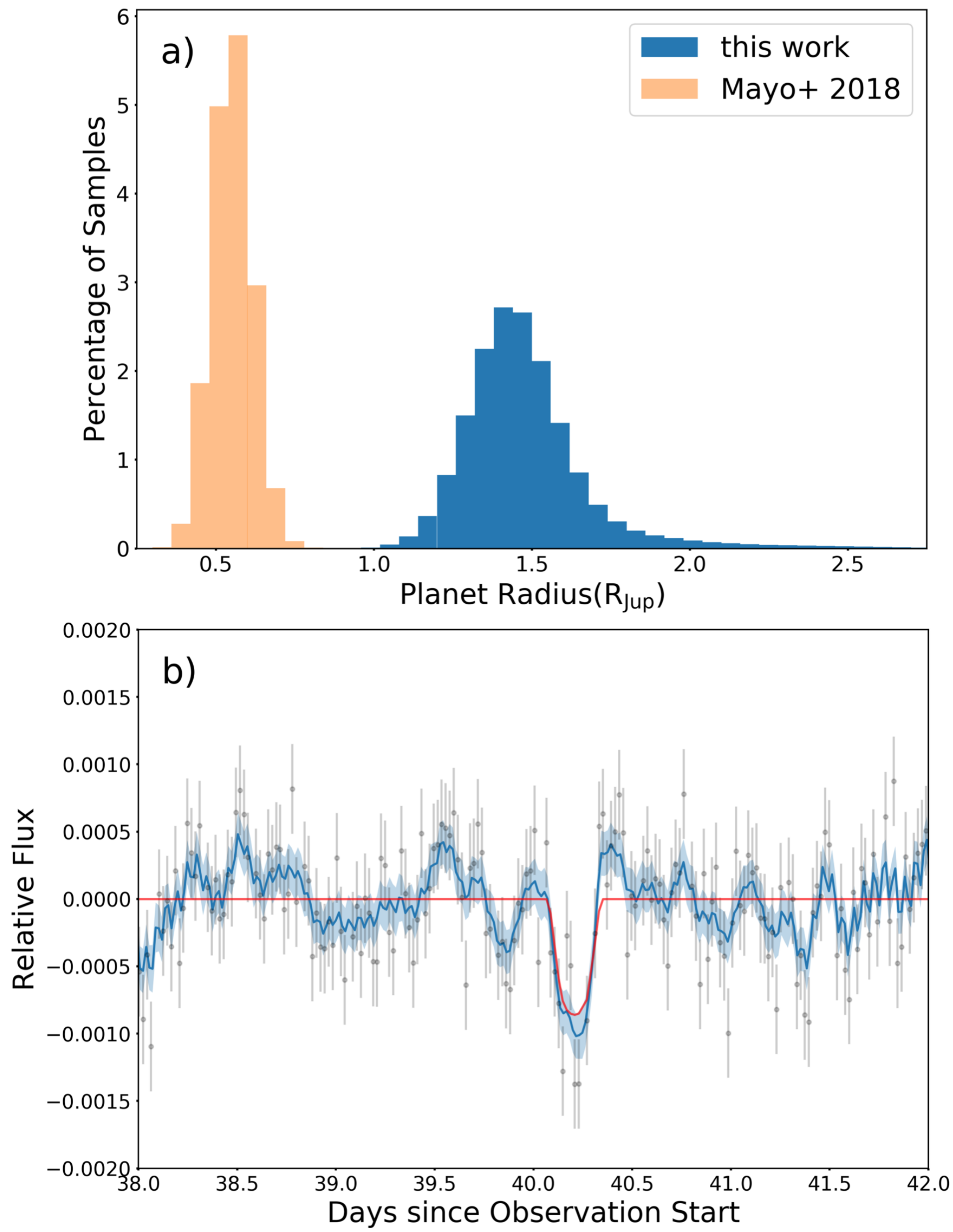

Figure 5.6 Panel a): Planet radius posterior distributions from our analysis of K2-161 b. We find a planet radius that is significantly larger that Mayo et al. (2018) due to an increase in our determined stellar radius from both asteroseismology and *Gaia* parallaxes. Posteriors for the other parameters of our transit + stellar variability model are available on request. Panel b): Our combined Gaussian process and transit fit to K2-161, shown in blue. *K2* data is shown in gray, a pure transit fit is given in red.

radius of K2-161 using a parallax measurement from *Gaia* Data Release 2 and colors using the MIST grid of stellar models via the `isoclassify` package to ensure that our asteroseismic estimates are robust (Choi et al. 2016; Huber et al. 2017). This parallax-driven stellar grid model analysis gives a stellar radius of 4.2 ± 0.2 $R_\odot$, in good agreement with the asteroseismic stellar radius determination. Thus, we report the asteroseismic stellar radius here and perform a reanalysis of validated planet K2-161 b using the asteroseismic stellar parameters determined by this work.

For our reanalysis of the K2-161 b transit signal in the *K2* lightcurve, we follow the analysis method of Grunblatt et al. (2017). We use the `celerite` package to model the stellar granulation and oscillations seen in the stellar light curve as a sum of periodic and aperiodic simple harmonic oscillator terms, as well as a white noise floor (Foreman-Mackey et al. 2017). We then use the package `python-bls` to identify the planet period using a box least-squares analysis (Kovács et al. 2002), and `ktransit` to model the planet transit and stellar variability simultaneously (Barclay et al. 2015). The best fit star and planet model was determined using `emcee` (Foreman-Mackey et al. 2013).

Using this approach and updated stellar parameters, we measure a planet radius of K2-161 b of $1.45\ ^{+0.19}_{-0.14}$ R_J (see Figure 5.6). This is significantly higher than the planet radius reported by Mayo et al. (2018) due to two reasons: the larger stellar radius determined by both *Gaia* data and asteroseismology implies that the planet transit duration is uncharacteristically short, which could be due to either a high planet eccentricity or a high impact parameter for the transit, making a larger planet radius more likely. The combination of a larger host star and higher likely impact parameter both imply a larger planet radius, resulting in the discrepancy between planet radii reported here and in Mayo et al. (2018).

Previous high-resolution imaging and spectroscopy shows that there are no bright stellar companions to K2-161 (Mayo et al. 2018). However, the increased planet radius of 1.45 R_J also raises the likelihood that K2-161 b could be a faint, low-mass stellar companion rather than a gas giant planet. Thus we obtained radial velocity measurements of K2-161 in order to place a maximum mass on K2-161 b and ensure that it falls in the planetary regime. Based on six radial velocity measurements taken by Keck/HIRES between January 7 and March 28, 2019, we found that the radial velocity of K2-161 is consistent at the 100 m s^{-1} level, implying that K2-161 b must be planetary mass and cannot be a stellar companion to K2-161. Thus we find that the statistical validation of K2-161 b as a planet remains valid regardless of the updated stellar and planetary parameters determined here.

5.4.2 Injection/recovery test

In order to determine sensitivity to transiting planets in our dataset, we apply the methodology of earlier planet occurrence studies (e.g., Petigura et al. 2013; van Sluijs & Van Eylen 2018) to our LLRGB star sample. We injected transit signals from simulated planets on logarithmically uniform, random distributions of periods between 3 and 50 days and linearly uniform planet-to-star radius ratios between 0 and 0.045 into all target light curves with measured asteroseismic signals. After injecting planet transits into our light curves, we then performed a box least-squares transit search on these light curves (Kovács et al. 2002) over the same 3-50 day range in orbital period to see if the transits injected could be recovered. We considered the transit to be recovered if the injected period and the recovered period of the planet agreed to within 0.05 days. Our choice of planet period cut is less stringent than previous studies with *Kepler* (e.g. Petigura et al. 2013), due to the shorter time baseline of *K2* campaigns, as well as the high intrinsic variability of evolved stars. This intrinsic variability introduces additional complications in accurately determining the mid-time of transit, limiting orbital period precision for giant stars.

We validate our transit recovery algorithm by visually inspecting light curves where either injected transits of planets larger than Jupiter on orbits shorter than 10 days were undetected, or planets smaller than 0.5 R_J on orbits shorter than 10 days were detected. We find that our visual inspection did not recover any of the >1 R_J planets that went undetected at short periods. Thus, we find that our automated planet detection is consistent with our visual planet detection where our transit injection recovery completeness is >50% (see next Section). Visual inspection also did recover ∼60% of planets smaller than 0.5 R_J on orbits shorter than 10 days recovered by our algorithm, indicating that occurrence estimates will be reasonably accurate but less precise in regimes where injection recovery completeness is low. We also test our transit recovery algorithm on the light curves without injected transits. Our algorithm successfully detects all three planet transits in our dataset, and does not detect any other false positive planet transits at similar durations and signal to noise ratios.

5.4.3 Transit Sensitivity and Survey Completeness

Figure 5.7 plots the our ability to recover signals injected into our light curves. We compare results of this injection/recovery test for our full sample of vetted asteroseismic stars to the subset of LLRGB stars identified by our study. We show (from left to right) the fraction of injected signals recovered as a function of orbital period, planet radius, transit signal to noise ratio, and stellar radius.

Figure 5.7a shows the fraction of injected signals recovered in our dataset as a function of orbital period. Sensitivity decreases as a function of orbital period, as fewer transits can be identified in a single 80-day *K2* campaign. Little variation between the LLRGB stars and the full asteroseismic sample is seen.

The fraction of injected transits recovered as a function of planet radius is shown in Figure 5.7b. Sensitivity increases with planet radius, reaching a plateau of about 60% by a radius of 1.5 R_J. This detection plateau feature may be due to intrinsic faintness of certain stars, systematic variability that is simply too large to allow any planet transit to be detected through a straightforward box least-squares search, or the limited detection opportunities for planets injected on long period orbits that have only one or two transits in a *K2* campaign.

Figure 5.7c displays the number and fraction of transits detected as a function of signal to noise ratio in our sample. We can detect more than half of planet transits at signal to noise ratios of 5 or better, and more than 95% at signal to noise rations above 16, in agreement with previous *Kepler* occurrence studies (Fressin et al. 2013). Thus we expect that >50% of planets with a transit signal to noise of 5 or better and an orbital period less than 50 days have been detected in our sample, in good agreement with our findings in Figure 5.7b.

However, recovery of transit signals for a given planet radius does depend on the stellar radius. Figure 5.7d illustrates the fraction of injected signals recovered in our dataset as a function of stellar radius. We can see that detectability decreases with stellar size. Below $\sim$4 $R_\odot$ and above $\sim$10 $R_\odot$, our stellar sample becomes too small for reliable statistics, resulting in imprecise estimates of transit recovery.

In order to evaluate our survey completeness and calculate the occurrence of planets around these stars, we need to understand the properties of planets that could have been detected by our survey, and compare it to the planets we actually found. The left panel of Figure 5.8 illustrates the distribution of transits as a function of planet radius and period injected in our transit injection and recovery test. Injected signals that were recovered are shown in red, while those that went undetected by the box least-squares search are shown in blue. We inject transits around all 2476 LLRGB stars in our sample.

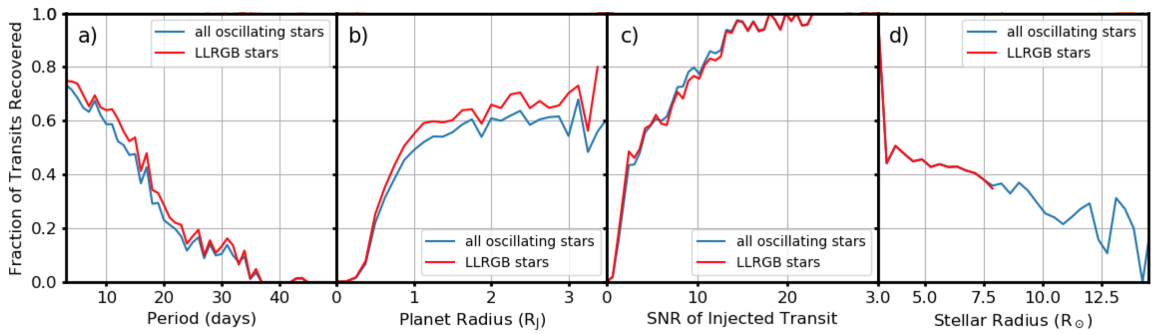

Figure 5.7 Panel a): Sensitivity to injected transit signals as a function of orbital period. Planets are less detectable at longer orbital periods around all stars. Panel b): Sensitivity to injected transit signals as a function of planet radius. Using only stars smaller than 8 $R_\odot$, more than 60% of planets larger than Jupiter are detected. Panel c): Fraction of injected transits recovered by our pipeline, as a function of injected transit signal to noise ratio in the light curve. Restricting our sample to only LLRGB stars has no significant effect on our results. Panel d): Sensitivity to injected transit signals as a function of stellar radius. Stellar radii have been determined through asteroseismology. Above 8 $R_\odot$, planet transit detectability drops below 40%.

We then evaluate our completeness fraction in bins of planet radius and orbital period, with upper and lower uncertainties estimated by calculating completeness with a period precision threshold of our injection/recovery pipeline set to 0.1 and 0.03 day precision, respectively. For our completeness estimate, we require our recovered period to agree with the injected period by 0.05 days, comparable to the period precision required by earlier *Kepler* transit injection/recovery tests (Petigura et al. 2013). Completeness may also vary within the bins in orbital period and planet radius specified here. The right panel of Figure 5.8 illustrates the completeness of our survey. We find that we are sensitive to almost all planets at periods between 3.5 and 10 days and larger than Jupiter, with sensitivity dropping at larger periods and smaller planet radii, reaching less than 50% completeness at periods greater than 29 days and planet radii smaller than 0.5 R_J.

5.4.4 Planet Occurrence Calculation

In order to calculate planet occurrence, we followed the prescription of Howard et al. (2012), using our survey completeness to estimate how many planets we could have found, and then compare that to the number of planets we actually found in each bin.

For each orbital period/planet radius (P–R_P) bin, we count the number of transiting planets, $n_{\rm pl,bin}$. As we assume planetary orbits to be randomly oriented, each transiting planet represents a

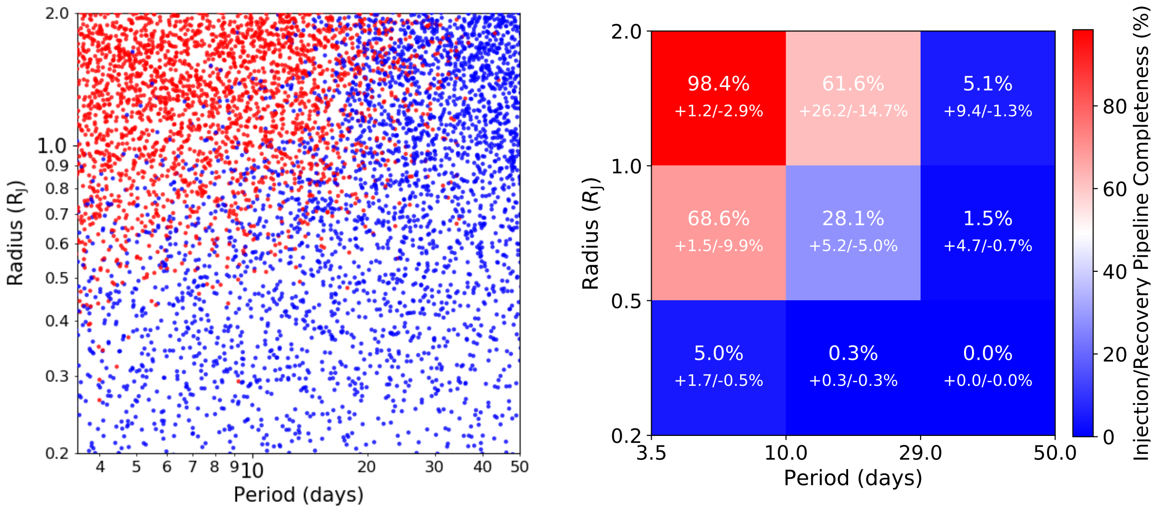

Figure 5.8 Left: Transits injected into our LLRGB light curves, as a function of planet radius and orbital period. Transits that were recovered are shown in red, while those missed are shown in blue. Right: Injection/recovery survey completeness for our sample of oscillating, <8 $R_\odot$ stars. We see that the survey is largely complete for planets larger than 1 R_J on orbital periods shorter than 10 days, and are more than 50% complete for planets down to 0.5 R_J as well as super-Jupiter sized planets out to 25 day orbital periods.

larger number of planets that are not transiting. We compute this augmented number of planets,

$$n_{\mathrm{pl,aug,bin}} = \sum_{n=0}^{i} a_i/R_i, \tag{5.6}$$

where i is the number of planets per bin, a_i is the semimajor axis of a given planet i, and R_i is the stellar host radius, to account for non-transiting planets. We note that this overestimates the detection efficiency, and underestimates the occurrence in our case, if the intrinsic detection efficiency changes significantly across the finite width of the bin in both orbital period and planet radius (Hsu et al. 2018). However, we use this method to allow for direct comparison to the results of Howard et al. (2012), which were computed using the same inverse detection efficiency method.

The planets considered by our survey and their physical properties are listed in Table 5.2. To compute occurrence, we divide the number of stars with detected transiting planets in a particular bin by the number of stars around which a transiting planet could have been detected in a given bin, $n_{*,\mathrm{amen}}$. This number is just our total number of LLRGB stars, N = 2476 , multiplied by the completeness in a bin computed in our injection/recovery test. The debiased fraction of stars with

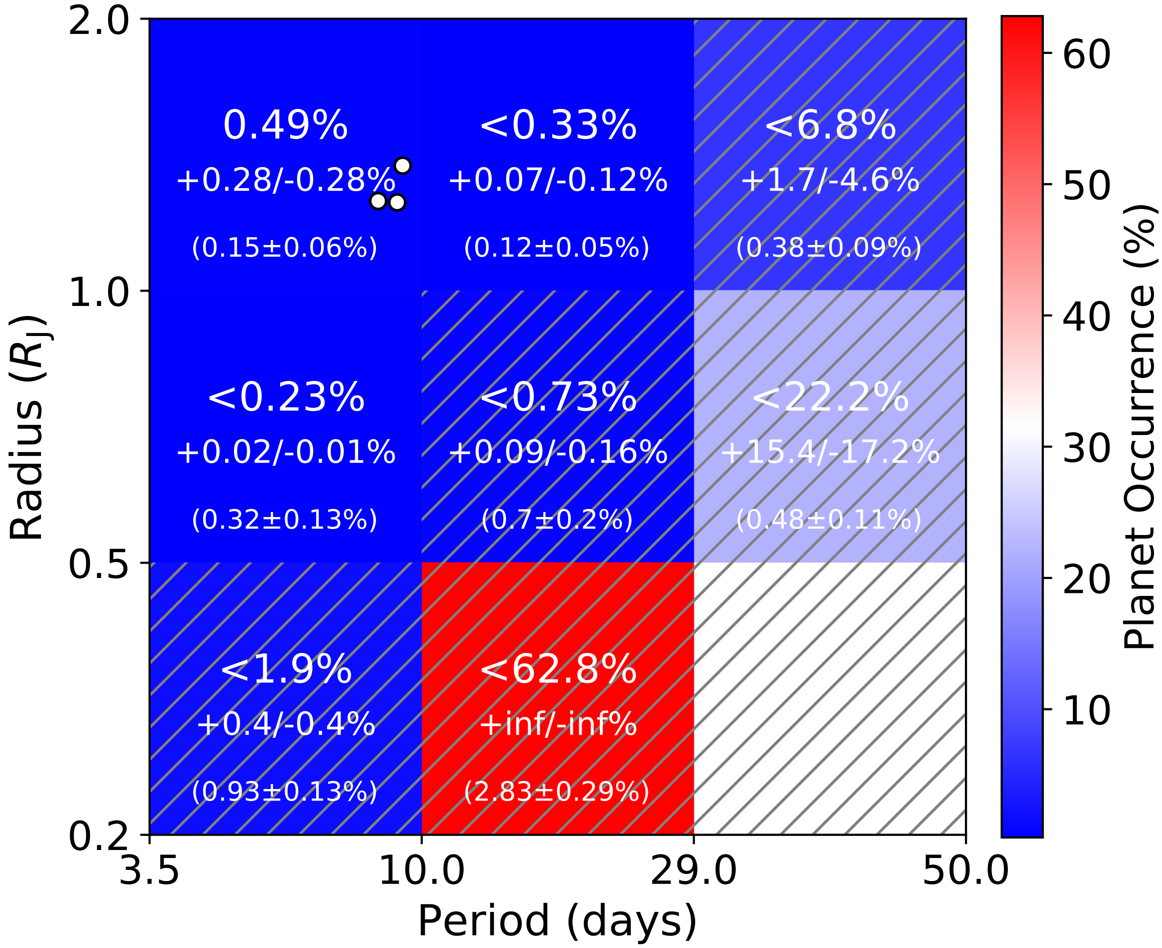

Figure 5.9 Planet occurrence around 3.5-8 $R_\odot$ stars observed by *K2*, as a function of orbital period and radius. In those bins where no planets were found, upper limits were calculated for planet occurrence. Hatched cells designate where injection/recovery completeness is below 50% for our stellar sample. Main sequence occurrence rates from Howard et al. (2012) are shown in parentheses at the bottom of each bin. Planets detected in this survey are shown by the white markers. For planets with radii larger than Jupiter at orbital periods less than 10 days, we find a consistent yet tentatively higher number of planets orbiting our sample of LLRGB stars than main sequence stars. For all regions of parameter space where planets were not found, the upper limits of planet occurrence calculated by this survey are in agreement with the main sequence occurrence rates reported by Howard et al. (2012).

planets per P–R_p bin, f_{bin}, is given by

$$f_{\mathrm{bin}} = n_{\mathrm{pl,aug,bin}}/n_{*,\mathrm{amen}}. \tag{5.7}$$

For those bins where no planets were found, we place an upper limit on planet occurrence by calculating the planet occurrence if one planet had been detected in that bin. In those bins where we have detected planets, we find that our errors in completeness are negligible compared to Poisson errors introduced by our small sample of detected planets, which dominate our errors in planet occurrence. Errors on occurrence upper limits are calculated by propagating our errors in survey completeness forward, and adding Poisson errors in quadrature where planets were detected. Poisson errors dominate where planets were detected around both main sequence and LLRGB stars.

Figure 5.9 shows planet occurrence in our sample. Our occurrence estimate and errors are shown at the center of each bin, while main sequence occurrence rates determined from Howard et al. (2012) for that bin are given in parentheses below our estimates. In order to test our sensitivity to stellar radius, we also repeat our experiment, excluding all stars with asteroseismic radii larger than 6 $R_\odot$, a subsample of 1630 stars. The results of this test, along with all of our other occurrence estimates, are shown in Table 5.3.

5.5 Discussion

5.5.1 Close-In Giant Planet Occurrence of Evolved Stars

Based on our analysis of 2476 oscillating stars, we find that 0.49% $\pm$ 0.28% of stars with radii between 3.5 and 8 $R_\odot$ host planets larger than 1 R_J on 3.5–10 day orbits, a consistent yet tentatively larger fraction than the 0.15% $\pm$ 0.06% of main sequence stars found to be hosting similar planets by Howard et al. (2012). We also find that fewer than $0.23\%^{+0.02\%}_{-0.01\%}$ of LLRGB stars host planets with radii between 0.5 and 1 R_J and orbital periods of 3.5–10 days, in agreement with the 0.32% $\pm$ 0.13% of systems found around main sequence *Kepler* stars. Our upper limit of $0.33\%^{+0.07\%}_{-0.12\%}$ of stars hosting planets > 1 R_J on 10–29 day orbital periods is also in agreement with the 0.12%$\pm$0.05% of stars found to be hosting such planets on the main sequence (Howard et al. 2012). Due to the intrinsic variability of giant stars and the limited duration of *K2* time-series, we are not sensitive to

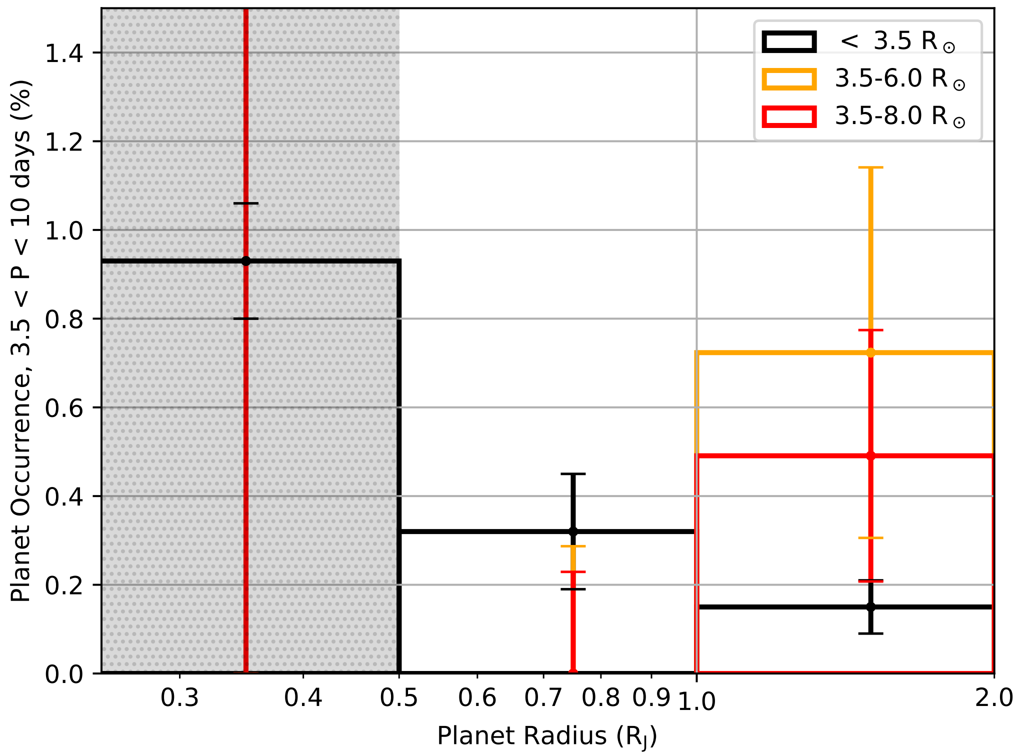

Figure 5.10 Planet occurrence within 3.5-10 days as a function of planet radius, with different stellar radius populations broken into groups. Planet radius is given on the x-axis, while different stellar populations separated by radius are indicated in the plot legend in the upper right. Errors indicate 68% confidence intervals. Planet occurrence appears consistent yet tentatively higher around evolved stars with radii between 3.5 and 8 $R_\odot$ than main sequence stars for planets larger than Jupiter. This difference seems enhanced when only evolved stars between 3.5 and 6 $R_\odot$ are considered. Close-in planet occurrence may be similar or lower around evolved stars than main sequence stars at planet radii between 0.5 and 1 R_J.

transit signals from planets at orbital periods of 29 days or longer, or 0.5 Jupiter radii or smaller, or for planets between 0.5 and 1.0 R_J on 10 to 29 day orbital periods in our sample.

If we restrict ourselves to stars smaller than 6 $R_\odot$, we find that occurrence is enhanced at the smallest orbital periods and largest planet radii, as all planets considered in our survey orbit relatively small ($\sim$4 $R_\odot$) stars in our sample at periods <10 days. We find that 0.72% $\pm$ 0.41% of stars with radii between 3.5 and 6 $R_\odot$ host planets larger than 1 R_J on 3.5–10 day orbits. Upper limits on planet occurrence are particularly large in the longer period bins for these less evolved stars, due to the smaller sample size. At orbital periods greater than 10 days, our maximum planet occurrence estimates are in complete agreement with main sequence planet occurrence rates (Howard et al. 2012; Fressin et al. 2013). We state these planet occurrence findings in Figure 5.10 and Table 5.3.

Table 5.3. Comparison of Planet Occurrence Around Main Sequence and Evolved Stars

Planet Radius	Planet Sample	Stellar Sample	Orbital Period		
			3.5-10 days	10-29 days	29-50 days
1-2 R_J	Main Sequence	Main Sequence	0.15 ± 0.06	0.12 ± 0.05	0.38 ± 0.09
	Main Sequence	LLRGB	0.28 ± 0.16	0.27 ± 0.16	*
	LLRGB	LLRGB	0.49 ± 0.28	$<0.33^{+0.07}_{-0.12}$	$<6.8^{+1.7}_{-4.6}$*
	LLRGB (<6 $R_\odot$)	LLRGB (<6 $R_\odot$)	0.72 ± 0.41	$<0.46^{+0.10}_{-0.26}$	$<10.2^{+1.8}_{-8.2}$*
0.5-1 R_J	Main Sequence	Main Sequence	0.32 ± 0.13	0.70 ± 0.20	0.48 ± 0.11
	Main Sequence	LLRGB	0.27 ± 0.12	0.35 ± 0.04*	*
	LLRGB	LLRGB	$<0.23^{+0.02}_{-0.01}$	$<0.73^{+0.09}_{-0.16}$*	$<22.4^{+15.4}_{-17.2}$*
	LLRGB (<6 $R_\odot$)	LLRGB (<6 $R_\odot$)	$<0.28 \pm 0.11$	$<0.86^{+0.30}_{-0.46}$*	$<24.0^{+5.1}_{-20.3}$*
0.25-0.5 R_J	Main Sequence	Main Sequence	0.93 ± 0.13	2.83 ± 0.29	1.85 ± 0.41
	Main Sequence	LLRGB	23.4 ± 16.6*	*	*
	LLRGB	LLRGB	$<1.9 \pm 0.4$*	<62.8*	*
	LLRGB (<6 $R_\odot$)	LLRGB (<6 $R_\odot$)	$<2.2^{+0.5}_{-1.1}$*	<72.9*	*

*Injection/recovery tests indicate a completeness below 50% for these regimes. No value is reported in those regimes where no injected signal was recovered.

Note. — All occurrence values quoted are percentages. Main sequence planets orbiting main sequence star results are taken from Howard et al. (2012).

5.5.2 Reproducing Main Sequence Occurrence Rates with Our Pipeline

We confirm our results are robust by injecting a main sequence population of planets selected using the same constraints as Howard et al. (2012) around our targets. Specifically, we inject only confirmed planets with *Kepler* Object of Interest designations below 1650 around stars with $T_{\rm eff}$ = 4100–6100 K, log g = 4.0–4.9 dex, and *Kepler* magnitude $K_p < 15$ mag around a random subset of our LLRGB star sample.

We take this population of detected transiting planets around main sequence stars and use it to infer the true population of planets around main sequence stars. We do this by computing the inverse detection efficiency for each main sequence transiting planet detection to infer the total population, or augmented number of planets orbiting main sequence stars, equivalent to computing $n_{\rm pl,aug}$ for all planets in the main sequence sample. Given a main sequence sample of 58,041 stars (Howard et al. 2012), we use this to determine the number of planets per main sequence star, and then compute the expected number of planets orbiting our sample of LLRGB stars, assuming the main sequence and LLRGB planet populations are equivalent. We then inject this population of planets around our LLRGB stars, and use this injected planet population to determine planet occurrence if the main sequence and LLRGB planet populations are equivalent, accounting for transit detection bias differences between the main sequence and LLRGB stellar populations. We then compare this result to the planet occurrence determined by our K2 survey of LLRGB stars. We show our planet occurrence estimates from injecting the main sequence planet population around main sequence stars in Table 5.3.

We find that when placing the main sequence population of planets around LLRGB stars, transiting planets are detected around 0.4% of stars, comparable to the number of planets observed around main sequence stars where our survey completeness is greater than 50%. We find that our planet occurrence estimates generated using the reproduced Howard et al. (2012) planet sample agree within 1-σ with both our observed LLRGB planet population as well as the planet occurrence rates stated in Howard et al. (2012) in all bins where our LLRGB survey completeness is greater than 50%, including the bin where planets were detected in our *K2* survey. We measure a main sequence occurrence rate of 0.28 $\pm$ 0.16% for planets larger than Jupiter on 3.5–10 day orbits, 0.27 $\pm$ 0.16% for planets larger than Jupiter on 10–29 day orbits, and 0.27 $\pm$ 0.12% for planets between 0.5 and 1.0 R_J on 3.5–10 day orbits, in good agreement with the Howard et al. (2012) results.

5.5.3 Effects of Stellar Mass and Metallicity

It is important to account for the variation in stellar masses and metallicities in our sample to ensure that differences in occurrence are a result solely of evolution and not an effect of analyzing different stellar populations. Johnson et al. (2010) show that planet occurrence is proportional to stellar mass ($f \propto M$) and has a dependence on stellar metallicity as well ($f \propto 10^{1.2[\mathrm{Fe/H}]}$). The median mass and metallicity of the stars around which we did find planets is 1.09 $M_\odot$ and 0.1 dex higher than solar, respectively. The median mass of our entire sample is 1.20 $M_\odot$. We do not have metallicity estimates for our entire stellar sample, and thus assume the average metallicity of this sample is within 0.1 dex of solar metallicity. Based on these measurements and assumptions, we expect at most a $\approx$30% higher occurrence rate for our sample than that of truly solar-like stars. We find that the typical masses and metallicities of well-characterized stars in the Howard et al. (2012) sample have masses comparable to the planet-hosting stars in our study, and metallicities approximately 0.1 dex lower than the evolved systems studied here (Petigura et al. 2017; Johnson et al. 2017). Thus, the effects of stellar metallicity and mass may not be sufficient to fully account for the differences in planet occurrence found here, but a larger population of planets around evolved stars is needed to definitively distinguish between metallicity and evolutionary effects.

5.5.4 Constraints on Planet Dynamics

It is assumed that the evolution of a host star will strongly affect the orbital and atmospheric properties of any planets in orbit, which may explain the tentative enhancement in short period planets larger than Jupiter seen in this study (Villaver & Livio 2009; Lopez & Fortney 2016; Grunblatt et al. 2018). Using the planet occurrence distributions of both the main sequence and evolved stars, and assuming a uniform fractional radius inflation for all planets from the main sequence to the evolved stage, we can predict the observed change in planet occurrence as a function of planet radius. This will allow distinction between a static orbit scenario, where planets are inflated by stellar evolution but do not migrate, and a scenario where stellar evolution also causes orbital motion of its planets.

Using the main sequence planet sample of Howard et al. (2012), we assume a monotonic increase in radius of 50% for the 3.5-10 day orbital period, > 0.5 R_J main sequence planet population from planet inflation due to stellar evolution. This would increase the occurrence from 0.15% to 0.21% of

> 1 R_J planets at orbital periods of 3.5-10 days around evolved stars. This occurrence rate is smaller than that measured for evolved systems by this work and only marginally higher than the observed main sequence occurrence rate. We conclude that inflation of the main sequence population alone is not sufficient to explain the elevated occurrence around evolved stars. Instead, the observed evolved system, short-period super-Jupiters are likely both smaller and at larger orbital distances around main sequence stars.

During post-main sequence stellar evolution, planets on eccentric orbits are likely circularizing while spiraling into their host stars (Villaver & Livio 2009; Villaver et al. 2014). This process will presumably cause significant tidal distortion and potential dissipation within the planets, heating their interiors and inflating them to larger radii, producing a population of transient, moderately eccentric close-in planets falling into their host stars (Bodenheimer et al. 2001; Grunblatt et al. 2018). The increased irradiation of these planets by their host stars will have a similar effect (Lopez & Fortney 2016; Grunblatt et al. 2017). Given that a population of cold, gas giant planets exists around a higher fraction of main sequence stars than close-in planets around evolved stars (Bryan et al. 2016; Ghezzi et al. 2018), inspiral of some or all of the main sequence giant planet population could result in the close-in giant planet population found here. Furthermore, the increase in irradiation may result in photoevaporation of less massive planetary atmospheres, leaving behind undetectable rocky cores alongside the inflated planets we can detect (Owen & Wu 2017).

The timescale of inspiral of an eccentric, gaseous planet may be inferred from these observations. Following the reasoning of Grunblatt et al. (2018), if we assume a“constant phase lag” model for tidal evolution (Goldreich & Soter 1966; Patra et al. 2017), we calculate the inspiral timescale of the planet as

$$\tau = \frac{2Q_*}{27\pi}\left(\frac{M_*}{M_p}\right)\left(\frac{a}{R_*}\right)^5 P, \tag{5.8}$$

where M_*, R_* and Q_* are the mass, radius, and tidal quality factor of the star, M_p is the planet mass, a is the semimajor axis of the planet's orbit, and P is the planet period. Assuming a stellar tidal quality factor $Q_\star \sim 10^6$ as found in earlier studies (Essick & Weinberg 2016), we find an inspiral timescale of $\lesssim 2$ Gyr for all planets in our sample, potentially much longer than the LLRGB phase of stellar evolution.

However, the relatively high planet occurrence of the largest, shortest period planets around the smallest stars in our sample that is not seen for larger stars suggests that planetary systems can survive the subgiant phase of stellar evolution, and are being reshaped during this low-luminosity ascent of the red giant branch. A pile-up of planets at small orbital periods around $\sim$4 $R_\odot$ stars would imply that our inspiral timescale for these systems is overestimated, close-in planets only survive past this stellar radius size in rare cases, and may be engulfed soon after the star reaches this size. The strong dependence of inspiral timescale on stellar radius may reflect this change in inspiral speed at larger stellar radii. However, the small sample of planets found combined with a selection effect which strongly favors smaller stars may also be responsible for the stellar radius distribution we observe. Thus, additional systems must be observed to improve models of planet evolution significantly.

5.6 Conclusions

We have identified 2476 low-luminosity red giant branch (LLRGB) stars observed in 15 of the first 16 campaigns of the *K2* mission using parallaxes and asteroseismology to determine stellar radii and masses. We then perform a transit injection/recovery test to determine the transit survey completeness, and thus infer planet occurrence around these evolved stars. We find that:

- Using asteroseismology, we constrain masses and radii of 2476 LLRGB stars to 3.7% and 2.2% median uncertainties, respectively. Asteroseismic radii for LLRGB stars agree with radii calculated using *Gaia* parallaxes with both surface brightness-color relations and stellar grid modeling with a median offset of 3% and a scatter of 10%.

- At radii larger than 1 R_J and orbital periods 3.5-10 days, when compared to the main sequence population, planet occurrence appears tentatively higher around evolved stars, yet agrees with main sequence occurrence rates within errors. At orbital periods of 3.5-50 days and planet radii between 0.2 and 2 times the size of Jupiter, upper limits on planet occurrence around evolved stars are in agreement with planet occurrence determined around main sequence stars (Howard et al. 2012; Fressin et al. 2013).

- As all confirmed planet hosts in our sample are larger than 3.6 $R_\odot$, planetary systems can survive the subgiant phase of stellar evolution at least until the host star reaches the base of the red giant branch. As no planetary hosts in our sample are larger than 4.4 $R_\odot$, this implies that planetary systems are likely destroyed by their host stars during the early stages of ascent up the red giant branch. Planet occurrence likely varies as a function of stellar radius in our sample.

- Assuming a 50% increase in radius of all planets orbiting main sequence stars is insufficient to explain the larger fraction of short-period super-Jupiter sized planets. This suggests that if there is in fact a larger fraction of short-period super-Jupiter sized planets around evolved stars, orbital migration may contribute to this planet population. The difference in stellar mass distribution of our stars relative to main sequence stars is insufficient to account for the difference in planet distribution. The influence of metallicity is more unclear, as metallicities are only known precisely for the planet hosts in our sample, which are marginally more metal-rich than the main sequence planet host population.

Differences between the occurrence of planets around main sequence and evolved stars gives us valuable information about the evolution of planetary systems in conjunction with the evolution of their host star. However, these results rest on only three planet detections among 2476 stars, a sample less than 2% the size of *Kepler* main sequence occurrence studies, and thus a larger sample of stars and planets will be essential to determining whether these deviations in planet occurrence are significant.

The recently launched NASA *TESS* Mission is essential to further investigations of the planet population around evolved stars. *TESS* will observe two orders of magnitude more evolved stars than *K2*, and will cover more than 90% of the sky with a cadence, precision and depth sufficient to identify giant planets orbiting evolved, oscillating stars with orbital periods of 10 days or less at distances $\geq$ 1 kpc (Campante et al. 2016). Indeed, the first transiting planet orbiting an oscillating, evolved host star observed by *TESS* has already been found (Huber et al. 2019). A survey of the ~400,000 evolved stars observed by *TESS* will thus be instrumental in determining precisely what the fraction of 0.5-1.0 R_J planets is around evolved stars, and how depleted the population is relative to main sequence stars. Furthermore, due to Malmquist bias evolved stars tend to be further away than main sequence stars of similar magnitudes. Thus, a larger sample of transiting planets orbiting evolved stars could reveal deviations in planet occurrence as a function of location in the Galaxy out to kiloparsec distances.

Chapter 6

Fundamental Parameters and Radial Velocities of Red Giant Stars

The following sections of this chapter represent papers in progress that have begun as a result of this thesis work.

6.1 Accurate effective temperature and radius scales for asteroseismic giants

6.1.1 Motivation

Measuring precise and accurate stellar radii and temperatures is of utmost importance to the transiting exoplanet and galactic archaeology communities. The discovery of new features and discrepancies in the both the planet population and galactic stellar distribution has relied on accurate and precise stellar effective temperature and radius measurements (Pinsonneault et al. 2014; Fulton et al. 2017). These are both driving science cases for a number of current and future NASA and ESA missions, such as *TESS*, *Gaia*, and *PLATO* (Howell et al. 2014; Rauer et al. 2014; Gaia Collaboration et al. 2018). Thus, it is essential to use fundamental methods to estimate these parameters where possible, as well as use those fundamental methods to calibrate other methods which can be applied to measure the sizes of a larger number of stars.

One of the most fundamental ways to measure stellar radii and temperatures is to take advantage of the Stefan–Boltzmann relation between radius, luminosity and temperature of a star (Stefan 1879; Boltzmann 1884):

$$L_* = 4\pi R_*^2 \sigma T_{\rm eff}^4, \tag{6.1}$$

This relation can be rewritten in terms of physical observables of a star. By measuring an angular diameter and bolometric flux of a star, a temperature can be determined analytically using the following modified Stefan–Boltzmann equation:

$$T_{\rm eff} = 2341\Big(\frac{F_{\rm bol}}{\theta^2}\Big)^{1/4} \tag{6.2}$$

where θ is the angular diameter and $\mathrm{F_{bol}}$ is the stellar bolometric flux measured in units of 10^{-8} erg $\mathrm{s^{-1}}$ $\mathrm{cm^{-2}}$. If a parallax is also known, as is the case for all of the stars in our sample, the stellar radius can be computed from the parallax and angular diameters, and the luminosity can be determined from the bolometric flux and distance to the star.

Any star where a radius can be determined can then be used to calibrate more indirect methods of stellar property determination, such as asteroseismology, spectroscopy, or stellar model creation. Equivalently, if a stellar luminosity and radius are known, a stellar effective temperature can be determined. Measuring the effective temperatures of a wide range of stars allows the establishment of a relationship between stellar photometric colors and temperature.

6.1.2 Stellar Sample

Here we present a sample of spectrophotometric data of oscillating red giants to date in order to calibrate effective temperature and radius relations with fundamental observational constraints. We have obtained medium-resolution optical and infrared spectra between March 2016 and January 2019 using the Supernova Integrated Field Spectrograph (SNIFS) on the 2.2 meter University of Hawaii telescope and SpeX on the 3 meter Infrared Telescope Facility (IRTF), providing spectral resolution of 1000–2000 over a wavelength range from 0.3 to 5.5 microns (Lantz et al. 2004; Rayner et al. 2003) for over 200 stars, with over 500 having spectral coverage over a subset of this range. These stars have been selected for observation from the *K2* General Observer programs target LLRGB stars (see Chapter 5, Section 2 for a full list of *K2* targets.) Stars from all 15 GO campaigns have been observed for this study, with a preference for brighter targets with clear asteroseismic signals present in their *K2* photometry. We have additionally observed ∼20 stars over a wider range of the red giant branch which have observed angular diameters from interferometric observation from the CHARA

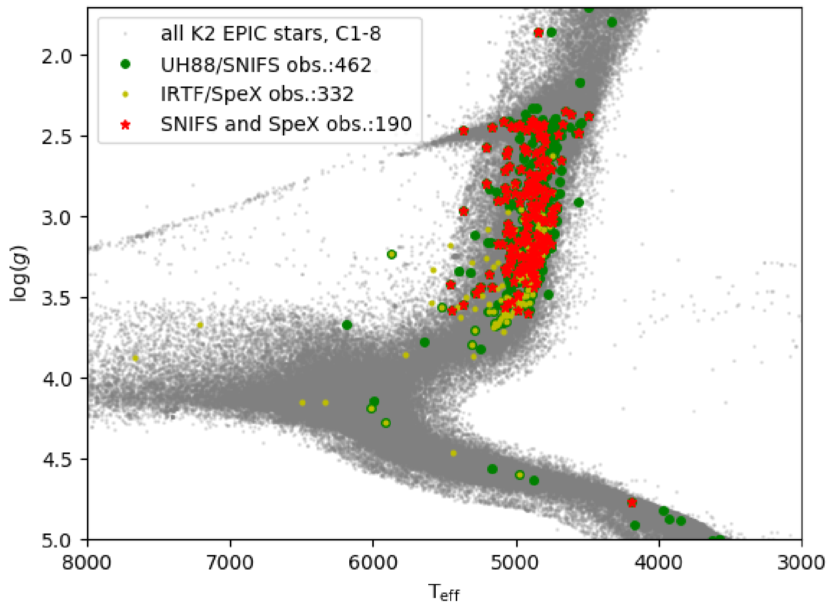

Figure 6.1 Effective temperature versus surface gravity from the EPIC catalog, highlighting stars of which we have obtained medium resolution spectra. Stars with only optical SNIFS spectra are shown in green, while stars with only NIR SpeX spectra are shown in yellow. Stars with both SNIFS and SpeX spectra are shown in red, and the total number of stars for each population is given in the plot legend.

array (White et al., *in prep.*). These stars will be used to calibrate a grid of model spectra, which will then be used to determine stellar luminosities, temperatures, and radii from flux-calibrated observed spectra. The results of this spectroscopic study can then be used to calibrate asteroseismic radius determination for LLRGB stars, and potentially improve models of stellar interiors and atmospheres.

6.1.3 Methodology

Perhaps the most fundamental method to measure a stellar radius is to combine a parallax measurement with an angular diameter. The stellar radius can be determined by

$$R_* \approx (\theta/\pi) \times 100 R_\odot \tag{6.3}$$

where θ is the angular diameter and π is the parallax of the star.

All stars in our sample have parallax measurements, thanks to the *Gaia* and HIPPARCOS surveys (Perryman et al. 1997; Gaia Collaboration et al. 2018). For those stars in our sample with both angular diameters and spectra, this means we can independently determine bolometric fluxes (and thus stellar luminosities and stellar radii), allowing us to calculate stellar effective temperatures from the Stefan–Boltzmann relation.

We then compare these observed spectra to a grid of model spectra with predetermined effective temperatures, surface gravities and metallicities. By combining this information with *Gaia* parallaxes, we can determine bolometric fluxes and angular diameters for these stars, and then compare the computed angular diameter values to the observed angular diameters of these stars. We then calibrate the fitting procedure such that computed and measured angular diameters agree, and use this along with the model-determined bolometric fluxes to determine accurate effective temperatures for all stars with measured angular diameters.

For those stars in our sample with spectra but without measured angular diameters, we can then use the spectral model grid to determine calibrated bolometric fluxes and temperatures, and thus calculate angular diameters using the modified Stefan–Boltzmann relation. These angular diameters will then be converted to stellar radii via *Gaia* parallax information, and compared to asteroseismically-determined stellar radii to see if any systematic trends between the independent stellar radius determinations appear. In addition, we use our flux-calibrated spectra to generate synthetic photometry for all stars in our sample at various bandpasses. We then use this to calculate synthetic photometry for multiple color combinations for all stars in our sample, which we use to test the uncertainties on our spectral fitting procedure by comparing the synthetic photometry to the true photometry of these stars. We then will use both the synthetic and observed photometry to calculate colors for all of the stars in our sample, and then use these colors along with our spectrally-determined effective temperatures to derive color-$T_{\rm eff}$ relations for red giant branch stars.

Figure 6.2 illustrates some representative stellar spectra taken by our survey. We joined and flux calibrated the SNIFS and SpeX spectra following the method outlined in Mann et al. (2015). We first obtained photometry from the Two-Micron All-Sky Survey (2MASS, Skrutskie et al. 2006), AAVSO All-Sky Photometric Survey (APASS, Henden et al. 2012), and The Wide-field Infrared Survey Explorer (WISE, Wright et al. 2010). The spectrum and all photometry were converted to physical fluxes using the appropriate zero-points and filter profiles (Cohen et al. 2003; Jarrett et al. 2011; Mann & von Braun 2015). We scaled the optical and NIR spectra to match the photometry and each other in overlapping regions (0.8-0.95 μm), accounting for correlated errors in the flux calibration. Regions of high telluric contamination or missing from our spectrum (e.g., beyond 2.4 μm) were replaced with a best-fit atmospheric model from the BT-SETTL grid (Allard et al. 2011, 2013).

We illustrate four calibrated, combined red giant spectra in Figure 6.2. These spectra have been organized from smallest to largest stellar radii, and the wavelength of peak emission can be seen to shift accordingly. The last spectrum is of HD175884, a bright red giant star which has been observed by CHARA interferometrically and thus has a measured angular diameter, which we will use to calibrate our spectral model fitting routine and determine accurate angular diameters (and therefore radii) for the other three stars with spectra shown here.

6.2 Radial velocities of red giant stars

RV followup is one of the most valuable techniques for determining both the planetary and stellar properties in a planetary system. Thus, building a large sample of measurements of a range of stars in our LLRGB population is essential to both measuring precise planetary properties, understanding planet detection limits, and characterizing the observed radial velocity signature of giant stars. Being able to distinguish between such stellar variability and planetary signals is essential to the future of planetary science around giant stars as well as Sun-like stars.

Here we present radial velocity observations of five stars observed as part of our LLRGB planet search program. We are able to identify a Keplerian signal which aligns with the transit signal seen in the light curve of K2-161, thus giving a planet mass constraint and confirming the planetary nature of this system. In the other four stars we observed, we were not able to identify a Keplerian planetary signal which matched the transit signals found in our LLRGB search, and thus use these measurements to try to identify features of stellar variability. We find that our measurements may disagree with variability predictions, and discuss in more detail in Section 6.2.2. We list all radial velocity measurements presented in this Section in Table 6.1.

Table 6.1: Radial Velocities

Star	**BJD**	**RV (m s^{-1})**	**Prec. (m s^{-1})**
K2-161	2458491.15094	-22.04	3.40
K2-161	2458492.08036	-17.65	3.27

Continued on next page

Table 6.1 – continued from previous page

Star	BJD	RV (m s^{-1})	Prec. (m s^{-1})
K2-161	2458533.01398	8.55	3.83
K2-161	2458559.970853	8.65	3.95
K2-161	2458566.995301	-21.02	3.89
K2-161	2458569.846175	7.84	3.58
K2-161	2458570.938685	14.85	3.17
K2-161	2458610.918811	-7.96	3.57
K2-161	2458615.841837	12.94	3.72
K2-161	2458616.891358	30.82	3.27
K2-161	2458622.828601	12.48	3.24
K2-161	2458623.821093	9.27	3.14
K2-161	2458627.834855	-11.76	3.49
K2-161	2458628.807298	-16.92	3.33
K2-161	2458632.847534	-2.53	3.18
K2-161	2458647.788033	-8.39	3.69
K2-161	2458650.819942	-16.28	3.45
EPIC230763211	2458263.009552	-4.81	2.02
EPIC230763211	2458264.970891	1.60	2.47
EPIC230763211	2458265.975737	0.12	2.23
EPIC230763211	2458284.904273	0.62	2.04
EPIC230763211	2458292.917764	-5.06	2.25
EPIC230763211	2458293.97593	5.40	2.58
EPIC230763211	2458299.848103	6.41	2.13
EPIC230763211	2458300.858262	-11.04	2.21
EPIC230763211	2458303.857643	5.60	1.95
EPIC247519660	2458099.893926	15.42	3.39
EPIC247519660	2458113.850915	-6.66	3.33
EPIC247519660	2458116.854714	-9.62	3.00
EPIC247519660	2458124.933038	-5.13	3.70
EPIC247519660	2458149.840155	-9.98	3.09
EPIC247519660	2458150.833245	6.01	3.10
EPIC247519660	2458154.925607	-3.75	3.10
EPIC201132839	2457764.084449	13.73	1.85
EPIC201132839	2457776.077956	-4.93	5.5
EPIC201132839	2457830.911212	-3.11	5.6
EPIC201132839	2457854.944314	-15.68	6.2
EPIC201132839	2457925.773179	-33.59	5.3
EPIC201132839	2458100.094831	-68.61	6.1
EPIC201132839	2458114.059166	-33.59	5.9
EPIC201132839	2458149.940583	-49.73	8.0
EPIC201132839	2458161.063803	-36.77	5.6
EPIC201132839	2458194.956267	-31.45	5.8
EPIC201132839	2458263.843188	46.44	6.4
EPIC201132839	2458299.764305	51.88	5.2
EPIC201132839	2458300.775042	34.13	5.1
EPIC201132839	2458303.762735	30.24	5.2
EPIC201132839	2458491.144195	-17.31	5.6
EPIC201132839	2458492.044500	26.80	5.2
EPIC201132839	2458532.924966	9.57	6.3

Continued on next page

Table 6.1 – continued from previous page

Star	BJD	RV (m s^{-1})	Prec. (m s^{-1})
EPIC201132839	2458559.877330	23.68	5.8
EPIC201132839	2458566.985695	35.57	6.6
EPIC201132839	2458569.826175	-6.84	5.8
EPIC201132839	2458570.931102	-11.04	5.4
EPIC201132839	2458610.910532	-7.89	5.7
EPIC201132839	2458615.835347	5.00	5.9
EPIC201132839	2458622.820338	5.96	5.2
EPIC201132839	2458623.793034	-30.37	5.8
EPIC201132839	2458627.810327	0.06	5.3
EPIC201132839	2458628.785264	13.58	5.5
EPIC201132839	2458632.814764	-6.45	5.6
EPIC201132839	2458646.769481	-8.87	5.2
EPIC201132839	2458647.780588	-3.87	5.2
EPIC201132839	2458650.811695	-1.57	5.4
EPIC247537447	2458350.113872	110.69	4.87
EPIC247537447	2458351.110087	44.22	5.27
EPIC247537447	2458361.133772	85.30	4.55
EPIC247537447	2458367.082792	31.51	6.21
EPIC247537447	2458370.098621	39.17	5.27
EPIC247537447	2458384.082456	91.11	4.56
EPIC247537447	2458386.061454	118.95	5.50
EPIC247537447	2458387.041339	52.49	5.44
EPIC247537447	2458388.087329	31.01	5.38
EPIC247537447	2458389.107495	35.21	5.24
EPIC247537447	2458394.069044	27.49	5.46
EPIC247537447	2458396.078694	56.18	5.18
EPIC247537447	2458396.959548	64.03	6.43
EPIC247537447	2458414.901277	71.90	5.15
EPIC247537447	2458426.94693	25.51	4.61
EPIC247537447	2458426.987905	10.52	4.51
EPIC247537447	2458438.961567	46.06	6.21
EPIC247537447	2458443.928115	39.23	5.30
EPIC247537447	2458462.800733	62.96	4.75
EPIC247537447	2458462.849228	71.74	5.02
EPIC247537447	2458462.900767	18.33	4.42
EPIC247537447	2458476.804221	74.49	5.13
EPIC247537447	2458479.010478	-107.44	4.97
EPIC247537447	2458479.069631	-103.26	4.86
EPIC247537447	2458490.799959	-16.16	6.53
EPIC247537447	2458490.898183	-29.61	5.92
EPIC247537447	2458490.96031	-34.93	6.81
EPIC247537447	2458491.811216	86.95	4.64
EPIC247537447	2458491.897936	-173.83	4.52
EPIC247537447	2458508.873645	-105.23	4.82
EPIC247537447	2458508.939682	-62.81	5.00
EPIC247537447	2458509.732192	23.87	5.20
EPIC247537447	2458528.794739	-96.24	5.78
EPIC247537447	2458528.902877	-28.98	8.57

Continued on next page

Table 6.1 – continued from previous page

Star	BJD	RV (m s^{-1})	Prec. (m s^{-1})
EPIC247537447	2458532.734033	-104.44	5.21
EPIC247537447	2458532.838364	-79.53	5.54
EPIC247537447	2458532.8933	-41.19	6.49
EPIC247537447	2458532.897525	-85.35	14.94
EPIC247537447	2458559.726318	-91.98	4.96
EPIC247537447	2458559.782238	-66.56	5.78
EPIC247537447	2458559.838795	-60.14	5.52
EPIC247537447	2458569.742523	-109.99	4.72

6.2.1 K2-161

K2-161 was identified as the host of a validated planet by Mayo et al. (2018), and was subsequently analyzed and confirmed through the reasoning presented in Section 5.4.1 of this document. This system was initially thought to be a ~ 0.5 R_J planet orbiting a subgiant star. However, additional processing of the stellar light curve uncovered asteroseismic oscillations, which revealed the star to be a LLRGB star. This meant that the planet had to be much larger, and was found to be 1.5 R_J in our subsequent analysis (see Figure 5.6). Here, we present additional radial velocity followup of this target which allows us to identify a Keplerian signal in the data with the same orbital period and expected phase offset from the transit observation using the Python package `radvel` (Fulton et al. 2018). 17 radial velocity observations of this target were taken between January 7 and June 16, 2019 using the high-resolution echelle spectrometer (HIRES) on the Keck-I telescope on Maunakea. These radial velocity observations were determined by observing the stellar spectrum through an iodine gas cell for reference. These measurements have revealed moderate evidence for a Keplerian signal due to the pull of the planet K2-161b on its host star. Though additional radial velocity measurements will be necessary to constrain the mass of this planet, as the relatively weak Keplerian signal, large stellar variability and faintness of this target limit the precision of our measurements, we can place an upper limit on the mass of this planet of 75 $M_\oplus$, or roughly 0.25 M_J, making K2-161b the most inflated planet found to be transiting an LLRGB star known to date. We present the radial velocity observations of this target, along with the best-fit Keplerian semi-amplitude, orbital period, and eccentricity in Figure 6.3. Due to the currently unconstrained planet parameters in this system, we do not consider this system in our study determining stellar RV variability in red giant stars outlined below.

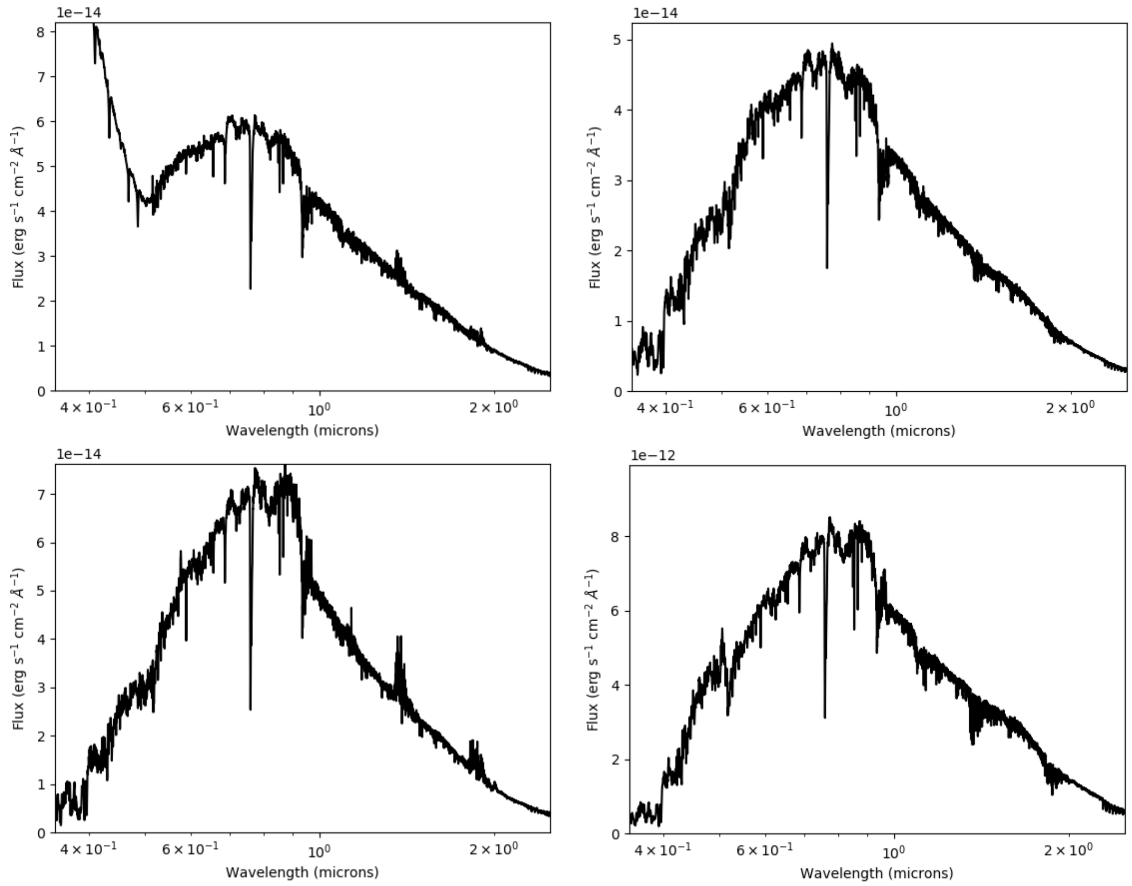

Figure 6.2 UH88/SNIFS and IRTF/SpeX spectra of EPIC211539813 (upper left), EPIC201115468 (upper right), EPIC211467466 (lower left), and HD175884 (lower right). The three EPIC stars are low luminosity red giant branch stars observed by *K2*, organized from smallest to largest, while the fourth star is a bright red giant star which has been observed interferometrically by the CHARA array. The UH88/SNIFS spectra have been joined to the IRTF/SpeX spectra at 0.95 μm. The blue channel of the SNIFS spectrum ($\lambda < 0.5\mu$m) shows strange discrepancies in the EPIC211429813 spectrum, but since the spectral peak is always redward of this channel, it has a minimal effect on our spectral fitting. Now that the stellar spectra have been flux normalized, accurate bolometric fluxes and temperatures can be computed, giving angular diameters to compare to CHARA interferometric measurements (for HD175884) and radii to compare to asteroseismic measurements (for the EPIC stars).

6.2.2 Exploring the RV jitter of red giant stars

One of the main challenges to measuring precise masses of extrasolar planets is that many stars exhibit Doppler noise with an amplitude comparable to or larger than the radial-velocity (RV) signal of the planet (e.g., Haywood et al. 2014; Grunblatt et al. 2015). This RV 'jitter' of the star may be correlated to coherent phenomena, such as spot crossings induced by magnetic activity, or

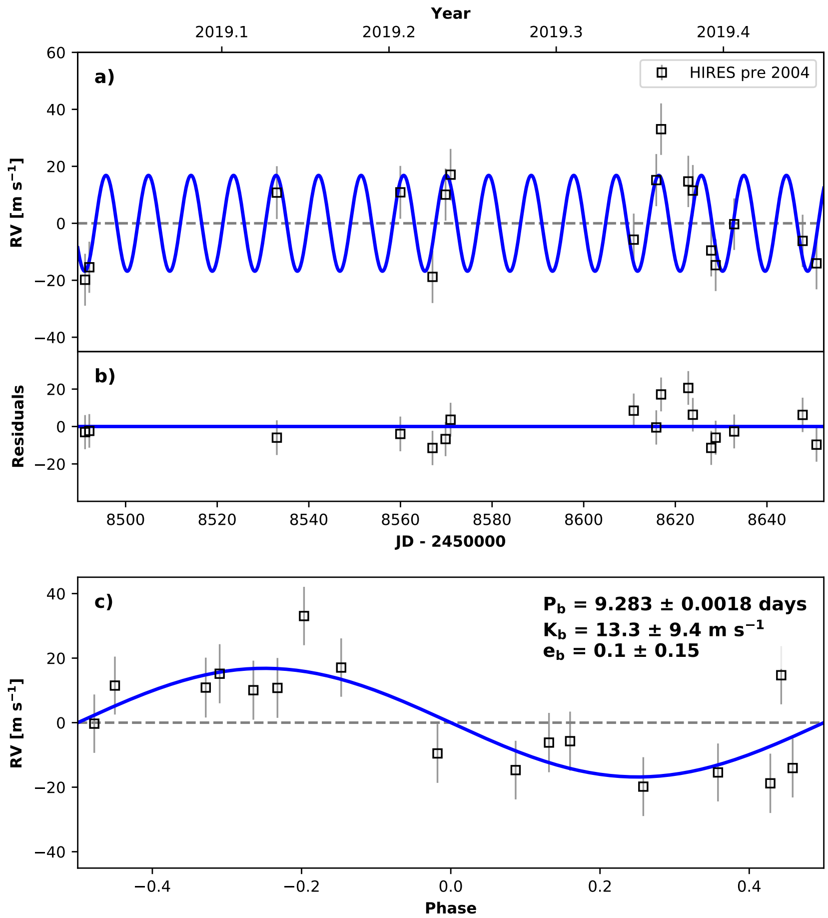

Figure 6.3 Radial velocity observations of K2-161 obtained between January 7 and June 16, 2019. These observations reveal a tentative Keplerian signal at the orbital period of K2-161, with a semi-amplitude of 13.3 ± 9.4 m s^{-1}. This implies an upper limit on the mass of K2-161b of $\sim$ 0.25 M_J, or $\sim$ 75 $M_\oplus$.

less coherent processes that are more poorly understood. Such signals are of particular concern for the detection of planets around red giant stars, where RV jitter has been observed in stars even without clear magnetic activity (Arentoft et al. 2019). This jitter is likely due to solar-like oscillations and granulation of the star's surface. Understanding the RV signal produced by these processes is essential to detecting Earth-like planets around Sun-like stars (Dumusque 2016). However, these signals have not yet been clearly decoupled from Earth-like planetary signals in radial velocity time-series of G-type main sequence stars or the Sun (Collier Cameron et al. 2019). Thus, red giant stars represent one of the few laboratories to understand properties of oscillation and granulation

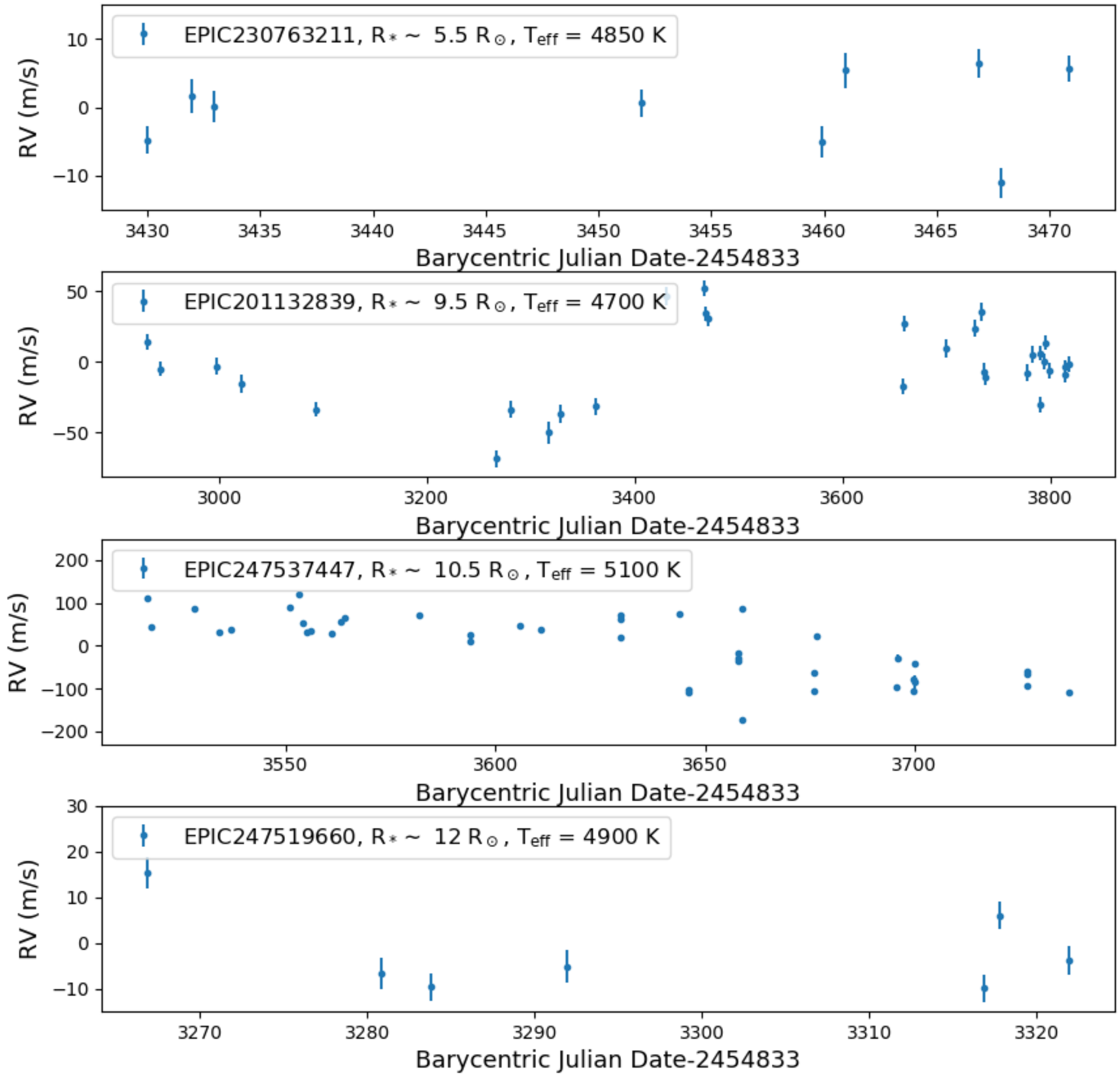

Figure 6.4 Radial velocity as a function of time for four red giant stars ranging from 5.5-12 $R_\odot$, observed by the *K2* mission. Observations have been taken between January 10, 2017 and June 16, 2019 using the HIRES spectrograph on the Keck-1 telescope on Mauna Kea. These four stars displays a wide range in stellar variability, with rms values of 6 to greater than 70 m s^{-1} over 6 months. Only one of the four stars is in agreement with theoretical predictions for its radial velocity jitter. Additionally, one of the stars, EPIC201132839, displays periodicity on long term timescales, which may be indicative of an non-transiting giant planet on a long-period orbit. Such a scenario is likely influencing the observed RV jitter of this star and potentially inflating it on long timescales.

congruently with planetary properties in currently obtainable radial velocity measurements. In addition, theories to predict RV stellar jitter in these stars have been proposed, but a large sample of RV targets covering the timescales of both oscillation and granulation in these stars has not yet been produced (Bastien et al. 2014; Yu et al. 2018; Tayar et al. 2018). A sample of red giant stars with photometric and radial velocity measurements taken over various timescales is essential to understanding RV jitter in solar-like oscillators.

Sample Selection

We obtained over 100 radial velocity observations of 4 LLRGB stars observed as part of our *K2* programs to characterize giants planets orbiting giant stars ranging from ~ 5.5 $R_\odot$ to ~ 12 $R_\odot$ in size with the high resolution spectrograph HIRES on board the 10-meter Keck-I telescope on Maunakea. These stars were selected for radial velocity observations as high priority targets selected by eye as part of our transiting planet search around evolved stars with *K2*. However, the signal-to-noise ratio in all of these systems was more than 5 times lower than that of the confirmed transiting planets in our survey. Perhaps unsurprisingly, none of these stars display periodicity at the measured transit period in our BLS search of these light curves. This implies that the transit signals found in these light curves were either false positives or the mass of the transiting planets observed in these systems is too low to warrant detection above the observed stellar variability in these stars. It also implies that the variability seen in these light curves is either due to the star itself or previously unseen, non-transiting planets in these systems, both of which are valuable results for this project. We present the radial velocity time series of our four targets in Figure 6.4. We note that while all four stars display wildly different degrees of variability in RV measurements, EPIC201132839 also seems to display long-term periodicity, indicative of a potentially non-transiting giant planet on a $\sim$700-day orbit around this star.

Comparison to Model Predictions

Tayar et al. (2018) predicts that as stars ascend the red giant branch, their stellar RV jitter should increase following the flicker-jitter relation of (Bastien et al. 2014). They predict a jitter of 5-10 m s^{-1} for stars below a $\log(g) = 3.0$, corresponding to a stellar radius of $\sim$5 $R_\odot$, and jitter values up to 20 m s^{-1} for stars up to ~ 10 $R_\odot$. We compare these predictions to our observations, and find that while this seems to describe stars at or below 6 $R_\odot$ without significant disagreement, both of the larger stars in our sample display RV jitter values which are significantly higher than predicted for their size. We illustrate the observed RV jitter of our stars relative to model predictions in Figure

6.5. However, if the long-term periodic signal is removed from EPIC201132839, its stellar variability is more in line with model predictions as well. EPIC247537447 displays an rms variability of 70 m s^{-1}, more than three times what is predicted for stars of its surface gravity. This variability does not display any periodicity and thus cannot be brought into agreement with model predictions using any periodic models.

As planets can also produce RV signatures of this strength, it is important to rule out a planetary hypothesis for these RV variations. To do so, we use the radial velocity orbit prediction software `radvel` (Fulton et al. 2018). This software is unable to converge to a final orbit for any of these systems, indicating that a single-planet planetary solution cannot explain the RV variability seen in these stars. In addition, the night-to-night variation seen in the more variable systems would imply a very massive planet on a short orbit, which is clearly not supported by the data.

Continued followup of these targets may reveal additional long-term periodic variability in some of these systems. In addition, more detailed analysis of the timescales of variability will allow us to measure stellar granulation and oscillation signals in radial velocities, and compare them to the observed signals seen in photometry. This will allow us to extend the observed relations between photometric flicker and RV jitter to a wider range of stars, and determine its dependence on specific types of stellar variability, whether due to granulation, oscillations, or orbiting planets. This will be used to produce a combined model to measure stellar variability and planetary orbits simultaneously using photometric and radial velocity data. This combined model is essential for detecting earth-like planet around Sun-like stars with future instruments such as *PLATO*.

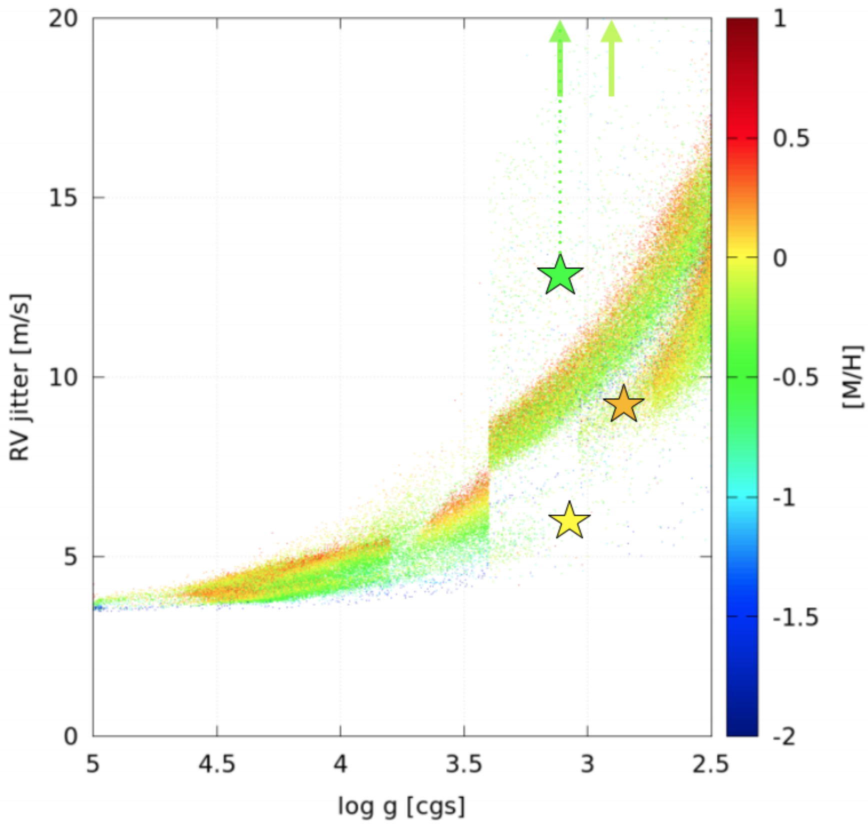

Figure 6.5 Radial velocity jitter predicted as a function of surface gravity for dwarfs and giant stars, taken from Tayar et al. (2018). Predictions are based on the observations of (Bastien et al. 2014). The radial velocity rms of stars observed by this study are shown as stars and arrows on this plot. Only one of the four stars discussed here clearly seems to closely follow the predicted and observed RV jitter trend, EPIC247519660 (orange star). EPIC230763211 (yellow star) seems slightly low relative to model predictions. EPIC201132839 (green arrow) lies far above the predicted trend. When long-term periodicity is removed from its RV measurements, it lies closer, but still above, the predicted trend (green star). EPIC247537447 (yellow-green arrow) displays no periodicity and lies above the predicted RV jitter curve by a factor of 6.

Chapter 7

Conclusion

Over the course of this thesis, I have determined the unique properties of planets orbiting evolved stars, performed asteroseismology of thousands of potential host stars in order to characterize their planet population accurately, and used Gaussian process regression to describe and model stellar variability in these systems to obtain the best possible stellar and planet parameters. While this work has provided clear advancements in our understanding of this population (see Figure 7.1), future facilities will lead to many more scientific discoveries in this subfield. I outline my main results and potential for future explorations below.

7.1 Thesis Results

7.1.1 Understanding planet re-inflation

In Chapters 2 and 3, I described the discovery and characterization of two gas giant planets discovered around red giant stars. **These planets were both larger than their main sequence counterparts, implying late stage planet re-inflation is a common process among close-in giant planets orbiting evolved stars (Lopez & Fortney 2016)**. Additional planet discoveries around evolved stars also support this hypothesis (Chapter 5, Huber et al. 2019). However, understanding the efficiency of re-inflation will require the detection of a wider mass, radius, and orbital period range of planets than were observed by *K2*. In addition, Chapter 2 revealed that different systematics treatment of *K2* light curves can dilute planet transits by up to 30%, dominating planet radius uncertainties. The development of new light curve detrending software is essential for detecting and accurately characterizing low signal-to-noise transits, as is often the case for planets transiting giant stars.

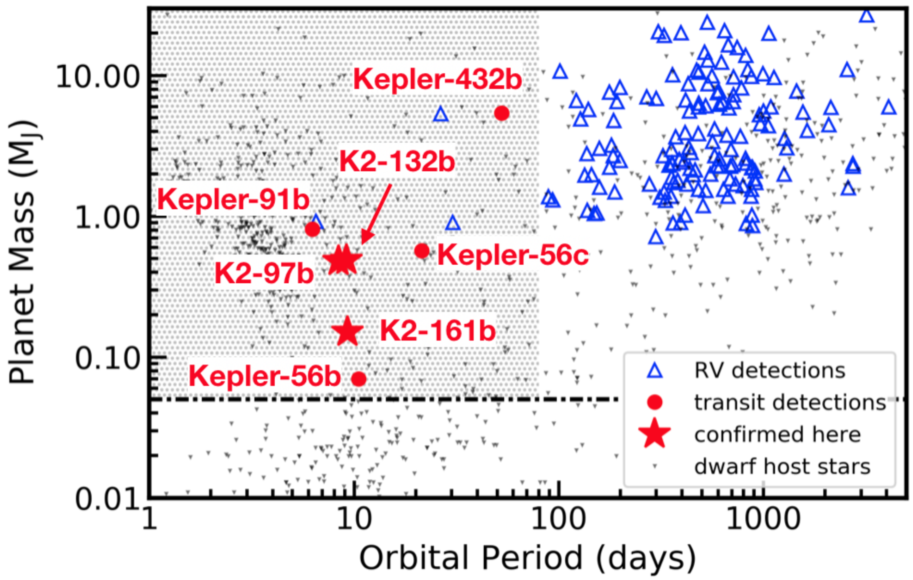

Figure 7.1 Planet mass versus orbital period for the main sequence and evolved star populations known at the completion of this thesis. Planets orbiting evolved stars ($R_* > 3.5\ R_\odot$, $T_{\mathrm{eff},*} < T_{\mathrm{eff},\odot}$) are designated in color, with blue triangles representing planets found using the radial velocity method, and red circles representing planets found via the transit method. Planets known orbiting main sequence stars are shown as black dots. The shaded region roughly corresponds to the region of sensitivity of past and current photometric searches for planet transits. This thesis has doubled the number of known transiting evolved planetary systems.

TESS will eventually detect tens to hundreds of these planets around hundreds of thousands of bright red giant stars throughout the sky (Barclay et al. 2018), more than an order of magnitude more red giants than were observed by *Kepler* and *K2* combined. This distribution of star and planet parameters will allow investigation of evolutionary properties of both planets and stars with unprecedented precision. The brightest of these targets will be some of the best potential targets for transmission spectroscopy with JWST, with large atmospheric scale heights and long duration transits, ideal for understanding atmospheric physics of planet inflation (Thorngren et al. 2015).

7.1.2 Close-in giant planets orbiting evolved stars prefer moderately eccentric orbits

Chapter 4 explores the evidence for a preference for moderately eccentric orbits in the close-in planet population around red giant stars, an effect which has been predicted by theory of planet evolution and eventual inspiral (Villaver et al. 2014). **This chapter shows that the**

known population of close-in giant planets orbiting giant stars displays a preference for moderate eccentricities. This implies planets circularize more quickly than they inspiral and eventually become engulfed by red giant stars. In order to understand the orbital dynamics of evolved planetary systems, radial velocity follow-up measurements are necessary from ground-based facilities. In the era of *Kepler/K2*, this was limited to the largest class of ground-based telescopes. However, the average brightness of *TESS* targets should be 100 times the brightness of a *Kepler* target, allowing follow-up with smaller apertures. In addition, the commissioning of multiple precision radial velocity instruments such as NEID, SpiROU, PARVI, MAROON-X and others in the near future will allow precise orbital characterization of a much larger population of evolved planetary systems than is currently known.

7.1.3 Close-in giant planets are as common around LLRGB stars as around their main sequence counterparts

In Chapter 5, I compared the occurrence of giant planets within 0.2 AU of their host stars around evolved stars to the same population of planets around main sequence stars. **Planet occurrences between main sequence and evolved systems agree within uncertainties, implying that planets are not destroyed by stellar evolution before the start of the red giant phase.** This is in contrast to earlier theories, as well as observational studies, which have predicted and found a dearth of close-in planets around evolved stars, believed to be evidence for rapid orbital evolution as host stars ascend the red giant branch (Villaver et al. 2014; Jones et al. 2016). This difference in result highlights the need to explore additional systems and employ various detection methods to characterize the planet population of evolved stars precisely.

Surveys of a much larger population of red giant stars with *TESS* will confirm or deny this result. During the primary mission duration of two years, *TESS* will record full-frame images of more than 90% of the observable sky every 30 minutes for at least 27 days (Ricker et al. 2014). Being 10-100 times brighter than *Kepler* targets and distributed over a solid angle that is nearly 300 times larger, *TESS* host stars will be well suited for follow-up spectroscopy. Thus, the *TESS* survey will be able to detect similar planets around bright LLRGB stars across the entire sky, likely revealing hundreds of new planets around evolved stars. This population will reveal greater details of the effects of evolution on planetary systems, and the correlations between evolution and stellar and planet properties.

Though red giant stars have lived full lives, they undoubtedly have many stories left to share with their cosmic grandchildren.

Appendix A

Appendix A: Full Table 5.1

We reproduce the full table 5.1 for all 2476 stars in our analysis here. Stellar masses and radii have been derived from asteroseismic scaling relations and effective temperatures determined using the González Hernández & Bonifacio (2009) color-$T_{\rm eff}$ relation. We note that uncertainties on $T_{\rm eff}$ are 94 K for all stars in our sample, based on the González Hernández & Bonifacio (2009) color-$T_{\rm eff}$ relation used in this analysis.

Table A.1: Asteroseismic Stellar Parameters

EPIC ID	$\nu_{\rm max}$ **(μHz)**	$\Delta\nu$ **(μHz)**	**Radius ($R_\odot$)**	**Mass ($M_\odot$)**	$T_{\rm eff}$ **(K)**
201089316	167.95 ± 1.14	13.78 ± 0.14	4.71 ± 0.11	1.11 ± 0.04	4875
201091253	116.82 ± 0.38	10.39 ± 0.09	5.71 ± 0.13	1.13 ± 0.04	4916
201092039	161.69 ± 1.87	13.95 ± 0.12	4.47 ± 0.11	0.96 ± 0.04	4946
201094853	132.25 ± 0.51	12.02 ± 0.18	4.91 ± 0.14	0.94 ± 0.04	4711
201102783	60.11 ± 0.77	6.24 ± 0.05	7.98 ± 0.2	1.12 ± 0.05	4793
201106507	191.07 ± 1.04	15.83 ± 0.13	4.27 ± 0.09	1.05 ± 0.04	5376
201115468	182.59 ± 1.65	15.09 ± 0.06	4.4 ± 0.09	1.06 ± 0.04	4999
201121245	198.13 ± 1.94	16.11 ± 0.08	4.15 ± 0.09	1.02 ± 0.04	4821
201124695	81.26 ± 0.84	8.18 ± 0.13	6.59 ± 0.2	1.05 ± 0.05	4902
201125915	181.15 ± 2.69	14.63 ± 0.19	4.65 ± 0.13	1.18 ± 0.06	5121
201126489	225.25 ± 1.84	17.15 ± 0.03	4.21 ± 0.08	1.2 ± 0.04	4969
201127658	213.2 ± 1.76	16.6 ± 0.29	4.24 ± 0.13	1.15 ± 0.05	5043
201128072	169.96 ± 1.0	13.64 ± 0.1	4.98 ± 0.11	1.27 ± 0.04	4953
201131490	271.56 ± 10.75	19.32 ± 0.13	3.94 ± 0.17	1.26 ± 0.1	4992
201136855	61.93 ± 1.16	6.28 ± 0.05	7.96 ± 0.23	1.14 ± 0.06	4642
201139015	215.31 ± 1.68	17.61 ± 0.23	3.98 ± 0.11	1.05 ± 0.04	5031
201145260	132.77 ± 1.38	11.8 ± 0.1	5.25 ± 0.12	1.1 ± 0.04	5070
201145884	126.86 ± 0.92	11.02 ± 0.13	5.7 ± 0.14	1.24 ± 0.05	4960
201155755	178.95 ± 2.48	15.23 ± 0.09	4.3 ± 0.1	0.99 ± 0.04	5061
201157745	188.61 ± 1.32	14.57 ± 0.06	4.67 ± 0.09	1.22 ± 0.04	4985
201160696	228.07 ± 4.64	17.45 ± 0.2	3.99 ± 0.13	1.08 ± 0.06	4932
201161185	70.98 ± 1.87	7.98 ± 0.11	6.27 ± 0.23	0.84 ± 0.05	4914
201168216	133.2 ± 1.35	11.13 ± 0.1	5.54 ± 0.13	1.2 ± 0.05	4821
201168250	162.95 ± 2.16	13.38 ± 0.06	4.74 ± 0.11	1.08 ± 0.04	4833
201171671	109.13 ± 2.85	10.29 ± 0.08	5.66 ± 0.19	1.04 ± 0.06	5120
201184886	78.29 ± 0.64	7.96 ± 0.05	6.94 ± 0.15	1.15 ± 0.04	5108
201186064	76.64 ± 0.88	7.47 ± 0.06	7.11 ± 0.17	1.14 ± 0.05	4803
201196426	216.11 ± 1.45	16.73 ± 0.13	4.12 ± 0.09	1.09 ± 0.04	4973

Continued on next page

Table A.1 – continued from previous page

EPIC ID	$\nu_{\max}$ (μHz)	$\Delta\nu$ (μHz)	Radius ($R_\odot$)	Mass ($M_\odot$)	$T_{\rm eff}$ (K)
201197836	190.48 ± 1.57	15.22 ± 0.03	4.39 ± 0.09	1.09 ± 0.04	4674
201200834	98.45 ± 1.13	8.95 ± 0.11	6.46 ± 0.18	1.22 ± 0.05	4924
201204296	93.99 ± 0.72	8.7 ± 0.06	6.65 ± 0.14	1.24 ± 0.04	4895
201205335	226.74 ± 0.82	17.2 ± 0.05	4.12 ± 0.08	1.15 ± 0.04	4917
201208229	99.22 ± 0.39	9.14 ± 0.05	6.17 ± 0.12	1.11 ± 0.04	4890
201211051	182.78 ± 0.77	15.03 ± 0.05	4.49 ± 0.08	1.11 ± 0.03	5077
201211472	231.7 ± 1.13	17.27 ± 0.06	4.35 ± 0.08	1.33 ± 0.04	4997
201213694	163.5 ± 1.15	12.01 ± 0.06	6.21 ± 0.12	1.91 ± 0.06	4955
201217382	168.95 ± 1.45	14.3 ± 0.3	4.59 ± 0.16	1.07 ± 0.06	5184
201228791	71.33 ± 0.19	7.02 ± 0.03	7.71 ± 0.15	1.26 ± 0.04	4874
201231064	217.63 ± 0.91	16.8 ± 0.04	4.12 ± 0.07	1.1 ± 0.03	5023
201233864	68.68 ± 0.39	6.82 ± 0.03	7.78 ± 0.15	1.23 ± 0.04	4700
201237594	75.82 ± 0.66	7.64 ± 0.11	7.26 ± 0.21	1.21 ± 0.05	5126
201239524	291.83 ± 1.09	20.41 ± 0.14	3.76 ± 0.08	1.23 ± 0.04	4926
201240269	138.55 ± 1.02	11.66 ± 0.07	5.26 ± 0.11	1.13 ± 0.04	4707
201249467	92.5 ± 0.7	8.85 ± 0.06	6.48 ± 0.14	1.17 ± 0.04	5064
201257461	135.74 ± 3.42	11.13 ± 0.07	5.67 ± 0.18	1.29 ± 0.07	4900
201257567	186.03 ± 1.13	14.1 ± 0.06	5.01 ± 0.1	1.39 ± 0.05	4904
201260655	210.23 ± 1.27	16.49 ± 0.13	4.16 ± 0.09	1.09 ± 0.04	5006
201260990	225.55 ± 1.77	16.76 ± 0.05	4.33 ± 0.09	1.27 ± 0.04	4947
201262663	225.03 ± 2.51	16.6 ± 0.35	4.39 ± 0.16	1.3 ± 0.07	5004
201264098	208.74 ± 0.96	16.36 ± 0.18	4.25 ± 0.1	1.13 ± 0.04	5030
201264806	93.72 ± 0.6	9.1 ± 0.11	6.06 ± 0.15	1.02 ± 0.04	4821
201265393	206.37 ± 0.85	14.4 ± 0.11	5.4 ± 0.11	1.82 ± 0.06	5048
201269396	172.53 ± 1.68	14.09 ± 0.09	4.69 ± 0.1	1.13 ± 0.04	5002
201269514	115.28 ± 0.5	10.15 ± 0.04	5.93 ± 0.11	1.2 ± 0.04	4952
201280281	272.61 ± 1.13	19.38 ± 0.04	3.77 ± 0.07	1.14 ± 0.04	4944
201284959	86.74 ± 0.74	8.23 ± 0.03	6.85 ± 0.14	1.21 ± 0.04	4937
201294827	139.45 ± 0.91	12.28 ± 0.15	4.99 ± 0.13	1.03 ± 0.04	4763
201307454	227.25 ± 1.0	17.32 ± 0.13	4.12 ± 0.09	1.16 ± 0.04	4927
201310086	100.72 ± 1.27	9.7 ± 0.06	6.07 ± 0.14	1.13 ± 0.04	5056
201313053	201.13 ± 1.09	16.2 ± 0.08	4.2 ± 0.08	1.06 ± 0.04	4942
201318590	92.86 ± 0.66	8.46 ± 0.04	6.64 ± 0.14	1.2 ± 0.04	4740
201320989	148.47 ± 1.13	12.97 ± 0.07	4.98 ± 0.1	1.12 ± 0.04	5049
201324469	267.79 ± 10.31	19.11 ± 0.12	4.01 ± 0.17	1.29 ± 0.1	5220
201324905	108.38 ± 1.01	10.17 ± 0.06	5.51 ± 0.12	0.97 ± 0.04	4724
201328052	93.13 ± 0.99	8.48 ± 0.06	6.8 ± 0.15	1.28 ± 0.05	4816
201336009	151.38 ± 1.05	12.44 ± 0.05	5.14 ± 0.1	1.18 ± 0.04	4786
201340219	78.27 ± 0.57	7.19 ± 0.08	7.86 ± 0.2	1.42 ± 0.06	4758
201342689	196.91 ± 5.92	15.91 ± 0.37	4.36 ± 0.21	1.13 ± 0.09	5093
201350252	65.28 ± 0.35	6.62 ± 0.06	7.85 ± 0.17	1.19 ± 0.04	4946
201351994	145.66 ± 1.04	12.68 ± 0.06	4.91 ± 0.1	1.05 ± 0.04	4875
201356060	243.98 ± 2.85	16.61 ± 0.06	4.58 ± 0.1	1.51 ± 0.06	4827
201356916	155.26 ± 1.24	12.67 ± 0.02	5.16 ± 0.1	1.23 ± 0.04	4959
201365210	155.52 ± 1.32	13.26 ± 0.09	4.85 ± 0.11	1.1 ± 0.04	4914
201370145	83.89 ± 1.5	8.4 ± 0.11	6.37 ± 0.2	1.01 ± 0.05	4769
201371295	185.58 ± 1.79	15.43 ± 0.03	4.28 ± 0.09	1.02 ± 0.04	5041
201371519	124.3 ± 2.14	10.53 ± 0.05	5.91 ± 0.15	1.29 ± 0.06	4916
201375436	140.14 ± 0.99	11.85 ± 0.05	5.1 ± 0.1	1.07 ± 0.04	4812
201379069	88.6 ± 0.85	8.1 ± 0.08	6.8 ± 0.17	1.19 ± 0.05	4742
201382898	78.34 ± 0.5	7.44 ± 0.06	7.58 ± 0.17	1.34 ± 0.05	4911
201387126	70.95 ± 0.63	6.82 ± 0.07	7.94 ± 0.19	1.32 ± 0.05	4632
201391174	98.4 ± 0.66	9.23 ± 0.07	6.38 ± 0.14	1.21 ± 0.04	4885
201394249	90.18 ± 0.75	8.2 ± 0.1	7.14 ± 0.19	1.37 ± 0.06	4711
201394607	250.48 ± 4.24	17.19 ± 0.1	4.65 ± 0.12	1.64 ± 0.07	5103
201400409	106.69 ± 0.9	9.66 ± 0.16	5.84 ± 0.17	1.06 ± 0.05	4980
201401038	162.06 ± 1.04	12.92 ± 0.09	5.15 ± 0.11	1.28 ± 0.04	4975
201405480	98.71 ± 1.24	10.1 ± 0.08	5.6 ± 0.13	0.95 ± 0.04	5175
201406921	173.3 ± 0.37	13.92 ± 0.04	4.9 ± 0.09	1.25 ± 0.04	4853
201408413	133.01 ± 0.73	11.27 ± 0.04	5.74 ± 0.11	1.32 ± 0.04	5211
201419689	117.19 ± 1.07	10.49 ± 0.02	5.69 ± 0.11	1.13 ± 0.04	4912

Continued on next page

Table A.1 – continued from previous page

EPIC ID	$\nu_{\max}$ (μHz)	$\Delta\nu$ (μHz)	Radius ($R_\odot$)	Mass ($M_\odot$)	$T_{\rm eff}$ (K)
201420000	187.45 ± 2.65	15.09 ± 0.06	4.48 ± 0.1	1.12 ± 0.04	5102
201423287	155.87 ± 2.21	12.55 ± 0.17	5.09 ± 0.15	1.18 ± 0.06	4960
201423959	89.15 ± 0.69	8.41 ± 0.12	6.78 ± 0.19	1.23 ± 0.05	4877
201429788	236.04 ± 3.9	17.36 ± 0.07	4.09 ± 0.1	1.17 ± 0.05	4881
201430487	235.18 ± 0.99	17.68 ± 0.06	3.91 ± 0.07	1.06 ± 0.03	4735
201430517	74.52 ± 0.53	7.03 ± 0.1	7.58 ± 0.21	1.25 ± 0.05	4733
201431429	117.19 ± 1.22	11.02 ± 0.1	5.5 ± 0.13	1.08 ± 0.04	5264
201431499	90.29 ± 0.64	8.19 ± 0.1	6.87 ± 0.18	1.25 ± 0.05	4813
201433687	113.5 ± 0.76	10.3 ± 0.03	5.68 ± 0.11	1.09 ± 0.04	4927
201436237	63.76 ± 0.62	6.41 ± 0.04	7.69 ± 0.17	1.09 ± 0.04	4904
201440668	75.97 ± 0.55	7.43 ± 0.2	7.03 ± 0.3	1.1 ± 0.07	5072
201442238	117.38 ± 0.62	10.8 ± 0.05	5.68 ± 0.11	1.15 ± 0.04	5135
201448860	259.53 ± 0.0	18.66 ± 0.08	4.03 ± 0.07	1.26 ± 0.04	4999
201451661	227.36 ± 2.46	18.57 ± 0.32	3.74 ± 0.12	0.97 ± 0.05	5192
201452729	118.62 ± 2.07	10.38 ± 0.04	5.72 ± 0.14	1.14 ± 0.05	4903
201453044	129.28 ± 1.56	11.37 ± 0.22	5.46 ± 0.19	1.16 ± 0.06	5073
201453981	85.85 ± 1.17	8.29 ± 0.07	6.46 ± 0.16	1.05 ± 0.04	4834
201458444	82.16 ± 0.78	8.42 ± 0.05	6.37 ± 0.14	1.0 ± 0.04	5035
201459314	116.34 ± 1.14	10.49 ± 0.08	5.55 ± 0.13	1.06 ± 0.04	4907
201461166	144.39 ± 2.05	13.31 ± 0.28	4.53 ± 0.17	0.89 ± 0.05	5105
201461467	132.0 ± 1.22	11.41 ± 0.05	5.42 ± 0.11	1.15 ± 0.04	4982
201462337	115.82 ± 0.97	10.46 ± 0.05	5.5 ± 0.11	1.03 ± 0.04	4795
201464249	134.35 ± 0.77	11.33 ± 0.09	5.43 ± 0.12	1.17 ± 0.04	4898
201465015	175.77 ± 1.16	14.84 ± 0.06	4.58 ± 0.09	1.13 ± 0.04	5074
201467033	209.36 ± 1.06	15.78 ± 0.09	4.73 ± 0.09	1.43 ± 0.05	5244
201468901	90.04 ± 1.04	8.45 ± 0.04	6.77 ± 0.15	1.23 ± 0.05	5030
201469205	114.19 ± 0.98	9.9 ± 0.1	6.02 ± 0.15	1.22 ± 0.05	4973
201473281	212.93 ± 1.34	15.99 ± 0.04	4.35 ± 0.08	1.19 ± 0.04	4817
201474238	158.84 ± 1.01	12.31 ± 0.04	5.61 ± 0.11	1.5 ± 0.05	4939
201477477	71.37 ± 0.86	7.11 ± 0.05	7.11 ± 0.17	1.05 ± 0.04	4718
201478150	187.02 ± 0.95	15.13 ± 0.06	4.55 ± 0.09	1.17 ± 0.04	5114
201478323	65.75 ± 0.49	6.59 ± 0.06	7.96 ± 0.19	1.23 ± 0.05	4928
201487929	79.4 ± 0.8	7.59 ± 0.07	7.08 ± 0.17	1.17 ± 0.05	4875
201490840	169.67 ± 0.96	14.21 ± 0.03	4.71 ± 0.09	1.14 ± 0.04	5046
201491210	135.88 ± 0.8	11.71 ± 0.07	5.23 ± 0.11	1.1 ± 0.04	4850
201494732	182.57 ± 1.33	15.31 ± 0.03	4.27 ± 0.08	0.99 ± 0.03	4873
201497749	232.73 ± 1.93	15.89 ± 0.29	4.99 ± 0.16	1.75 ± 0.09	5122
201500806	191.3 ± 1.29	15.56 ± 0.03	4.42 ± 0.08	1.13 ± 0.04	5237
201501574	91.66 ± 0.59	8.84 ± 0.19	6.37 ± 0.22	1.11 ± 0.06	5029
201503518	148.86 ± 0.82	12.33 ± 0.05	5.04 ± 0.1	1.11 ± 0.04	4996
201504400	112.61 ± 0.7	10.28 ± 0.04	5.67 ± 0.11	1.07 ± 0.03	5055
201504843	190.69 ± 1.44	14.29 ± 0.06	5.05 ± 0.1	1.46 ± 0.05	5293
201509931	72.97 ± 1.21	7.61 ± 0.14	6.8 ± 0.24	1.0 ± 0.05	5114
201512449	100.15 ± 1.08	9.24 ± 0.23	6.61 ± 0.27	1.33 ± 0.08	5151
201518675	206.28 ± 1.28	16.66 ± 0.11	3.89 ± 0.08	0.92 ± 0.03	4843
201520290	77.6 ± 0.58	7.37 ± 0.05	7.21 ± 0.16	1.17 ± 0.04	4818
201521671	132.27 ± 0.71	10.27 ± 0.07	6.67 ± 0.14	1.76 ± 0.06	5049
201521916	149.28 ± 1.87	12.61 ± 0.16	5.06 ± 0.14	1.14 ± 0.05	4971
201524971	121.11 ± 2.15	11.54 ± 0.29	5.03 ± 0.22	0.91 ± 0.06	5123
201533621	89.61 ± 0.54	8.59 ± 0.05	6.34 ± 0.13	1.06 ± 0.04	4816
201535193	213.04 ± 1.53	16.17 ± 0.05	4.24 ± 0.08	1.13 ± 0.04	4854
201549591	244.19 ± 3.61	20.23 ± 0.26	3.31 ± 0.1	0.79 ± 0.04	4793
201553565	99.01 ± 0.78	9.23 ± 0.05	6.19 ± 0.13	1.13 ± 0.04	4945
201557804	84.44 ± 0.58	8.01 ± 0.05	7.17 ± 0.15	1.3 ± 0.05	4881
201560488	139.1 ± 2.07	12.17 ± 0.03	5.03 ± 0.12	1.05 ± 0.04	4901
201571570	139.88 ± 0.65	12.34 ± 0.13	5.17 ± 0.12	1.14 ± 0.04	5178
201577272	135.16 ± 0.83	11.87 ± 0.12	5.17 ± 0.12	1.08 ± 0.04	5006
201577725	86.75 ± 1.31	8.26 ± 0.05	6.9 ± 0.17	1.24 ± 0.05	4970
201579693	141.51 ± 0.74	12.17 ± 0.05	5.11 ± 0.1	1.1 ± 0.04	4806
201580844	108.27 ± 0.6	10.23 ± 0.17	5.58 ± 0.16	1.0 ± 0.05	4978
201581724	125.29 ± 0.61	10.71 ± 0.05	5.83 ± 0.11	1.27 ± 0.04	4988

Continued on next page

Table A.1 – continued from previous page

EPIC ID	$\nu_{\max}$ (μHz)	$\Delta\nu$ (μHz)	Radius ($R_{\odot}$)	Mass ($M_{\odot}$)	T_{eff} (K)
201583607	96.49 ± 0.81	9.1 ± 0.15	6.16 ± 0.19	1.09 ± 0.05	4949
201583796	175.26 ± 0.67	13.61 ± 0.06	4.89 ± 0.09	1.23 ± 0.04	4805
201584014	195.2 ± 1.22	15.17 ± 0.03	4.49 ± 0.09	1.17 ± 0.04	4778
201584223	167.98 ± 0.94	13.86 ± 0.04	4.71 ± 0.09	1.11 ± 0.04	4952
201586336	84.11 ± 1.12	8.29 ± 0.08	6.58 ± 0.17	1.09 ± 0.05	4957
201589246	84.11 ± 0.37	8.22 ± 0.03	6.66 ± 0.13	1.11 ± 0.04	4984
201591424	136.5 ± 0.64	11.82 ± 0.04	5.15 ± 0.1	1.07 ± 0.03	4969
201596742	132.69 ± 0.72	11.65 ± 0.03	5.27 ± 0.1	1.1 ± 0.04	4965
201598925	68.12 ± 0.45	7.23 ± 0.05	7.16 ± 0.15	1.05 ± 0.04	5011
201600585	131.89 ± 0.83	11.73 ± 0.04	5.28 ± 0.1	1.11 ± 0.04	5190
201604216	101.92 ± 1.16	9.49 ± 0.08	6.08 ± 0.15	1.12 ± 0.05	4784
201607493	121.61 ± 0.89	10.42 ± 0.03	5.89 ± 0.11	1.25 ± 0.04	4860
201607541	148.61 ± 1.66	12.11 ± 0.08	5.44 ± 0.12	1.32 ± 0.05	4893
201607835	226.47 ± 1.65	16.86 ± 0.08	4.37 ± 0.09	1.31 ± 0.04	4917
201610313	171.16 ± 1.23	13.92 ± 0.05	4.79 ± 0.09	1.17 ± 0.04	5083
201615261	144.75 ± 1.0	12.25 ± 0.04	5.07 ± 0.1	1.1 ± 0.04	4853
201619600	96.74 ± 0.49	8.7 ± 0.11	6.81 ± 0.18	1.34 ± 0.05	4833
201621529	112.29 ± 1.3	10.56 ± 0.19	5.58 ± 0.19	1.05 ± 0.05	5107
201622061	75.36 ± 0.72	7.74 ± 0.06	7.03 ± 0.16	1.13 ± 0.04	5111
201622759	180.62 ± 0.89	14.15 ± 0.06	4.72 ± 0.09	1.19 ± 0.04	4786
201624732	118.29 ± 0.69	10.58 ± 0.08	5.83 ± 0.12	1.21 ± 0.04	5017
201626832	151.1 ± 1.55	12.77 ± 0.04	4.9 ± 0.1	1.07 ± 0.04	4913
201637289	70.95 ± 0.39	7.2 ± 0.06	7.23 ± 0.16	1.1 ± 0.04	4755
201640093	187.99 ± 1.26	14.28 ± 0.19	4.92 ± 0.13	1.36 ± 0.06	4930
201642613	61.19 ± 0.44	6.45 ± 0.05	7.86 ± 0.17	1.13 ± 0.04	4934
201643879	148.37 ± 0.58	12.72 ± 0.05	4.99 ± 0.09	1.11 ± 0.04	4904
201644547	99.9 ± 0.68	9.62 ± 0.05	5.88 ± 0.12	1.03 ± 0.04	4792
201648624	56.81 ± 2.07	6.17 ± 0.07	7.79 ± 0.34	1.01 ± 0.07	4830
201654448	197.85 ± 0.81	15.28 ± 0.31	4.43 ± 0.15	1.15 ± 0.06	4848
201655821	165.05 ± 1.23	13.39 ± 0.08	4.89 ± 0.1	1.17 ± 0.04	5066
201657724	155.0 ± 2.18	12.86 ± 0.27	5.04 ± 0.19	1.18 ± 0.07	5170
201658738	83.97 ± 0.72	8.32 ± 0.1	6.54 ± 0.17	1.07 ± 0.04	4999
201659867	72.76 ± 0.71	7.16 ± 0.03	7.3 ± 0.16	1.14 ± 0.04	4796
201662106	226.65 ± 1.29	17.85 ± 0.2	3.96 ± 0.1	1.07 ± 0.04	5083
201668891	184.14 ± 1.06	15.25 ± 0.08	4.28 ± 0.09	1.0 ± 0.03	4886
201675348	94.62 ± 1.22	8.92 ± 0.13	6.18 ± 0.18	1.06 ± 0.05	4800
201678821	212.52 ± 2.07	17.13 ± 0.29	3.92 ± 0.12	0.97 ± 0.05	4845
201685270	264.05 ± 0.8	18.91 ± 0.15	3.99 ± 0.08	1.26 ± 0.04	5021
201689074	73.18 ± 0.64	7.24 ± 0.09	7.55 ± 0.19	1.25 ± 0.05	4942
201689137	74.23 ± 0.46	7.84 ± 0.07	6.69 ± 0.15	1.0 ± 0.04	5042
201692474	159.54 ± 1.21	13.34 ± 0.03	4.85 ± 0.09	1.12 ± 0.04	4981
201695144	104.3 ± 1.06	9.37 ± 0.07	6.09 ± 0.14	1.13 ± 0.04	4908
201695150	108.22 ± 1.27	9.97 ± 0.05	5.61 ± 0.13	1.0 ± 0.04	4811
201696302	185.52 ± 1.11	14.66 ± 0.03	4.61 ± 0.09	1.17 ± 0.04	5007
201704052	129.7 ± 0.81	10.97 ± 0.07	5.86 ± 0.12	1.34 ± 0.05	5026
201704368	201.89 ± 1.52	16.46 ± 0.18	4.04 ± 0.1	0.98 ± 0.04	5007
201705355	186.83 ± 0.94	14.91 ± 0.05	4.61 ± 0.09	1.19 ± 0.04	5000
201709364	136.35 ± 0.89	10.82 ± 0.1	6.22 ± 0.14	1.58 ± 0.06	4987
201717672	175.32 ± 0.97	13.41 ± 0.04	5.09 ± 0.1	1.35 ± 0.04	4921
201717783	68.45 ± 1.05	7.07 ± 0.07	7.33 ± 0.19	1.09 ± 0.05	5017
201719360	229.41 ± 4.07	18.99 ± 0.2	3.54 ± 0.1	0.86 ± 0.04	4982
201720332	201.66 ± 0.96	16.45 ± 0.07	4.13 ± 0.08	1.03 ± 0.03	5049
201722849	212.61 ± 1.69	15.94 ± 0.04	4.61 ± 0.09	1.36 ± 0.05	5020
201725474	78.7 ± 0.49	7.59 ± 0.04	7.37 ± 0.14	1.28 ± 0.04	5119
201729357	108.96 ± 0.75	9.16 ± 0.06	6.55 ± 0.14	1.36 ± 0.05	4772
201730134	119.18 ± 0.62	10.59 ± 0.06	5.55 ± 0.11	1.08 ± 0.04	4948
201732694	277.94 ± 4.17	17.11 ± 0.08	4.96 ± 0.12	2.02 ± 0.08	4804
201733194	155.28 ± 1.89	13.74 ± 0.04	4.56 ± 0.1	0.97 ± 0.04	5039
201734914	235.47 ± 1.38	18.29 ± 0.05	3.91 ± 0.07	1.09 ± 0.04	4918
201741738	137.27 ± 0.82	11.96 ± 0.08	5.12 ± 0.11	1.07 ± 0.04	4920
201741965	233.72 ± 0.95	17.63 ± 0.03	3.98 ± 0.07	1.1 ± 0.03	4905

Continued on next page

Table A.1 – continued from previous page

EPIC ID	$\nu_{\max}$ (μHz)	$\Delta\nu$ (μHz)	Radius ($R_\odot$)	Mass ($M_\odot$)	T_{eff} (K)
201743488	115.79 ± 0.91	10.44 ± 0.04	5.65 ± 0.11	1.1 ± 0.04	4787
201749699	110.68 ± 1.25	10.09 ± 0.03	5.85 ± 0.12	1.13 ± 0.04	4938
201757842	148.45 ± 0.8	12.45 ± 0.04	5.02 ± 0.09	1.1 ± 0.04	5054
201761366	186.25 ± 1.66	14.99 ± 0.13	4.62 ± 0.1	1.2 ± 0.04	5230
201762717	89.07 ± 0.38	8.52 ± 0.09	6.4 ± 0.15	1.08 ± 0.04	4857
201764418	191.04 ± 3.49	14.92 ± 0.32	4.72 ± 0.18	1.28 ± 0.08	5139
201774330	256.0 ± 3.33	19.52 ± 0.05	3.76 ± 0.08	1.1 ± 0.04	4967
201781614	234.13 ± 2.23	17.75 ± 0.05	3.89 ± 0.08	1.04 ± 0.04	4849
201782939	57.64 ± 1.02	6.29 ± 0.04	7.79 ± 0.21	1.04 ± 0.05	4906
201785415	189.03 ± 1.15	15.25 ± 0.08	4.37 ± 0.09	1.07 ± 0.04	5142
201785890	68.79 ± 0.41	7.06 ± 0.04	7.39 ± 0.15	1.12 ± 0.04	5013
201786494	100.95 ± 1.38	9.06 ± 0.16	6.41 ± 0.22	1.22 ± 0.06	5006
201790028	231.55 ± 2.23	17.2 ± 0.1	4.22 ± 0.09	1.23 ± 0.04	5050
201791546	224.42 ± 1.0	17.46 ± 0.06	4.02 ± 0.08	1.08 ± 0.04	4841
201795992	113.41 ± 1.05	10.16 ± 0.1	5.97 ± 0.14	1.21 ± 0.05	4958
201796757	163.26 ± 1.08	13.99 ± 0.09	4.54 ± 0.1	1.0 ± 0.04	4890
201798404	279.19 ± 3.08	20.66 ± 0.17	3.66 ± 0.09	1.13 ± 0.04	5082
201801438	73.97 ± 1.35	7.35 ± 0.05	7.08 ± 0.19	1.09 ± 0.05	4675
201803382	142.04 ± 0.77	12.22 ± 0.1	5.05 ± 0.11	1.07 ± 0.04	4995
201805635	114.61 ± 0.88	10.36 ± 0.11	5.86 ± 0.14	1.18 ± 0.05	5099
201808262	143.56 ± 0.9	12.68 ± 0.05	4.94 ± 0.09	1.05 ± 0.03	4967
201808824	135.03 ± 0.59	11.46 ± 0.1	5.43 ± 0.12	1.18 ± 0.04	4697
201811869	140.06 ± 2.27	12.37 ± 0.08	5.09 ± 0.13	1.09 ± 0.05	5000
201812416	274.85 ± 5.32	19.5 ± 0.06	3.86 ± 0.1	1.22 ± 0.06	4902
201812972	59.84 ± 0.55	6.24 ± 0.04	7.99 ± 0.17	1.12 ± 0.04	4915
201815570	114.51 ± 1.02	10.7 ± 0.26	5.46 ± 0.22	1.02 ± 0.06	4664
201821648	135.91 ± 0.89	10.71 ± 0.03	6.75 ± 0.13	1.9 ± 0.06	5127
201825829	178.11 ± 1.53	14.77 ± 0.08	4.48 ± 0.09	1.07 ± 0.04	4773
201826575	197.2 ± 1.01	15.88 ± 0.04	4.35 ± 0.08	1.13 ± 0.04	4908
201832269	84.53 ± 0.5	8.1 ± 0.08	6.9 ± 0.16	1.2 ± 0.04	4925
201834501	252.15 ± 1.68	18.19 ± 0.02	4.12 ± 0.08	1.28 ± 0.04	5015
201837938	98.47 ± 0.55	9.46 ± 0.12	6.04 ± 0.15	1.07 ± 0.04	5106
201839151	119.86 ± 0.88	10.74 ± 0.08	5.31 ± 0.12	0.99 ± 0.04	4744
201853779	163.82 ± 0.55	13.99 ± 0.05	4.53 ± 0.08	1.0 ± 0.03	4789
201854058	220.32 ± 1.67	16.62 ± 0.19	4.2 ± 0.1	1.15 ± 0.05	5023
201856481	155.61 ± 1.22	12.85 ± 0.2	5.07 ± 0.15	1.19 ± 0.05	5020
201860035	177.1 ± 1.5	13.44 ± 0.05	5.44 ± 0.11	1.59 ± 0.05	5264
201868205	234.6 ± 1.27	17.57 ± 0.18	4.11 ± 0.09	1.19 ± 0.04	5131
201870250	104.52 ± 1.19	9.74 ± 0.04	5.87 ± 0.13	1.07 ± 0.04	5027
201873790	139.82 ± 0.84	12.5 ± 0.05	4.92 ± 0.09	1.01 ± 0.03	5077
201877455	76.89 ± 1.04	7.53 ± 0.09	6.61 ± 0.19	0.96 ± 0.04	4648
201878009	185.5 ± 0.67	14.07 ± 0.08	4.97 ± 0.1	1.36 ± 0.05	4925
201882477	102.55 ± 1.1	9.95 ± 0.06	5.49 ± 0.12	0.91 ± 0.03	4924
201893802	183.51 ± 0.96	14.06 ± 0.38	5.07 ± 0.21	1.42 ± 0.09	5069
201896083	184.02 ± 0.64	14.84 ± 0.05	4.44 ± 0.08	1.08 ± 0.03	4955
201897378	221.48 ± 1.96	17.77 ± 0.07	3.94 ± 0.08	1.04 ± 0.04	5167
201903365	274.02 ± 0.0	19.45 ± 0.12	4.0 ± 0.08	1.32 ± 0.04	5159
201911755	123.76 ± 0.74	10.86 ± 0.03	5.69 ± 0.11	1.2 ± 0.04	4996
201911818	102.16 ± 0.99	9.38 ± 0.15	6.29 ± 0.19	1.21 ± 0.06	5032
201912723	278.82 ± 3.93	18.35 ± 0.14	4.39 ± 0.11	1.6 ± 0.07	5010
201920393	229.92 ± 0.79	17.07 ± 0.12	4.17 ± 0.09	1.19 ± 0.04	4788
201924393	214.53 ± 2.7	16.99 ± 0.05	4.09 ± 0.09	1.08 ± 0.04	4930
201930481	145.07 ± 0.64	12.17 ± 0.18	5.21 ± 0.14	1.17 ± 0.05	5021
201930509	113.98 ± 1.01	9.41 ± 0.04	6.66 ± 0.14	1.49 ± 0.05	4838
201931989	96.57 ± 0.91	9.27 ± 0.05	6.15 ± 0.13	1.09 ± 0.04	4917
201933325	220.28 ± 5.15	17.07 ± 0.29	4.12 ± 0.16	1.12 ± 0.07	5027
201933678	115.94 ± 0.7	10.46 ± 0.11	5.7 ± 0.13	1.12 ± 0.04	5031
201950789	123.23 ± 0.46	10.9 ± 0.05	5.52 ± 0.1	1.11 ± 0.04	4946
202789423	180.37 ± 1.35	13.67 ± 0.09	5.52 ± 0.12	1.7 ± 0.06	4549
202804648	91.64 ± 0.83	8.4 ± 0.06	6.57 ± 0.15	1.15 ± 0.04	4358
203094314	98.11 ± 1.27	9.03 ± 0.06	6.21 ± 0.15	1.11 ± 0.05	4625

Continued on next page

Table A.1 – continued from previous page

EPIC ID	$\nu_{\max}$ (μHz)	$\Delta\nu$ (μHz)	Radius ($R_\odot$)	Mass ($M_\odot$)	$T_{\rm eff}$ (K)
203117292	144.14 ± 1.89	12.63 ± 0.05	4.96 ± 0.12	1.06 ± 0.04	4597
203167148	93.52 ± 0.68	8.24 ± 0.13	7.18 ± 0.22	1.43 ± 0.07	4661
203226249	90.1 ± 1.14	7.87 ± 0.06	7.37 ± 0.18	1.43 ± 0.06	4675
203413979	236.23 ± 2.41	17.93 ± 0.44	3.99 ± 0.16	1.12 ± 0.07	4823
203610409	109.14 ± 0.71	9.6 ± 0.04	6.01 ± 0.12	1.15 ± 0.04	4570
203684609	188.39 ± 2.32	14.6 ± 0.11	4.68 ± 0.11	1.22 ± 0.05	4712
203686088	188.66 ± 0.93	14.8 ± 0.11	4.67 ± 0.1	1.23 ± 0.04	4771
203689469	197.15 ± 1.75	15.18 ± 0.08	4.73 ± 0.1	1.33 ± 0.05	4585
203690974	169.65 ± 0.9	13.44 ± 0.04	4.92 ± 0.1	1.22 ± 0.04	4510
203752443	58.66 ± 0.73	6.33 ± 0.03	7.64 ± 0.18	1.01 ± 0.04	4551
203752634	75.97 ± 1.62	7.95 ± 0.21	6.37 ± 0.3	0.91 ± 0.06	4762
203766158	157.89 ± 4.22	13.37 ± 0.11	4.66 ± 0.16	1.01 ± 0.06	4643
203775139	88.07 ± 1.31	7.77 ± 0.06	7.47 ± 0.2	1.44 ± 0.06	4597
203856507	177.23 ± 2.54	15.13 ± 0.42	4.22 ± 0.19	0.94 ± 0.06	4620
203873084	181.78 ± 1.84	15.55 ± 0.2	4.32 ± 0.12	1.04 ± 0.05	4858
203945108	70.47 ± 0.33	7.08 ± 0.04	7.37 ± 0.15	1.13 ± 0.04	4640
203953815	162.65 ± 1.89	13.06 ± 0.04	5.08 ± 0.11	1.25 ± 0.05	4671
204020034	126.47 ± 2.0	10.72 ± 0.09	5.82 ± 0.15	1.27 ± 0.06	4713
204042621	106.64 ± 0.84	10.1 ± 0.22	5.61 ± 0.21	0.99 ± 0.06	4662
204119597	160.83 ± 1.26	12.35 ± 0.09	5.52 ± 0.12	1.45 ± 0.05	4652
204255611	93.55 ± 0.74	8.51 ± 0.14	6.85 ± 0.21	1.3 ± 0.06	4868
204292409	174.76 ± 2.98	13.38 ± 0.03	5.16 ± 0.13	1.39 ± 0.06	4399
204300404	68.45 ± 0.74	6.9 ± 0.12	7.73 ± 0.25	1.22 ± 0.06	4616
204318290	79.27 ± 1.94	7.37 ± 0.18	7.22 ± 0.34	1.19 ± 0.09	4153
204349628	200.06 ± 1.63	15.32 ± 0.05	4.63 ± 0.1	1.29 ± 0.05	4595
204351528	187.68 ± 1.25	14.74 ± 0.06	4.57 ± 0.1	1.16 ± 0.04	4406
204397322	216.55 ± 1.46	16.34 ± 0.07	4.37 ± 0.09	1.24 ± 0.04	4642
204415041	64.45 ± 0.99	6.84 ± 0.07	7.25 ± 0.2	1.0 ± 0.05	4634
204465053	89.12 ± 0.55	8.69 ± 0.1	6.31 ± 0.16	1.06 ± 0.04	4673
204511875	164.42 ± 0.73	13.41 ± 0.12	4.79 ± 0.11	1.11 ± 0.04	4688
204519942	180.88 ± 1.39	14.21 ± 0.07	4.66 ± 0.1	1.16 ± 0.04	4446
204520723	113.49 ± 2.11	10.08 ± 0.15	5.79 ± 0.19	1.12 ± 0.06	4590
204524266	183.39 ± 2.15	13.52 ± 0.1	5.37 ± 0.13	1.58 ± 0.06	4728
204542778	137.43 ± 0.99	11.55 ± 0.1	5.31 ± 0.12	1.14 ± 0.04	4717
204564716	101.37 ± 0.71	8.88 ± 0.13	6.64 ± 0.19	1.31 ± 0.06	4384
204651310	155.74 ± 0.76	12.7 ± 0.06	4.92 ± 0.1	1.1 ± 0.04	4503
204678879	172.18 ± 1.32	13.79 ± 0.09	4.69 ± 0.11	1.11 ± 0.04	4403
204680132	104.04 ± 0.67	9.52 ± 0.13	5.93 ± 0.17	1.07 ± 0.05	4239
204702971	146.85 ± 3.08	12.95 ± 0.16	4.78 ± 0.16	1.0 ± 0.05	4659
204711962	125.15 ± 0.62	10.25 ± 0.04	6.18 ± 0.12	1.41 ± 0.05	4644
204785883	67.23 ± 0.74	6.89 ± 0.07	7.75 ± 0.2	1.21 ± 0.05	4704
204804227	137.74 ± 1.29	10.89 ± 0.08	6.02 ± 0.14	1.47 ± 0.06	4402
204971078	175.81 ± 1.2	13.39 ± 0.15	5.18 ± 0.13	1.4 ± 0.06	4682
205019767	118.3 ± 1.55	11.02 ± 0.12	5.4 ± 0.15	1.03 ± 0.05	4704
205184586	218.82 ± 2.42	16.74 ± 0.1	4.1 ± 0.09	1.09 ± 0.04	4591
205441962	106.59 ± 0.98	10.19 ± 0.14	5.62 ± 0.16	1.01 ± 0.05	4574
205462728	180.32 ± 1.82	14.81 ± 0.25	4.52 ± 0.15	1.11 ± 0.06	4342
205658583	165.67 ± 2.43	13.6 ± 0.08	4.62 ± 0.12	1.03 ± 0.04	4508
205912715	114.94 ± 0.52	10.05 ± 0.03	5.74 ± 0.11	1.1 ± 0.04	4704
205921032	52.52 ± 0.47	5.96 ± 0.1	8.0 ± 0.25	1.0 ± 0.05	4966
205924248	225.12 ± 1.56	16.65 ± 0.09	4.39 ± 0.09	1.3 ± 0.04	5105
205925504	176.52 ± 1.35	14.29 ± 0.06	4.59 ± 0.09	1.11 ± 0.04	4938
205927877	75.81 ± 1.25	7.08 ± 0.04	7.72 ± 0.2	1.32 ± 0.06	4733
205930855	110.96 ± 0.81	10.16 ± 0.05	5.81 ± 0.12	1.12 ± 0.04	5043
205935953	166.03 ± 1.06	13.14 ± 0.05	5.07 ± 0.1	1.27 ± 0.04	4882
205945797	255.23 ± 3.03	19.52 ± 0.18	3.7 ± 0.09	1.05 ± 0.04	5139
205946356	192.52 ± 1.8	15.12 ± 0.07	4.46 ± 0.09	1.14 ± 0.04	4934
205953049	147.13 ± 1.77	11.71 ± 0.03	5.66 ± 0.12	1.4 ± 0.05	4862
205954042	157.45 ± 1.18	13.22 ± 0.04	4.96 ± 0.1	1.16 ± 0.04	4995
205955544	179.61 ± 1.97	14.55 ± 0.04	4.42 ± 0.09	1.03 ± 0.04	4802
205955888	143.13 ± 1.19	12.2 ± 0.08	5.15 ± 0.11	1.13 ± 0.04	4861

Continued on next page

Table A.1 – continued from previous page

EPIC ID	$\nu_{\max}$ (μHz)	$\Delta\nu$ (μHz)	Radius ($R_\odot$)	Mass ($M_\odot$)	$T_{\rm eff}$ (K)
205961647	65.8 ± 0.56	6.9 ± 0.05	7.59 ± 0.17	1.14 ± 0.04	4959
205961895	194.71 ± 0.96	14.12 ± 0.14	5.39 ± 0.12	1.71 ± 0.06	5193
205962447	119.78 ± 0.66	10.98 ± 0.06	5.53 ± 0.11	1.11 ± 0.04	5041
205964443	125.3 ± 0.55	11.17 ± 0.05	5.46 ± 0.1	1.12 ± 0.04	4981
205965538	94.31 ± 0.53	8.67 ± 0.09	6.62 ± 0.15	1.23 ± 0.05	5169
205965742	212.9 ± 0.85	16.28 ± 0.05	4.2 ± 0.08	1.11 ± 0.04	4835
205970868	103.33 ± 0.73	9.6 ± 0.14	6.14 ± 0.17	1.17 ± 0.05	5118
205973739	148.2 ± 1.46	12.61 ± 0.09	5.11 ± 0.11	1.16 ± 0.04	5000
205976299	158.56 ± 1.27	12.04 ± 0.08	5.97 ± 0.13	1.71 ± 0.06	5181
205977024	133.88 ± 0.7	11.62 ± 0.06	5.41 ± 0.1	1.17 ± 0.04	5100
205977363	191.25 ± 1.51	14.69 ± 0.07	4.61 ± 0.09	1.2 ± 0.04	4908
205979159	61.73 ± 0.3	6.6 ± 0.06	7.94 ± 0.18	1.18 ± 0.04	5191
205982347	117.68 ± 1.01	10.17 ± 0.07	6.07 ± 0.13	1.3 ± 0.05	4820
205984114	97.19 ± 1.65	9.51 ± 0.21	6.08 ± 0.24	1.09 ± 0.07	5064
205992539	103.99 ± 0.91	8.7 ± 0.07	7.17 ± 0.16	1.58 ± 0.06	4730
205994284	164.15 ± 0.87	13.77 ± 0.07	4.64 ± 0.09	1.05 ± 0.04	4753
205994591	83.18 ± 1.33	7.43 ± 0.05	7.6 ± 0.19	1.4 ± 0.06	4781
205997047	86.6 ± 0.71	8.36 ± 0.22	6.89 ± 0.29	1.25 ± 0.08	4977
206001422	65.7 ± 0.55	6.66 ± 0.1	7.41 ± 0.21	1.05 ± 0.05	4692
206005808	175.09 ± 1.82	14.66 ± 0.15	4.48 ± 0.11	1.05 ± 0.04	5109
206010061	130.0 ± 0.81	11.27 ± 0.09	5.42 ± 0.12	1.13 ± 0.04	4911
206011686	221.36 ± 0.88	16.87 ± 0.05	4.3 ± 0.08	1.23 ± 0.04	5013
206013104	122.29 ± 1.02	10.51 ± 0.04	5.93 ± 0.12	1.28 ± 0.04	4885
206013893	66.09 ± 0.34	6.66 ± 0.08	7.84 ± 0.2	1.2 ± 0.05	4702
206015475	167.81 ± 1.58	13.05 ± 0.09	5.09 ± 0.11	1.28 ± 0.05	4854
206015636	228.31 ± 1.36	16.87 ± 0.11	4.34 ± 0.09	1.29 ± 0.04	4908
206017673	151.68 ± 2.12	13.45 ± 0.03	4.7 ± 0.1	1.01 ± 0.04	5134
206018092	91.01 ± 0.91	8.7 ± 0.08	6.77 ± 0.16	1.27 ± 0.05	5141
206023175	182.04 ± 0.86	14.84 ± 0.04	4.54 ± 0.08	1.13 ± 0.04	4971
206023362	227.85 ± 1.26	17.98 ± 0.08	3.95 ± 0.08	1.07 ± 0.04	4916
206024119	110.71 ± 0.82	10.22 ± 0.04	5.88 ± 0.11	1.16 ± 0.04	5176
206027732	196.43 ± 1.26	15.2 ± 0.07	4.52 ± 0.09	1.19 ± 0.04	4894
206028879	142.35 ± 0.49	11.65 ± 0.03	5.42 ± 0.1	1.23 ± 0.04	4864
206030199	63.56 ± 0.77	6.71 ± 0.06	7.62 ± 0.19	1.1 ± 0.04	4810
206030200	63.56 ± 0.65	6.71 ± 0.08	7.62 ± 0.2	1.1 ± 0.05	4810
206031811	171.23 ± 0.84	13.67 ± 0.04	4.79 ± 0.09	1.16 ± 0.04	4789
206034924	208.67 ± 2.77	16.54 ± 0.36	4.01 ± 0.15	0.99 ± 0.06	4945
206035736	120.57 ± 0.61	11.13 ± 0.11	5.44 ± 0.12	1.08 ± 0.04	4970
206036741	116.02 ± 0.7	10.13 ± 0.09	5.99 ± 0.13	1.24 ± 0.04	5020
206037748	206.79 ± 2.13	16.5 ± 0.13	4.19 ± 0.1	1.09 ± 0.04	5054
206038596	88.74 ± 0.85	8.46 ± 0.22	6.63 ± 0.28	1.16 ± 0.07	4977
206039266	219.42 ± 1.37	17.11 ± 0.22	4.18 ± 0.11	1.16 ± 0.05	4971
206041664	177.51 ± 1.3	14.61 ± 0.06	4.66 ± 0.09	1.17 ± 0.04	5043
206042941	147.01 ± 1.38	12.6 ± 0.21	5.14 ± 0.16	1.17 ± 0.05	5189
206044110	62.69 ± 0.83	6.55 ± 0.04	7.77 ± 0.18	1.13 ± 0.04	4880
206045926	225.66 ± 2.46	16.51 ± 0.1	4.55 ± 0.1	1.41 ± 0.05	4983
206046054	189.15 ± 1.4	15.28 ± 0.05	4.34 ± 0.08	1.06 ± 0.04	4891
206048937	115.41 ± 0.28	10.29 ± 0.05	5.76 ± 0.11	1.13 ± 0.04	4668
206049476	211.79 ± 1.09	16.86 ± 0.13	4.14 ± 0.09	1.1 ± 0.04	4958
206052235	178.25 ± 1.08	14.13 ± 0.13	4.66 ± 0.11	1.14 ± 0.04	4864
206052599	75.92 ± 0.47	7.25 ± 0.07	7.84 ± 0.18	1.4 ± 0.05	4889
206055865	207.99 ± 1.7	16.31 ± 0.07	4.21 ± 0.09	1.1 ± 0.04	4985
206057154	173.12 ± 1.71	13.69 ± 0.11	5.1 ± 0.12	1.36 ± 0.05	5017
206059508	191.52 ± 1.49	15.47 ± 0.09	4.48 ± 0.09	1.16 ± 0.04	5116
206060248	113.69 ± 1.29	9.9 ± 0.06	6.16 ± 0.14	1.28 ± 0.05	4825
206062541	120.83 ± 1.04	11.17 ± 0.08	5.39 ± 0.12	1.06 ± 0.04	5064
206062898	187.01 ± 1.16	15.47 ± 0.04	4.28 ± 0.08	1.03 ± 0.03	4962
206064541	175.35 ± 0.6	13.93 ± 0.06	4.81 ± 0.09	1.21 ± 0.04	4996
206066790	175.44 ± 2.22	14.4 ± 0.16	4.66 ± 0.12	1.15 ± 0.05	5037
206068894	147.95 ± 1.25	12.48 ± 0.1	5.13 ± 0.12	1.17 ± 0.04	4921
206070627	133.34 ± 0.9	10.64 ± 0.09	6.47 ± 0.14	1.69 ± 0.06	5033

Continued on next page

Table A.1 – continued from previous page

EPIC ID	$\nu_{\max}$ (μHz)	$\Delta\nu$ (μHz)	Radius ($R_\odot$)	Mass ($M_\odot$)	T_{eff} (K)
206070824	127.04 ± 1.83	11.21 ± 0.14	5.4 ± 0.16	1.1 ± 0.05	4787
206073474	151.16 ± 2.83	13.09 ± 0.19	4.91 ± 0.16	1.1 ± 0.06	5049
206073788	167.51 ± 2.41	14.09 ± 0.07	4.69 ± 0.11	1.11 ± 0.04	5029
206074162	117.38 ± 0.56	10.42 ± 0.06	5.61 ± 0.11	1.09 ± 0.04	4840
206074360	205.99 ± 1.66	16.56 ± 0.11	4.16 ± 0.09	1.07 ± 0.04	5071
206075005	189.29 ± 1.51	14.6 ± 0.04	4.63 ± 0.09	1.2 ± 0.04	4955
206076660	193.71 ± 1.39	15.02 ± 0.24	4.65 ± 0.13	1.26 ± 0.06	5058
206081439	85.03 ± 1.07	8.05 ± 0.06	6.71 ± 0.16	1.12 ± 0.05	4802
206086037	183.55 ± 1.02	15.07 ± 0.04	4.41 ± 0.08	1.07 ± 0.03	4944
206086531	150.82 ± 0.92	12.9 ± 0.1	4.87 ± 0.1	1.06 ± 0.04	4974
206088822	177.44 ± 0.94	13.84 ± 0.05	4.93 ± 0.09	1.28 ± 0.04	4960
206090123	125.37 ± 0.71	10.83 ± 0.06	5.7 ± 0.11	1.21 ± 0.04	5051
206092674	117.06 ± 0.81	10.59 ± 0.04	5.71 ± 0.11	1.14 ± 0.04	4737
206094098	85.34 ± 1.61	8.28 ± 0.06	6.47 ± 0.18	1.05 ± 0.05	4856
206094352	135.71 ± 0.82	11.11 ± 0.14	5.84 ± 0.15	1.38 ± 0.06	4851
206097958	110.03 ± 0.98	9.93 ± 0.04	5.79 ± 0.12	1.09 ± 0.04	4809
206098148	216.57 ± 2.49	14.75 ± 0.21	5.18 ± 0.15	1.71 ± 0.08	4902
206098383	174.33 ± 1.43	13.1 ± 0.23	5.27 ± 0.17	1.43 ± 0.07	5041
206100164	167.93 ± 0.73	13.13 ± 0.07	5.26 ± 0.1	1.4 ± 0.05	4962
206102006	196.89 ± 1.56	16.27 ± 0.09	4.21 ± 0.09	1.06 ± 0.04	5071
206105068	181.26 ± 3.37	14.35 ± 0.07	4.64 ± 0.12	1.15 ± 0.05	4676
206106206	93.79 ± 1.93	9.62 ± 0.14	5.79 ± 0.2	0.96 ± 0.05	4961
206109324	131.07 ± 1.12	11.06 ± 0.1	5.4 ± 0.13	1.11 ± 0.04	4866
206111552	201.23 ± 1.82	16.12 ± 0.05	4.15 ± 0.09	1.03 ± 0.04	4808
206113461	175.35 ± 0.91	14.29 ± 0.14	4.77 ± 0.11	1.2 ± 0.04	4976
206118504	168.85 ± 1.22	13.39 ± 0.03	4.83 ± 0.09	1.15 ± 0.04	4775
206124395	86.45 ± 0.73	7.99 ± 0.06	7.02 ± 0.16	1.25 ± 0.05	4873
206126654	169.4 ± 1.44	14.07 ± 0.05	4.64 ± 0.09	1.09 ± 0.04	5085
206129709	73.85 ± 0.66	7.61 ± 0.12	6.97 ± 0.21	1.07 ± 0.05	5060
206130242	134.53 ± 1.53	12.04 ± 0.04	5.09 ± 0.11	1.04 ± 0.04	5219
206131981	136.63 ± 0.76	10.65 ± 0.16	6.64 ± 0.19	1.83 ± 0.08	5151
206134716	121.11 ± 1.17	10.8 ± 0.13	5.8 ± 0.15	1.23 ± 0.05	4979
206134946	76.73 ± 0.86	7.09 ± 0.07	7.92 ± 0.21	1.42 ± 0.06	4696
206138101	238.47 ± 2.78	18.36 ± 0.16	3.83 ± 0.09	1.04 ± 0.04	5043
206139372	151.0 ± 1.05	12.79 ± 0.06	5.12 ± 0.1	1.19 ± 0.04	4959
206140798	145.56 ± 1.44	12.56 ± 0.07	5.23 ± 0.11	1.21 ± 0.04	5159
206141983	227.95 ± 1.24	16.74 ± 0.06	4.17 ± 0.08	1.16 ± 0.04	4797
206144635	108.14 ± 0.67	9.27 ± 0.06	6.75 ± 0.14	1.47 ± 0.05	4969
206145206	163.76 ± 1.17	13.21 ± 0.12	4.93 ± 0.11	1.18 ± 0.04	4944
206146161	182.28 ± 0.86	13.14 ± 0.2	5.65 ± 0.16	1.74 ± 0.07	4998
206146170	155.27 ± 1.11	12.98 ± 0.04	4.94 ± 0.09	1.13 ± 0.04	5075
206153489	192.6 ± 1.12	15.73 ± 0.03	4.2 ± 0.08	1.01 ± 0.03	4935
206153754	103.63 ± 0.76	9.5 ± 0.09	6.33 ± 0.14	1.25 ± 0.05	4937
206157503	176.22 ± 1.22	15.19 ± 0.08	4.26 ± 0.09	0.96 ± 0.03	5048
206163196	163.84 ± 0.92	12.09 ± 0.15	5.93 ± 0.15	1.72 ± 0.07	5077
206166135	191.89 ± 1.42	15.14 ± 0.04	4.62 ± 0.09	1.23 ± 0.04	5029
206172157	230.07 ± 4.34	17.85 ± 0.09	3.89 ± 0.1	1.04 ± 0.05	5061
206175747	100.35 ± 1.11	9.09 ± 0.2	6.29 ± 0.24	1.17 ± 0.07	4867
206182393	155.28 ± 1.0	13.25 ± 0.04	4.8 ± 0.09	1.07 ± 0.04	4958
206184489	195.53 ± 1.21	15.43 ± 0.09	4.39 ± 0.09	1.12 ± 0.04	4920
206188223	174.26 ± 1.09	14.13 ± 0.07	4.66 ± 0.09	1.13 ± 0.04	4950
206189690	84.99 ± 0.52	8.19 ± 0.06	6.6 ± 0.14	1.09 ± 0.04	4899
206191788	75.03 ± 0.71	7.44 ± 0.11	7.33 ± 0.21	1.21 ± 0.06	4891
206191836	151.07 ± 0.77	12.4 ± 0.08	5.15 ± 0.1	1.19 ± 0.04	4938
206194314	214.73 ± 1.95	17.14 ± 0.45	3.99 ± 0.17	1.02 ± 0.06	5155
206195829	145.81 ± 0.93	12.7 ± 0.04	4.86 ± 0.09	1.02 ± 0.03	4913
206201272	113.3 ± 1.23	10.25 ± 0.06	5.7 ± 0.13	1.09 ± 0.04	4930
206204771	109.14 ± 0.82	9.7 ± 0.08	6.25 ± 0.14	1.28 ± 0.05	4964
206205027	170.28 ± 0.81	12.68 ± 0.16	5.95 ± 0.15	1.84 ± 0.07	5158
206206667	151.13 ± 1.93	13.13 ± 0.12	4.83 ± 0.12	1.06 ± 0.04	5017
206210256	229.5 ± 0.96	17.6 ± 0.05	4.04 ± 0.08	1.12 ± 0.04	4860

Continued on next page

Table A.1 – continued from previous page

EPIC ID	$\nu_{\rm max}$ (μHz)	$\Delta\nu$ (μHz)	Radius ($R_\odot$)	Mass ($M_\odot$)	$T_{\rm eff}$ (K)
206211295	228.7 ± 1.3	17.63 ± 0.04	4.09 ± 0.08	1.16 ± 0.04	4959
206211780	89.39 ± 0.77	8.36 ± 0.05	6.76 ± 0.14	1.21 ± 0.04	4910
206211955	83.08 ± 1.85	8.24 ± 0.19	6.6 ± 0.28	1.08 ± 0.07	4942
206214910	76.94 ± 0.84	7.31 ± 0.1	7.74 ± 0.22	1.38 ± 0.06	4765
206218497	151.77 ± 0.88	13.11 ± 0.05	4.94 ± 0.09	1.12 ± 0.04	4940
206220686	91.33 ± 0.81	8.66 ± 0.05	6.55 ± 0.14	1.17 ± 0.04	5071
206221024	136.14 ± 0.95	11.75 ± 0.05	5.35 ± 0.11	1.16 ± 0.04	5033
206221118	114.69 ± 0.8	10.57 ± 0.12	5.67 ± 0.14	1.11 ± 0.04	5026
206227713	58.3 ± 1.27	6.52 ± 0.06	7.58 ± 0.23	1.0 ± 0.05	4774
206242642	112.15 ± 1.09	9.91 ± 0.08	5.88 ± 0.14	1.14 ± 0.04	4754
206245474	85.93 ± 0.53	8.31 ± 0.05	6.82 ± 0.14	1.2 ± 0.04	5040
206249125	133.38 ± 0.89	11.39 ± 0.14	5.53 ± 0.14	1.22 ± 0.05	4895
206254392	77.77 ± 0.44	7.57 ± 0.16	7.0 ± 0.24	1.12 ± 0.06	4741
206259009	261.08 ± 2.98	18.48 ± 0.06	4.11 ± 0.09	1.32 ± 0.05	4880
206271510	61.58 ± 0.6	6.54 ± 0.11	7.41 ± 0.24	0.99 ± 0.05	4737
206277585	211.52 ± 1.79	16.14 ± 0.05	4.5 ± 0.09	1.3 ± 0.04	4912
206282803	210.77 ± 1.27	16.35 ± 0.05	4.16 ± 0.08	1.08 ± 0.04	4866
206282939	101.81 ± 0.72	9.26 ± 0.06	6.44 ± 0.14	1.26 ± 0.04	4896
206287342	76.92 ± 0.78	8.14 ± 0.12	6.73 ± 0.19	1.08 ± 0.05	5363
206288336	187.31 ± 1.51	15.35 ± 0.06	4.25 ± 0.09	1.0 ± 0.03	4794
206292233	222.93 ± 1.28	16.16 ± 0.39	4.48 ± 0.18	1.33 ± 0.08	4830
206295632	145.06 ± 1.19	12.08 ± 0.06	5.3 ± 0.11	1.21 ± 0.04	4814
206298612	114.08 ± 1.45	10.71 ± 0.13	5.66 ± 0.15	1.12 ± 0.05	5054
206306011	166.07 ± 0.95	13.74 ± 0.1	4.86 ± 0.1	1.18 ± 0.04	4964
206306681	243.62 ± 1.08	17.19 ± 0.06	4.33 ± 0.08	1.36 ± 0.04	4900
206311391	131.29 ± 1.18	11.24 ± 0.06	5.73 ± 0.12	1.3 ± 0.04	5247
206320221	213.44 ± 2.89	16.76 ± 0.15	4.0 ± 0.1	1.01 ± 0.04	4872
206326967	294.66 ± 0.17	20.56 ± 0.2	3.93 ± 0.08	1.39 ± 0.05	5350
206339184	102.62 ± 0.93	9.44 ± 0.06	6.21 ± 0.13	1.18 ± 0.04	4991
206340815	179.52 ± 0.94	13.97 ± 0.04	4.79 ± 0.09	1.22 ± 0.04	4932
206345625	107.84 ± 2.03	8.83 ± 0.08	7.34 ± 0.21	1.73 ± 0.08	5141
206350062	244.84 ± 3.05	18.43 ± 0.07	3.83 ± 0.09	1.07 ± 0.04	4699
206351132	150.77 ± 1.33	13.05 ± 0.17	4.81 ± 0.13	1.04 ± 0.04	4841
206355996	206.44 ± 2.17	16.55 ± 0.09	4.15 ± 0.09	1.07 ± 0.04	4962
206367826	198.78 ± 4.45	15.22 ± 0.44	4.66 ± 0.23	1.3 ± 0.1	4929
206371409	91.53 ± 0.83	8.61 ± 0.05	6.45 ± 0.14	1.12 ± 0.04	4749
206375929	158.84 ± 1.2	13.62 ± 0.07	4.62 ± 0.09	1.01 ± 0.03	4895
206376358	177.22 ± 1.27	13.65 ± 0.07	4.96 ± 0.1	1.29 ± 0.04	4879
206376625	123.96 ± 0.87	10.49 ± 0.04	5.91 ± 0.12	1.28 ± 0.04	4799
206381683	158.0 ± 2.08	13.94 ± 0.12	4.62 ± 0.11	1.03 ± 0.04	5317
206392586	182.1 ± 1.99	14.7 ± 0.08	4.44 ± 0.1	1.06 ± 0.04	4988
206395744	128.85 ± 1.71	11.72 ± 0.09	5.18 ± 0.13	1.04 ± 0.04	5036
206398709	118.57 ± 0.86	10.46 ± 0.07	5.74 ± 0.12	1.16 ± 0.04	4820
206400223	115.59 ± 0.55	10.46 ± 0.19	5.58 ± 0.18	1.07 ± 0.05	4717
206410902	178.11 ± 1.56	14.57 ± 0.08	4.65 ± 0.1	1.16 ± 0.04	5020
206411038	99.28 ± 0.98	9.48 ± 0.06	5.88 ± 0.13	1.02 ± 0.04	4903
206412084	134.38 ± 2.04	10.43 ± 0.11	6.66 ± 0.18	1.8 ± 0.08	5023
206413231	136.78 ± 1.14	11.87 ± 0.14	5.51 ± 0.14	1.27 ± 0.05	5123
206413241	160.36 ± 1.06	13.05 ± 0.08	4.89 ± 0.1	1.13 ± 0.04	4843
206414782	154.35 ± 1.57	13.15 ± 0.05	4.93 ± 0.1	1.13 ± 0.04	4985
206420120	93.32 ± 0.67	8.65 ± 0.08	6.51 ± 0.15	1.17 ± 0.04	4633
206422172	73.1 ± 0.88	7.32 ± 0.07	7.21 ± 0.18	1.13 ± 0.05	4789
206429750	190.38 ± 0.88	15.09 ± 0.09	4.49 ± 0.09	1.14 ± 0.04	4773
206440758	115.34 ± 1.0	10.43 ± 0.07	5.49 ± 0.12	1.02 ± 0.04	4839
206441949	125.88 ± 0.87	11.34 ± 0.04	5.26 ± 0.1	1.04 ± 0.03	4918
206449703	210.26 ± 2.19	13.32 ± 0.1	6.31 ± 0.14	2.47 ± 0.09	4891
206450592	222.21 ± 1.7	16.81 ± 0.28	4.28 ± 0.13	1.22 ± 0.06	5132
206455464	53.76 ± 1.31	5.91 ± 0.06	7.89 ± 0.26	0.98 ± 0.05	4710
206456462	205.7 ± 3.01	15.27 ± 0.13	4.88 ± 0.13	1.49 ± 0.06	4891
206457928	106.16 ± 0.37	9.56 ± 0.05	6.19 ± 0.12	1.21 ± 0.04	4890
206458726	210.61 ± 1.23	16.35 ± 0.08	4.25 ± 0.08	1.14 ± 0.04	5096

Continued on next page

Table A.1 – continued from previous page

EPIC ID	$\nu_{\max}$ (μHz)	$\Delta\nu$ (μHz)	Radius ($R_\odot$)	Mass ($M_\odot$)	$T_{\rm eff}$ (K)
206469672	177.88 ± 1.51	14.63 ± 0.07	4.38 ± 0.09	1.01 ± 0.04	4800
206474004	142.09 ± 0.77	11.64 ± 0.04	5.49 ± 0.1	1.27 ± 0.04	4971
206483102	184.89 ± 7.67	13.91 ± 0.08	5.39 ± 0.25	1.64 ± 0.13	5160
206484607	75.71 ± 0.59	7.36 ± 0.04	7.28 ± 0.15	1.18 ± 0.04	4847
206493427	146.64 ± 0.55	12.36 ± 0.05	5.27 ± 0.1	1.22 ± 0.04	4958
206497556	100.83 ± 0.58	9.47 ± 0.06	6.11 ± 0.12	1.13 ± 0.04	4966
206498471	86.69 ± 0.82	8.23 ± 0.04	6.65 ± 0.14	1.13 ± 0.04	4728
206500261	185.04 ± 1.78	14.41 ± 0.06	4.73 ± 0.1	1.23 ± 0.04	4874
206508351	102.51 ± 0.46	9.68 ± 0.06	5.76 ± 0.12	1.0 ± 0.03	4689
206515124	185.77 ± 2.34	15.58 ± 0.03	4.21 ± 0.09	0.98 ± 0.04	4775
206518170	221.03 ± 1.18	17.19 ± 0.09	4.18 ± 0.08	1.17 ± 0.04	5027
206519413	155.66 ± 1.64	12.73 ± 0.04	5.19 ± 0.11	1.25 ± 0.05	4952
210319568	252.86 ± 2.06	18.9 ± 0.14	3.85 ± 0.09	1.12 ± 0.04	4624
210352451	140.68 ± 1.46	11.66 ± 0.06	5.54 ± 0.12	1.29 ± 0.05	4590
210355363	144.05 ± 1.51	11.41 ± 0.24	5.95 ± 0.21	1.53 ± 0.08	4831
210357016	279.17 ± 2.31	20.26 ± 0.07	3.81 ± 0.08	1.23 ± 0.04	4744
210363615	97.89 ± 1.76	8.66 ± 0.09	6.75 ± 0.2	1.31 ± 0.07	4375
210376310	204.41 ± 1.73	16.03 ± 0.08	4.3 ± 0.09	1.13 ± 0.04	4566
210384520	165.72 ± 1.02	12.34 ± 0.1	5.66 ± 0.13	1.57 ± 0.06	4421
210401938	155.04 ± 1.15	12.56 ± 0.05	5.21 ± 0.11	1.25 ± 0.04	4701
210402468	202.74 ± 2.31	15.78 ± 0.14	4.52 ± 0.11	1.25 ± 0.05	4623
210425787	209.24 ± 5.68	16.35 ± 0.22	4.22 ± 0.16	1.11 ± 0.07	4403
210437844	168.47 ± 2.7	13.59 ± 0.04	4.82 ± 0.12	1.16 ± 0.05	4489
210460485	105.97 ± 0.63	9.13 ± 0.07	6.88 ± 0.16	1.51 ± 0.06	4331
210467837	157.12 ± 1.02	13.01 ± 0.07	5.07 ± 0.11	1.21 ± 0.04	4629
210472541	190.72 ± 5.2	15.14 ± 0.06	4.5 ± 0.15	1.15 ± 0.07	4788
210475095	264.24 ± 8.17	18.92 ± 0.08	3.89 ± 0.14	1.19 ± 0.07	4628
210479475	99.46 ± 1.19	9.2 ± 0.05	6.12 ± 0.14	1.1 ± 0.04	4507
210482409	237.7 ± 2.06	17.6 ± 0.05	4.02 ± 0.08	1.14 ± 0.04	4465
210488965	247.58 ± 2.48	19.39 ± 0.11	3.63 ± 0.08	0.98 ± 0.04	4594
210500981	112.42 ± 0.96	9.93 ± 0.04	6.0 ± 0.13	1.2 ± 0.04	4519
210503728	83.0 ± 0.74	7.8 ± 0.08	7.24 ± 0.18	1.3 ± 0.05	4711
210504998	122.79 ± 0.96	10.66 ± 0.05	5.61 ± 0.12	1.14 ± 0.04	4539
210508104	133.69 ± 2.09	11.36 ± 0.06	5.47 ± 0.14	1.18 ± 0.05	4790
210511471	239.33 ± 1.24	17.25 ± 0.09	4.32 ± 0.09	1.33 ± 0.05	4689
210516858	95.33 ± 2.36	8.8 ± 0.12	6.29 ± 0.23	1.11 ± 0.07	4363
210519764	118.49 ± 0.87	10.31 ± 0.04	5.62 ± 0.12	1.09 ± 0.04	4429
210521503	110.89 ± 0.92	9.85 ± 0.12	6.04 ± 0.16	1.2 ± 0.05	4566
210524708	212.22 ± 0.78	16.11 ± 0.04	4.27 ± 0.08	1.14 ± 0.04	4555
210532367	152.19 ± 1.07	13.19 ± 0.13	3.76 ± 0.09	0.57 ± 0.02	4398
210533695	138.54 ± 0.81	12.17 ± 0.04	5.03 ± 0.1	1.04 ± 0.03	4748
210534547	145.7 ± 0.84	12.11 ± 0.03	5.29 ± 0.1	1.21 ± 0.04	4570
210547552	96.97 ± 1.06	9.21 ± 0.03	6.24 ± 0.14	1.13 ± 0.04	4624
210548781	171.37 ± 1.0	13.6 ± 0.04	4.84 ± 0.1	1.18 ± 0.04	4488
210549349	117.58 ± 0.99	10.64 ± 0.05	5.74 ± 0.12	1.17 ± 0.04	4726
210558546	169.72 ± 3.65	13.89 ± 0.12	4.84 ± 0.15	1.2 ± 0.06	4426
210563555	115.0 ± 2.72	10.06 ± 0.03	6.36 ± 0.19	1.41 ± 0.07	4573
210566419	137.44 ± 0.69	11.34 ± 0.07	5.65 ± 0.12	1.3 ± 0.05	4409
210567284	207.17 ± 1.33	16.79 ± 0.14	4.24 ± 0.09	1.14 ± 0.04	4760
210573261	85.4 ± 0.52	7.85 ± 0.05	7.5 ± 0.16	1.44 ± 0.05	4609
210609023	157.46 ± 0.58	12.91 ± 0.05	5.02 ± 0.1	1.18 ± 0.04	4659
210614836	184.96 ± 1.64	15.04 ± 0.14	4.58 ± 0.11	1.18 ± 0.05	4750
210627824	222.19 ± 1.52	17.7 ± 0.05	3.88 ± 0.08	1.0 ± 0.03	4477
210631378	104.18 ± 1.3	9.01 ± 0.07	6.8 ± 0.17	1.43 ± 0.06	4531
210634895	156.92 ± 0.91	12.74 ± 0.11	5.2 ± 0.12	1.27 ± 0.05	4570
210639440	153.95 ± 1.29	12.47 ± 0.05	5.5 ± 0.11	1.41 ± 0.05	4921
210642549	211.66 ± 1.5	16.64 ± 0.37	4.3 ± 0.16	1.19 ± 0.07	4954
210643194	126.4 ± 0.71	10.76 ± 0.05	5.83 ± 0.12	1.28 ± 0.04	4657
210644203	220.69 ± 4.15	16.67 ± 0.08	4.4 ± 0.12	1.29 ± 0.06	4704
210660201	157.13 ± 1.63	12.29 ± 0.05	5.49 ± 0.12	1.4 ± 0.05	4659
210660521	125.14 ± 1.41	9.35 ± 0.26	7.56 ± 0.34	2.12 ± 0.14	4517

Continued on next page

Table A.1 – continued from previous page

EPIC ID	$\nu_{\max}$ (μHz)	$\Delta\nu$ (μHz)	Radius ($R_\odot$)	Mass ($M_\odot$)	$T_{\rm eff}$ (K)
210660949	145.89 ± 0.95	11.68 ± 0.05	6.01 ± 0.12	1.61 ± 0.05	4729
210663972	115.94 ± 2.66	9.94 ± 0.07	6.04 ± 0.19	1.24 ± 0.07	4478
210665262	137.06 ± 0.65	11.5 ± 0.12	5.4 ± 0.13	1.18 ± 0.05	4420
210666560	72.34 ± 0.81	6.86 ± 0.04	7.69 ± 0.19	1.24 ± 0.05	4002
210685306	114.93 ± 0.88	10.53 ± 0.11	5.83 ± 0.14	1.19 ± 0.05	4696
210685924	93.27 ± 0.76	8.72 ± 0.08	6.45 ± 0.15	1.15 ± 0.05	4586
210686716	102.47 ± 0.81	8.96 ± 0.05	6.52 ± 0.15	1.28 ± 0.05	4279
210689355	165.59 ± 1.65	12.71 ± 0.12	5.69 ± 0.14	1.63 ± 0.07	4835
210690537	124.97 ± 1.41	10.72 ± 0.12	5.71 ± 0.15	1.21 ± 0.05	4878
210690609	144.83 ± 1.37	12.07 ± 0.09	5.47 ± 0.13	1.31 ± 0.05	4855
210690749	98.8 ± 0.91	9.06 ± 0.03	6.32 ± 0.14	1.17 ± 0.04	4412
210695757	104.72 ± 1.07	9.42 ± 0.04	6.43 ± 0.14	1.3 ± 0.05	4692
210700174	67.73 ± 0.57	6.82 ± 0.04	7.89 ± 0.17	1.26 ± 0.05	4793
210703566	216.23 ± 1.09	16.48 ± 0.51	4.3 ± 0.21	1.2 ± 0.09	4340
210705972	240.44 ± 1.8	17.92 ± 0.16	4.1 ± 0.09	1.21 ± 0.05	4878
210709725	196.88 ± 1.7	15.5 ± 0.05	4.33 ± 0.09	1.1 ± 0.04	4370
210718775	159.32 ± 0.97	12.83 ± 0.07	5.3 ± 0.11	1.35 ± 0.05	4880
210722412	133.04 ± 1.23	11.67 ± 0.11	5.33 ± 0.13	1.13 ± 0.05	4694
210722444	157.8 ± 1.03	12.31 ± 0.17	5.54 ± 0.15	1.45 ± 0.06	4779
210723607	143.88 ± 2.53	11.12 ± 0.29	6.36 ± 0.28	1.76 ± 0.12	4912
210723779	162.06 ± 2.16	13.22 ± 0.04	5.03 ± 0.11	1.23 ± 0.05	4764
210724744	136.35 ± 0.79	12.05 ± 0.03	5.2 ± 0.1	1.11 ± 0.04	4791
210731260	94.52 ± 0.52	8.96 ± 0.07	6.45 ± 0.15	1.18 ± 0.04	4297
210733885	164.85 ± 0.91	13.89 ± 0.09	4.69 ± 0.1	1.09 ± 0.04	4648
210735731	197.31 ± 1.79	15.02 ± 0.24	4.63 ± 0.14	1.25 ± 0.06	4727
210737087	108.97 ± 1.83	9.75 ± 0.05	6.22 ± 0.16	1.26 ± 0.06	4668
210737808	194.94 ± 1.28	15.1 ± 0.04	4.54 ± 0.09	1.19 ± 0.04	4716
210738140	181.51 ± 1.56	14.45 ± 0.08	4.77 ± 0.1	1.24 ± 0.04	4824
210743223	132.39 ± 1.13	11.5 ± 0.05	5.39 ± 0.11	1.15 ± 0.04	4636
210743416	113.12 ± 0.86	9.67 ± 0.08	6.49 ± 0.15	1.43 ± 0.05	4784
210744824	189.13 ± 1.86	14.94 ± 0.11	4.71 ± 0.11	1.27 ± 0.05	4250
210745299	203.14 ± 1.78	15.9 ± 0.08	4.6 ± 0.1	1.32 ± 0.05	4901
210749402	145.58 ± 1.19	12.45 ± 0.08	5.05 ± 0.11	1.11 ± 0.04	4478
210750052	129.39 ± 2.3	10.32 ± 0.05	6.42 ± 0.17	1.59 ± 0.07	4723
210751042	188.48 ± 1.29	14.81 ± 0.06	4.59 ± 0.09	1.18 ± 0.04	4765
210755929	146.68 ± 1.0	11.22 ± 0.27	6.16 ± 0.24	1.66 ± 0.1	4768
210763179	162.1 ± 2.12	13.02 ± 0.03	5.23 ± 0.12	1.34 ± 0.05	4782
210774952	134.34 ± 1.01	11.52 ± 0.08	5.45 ± 0.12	1.19 ± 0.04	4786
210777311	167.06 ± 2.25	13.67 ± 0.14	4.73 ± 0.13	1.11 ± 0.05	4765
210784314	121.07 ± 0.98	10.47 ± 0.14	6.16 ± 0.17	1.4 ± 0.06	4679
210786778	207.85 ± 3.15	16.27 ± 0.19	4.6 ± 0.13	1.37 ± 0.06	4561
210791216	193.95 ± 2.15	15.19 ± 0.08	4.6 ± 0.1	1.23 ± 0.05	4795
210792787	111.48 ± 0.56	10.12 ± 0.04	5.94 ± 0.12	1.18 ± 0.04	4693
210795579	136.62 ± 0.62	11.49 ± 0.05	5.48 ± 0.11	1.22 ± 0.04	4516
210798382	101.27 ± 0.49	9.0 ± 0.04	6.59 ± 0.13	1.3 ± 0.04	4647
210804640	66.71 ± 1.72	6.78 ± 0.07	7.69 ± 0.27	1.17 ± 0.07	4609
210805432	70.27 ± 0.61	6.99 ± 0.08	7.7 ± 0.2	1.24 ± 0.05	4663
210806073	61.31 ± 0.92	6.43 ± 0.04	7.26 ± 0.2	0.93 ± 0.04	3968
210807191	237.78 ± 3.25	17.52 ± 0.08	4.15 ± 0.1	1.22 ± 0.05	4697
210807803	147.36 ± 1.42	11.72 ± 0.29	5.8 ± 0.24	1.49 ± 0.09	4722
210817076	86.06 ± 3.03	7.81 ± 0.13	7.36 ± 0.34	1.38 ± 0.11	4424
210823027	91.7 ± 1.27	8.57 ± 0.04	6.8 ± 0.16	1.27 ± 0.05	4788
210835829	79.97 ± 0.74	8.01 ± 0.04	6.81 ± 0.15	1.11 ± 0.04	4629
210836897	261.2 ± 0.0	18.75 ± 0.06	4.17 ± 0.08	1.38 ± 0.04	4637
210845326	227.53 ± 1.1	17.4 ± 0.08	4.14 ± 0.08	1.17 ± 0.04	4613
210847389	120.69 ± 1.16	10.72 ± 0.05	5.79 ± 0.12	1.22 ± 0.04	4758
210847508	108.46 ± 2.59	9.41 ± 0.1	6.63 ± 0.22	1.43 ± 0.08	4669
210848772	223.98 ± 1.64	17.28 ± 0.04	4.1 ± 0.08	1.13 ± 0.04	4720
210853993	87.31 ± 1.41	8.75 ± 0.07	6.5 ± 0.18	1.13 ± 0.05	4483
210854579	229.62 ± 1.41	16.25 ± 0.09	4.69 ± 0.1	1.52 ± 0.05	4832
210855771	89.09 ± 1.07	8.55 ± 0.12	6.45 ± 0.19	1.1 ± 0.05	4655

Continued on next page

Table A.1 – continued from previous page

EPIC ID	$\nu_{\max}$ (μHz)	$\Delta\nu$ (μHz)	Radius ($R_\odot$)	Mass ($M_\odot$)	$T_{\rm eff}$ (K)
210858949	176.97 ± 0.97	14.13 ± 0.08	5.01 ± 0.1	1.35 ± 0.05	4722
210859795	126.26 ± 0.79	10.84 ± 0.04	5.78 ± 0.11	1.26 ± 0.04	4668
210866657	155.27 ± 1.69	12.51 ± 0.08	5.5 ± 0.13	1.42 ± 0.05	4726
210869583	91.41 ± 1.17	8.26 ± 0.03	7.24 ± 0.17	1.44 ± 0.06	4566
210873190	168.77 ± 1.16	13.15 ± 0.03	5.13 ± 0.1	1.32 ± 0.05	4599
210875371	72.96 ± 1.67	7.38 ± 0.06	6.83 ± 0.22	0.99 ± 0.05	4072
210891952	107.47 ± 1.45	9.94 ± 0.06	6.01 ± 0.14	1.17 ± 0.05	4669
210894525	81.78 ± 0.5	7.65 ± 0.12	7.38 ± 0.22	1.32 ± 0.06	4388
210896356	103.3 ± 1.07	9.31 ± 0.04	5.96 ± 0.14	1.06 ± 0.04	4254
210896838	195.95 ± 1.26	15.01 ± 0.1	4.81 ± 0.1	1.37 ± 0.05	4821
210897476	185.0 ± 2.28	14.88 ± 0.16	4.43 ± 0.12	1.08 ± 0.05	4542
210898348	219.14 ± 1.45	16.4 ± 0.04	4.32 ± 0.09	1.22 ± 0.04	4647
210901052	143.12 ± 1.4	12.1 ± 0.02	5.12 ± 0.11	1.11 ± 0.04	4544
210909708	132.53 ± 1.17	11.0 ± 0.14	5.76 ± 0.16	1.3 ± 0.06	4248
210911220	129.3 ± 1.23	11.33 ± 0.08	5.58 ± 0.13	1.21 ± 0.05	4768
210922216	215.72 ± 1.76	15.88 ± 0.05	4.83 ± 0.1	1.54 ± 0.05	4910
210924738	51.61 ± 0.57	6.22 ± 0.03	7.26 ± 0.16	0.8 ± 0.03	4468
210929758	96.98 ± 0.48	9.02 ± 0.04	6.59 ± 0.13	1.27 ± 0.04	4781
210933818	142.92 ± 3.92	12.7 ± 0.26	4.91 ± 0.21	1.04 ± 0.07	4690
210937624	106.57 ± 0.64	9.04 ± 0.06	6.83 ± 0.15	1.47 ± 0.05	4567
210941329	143.75 ± 1.15	12.18 ± 0.06	5.32 ± 0.11	1.22 ± 0.04	4502
210942697	109.35 ± 0.43	9.94 ± 0.09	5.97 ± 0.14	1.16 ± 0.04	4669
210954702	72.08 ± 1.77	7.21 ± 0.08	7.73 ± 0.27	1.3 ± 0.08	4677
210954875	153.59 ± 2.1	13.34 ± 0.02	4.84 ± 0.11	1.09 ± 0.04	4653
210963267	130.97 ± 0.84	10.78 ± 0.04	6.04 ± 0.12	1.43 ± 0.05	4745
210966371	226.24 ± 1.27	16.99 ± 0.13	4.29 ± 0.09	1.25 ± 0.05	4606
210966783	96.58 ± 0.98	8.13 ± 0.15	8.0 ± 0.27	1.87 ± 0.1	4834
210967940	279.83 ± 1.2	18.44 ± 0.08	4.39 ± 0.09	1.61 ± 0.05	4554
210968621	122.33 ± 0.91	10.77 ± 0.05	5.82 ± 0.12	1.25 ± 0.04	4629
210970373	97.79 ± 0.96	8.72 ± 0.04	6.85 ± 0.15	1.37 ± 0.05	4510
210971783	264.34 ± 6.13	18.28 ± 0.51	4.3 ± 0.21	1.48 ± 0.11	4873
210974526	110.01 ± 0.89	10.09 ± 0.08	5.88 ± 0.13	1.14 ± 0.04	4696
210979656	170.73 ± 2.05	13.3 ± 0.03	5.12 ± 0.11	1.33 ± 0.05	4836
210980849	104.47 ± 0.43	9.47 ± 0.11	6.13 ± 0.15	1.16 ± 0.05	4573
210981854	220.34 ± 2.11	16.68 ± 0.2	4.25 ± 0.11	1.19 ± 0.05	4752
210982106	133.48 ± 0.78	10.86 ± 0.04	5.84 ± 0.12	1.34 ± 0.05	4331
210984890	121.47 ± 3.61	10.75 ± 0.18	5.65 ± 0.24	1.16 ± 0.08	4799
210989786	119.33 ± 1.33	10.29 ± 0.1	5.97 ± 0.15	1.26 ± 0.05	4499
210991971	186.08 ± 1.99	14.06 ± 0.1	5.11 ± 0.12	1.46 ± 0.06	4845
210993645	136.86 ± 1.09	11.43 ± 0.08	5.43 ± 0.12	1.19 ± 0.04	4580
210994135	61.97 ± 0.83	6.62 ± 0.09	7.38 ± 0.22	0.99 ± 0.05	4724
210998636	179.2 ± 2.55	14.82 ± 0.16	4.52 ± 0.12	1.1 ± 0.05	4854
211000571	104.38 ± 1.01	9.46 ± 0.07	6.27 ± 0.15	1.22 ± 0.05	4712
211004779	241.94 ± 1.97	17.48 ± 0.13	4.29 ± 0.09	1.34 ± 0.05	4889
211006532	68.14 ± 0.59	6.77 ± 0.06	7.81 ± 0.19	1.23 ± 0.05	4617
211006980	201.37 ± 1.86	15.08 ± 0.11	4.76 ± 0.11	1.36 ± 0.05	4842
211006983	102.74 ± 0.82	9.6 ± 0.2	6.13 ± 0.22	1.16 ± 0.06	4742
211008148	111.76 ± 1.18	9.45 ± 0.09	6.96 ± 0.17	1.65 ± 0.07	4906
211010262	167.86 ± 1.15	13.79 ± 0.23	4.93 ± 0.15	1.24 ± 0.06	4803
211010294	183.66 ± 2.19	14.47 ± 0.1	4.85 ± 0.11	1.3 ± 0.05	4891
211011089	251.51 ± 2.39	18.16 ± 0.18	4.29 ± 0.1	1.41 ± 0.06	4950
211013838	181.47 ± 4.78	15.22 ± 0.17	4.29 ± 0.15	1.0 ± 0.06	4614
211014845	249.04 ± 3.46	19.41 ± 0.3	3.68 ± 0.12	1.01 ± 0.05	4824
211016468	226.69 ± 1.35	17.18 ± 0.06	4.11 ± 0.08	1.14 ± 0.04	4720
211018695	88.76 ± 2.91	8.46 ± 0.16	6.51 ± 0.3	1.11 ± 0.08	4546
211019359	198.36 ± 2.76	15.39 ± 0.09	4.76 ± 0.11	1.38 ± 0.06	4943
211020824	152.32 ± 1.08	12.66 ± 0.14	5.3 ± 0.13	1.3 ± 0.05	4915
211023068	104.35 ± 0.95	9.28 ± 0.05	6.36 ± 0.14	1.25 ± 0.05	4591
211023763	175.75 ± 1.6	13.43 ± 0.05	5.12 ± 0.11	1.36 ± 0.05	4572
211024404	163.37 ± 1.78	13.33 ± 0.1	4.97 ± 0.12	1.21 ± 0.05	4892
211031854	123.84 ± 0.91	10.51 ± 0.07	5.72 ± 0.12	1.19 ± 0.04	4677

Continued on next page

Table A.1 – continued from previous page

EPIC ID	$\nu_{\max}$ (μHz)	$\Delta\nu$ (μHz)	Radius ($R_\odot$)	Mass ($M_\odot$)	T_{eff} (K)
211032899	93.01 ± 0.39	8.38 ± 0.05	6.85 ± 0.14	1.29 ± 0.04	4598
211033461	97.9 ± 0.77	9.36 ± 0.15	6.08 ± 0.18	1.08 ± 0.05	4639
211046089	116.78 ± 1.63	10.49 ± 0.11	5.67 ± 0.15	1.12 ± 0.05	4753
211047297	129.37 ± 3.94	10.43 ± 0.1	6.26 ± 0.24	1.5 ± 0.1	4640
211049052	216.37 ± 0.9	16.73 ± 0.06	4.14 ± 0.08	1.1 ± 0.04	4711
211052102	221.73 ± 3.14	17.19 ± 0.19	3.98 ± 0.11	1.04 ± 0.05	4547
211058610	101.82 ± 1.33	9.25 ± 0.16	6.33 ± 0.21	1.22 ± 0.06	4722
211064725	113.5 ± 0.9	10.19 ± 0.06	5.98 ± 0.13	1.22 ± 0.04	4780
211067525	202.93 ± 1.44	15.91 ± 0.1	4.28 ± 0.09	1.11 ± 0.04	4717
211069231	214.6 ± 3.35	16.65 ± 0.28	4.16 ± 0.14	1.1 ± 0.06	4837
211070231	173.89 ± 1.42	14.17 ± 0.23	4.61 ± 0.14	1.1 ± 0.05	4505
211076236	200.14 ± 3.5	15.23 ± 0.2	4.88 ± 0.15	1.46 ± 0.07	4915
211078923	167.78 ± 7.19	14.31 ± 0.04	4.5 ± 0.21	1.02 ± 0.08	4842
211081828	169.79 ± 1.99	13.6 ± 0.08	5.06 ± 0.11	1.31 ± 0.05	4980
211091759	88.98 ± 0.94	8.31 ± 0.06	7.04 ± 0.16	1.33 ± 0.05	4868
211095581	135.23 ± 1.16	11.91 ± 0.03	5.19 ± 0.11	1.09 ± 0.04	4573
211096542	76.39 ± 1.31	7.37 ± 0.1	7.58 ± 0.24	1.31 ± 0.07	4602
211099781	73.79 ± 0.89	7.58 ± 0.02	7.82 ± 0.16	1.51 ± 0.05	5667
211109320	205.31 ± 1.46	15.88 ± 0.06	4.27 ± 0.09	1.11 ± 0.04	4400
211110428	137.3 ± 1.88	11.85 ± 0.05	5.31 ± 0.12	1.16 ± 0.05	4664
211129190	55.9 ± 0.56	6.44 ± 0.11	7.05 ± 0.23	0.81 ± 0.04	4420
211133199	130.19 ± 0.91	11.31 ± 0.05	5.41 ± 0.11	1.13 ± 0.04	4660
211143318	193.6 ± 2.29	14.91 ± 0.31	4.69 ± 0.17	1.27 ± 0.07	4824
211144117	140.98 ± 2.48	11.81 ± 0.06	5.49 ± 0.14	1.28 ± 0.06	4776
211152708	65.06 ± 1.99	6.66 ± 0.09	7.92 ± 0.32	1.22 ± 0.08	4736
211161932	84.56 ± 2.6	8.09 ± 0.05	7.02 ± 0.26	1.25 ± 0.08	4615
211166778	89.48 ± 0.45	8.0 ± 0.07	7.66 ± 0.17	1.59 ± 0.06	4756
211182451	193.0 ± 1.26	14.69 ± 0.17	5.0 ± 0.13	1.47 ± 0.06	4921
211304005	100.68 ± 0.65	9.52 ± 0.12	6.05 ± 0.16	1.1 ± 0.05	5063
211304050	175.58 ± 1.66	14.53 ± 0.05	4.57 ± 0.09	1.1 ± 0.04	4836
211304446	214.03 ± 2.88	17.44 ± 0.26	3.89 ± 0.12	0.97 ± 0.05	5118
211305895	119.88 ± 0.76	10.72 ± 0.06	5.66 ± 0.11	1.15 ± 0.04	4934
211305959	72.26 ± 0.65	7.11 ± 0.04	7.51 ± 0.16	1.21 ± 0.04	4860
211307095	176.16 ± 2.44	13.46 ± 0.16	5.05 ± 0.14	1.33 ± 0.06	4934
211307434	146.84 ± 0.59	12.12 ± 0.07	5.25 ± 0.1	1.2 ± 0.04	4891
211311260	243.26 ± 2.21	18.83 ± 0.18	3.74 ± 0.09	1.02 ± 0.04	4996
211314650	104.48 ± 0.71	9.99 ± 0.1	5.55 ± 0.13	0.95 ± 0.04	4842
211315640	62.18 ± 0.7	6.56 ± 0.11	7.79 ± 0.24	1.13 ± 0.05	4966
211319598	121.69 ± 2.49	10.63 ± 0.06	5.79 ± 0.16	1.22 ± 0.06	4991
211320263	57.78 ± 0.36	6.29 ± 0.05	7.78 ± 0.17	1.04 ± 0.04	4900
211321063	232.34 ± 1.46	17.98 ± 0.24	3.95 ± 0.1	1.09 ± 0.05	5096
211323218	76.42 ± 0.59	7.36 ± 0.12	7.07 ± 0.21	1.11 ± 0.05	4709
211326888	209.19 ± 1.84	16.3 ± 0.07	4.31 ± 0.09	1.16 ± 0.04	5108
211329249	97.27 ± 2.2	9.12 ± 0.12	6.35 ± 0.22	1.17 ± 0.07	4867
211330362	85.75 ± 0.52	8.11 ± 0.05	6.92 ± 0.14	1.22 ± 0.04	4879
211330883	75.49 ± 1.3	7.07 ± 0.05	7.92 ± 0.21	1.4 ± 0.06	5034
211331722	131.99 ± 0.59	11.14 ± 0.1	5.64 ± 0.12	1.25 ± 0.04	4999
211337633	195.59 ± 1.82	15.83 ± 0.25	4.27 ± 0.13	1.06 ± 0.05	5078
211339707	104.44 ± 1.84	8.47 ± 0.07	7.79 ± 0.21	1.9 ± 0.09	4956
211339898	197.75 ± 1.42	15.67 ± 0.06	4.33 ± 0.09	1.11 ± 0.04	4920
211339974	118.24 ± 1.81	10.94 ± 0.11	5.44 ± 0.15	1.05 ± 0.05	5128
211344224	113.49 ± 1.5	9.87 ± 0.13	6.26 ± 0.18	1.33 ± 0.06	5070
211344387	200.33 ± 1.74	15.61 ± 0.1	4.37 ± 0.1	1.14 ± 0.04	4903
211347690	288.86 ± 0.55	20.25 ± 0.02	3.81 ± 0.07	1.26 ± 0.04	5010
211348478	125.12 ± 3.61	11.53 ± 0.11	5.22 ± 0.19	1.03 ± 0.06	5150
211349759	103.9 ± 1.7	9.64 ± 0.26	6.04 ± 0.27	1.13 ± 0.08	5016
211351816	222.62 ± 2.42	16.93 ± 0.08	4.0 ± 0.09	1.04 ± 0.04	4806
211351885	69.24 ± 0.76	6.68 ± 0.04	7.86 ± 0.18	1.25 ± 0.05	4764
211352492	152.89 ± 2.59	12.31 ± 0.09	5.49 ± 0.14	1.39 ± 0.06	5000
211353249	209.48 ± 3.63	16.1 ± 0.3	4.3 ± 0.15	1.15 ± 0.07	5074
211353291	164.7 ± 1.91	13.76 ± 0.05	4.83 ± 0.1	1.16 ± 0.04	5138

Continued on next page

Table A.1 – continued from previous page

EPIC ID	$\nu_{\max}$ (μHz)	$\Delta\nu$ (μHz)	Radius ($R_\odot$)	Mass ($M_\odot$)	$T_{\rm eff}$ (K)
211354832	134.09 ± 1.98	11.87 ± 0.04	5.13 ± 0.12	1.05 ± 0.04	4918
211356115	241.47 ± 2.94	17.8 ± 0.12	4.16 ± 0.09	1.25 ± 0.05	5166
211358096	74.35 ± 0.26	7.35 ± 0.04	7.14 ± 0.14	1.12 ± 0.04	5036
211358640	110.23 ± 0.84	9.54 ± 0.1	6.05 ± 0.15	1.17 ± 0.05	4738
211359723	218.2 ± 1.17	16.82 ± 0.12	4.18 ± 0.09	1.14 ± 0.04	5008
211363503	125.82 ± 0.52	10.22 ± 0.07	6.31 ± 0.13	1.48 ± 0.05	4942
211364137	185.83 ± 2.12	14.96 ± 0.1	4.58 ± 0.1	1.17 ± 0.04	4976
211367059	195.58 ± 1.21	15.71 ± 0.03	4.31 ± 0.08	1.09 ± 0.04	4939
211367825	101.22 ± 0.43	9.18 ± 0.13	6.28 ± 0.17	1.18 ± 0.05	4963
211371616	186.49 ± 0.74	14.43 ± 0.23	4.79 ± 0.14	1.27 ± 0.06	5138
211372657	147.13 ± 1.2	11.6 ± 0.06	5.84 ± 0.12	1.5 ± 0.05	4897
211378233	131.48 ± 0.87	11.1 ± 0.08	5.72 ± 0.12	1.28 ± 0.05	4924
211379603	196.59 ± 1.76	15.2 ± 0.04	4.67 ± 0.09	1.29 ± 0.04	5059
211380235	140.1 ± 1.65	12.92 ± 0.19	4.7 ± 0.14	0.93 ± 0.04	5026
211382928	145.69 ± 0.77	12.03 ± 0.06	5.16 ± 0.1	1.13 ± 0.04	4847
211384259	173.2 ± 1.54	13.77 ± 0.03	4.75 ± 0.09	1.15 ± 0.04	4983
211385801	277.25 ± 3.33	19.11 ± 0.05	4.1 ± 0.09	1.4 ± 0.05	4966
211385977	98.73 ± 1.1	9.31 ± 0.21	6.24 ± 0.24	1.15 ± 0.07	5063
211386637	204.21 ± 1.45	16.33 ± 0.39	4.19 ± 0.16	1.07 ± 0.06	4938
211386875	121.11 ± 1.89	10.68 ± 0.06	5.48 ± 0.14	1.07 ± 0.05	4895
211388483	112.78 ± 1.44	9.92 ± 0.05	5.81 ± 0.14	1.11 ± 0.04	4702
211391152	219.39 ± 3.06	15.6 ± 0.1	4.97 ± 0.12	1.64 ± 0.07	5105
211392399	94.72 ± 0.76	8.48 ± 0.05	6.88 ± 0.14	1.33 ± 0.05	4867
211395263	98.37 ± 1.03	9.51 ± 0.05	6.05 ± 0.13	1.08 ± 0.04	5010
211395962	108.45 ± 2.29	10.01 ± 0.05	5.69 ± 0.16	1.04 ± 0.05	4853
211400524	151.78 ± 1.06	12.64 ± 0.06	5.16 ± 0.1	1.21 ± 0.04	4959
211401305	113.2 ± 0.94	9.88 ± 0.04	6.27 ± 0.12	1.33 ± 0.05	5032
211403606	149.15 ± 1.64	12.56 ± 0.1	5.02 ± 0.12	1.12 ± 0.04	4944
211404980	78.68 ± 1.01	7.65 ± 0.1	7.09 ± 0.2	1.17 ± 0.05	4895
211406144	188.09 ± 5.37	14.49 ± 0.06	4.71 ± 0.16	1.23 ± 0.07	5020
211406549	159.28 ± 1.07	12.73 ± 0.24	5.27 ± 0.17	1.32 ± 0.07	4948
211410185	201.4 ± 0.84	14.9 ± 0.1	5.09 ± 0.1	1.59 ± 0.05	5225
211411711	161.61 ± 1.62	13.57 ± 0.05	4.86 ± 0.1	1.15 ± 0.04	5008
211413430	73.13 ± 0.72	7.22 ± 0.08	7.38 ± 0.19	1.18 ± 0.05	4848
211413607	145.18 ± 1.53	12.45 ± 0.08	4.97 ± 0.11	1.06 ± 0.04	5023
211414061	193.68 ± 2.54	16.32 ± 0.16	4.08 ± 0.1	0.97 ± 0.04	5062
211414367	91.74 ± 2.45	9.32 ± 0.12	5.85 ± 0.21	0.94 ± 0.06	5051
211416288	135.39 ± 1.13	11.25 ± 0.05	5.57 ± 0.12	1.24 ± 0.04	4805
211416749	230.56 ± 0.92	16.65 ± 0.11	4.37 ± 0.09	1.31 ± 0.04	5040
211417815	207.15 ± 2.87	16.41 ± 0.02	4.22 ± 0.09	1.11 ± 0.04	5028
211418946	246.89 ± 2.49	19.92 ± 0.07	3.35 ± 0.07	0.81 ± 0.03	4751
211419226	149.39 ± 1.42	11.51 ± 0.25	6.09 ± 0.22	1.67 ± 0.09	5035
211421985	202.7 ± 1.62	15.47 ± 0.38	4.37 ± 0.17	1.14 ± 0.07	4809
211425629	107.63 ± 0.67	9.7 ± 0.19	5.96 ± 0.2	1.13 ± 0.06	4936
211426713	62.99 ± 0.77	6.51 ± 0.1	7.46 ± 0.23	1.02 ± 0.05	4830
211426934	213.15 ± 2.39	16.62 ± 0.1	4.05 ± 0.09	1.03 ± 0.04	4852
211427693	199.43 ± 2.87	15.06 ± 0.2	4.88 ± 0.14	1.44 ± 0.07	5123
211428734	120.78 ± 1.58	10.5 ± 0.08	5.97 ± 0.15	1.29 ± 0.05	4987
211432977	98.84 ± 3.15	8.62 ± 0.17	7.04 ± 0.32	1.46 ± 0.11	4951
211433194	173.93 ± 1.63	13.39 ± 0.05	5.27 ± 0.11	1.45 ± 0.05	4896
211434065	107.35 ± 0.62	9.74 ± 0.04	5.97 ± 0.12	1.13 ± 0.04	4900
211435372	161.24 ± 1.96	14.25 ± 0.06	4.34 ± 0.09	0.9 ± 0.03	5078
211436513	91.62 ± 2.35	9.29 ± 0.13	5.78 ± 0.21	0.91 ± 0.05	4919
211436963	113.04 ± 0.66	10.11 ± 0.05	5.95 ± 0.12	1.2 ± 0.04	4960
211437275	129.05 ± 0.71	10.78 ± 0.05	5.93 ± 0.11	1.35 ± 0.04	4933
211439170	104.58 ± 0.82	9.82 ± 0.07	5.81 ± 0.12	1.05 ± 0.04	4944
211441403	174.04 ± 4.06	13.72 ± 0.13	5.03 ± 0.16	1.32 ± 0.07	4988
211467466	110.23 ± 1.14	9.48 ± 0.04	6.4 ± 0.14	1.33 ± 0.05	4957
211479995	63.53 ± 1.51	6.49 ± 0.03	7.88 ± 0.24	1.17 ± 0.06	4888
211481212	127.18 ± 0.8	11.01 ± 0.04	5.6 ± 0.11	1.19 ± 0.04	4970
211481840	104.41 ± 1.02	9.6 ± 0.06	5.99 ± 0.13	1.11 ± 0.04	4923

Continued on next page

Table A.1 – continued from previous page

EPIC ID	$\nu_{\max}$ (μHz)	$\Delta\nu$ (μHz)	Radius ($R_\odot$)	Mass ($M_\odot$)	T_{eff} (K)
211482861	136.77 ± 1.2	10.82 ± 0.11	6.43 ± 0.16	1.71 ± 0.07	4997
211483677	182.2 ± 1.62	14.92 ± 0.22	4.5 ± 0.13	1.1 ± 0.05	4956
211488208	232.14 ± 2.53	17.8 ± 0.05	4.05 ± 0.08	1.15 ± 0.04	5132
211488223	77.87 ± 1.22	7.38 ± 0.07	7.43 ± 0.2	1.27 ± 0.06	4869
211489243	234.62 ± 1.84	18.04 ± 0.5	3.92 ± 0.17	1.08 ± 0.07	4995
211490280	89.02 ± 1.23	8.71 ± 0.09	6.42 ± 0.17	1.1 ± 0.05	5006
211490330	118.46 ± 0.54	10.54 ± 0.05	5.72 ± 0.11	1.16 ± 0.04	4947
211490818	210.93 ± 1.96	16.91 ± 0.04	4.06 ± 0.08	1.04 ± 0.04	4973
211491044	146.79 ± 1.82	11.9 ± 0.07	5.73 ± 0.13	1.46 ± 0.06	5196
211491091	79.31 ± 1.1	7.94 ± 0.14	6.81 ± 0.23	1.1 ± 0.06	5028
211497301	231.63 ± 1.15	17.82 ± 0.05	3.98 ± 0.07	1.1 ± 0.04	4953
211500849	139.42 ± 1.2	11.91 ± 0.04	5.25 ± 0.11	1.14 ± 0.04	4862
211501235	63.66 ± 0.53	6.8 ± 0.19	7.47 ± 0.33	1.06 ± 0.07	4979
211501526	85.33 ± 0.81	7.67 ± 0.03	7.56 ± 0.16	1.44 ± 0.05	4770
211503152	113.2 ± 0.85	9.55 ± 0.06	6.66 ± 0.14	1.5 ± 0.05	5095
211503295	71.1 ± 0.67	7.16 ± 0.07	7.42 ± 0.18	1.17 ± 0.05	4930
211503398	106.73 ± 2.12	9.94 ± 0.1	5.83 ± 0.17	1.08 ± 0.05	5005
211503597	195.08 ± 2.23	15.43 ± 0.07	4.38 ± 0.1	1.11 ± 0.04	4888
211503657	184.9 ± 1.79	14.12 ± 0.09	5.07 ± 0.11	1.43 ± 0.05	5129
211503675	263.6 ± 5.01	19.16 ± 0.4	3.93 ± 0.15	1.22 ± 0.07	5080
211504012	71.67 ± 0.65	7.26 ± 0.06	7.35 ± 0.17	1.16 ± 0.04	4936
211504733	119.16 ± 1.72	9.74 ± 0.11	6.6 ± 0.18	1.54 ± 0.07	4933
211505876	168.56 ± 1.02	13.59 ± 0.04	4.81 ± 0.09	1.16 ± 0.04	4982
211507088	75.06 ± 0.55	7.18 ± 0.07	7.54 ± 0.18	1.26 ± 0.05	4848
211510561	113.39 ± 0.65	10.05 ± 0.05	5.86 ± 0.12	1.15 ± 0.04	4885
211510748	289.54 ± 0.0	20.29 ± 0.15	3.93 ± 0.08	1.36 ± 0.04	5124
211512022	137.81 ± 2.1	11.78 ± 0.05	5.24 ± 0.13	1.12 ± 0.05	4872
211512140	163.71 ± 1.01	13.16 ± 0.06	5.14 ± 0.1	1.3 ± 0.04	5039
211513203	97.31 ± 0.76	8.79 ± 0.06	6.84 ± 0.15	1.37 ± 0.05	4979
211513489	219.26 ± 1.12	16.45 ± 0.04	4.11 ± 0.08	1.08 ± 0.03	4873
211514509	213.13 ± 2.22	16.02 ± 0.27	4.55 ± 0.14	1.33 ± 0.07	4849
211514937	60.94 ± 1.02	6.46 ± 0.06	7.98 ± 0.22	1.16 ± 0.05	5034
211516467	99.34 ± 1.68	8.81 ± 0.09	6.72 ± 0.19	1.33 ± 0.06	4881
211518574	241.11 ± 2.21	19.26 ± 0.23	3.55 ± 0.09	0.9 ± 0.04	4973
211518751	81.55 ± 0.59	7.92 ± 0.08	6.78 ± 0.16	1.11 ± 0.04	4801
211522310	87.97 ± 0.92	8.38 ± 0.06	6.7 ± 0.15	1.17 ± 0.04	4903
211524654	63.44 ± 0.72	6.55 ± 0.04	7.79 ± 0.17	1.14 ± 0.04	4849
211527363	225.88 ± 1.58	17.72 ± 0.03	4.12 ± 0.08	1.17 ± 0.04	5174
211527861	108.42 ± 0.83	9.92 ± 0.09	6.01 ± 0.14	1.18 ± 0.04	5026
211528979	85.32 ± 0.81	8.52 ± 0.05	6.49 ± 0.14	1.08 ± 0.04	4948
211529813	88.66 ± 0.61	8.35 ± 0.05	6.69 ± 0.14	1.17 ± 0.04	4934
211529943	107.23 ± 1.77	9.77 ± 0.03	5.9 ± 0.15	1.11 ± 0.05	4839
211530141	99.93 ± 0.54	8.81 ± 0.06	6.6 ± 0.14	1.28 ± 0.05	4754
211530973	175.3 ± 1.71	15.28 ± 0.41	4.21 ± 0.18	0.93 ± 0.06	5160
211531005	129.87 ± 0.87	10.94 ± 0.04	5.66 ± 0.11	1.23 ± 0.04	4813
211531780	103.8 ± 1.71	9.13 ± 0.08	6.77 ± 0.18	1.43 ± 0.06	5110
211534167	94.85 ± 1.0	9.16 ± 0.19	6.17 ± 0.22	1.08 ± 0.06	4955
211535133	152.91 ± 0.87	12.43 ± 0.07	5.33 ± 0.11	1.3 ± 0.04	5041
211535288	199.15 ± 2.09	15.07 ± 0.06	4.62 ± 0.1	1.26 ± 0.05	4999
211535748	89.75 ± 0.95	8.59 ± 0.03	6.54 ± 0.14	1.15 ± 0.04	4995
211540713	169.4 ± 1.68	13.44 ± 0.11	4.98 ± 0.11	1.25 ± 0.05	4881
211542268	146.72 ± 1.05	12.77 ± 0.06	4.91 ± 0.1	1.06 ± 0.04	5053
211542700	114.84 ± 0.75	9.73 ± 0.18	6.45 ± 0.21	1.42 ± 0.07	4997
211545116	145.12 ± 1.2	10.73 ± 0.03	6.85 ± 0.13	2.05 ± 0.07	5052
211546117	235.92 ± 2.16	17.28 ± 0.07	4.3 ± 0.09	1.31 ± 0.05	5103
211546164	145.5 ± 1.37	12.32 ± 0.07	5.24 ± 0.11	1.2 ± 0.04	5093
211546236	193.41 ± 1.69	16.02 ± 0.06	4.15 ± 0.08	0.99 ± 0.03	4928
211547053	241.25 ± 1.33	17.75 ± 0.1	3.97 ± 0.08	1.12 ± 0.04	4854
211547836	104.35 ± 1.06	8.81 ± 0.04	7.09 ± 0.15	1.56 ± 0.06	4894
211550523	143.01 ± 1.23	12.65 ± 0.03	4.95 ± 0.1	1.05 ± 0.04	4999
211551707	168.68 ± 2.04	12.98 ± 0.07	5.38 ± 0.12	1.46 ± 0.06	4961

Continued on next page

Table A.1 – continued from previous page

EPIC ID	$\nu_{\max}$ (μHz)	$\Delta\nu$ (μHz)	Radius ($R_\odot$)	Mass ($M_\odot$)	$T_{\rm eff}$ (K)
211552466	125.54 ± 0.97	10.56 ± 0.03	5.83 ± 0.12	1.26 ± 0.04	4744
211555699	108.56 ± 0.86	9.47 ± 0.13	6.28 ± 0.17	1.26 ± 0.05	4860
211556356	246.74 ± 0.05	19.26 ± 0.12	3.68 ± 0.07	1.0 ± 0.03	5012
211558985	173.78 ± 1.49	13.87 ± 0.08	5.07 ± 0.1	1.36 ± 0.05	5301
211561946	225.27 ± 2.76	16.57 ± 0.14	4.4 ± 0.11	1.31 ± 0.05	5151
211565001	167.8 ± 0.94	13.42 ± 0.05	4.96 ± 0.1	1.23 ± 0.04	4899
211565649	148.07 ± 1.3	12.34 ± 0.05	5.07 ± 0.1	1.12 ± 0.04	4883
211566875	93.3 ± 1.12	8.18 ± 0.06	7.3 ± 0.17	1.47 ± 0.06	4951
211568691	192.88 ± 0.89	15.62 ± 0.05	4.4 ± 0.08	1.13 ± 0.04	5017
211569727	71.79 ± 0.89	7.33 ± 0.06	6.91 ± 0.17	1.01 ± 0.04	4730
211571114	125.4 ± 2.12	10.46 ± 0.05	6.16 ± 0.15	1.43 ± 0.06	5120
211572684	184.12 ± 3.9	14.99 ± 0.1	4.42 ± 0.13	1.07 ± 0.05	5029
211573126	243.73 ± 2.0	18.07 ± 0.37	3.94 ± 0.14	1.12 ± 0.06	4991
211573268	58.76 ± 0.93	6.29 ± 0.04	7.9 ± 0.2	1.09 ± 0.05	4878
211574947	141.3 ± 0.93	11.81 ± 0.06	5.41 ± 0.11	1.24 ± 0.04	4854
211578178	79.37 ± 1.04	7.88 ± 0.07	6.79 ± 0.17	1.09 ± 0.05	4931
211578654	117.95 ± 0.88	9.33 ± 0.14	7.12 ± 0.2	1.77 ± 0.08	4929
211582342	86.93 ± 3.07	8.27 ± 0.09	6.89 ± 0.29	1.23 ± 0.09	4973
211582529	181.73 ± 3.17	14.42 ± 0.19	4.71 ± 0.14	1.2 ± 0.06	5124
211582680	231.43 ± 2.34	16.82 ± 0.26	4.39 ± 0.13	1.33 ± 0.06	4855
211582801	197.52 ± 4.23	15.42 ± 0.11	4.45 ± 0.13	1.17 ± 0.06	4921
211583365	75.68 ± 1.29	7.01 ± 0.06	7.77 ± 0.21	1.33 ± 0.06	4805
211583401	82.82 ± 0.6	7.45 ± 0.07	7.78 ± 0.18	1.48 ± 0.06	4918
211583429	67.37 ± 0.69	6.92 ± 0.09	7.5 ± 0.2	1.13 ± 0.05	4910
211583795	144.55 ± 0.92	12.38 ± 0.05	4.99 ± 0.1	1.06 ± 0.04	4945
211593620	220.42 ± 3.49	16.97 ± 0.11	4.27 ± 0.11	1.21 ± 0.05	5084
211594491	215.96 ± 2.38	17.2 ± 0.24	4.01 ± 0.11	1.04 ± 0.05	5021
211597156	126.69 ± 1.01	10.69 ± 0.07	5.82 ± 0.12	1.27 ± 0.05	4846
211601757	124.63 ± 1.32	11.55 ± 0.15	5.19 ± 0.14	1.01 ± 0.04	5022
211602827	149.59 ± 1.64	12.53 ± 0.06	5.2 ± 0.11	1.21 ± 0.04	5024
211604162	103.67 ± 0.62	9.56 ± 0.04	6.08 ± 0.12	1.14 ± 0.04	4997
211605168	102.74 ± 0.72	9.86 ± 0.04	5.56 ± 0.11	0.94 ± 0.03	4896
211605895	294.33 ± 1.78	20.54 ± 0.03	3.7 ± 0.07	1.2 ± 0.04	4863
211606477	123.63 ± 1.15	10.67 ± 0.04	5.78 ± 0.12	1.23 ± 0.04	5046
211606943	94.72 ± 0.65	8.32 ± 0.04	7.0 ± 0.14	1.36 ± 0.05	4977
211607740	113.34 ± 1.8	10.12 ± 0.12	6.0 ± 0.17	1.22 ± 0.06	5000
211609177	195.42 ± 0.87	15.51 ± 0.03	4.44 ± 0.08	1.15 ± 0.04	4845
211609684	225.88 ± 1.37	15.75 ± 0.05	4.96 ± 0.09	1.67 ± 0.05	5145
211609959	172.43 ± 0.8	14.35 ± 0.05	4.55 ± 0.08	1.07 ± 0.03	5007
211613243	187.61 ± 1.33	15.05 ± 0.1	4.58 ± 0.09	1.18 ± 0.04	5079
211614234	190.88 ± 1.83	15.87 ± 0.04	4.11 ± 0.08	0.96 ± 0.03	4962
211615544	218.1 ± 1.29	17.43 ± 0.06	4.03 ± 0.07	1.07 ± 0.03	5157
211617832	183.06 ± 0.83	14.0 ± 0.09	4.95 ± 0.1	1.34 ± 0.05	4917
211618612	240.41 ± 2.01	18.12 ± 0.05	3.9 ± 0.08	1.09 ± 0.04	4923
211618659	170.81 ± 1.26	13.15 ± 0.33	5.45 ± 0.22	1.54 ± 0.09	5246
211620134	94.9 ± 2.03	8.49 ± 0.07	6.77 ± 0.2	1.28 ± 0.07	4928
211623043	104.02 ± 0.43	9.53 ± 0.03	5.9 ± 0.11	1.06 ± 0.03	4728
211623945	186.77 ± 1.99	15.03 ± 0.09	4.4 ± 0.1	1.07 ± 0.04	4975
211624966	162.87 ± 0.73	13.15 ± 0.05	5.03 ± 0.09	1.23 ± 0.04	5018
211626302	218.42 ± 1.59	16.83 ± 0.15	4.23 ± 0.09	1.17 ± 0.04	5046
211626429	228.27 ± 4.21	17.99 ± 0.2	4.01 ± 0.12	1.12 ± 0.05	5181
211626707	72.52 ± 0.8	7.4 ± 0.05	7.16 ± 0.16	1.11 ± 0.04	4991
211626748	190.9 ± 3.63	14.68 ± 0.18	4.71 ± 0.15	1.26 ± 0.06	5008
211627270	168.17 ± 0.95	14.01 ± 0.04	4.5 ± 0.09	1.0 ± 0.03	4841
211627314	189.66 ± 1.0	14.95 ± 0.04	4.46 ± 0.08	1.11 ± 0.04	4808
211627934	138.12 ± 0.88	11.29 ± 0.06	5.53 ± 0.11	1.23 ± 0.04	4878
211630302	193.01 ± 5.33	16.16 ± 0.21	4.11 ± 0.15	0.98 ± 0.06	5173
211630894	62.44 ± 1.38	6.42 ± 0.09	7.88 ± 0.27	1.14 ± 0.06	4852
211631043	139.29 ± 1.1	11.8 ± 0.1	5.18 ± 0.12	1.1 ± 0.04	4897
211631213	60.85 ± 0.74	6.49 ± 0.04	7.6 ± 0.17	1.04 ± 0.04	4911
211632586	116.2 ± 0.72	10.5 ± 0.05	5.61 ± 0.11	1.09 ± 0.04	4861

Continued on next page

Table A.1 – continued from previous page

EPIC ID	$\nu_{\max}$ (μHz)	$\Delta\nu$ (μHz)	Radius ($R_\odot$)	Mass ($M_\odot$)	$T_{\rm eff}$ (K)
211634588	123.85 ± 0.84	10.85 ± 0.08	5.5 ± 0.12	1.11 ± 0.04	4736
211637875	192.73 ± 1.5	14.61 ± 0.05	4.99 ± 0.1	1.45 ± 0.05	5229
211638329	75.93 ± 0.56	7.32 ± 0.05	7.03 ± 0.16	1.08 ± 0.04	4724
211640755	114.82 ± 2.63	10.22 ± 0.08	5.73 ± 0.18	1.11 ± 0.06	5031
211640925	159.56 ± 0.42	12.94 ± 0.03	5.09 ± 0.09	1.23 ± 0.04	4778
211640956	66.77 ± 0.46	6.8 ± 0.11	7.44 ± 0.21	1.09 ± 0.05	5097
211641593	183.18 ± 1.78	14.72 ± 0.29	4.53 ± 0.15	1.12 ± 0.06	4916
211645614	99.73 ± 3.19	9.52 ± 0.2	6.32 ± 0.3	1.23 ± 0.09	5080
211674232	78.61 ± 0.69	7.6 ± 0.03	7.17 ± 0.15	1.2 ± 0.04	4856
211677344	166.31 ± 1.22	14.22 ± 0.04	4.63 ± 0.09	1.08 ± 0.04	5091
211678182	124.02 ± 0.82	11.07 ± 0.04	5.46 ± 0.11	1.1 ± 0.04	4936
211678470	161.32 ± 1.05	13.22 ± 0.03	4.81 ± 0.09	1.1 ± 0.04	4777
211679122	173.08 ± 0.92	14.53 ± 0.1	4.55 ± 0.09	1.08 ± 0.04	5144
211679357	137.42 ± 0.71	11.64 ± 0.08	5.38 ± 0.11	1.18 ± 0.04	4940
211680013	155.59 ± 0.85	13.02 ± 0.11	4.87 ± 0.11	1.09 ± 0.04	4806
211683902	126.06 ± 1.06	11.29 ± 0.11	5.29 ± 0.13	1.05 ± 0.04	4962
211684602	140.42 ± 2.33	12.05 ± 0.1	5.3 ± 0.14	1.19 ± 0.05	5104
211685442	188.79 ± 3.21	13.25 ± 0.34	6.05 ± 0.26	2.11 ± 0.14	5376
211688047	228.66 ± 2.32	18.07 ± 0.06	3.93 ± 0.08	1.07 ± 0.04	5248
211688159	171.41 ± 0.57	14.16 ± 0.06	4.65 ± 0.09	1.11 ± 0.04	5008
211691174	172.01 ± 6.32	13.7 ± 0.03	5.06 ± 0.21	1.33 ± 0.09	5052
211691448	157.48 ± 1.85	12.7 ± 0.07	5.19 ± 0.11	1.26 ± 0.05	5051
211692043	221.86 ± 1.76	16.59 ± 0.05	4.28 ± 0.08	1.21 ± 0.04	4878
211692188	95.66 ± 0.81	9.01 ± 0.05	6.6 ± 0.14	1.26 ± 0.04	4968
211692665	118.02 ± 0.72	9.88 ± 0.04	6.17 ± 0.12	1.31 ± 0.04	4792
211693588	159.63 ± 1.28	13.47 ± 0.04	4.92 ± 0.1	1.17 ± 0.04	5091
211693712	126.42 ± 1.3	11.05 ± 0.07	5.59 ± 0.12	1.18 ± 0.04	5091
211693752	71.52 ± 0.55	7.21 ± 0.06	7.46 ± 0.17	1.19 ± 0.04	4906
211694517	116.78 ± 0.82	10.23 ± 0.06	5.75 ± 0.12	1.13 ± 0.04	4821
211696694	148.83 ± 4.97	12.69 ± 0.09	5.08 ± 0.2	1.16 ± 0.08	4973
211696736	223.68 ± 0.83	17.01 ± 0.04	4.13 ± 0.08	1.13 ± 0.04	4884
211697610	215.64 ± 3.48	18.16 ± 0.08	3.66 ± 0.09	0.87 ± 0.04	4933
211697650	107.32 ± 1.41	10.17 ± 0.1	5.67 ± 0.15	1.03 ± 0.04	4952
211698152	145.29 ± 1.07	12.26 ± 0.05	4.93 ± 0.1	1.03 ± 0.04	4758
211701176	84.04 ± 0.61	8.09 ± 0.14	6.7 ± 0.21	1.11 ± 0.05	4866
211701416	228.0 ± 1.83	16.9 ± 0.27	4.29 ± 0.13	1.25 ± 0.06	5072
211702042	90.97 ± 0.78	8.01 ± 0.13	7.65 ± 0.23	1.6 ± 0.08	5026
211702423	156.66 ± 0.52	12.63 ± 0.03	5.03 ± 0.09	1.16 ± 0.03	5375
211703134	169.89 ± 2.04	13.67 ± 0.11	4.86 ± 0.12	1.2 ± 0.05	5017
211704034	83.14 ± 0.78	7.9 ± 0.04	6.92 ± 0.15	1.17 ± 0.04	4859
211704166	175.66 ± 0.85	14.31 ± 0.06	4.53 ± 0.09	1.06 ± 0.03	4884
211704574	205.14 ± 1.07	15.79 ± 0.08	4.24 ± 0.08	1.08 ± 0.04	4909
211705076	99.76 ± 0.6	9.01 ± 0.04	6.36 ± 0.13	1.19 ± 0.04	4782
211705781	119.72 ± 1.38	10.62 ± 0.05	5.84 ± 0.13	1.23 ± 0.05	5067
211706667	249.8 ± 2.48	18.01 ± 0.1	4.08 ± 0.09	1.23 ± 0.04	5024
211706751	153.62 ± 1.54	12.19 ± 0.04	5.49 ± 0.11	1.38 ± 0.05	5131
211707086	219.34 ± 1.21	15.8 ± 0.05	4.72 ± 0.09	1.46 ± 0.05	4877
211710466	105.48 ± 0.9	9.51 ± 0.05	6.06 ± 0.12	1.14 ± 0.04	5102
211711111	91.46 ± 0.59	8.9 ± 0.06	6.28 ± 0.13	1.08 ± 0.04	5186
211712410	239.02 ± 2.69	17.36 ± 0.04	4.4 ± 0.09	1.4 ± 0.05	5099
211715704	228.91 ± 1.91	17.48 ± 0.06	4.02 ± 0.08	1.1 ± 0.04	4920
211716332	128.54 ± 1.93	10.44 ± 0.09	6.41 ± 0.17	1.59 ± 0.07	5140
211717478	132.45 ± 0.9	11.31 ± 0.05	5.73 ± 0.11	1.31 ± 0.04	5129
211720691	188.73 ± 1.43	14.92 ± 0.48	4.52 ± 0.22	1.14 ± 0.08	5032
211721075	196.27 ± 1.89	15.29 ± 0.13	4.57 ± 0.11	1.23 ± 0.05	5106
211721145	60.41 ± 1.32	6.56 ± 0.17	7.77 ± 0.36	1.1 ± 0.08	5137
211722159	118.33 ± 0.66	10.56 ± 0.04	5.57 ± 0.11	1.08 ± 0.04	4983
211722412	67.83 ± 0.25	6.75 ± 0.08	7.97 ± 0.19	1.29 ± 0.05	4969
211723444	122.61 ± 0.72	11.07 ± 0.17	5.31 ± 0.15	1.02 ± 0.05	4901
211725403	236.66 ± 3.33	17.62 ± 0.04	4.04 ± 0.09	1.14 ± 0.04	4935
211727496	54.31 ± 0.61	5.93 ± 0.05	7.94 ± 0.19	1.0 ± 0.04	4793

Continued on next page

Table A.1 – continued from previous page

EPIC ID	$\nu_{\max}$ (μHz)	$\Delta\nu$ (μHz)	Radius ($R_{\odot}$)	Mass ($M_{\odot}$)	$T_{\rm eff}$ (K)
211730536	120.08 ± 1.1	10.79 ± 0.07	5.6 ± 0.12	1.13 ± 0.04	5089
211730652	201.33 ± 1.86	15.67 ± 0.05	4.41 ± 0.09	1.17 ± 0.04	4993
211732416	235.9 ± 2.01	17.51 ± 0.1	4.12 ± 0.08	1.19 ± 0.04	5132
211732772	190.7 ± 1.22	14.89 ± 0.07	4.62 ± 0.09	1.22 ± 0.04	4924
211733275	123.66 ± 0.51	10.27 ± 0.04	6.28 ± 0.12	1.46 ± 0.05	4964
211734506	177.58 ± 1.73	14.05 ± 0.07	4.74 ± 0.1	1.18 ± 0.04	5120
211736035	119.43 ± 0.91	10.39 ± 0.05	5.67 ± 0.12	1.12 ± 0.04	4798
211737259	220.26 ± 1.38	16.98 ± 0.08	4.15 ± 0.08	1.13 ± 0.04	5068
211737665	102.15 ± 0.67	9.29 ± 0.05	6.54 ± 0.13	1.32 ± 0.04	5120
211739709	222.71 ± 1.32	16.62 ± 0.08	4.19 ± 0.08	1.15 ± 0.04	4730
211742348	151.37 ± 0.93	12.71 ± 0.07	5.02 ± 0.1	1.13 ± 0.04	5021
211742649	214.74 ± 2.73	17.25 ± 0.12	3.85 ± 0.09	0.94 ± 0.04	5021
211743010	117.23 ± 1.27	9.33 ± 0.1	6.95 ± 0.18	1.67 ± 0.07	4825
211743844	162.03 ± 1.05	13.53 ± 0.05	4.75 ± 0.09	1.09 ± 0.04	4912
211744390	216.77 ± 1.1	16.71 ± 0.06	4.16 ± 0.08	1.12 ± 0.04	5009
211745885	138.87 ± 0.64	12.02 ± 0.27	5.23 ± 0.19	1.14 ± 0.06	5046
211746567	217.0 ± 2.02	17.28 ± 0.05	4.0 ± 0.08	1.04 ± 0.04	5034
211747238	177.53 ± 1.27	14.17 ± 0.07	4.64 ± 0.09	1.13 ± 0.04	4919
211748236	171.75 ± 1.35	13.96 ± 0.08	4.67 ± 0.1	1.11 ± 0.04	4974
211749127	140.83 ± 1.72	11.11 ± 0.05	5.93 ± 0.13	1.46 ± 0.06	4823
211750060	100.38 ± 0.9	9.56 ± 0.1	5.94 ± 0.14	1.05 ± 0.04	4915
211750732	129.75 ± 1.37	10.83 ± 0.06	5.77 ± 0.13	1.28 ± 0.05	4934
211751684	223.04 ± 1.08	16.7 ± 0.14	4.19 ± 0.09	1.16 ± 0.04	4854
211754315	179.02 ± 1.82	14.82 ± 0.27	4.63 ± 0.15	1.17 ± 0.06	5254
211756258	84.11 ± 0.47	8.02 ± 0.22	6.77 ± 0.29	1.14 ± 0.07	4869
211759089	69.11 ± 0.44	6.97 ± 0.08	7.66 ± 0.18	1.21 ± 0.05	5076
211760149	102.45 ± 0.62	9.41 ± 0.05	6.21 ± 0.12	1.18 ± 0.04	4903
211760355	203.76 ± 1.18	15.07 ± 0.08	4.82 ± 0.09	1.42 ± 0.05	5158
211760664	140.52 ± 1.82	11.56 ± 0.15	5.79 ± 0.16	1.42 ± 0.06	5038
211762723	233.95 ± 1.42	17.72 ± 0.06	4.12 ± 0.08	1.19 ± 0.04	5191
211763164	113.52 ± 0.51	10.15 ± 0.05	5.9 ± 0.11	1.18 ± 0.04	4941
211764055	227.24 ± 1.29	17.58 ± 0.08	4.2 ± 0.08	1.23 ± 0.04	5015
211764482	222.39 ± 0.95	16.61 ± 0.11	4.31 ± 0.09	1.23 ± 0.04	5017
211769069	149.49 ± 1.91	13.25 ± 0.21	4.7 ± 0.15	0.99 ± 0.05	4922
211770011	82.43 ± 0.67	7.74 ± 0.06	7.27 ± 0.17	1.29 ± 0.05	4695
211770510	111.58 ± 1.07	10.26 ± 0.06	5.73 ± 0.12	1.09 ± 0.04	5021
211771546	77.3 ± 0.78	7.38 ± 0.05	7.6 ± 0.17	1.33 ± 0.05	5033
211771842	105.74 ± 0.78	9.1 ± 0.12	6.43 ± 0.17	1.27 ± 0.05	4821
211774082	100.51 ± 0.68	9.22 ± 0.05	6.2 ± 0.13	1.14 ± 0.04	4935
211777695	154.11 ± 1.07	12.92 ± 0.03	4.94 ± 0.09	1.12 ± 0.04	4957
211777948	154.38 ± 1.0	11.31 ± 0.21	6.35 ± 0.21	1.85 ± 0.09	4938
211778026	107.12 ± 0.58	9.69 ± 0.03	5.97 ± 0.11	1.13 ± 0.04	4870
211778209	158.51 ± 0.78	13.62 ± 0.04	4.84 ± 0.09	1.13 ± 0.04	5073
211781371	164.0 ± 0.79	13.19 ± 0.03	4.88 ± 0.09	1.15 ± 0.04	4827
211781446	225.98 ± 1.31	16.69 ± 0.05	4.44 ± 0.08	1.34 ± 0.04	5083
211782243	109.49 ± 0.74	9.64 ± 0.05	6.31 ± 0.13	1.3 ± 0.04	4905
211785093	214.09 ± 0.86	17.01 ± 0.06	4.13 ± 0.08	1.11 ± 0.03	5069
211785379	129.92 ± 0.94	10.9 ± 0.05	5.68 ± 0.12	1.24 ± 0.04	4809
211787053	141.93 ± 1.85	12.11 ± 0.04	5.2 ± 0.11	1.14 ± 0.04	5096
211790237	148.4 ± 2.92	12.08 ± 0.06	5.44 ± 0.15	1.31 ± 0.06	4813
211791171	232.95 ± 1.39	17.14 ± 0.28	4.23 ± 0.12	1.24 ± 0.06	5054
211791574	97.83 ± 0.86	8.92 ± 0.05	6.53 ± 0.14	1.24 ± 0.04	4931
211792032	96.22 ± 0.71	8.1 ± 0.09	7.88 ± 0.2	1.79 ± 0.07	5106
211793455	161.22 ± 0.88	12.02 ± 0.09	6.06 ± 0.13	1.79 ± 0.06	5076
211793489	179.53 ± 1.16	14.66 ± 0.08	4.5 ± 0.09	1.09 ± 0.04	5037
211794143	108.74 ± 0.87	9.69 ± 0.03	6.31 ± 0.12	1.3 ± 0.04	5102
211795689	157.24 ± 0.72	12.26 ± 0.06	5.65 ± 0.11	1.51 ± 0.05	5003
211798489	168.3 ± 1.52	13.71 ± 0.03	4.87 ± 0.1	1.2 ± 0.04	5084
211798515	168.25 ± 1.18	13.86 ± 0.15	4.69 ± 0.11	1.1 ± 0.04	5029
211801677	135.63 ± 1.81	11.83 ± 0.04	5.31 ± 0.12	1.15 ± 0.04	5111
211802496	186.52 ± 4.07	15.58 ± 0.16	4.19 ± 0.13	0.98 ± 0.05	5059

Continued on next page

Table A.1 – continued from previous page

EPIC ID	$\nu_{\max}$ (μHz)	$\Delta\nu$ (μHz)	Radius ($R_\odot$)	Mass ($M_\odot$)	$T_{\rm eff}$ (K)
211803045	196.2 ± 1.94	15.79 ± 0.09	4.5 ± 0.09	1.22 ± 0.04	5267
211803126	162.09 ± 0.97	13.19 ± 0.04	5.13 ± 0.1	1.29 ± 0.04	5009
211804222	103.41 ± 0.78	8.96 ± 0.06	7.02 ± 0.15	1.54 ± 0.05	5127
211806545	158.85 ± 0.53	12.83 ± 0.08	5.11 ± 0.1	1.23 ± 0.04	4885
211806560	158.85 ± 0.48	12.83 ± 0.1	5.11 ± 0.11	1.23 ± 0.04	4885
211806774	155.31 ± 0.98	12.95 ± 0.03	4.9 ± 0.09	1.11 ± 0.04	4932
211807517	112.58 ± 0.43	10.09 ± 0.09	5.96 ± 0.13	1.19 ± 0.04	4893
211809559	153.01 ± 0.66	12.35 ± 0.05	5.45 ± 0.1	1.37 ± 0.04	4933
211810367	256.34 ± 2.17	18.83 ± 0.33	3.91 ± 0.12	1.17 ± 0.06	5020
211811261	111.58 ± 0.82	9.27 ± 0.2	6.76 ± 0.24	1.5 ± 0.08	4877
211811597	171.15 ± 1.44	14.31 ± 0.14	4.6 ± 0.11	1.09 ± 0.04	4975
211813244	145.9 ± 1.65	12.05 ± 0.04	5.63 ± 0.12	1.41 ± 0.05	5072
211813917	68.34 ± 0.49	6.94 ± 0.04	7.42 ± 0.15	1.11 ± 0.04	4846
211817088	159.79 ± 1.51	12.33 ± 0.08	5.56 ± 0.12	1.47 ± 0.05	5025
211821939	124.66 ± 2.04	10.86 ± 0.1	5.78 ± 0.16	1.25 ± 0.06	5090
211825014	221.13 ± 1.98	17.12 ± 0.15	4.18 ± 0.1	1.16 ± 0.04	5085
211826360	145.2 ± 1.3	12.36 ± 0.08	5.06 ± 0.11	1.1 ± 0.04	4954
211827785	211.15 ± 1.65	16.65 ± 0.19	4.18 ± 0.1	1.11 ± 0.04	4952
211828487	72.36 ± 1.84	7.16 ± 0.08	7.6 ± 0.26	1.25 ± 0.07	4948
211828903	187.91 ± 0.87	14.82 ± 0.04	4.78 ± 0.09	1.31 ± 0.04	4988
211829951	151.63 ± 1.0	12.41 ± 0.08	5.4 ± 0.11	1.33 ± 0.05	5099
211830799	169.24 ± 0.51	13.72 ± 0.06	4.91 ± 0.09	1.22 ± 0.04	5000
211831510	218.23 ± 1.23	16.34 ± 0.05	4.42 ± 0.08	1.28 ± 0.04	5180
211835265	158.8 ± 4.06	13.3 ± 0.06	4.74 ± 0.15	1.06 ± 0.06	4946
211836089	206.77 ± 2.55	16.15 ± 0.07	4.25 ± 0.09	1.11 ± 0.04	4964
211837297	71.23 ± 2.22	7.47 ± 0.03	6.71 ± 0.24	0.95 ± 0.06	4801
211837339	119.3 ± 0.55	10.11 ± 0.04	6.06 ± 0.11	1.29 ± 0.04	4995
211839527	262.66 ± 3.37	18.44 ± 0.55	4.07 ± 0.19	1.29 ± 0.09	4837
211841387	171.43 ± 1.69	13.72 ± 0.05	5.2 ± 0.11	1.42 ± 0.05	4979
211841434	175.09 ± 0.87	14.13 ± 0.11	4.79 ± 0.1	1.21 ± 0.04	5038
211841710	110.71 ± 1.14	9.17 ± 0.22	7.03 ± 0.27	1.63 ± 0.1	4986
211844412	114.25 ± 0.68	9.74 ± 0.06	6.27 ± 0.13	1.32 ± 0.05	4700
211845267	80.68 ± 0.61	7.62 ± 0.05	7.65 ± 0.16	1.43 ± 0.05	5146
211846174	57.44 ± 0.53	6.34 ± 0.06	7.72 ± 0.19	1.02 ± 0.04	4791
211880564	149.91 ± 1.69	12.57 ± 0.04	5.04 ± 0.11	1.13 ± 0.04	4976
211881057	179.92 ± 1.92	14.55 ± 0.1	4.52 ± 0.1	1.09 ± 0.04	4855
211882848	77.81 ± 0.44	7.31 ± 0.15	7.37 ± 0.26	1.23 ± 0.06	4821
211884233	184.84 ± 1.23	15.46 ± 0.05	4.39 ± 0.08	1.09 ± 0.04	5118
211885863	117.17 ± 1.26	10.67 ± 0.1	5.69 ± 0.14	1.14 ± 0.05	5213
211886119	101.67 ± 0.88	9.27 ± 0.07	6.25 ± 0.14	1.18 ± 0.04	4919
211886586	91.21 ± 0.64	8.25 ± 0.04	7.24 ± 0.15	1.44 ± 0.05	4984
211891545	60.6 ± 0.6	6.73 ± 0.07	7.81 ± 0.19	1.15 ± 0.04	5328
211892429	177.48 ± 2.25	13.93 ± 0.33	5.0 ± 0.2	1.34 ± 0.08	5044
211892512	219.9 ± 0.98	17.87 ± 0.04	3.85 ± 0.07	0.98 ± 0.03	4927
211893262	126.67 ± 1.63	11.18 ± 0.05	5.61 ± 0.12	1.2 ± 0.05	5143
211894254	165.67 ± 2.05	14.0 ± 0.1	4.7 ± 0.11	1.1 ± 0.04	5011
211896896	197.43 ± 4.64	15.72 ± 0.12	4.5 ± 0.14	1.22 ± 0.06	5110
211897908	187.5 ± 1.03	15.25 ± 0.05	4.53 ± 0.08	1.16 ± 0.04	5064
211898141	131.12 ± 0.77	10.99 ± 0.05	5.58 ± 0.11	1.2 ± 0.04	4746
211898174	137.1 ± 1.74	11.8 ± 0.05	5.3 ± 0.12	1.15 ± 0.04	4968
211898648	225.1 ± 1.31	16.28 ± 0.25	4.49 ± 0.13	1.35 ± 0.06	4874
211899203	161.43 ± 1.06	13.47 ± 0.11	4.87 ± 0.11	1.15 ± 0.04	4950
211899798	62.2 ± 0.82	6.48 ± 0.05	7.57 ± 0.19	1.04 ± 0.04	4777
211903419	196.0 ± 2.01	15.49 ± 0.15	4.34 ± 0.11	1.09 ± 0.04	4870
211904928	88.75 ± 2.83	8.57 ± 0.15	6.7 ± 0.3	1.2 ± 0.09	5016
211905228	119.37 ± 1.2	11.06 ± 0.07	5.27 ± 0.11	0.98 ± 0.04	5111
211906415	170.51 ± 1.11	12.96 ± 0.04	5.31 ± 0.1	1.42 ± 0.05	5030
211906947	242.84 ± 4.58	18.42 ± 0.09	3.75 ± 0.1	1.0 ± 0.05	4809
211907092	119.91 ± 0.94	10.57 ± 0.05	5.55 ± 0.11	1.08 ± 0.04	5086
211908570	86.66 ± 0.63	8.26 ± 0.05	6.84 ± 0.14	1.21 ± 0.04	4921
211908784	148.82 ± 1.57	12.64 ± 0.04	5.12 ± 0.11	1.17 ± 0.04	4952

Continued on next page

Table A.1 – continued from previous page

EPIC ID	$\nu_{\max}$ (μHz)	$\Delta\nu$ (μHz)	Radius ($R_\odot$)	Mass ($M_\odot$)	$T_{\rm eff}$ (K)
211909021	122.3 ± 1.37	10.69 ± 0.07	5.81 ± 0.13	1.24 ± 0.05	5039
211910916	99.61 ± 1.08	9.48 ± 0.03	5.93 ± 0.13	1.04 ± 0.04	4894
211911400	231.27 ± 1.17	18.05 ± 0.06	3.99 ± 0.07	1.12 ± 0.04	4982
211912252	151.86 ± 0.69	12.31 ± 0.03	5.19 ± 0.1	1.2 ± 0.04	4835
211912867	89.31 ± 0.69	8.08 ± 0.07	7.49 ± 0.17	1.51 ± 0.06	5028
211913059	98.9 ± 0.62	8.84 ± 0.04	6.5 ± 0.13	1.23 ± 0.04	4709
211913099	99.54 ± 0.79	9.33 ± 0.13	6.22 ± 0.17	1.15 ± 0.05	4860
211914544	158.32 ± 0.84	12.52 ± 0.07	5.29 ± 0.11	1.31 ± 0.04	4829
211914760	120.17 ± 0.96	11.08 ± 0.09	5.54 ± 0.12	1.12 ± 0.04	5282
211914776	93.17 ± 1.03	8.1 ± 0.05	7.41 ± 0.17	1.52 ± 0.06	4962
211915402	109.13 ± 0.82	10.12 ± 0.04	5.86 ± 0.11	1.13 ± 0.04	5011
211915987	238.54 ± 1.55	18.04 ± 0.07	4.0 ± 0.08	1.14 ± 0.04	5063
211916495	250.57 ± 3.56	18.57 ± 0.27	3.93 ± 0.12	1.16 ± 0.06	4889
211917597	92.56 ± 0.86	8.27 ± 0.06	7.09 ± 0.16	1.38 ± 0.05	4873
211919373	68.0 ± 0.58	6.88 ± 0.03	7.52 ± 0.16	1.14 ± 0.04	4786
211920507	174.64 ± 0.78	14.23 ± 0.06	4.73 ± 0.09	1.18 ± 0.04	5070
211920608	133.06 ± 0.78	11.0 ± 0.05	5.78 ± 0.11	1.32 ± 0.04	4936
211920811	98.75 ± 1.07	8.61 ± 0.1	6.8 ± 0.18	1.34 ± 0.06	4836
211921055	77.24 ± 0.7	7.74 ± 0.15	6.86 ± 0.23	1.08 ± 0.06	4928
211922248	60.44 ± 0.78	6.74 ± 0.05	7.17 ± 0.17	0.92 ± 0.04	4896
211922862	130.67 ± 1.54	10.48 ± 0.07	6.46 ± 0.15	1.65 ± 0.06	5111
211925044	153.47 ± 1.21	13.07 ± 0.05	4.85 ± 0.1	1.08 ± 0.04	5003
211926203	207.01 ± 3.17	16.01 ± 0.21	4.5 ± 0.13	1.27 ± 0.06	5177
211928450	78.89 ± 1.24	7.44 ± 0.05	7.49 ± 0.19	1.31 ± 0.06	4792
211928836	127.34 ± 0.55	10.7 ± 0.07	5.65 ± 0.12	1.18 ± 0.04	4725
211928896	151.04 ± 1.67	12.86 ± 0.06	5.04 ± 0.11	1.16 ± 0.04	4912
211929084	92.52 ± 0.45	9.24 ± 0.04	6.1 ± 0.11	1.04 ± 0.03	5062
211929298	171.94 ± 0.67	14.25 ± 0.2	4.61 ± 0.12	1.09 ± 0.05	4858
211935353	195.28 ± 1.34	15.4 ± 0.07	4.63 ± 0.09	1.27 ± 0.04	5163
211936162	157.68 ± 2.52	12.99 ± 0.04	5.19 ± 0.12	1.28 ± 0.05	5211
211937330	147.03 ± 0.83	11.89 ± 0.05	5.44 ± 0.1	1.29 ± 0.04	4996
211937804	118.46 ± 0.72	10.62 ± 0.09	5.72 ± 0.13	1.16 ± 0.04	5022
211939542	57.84 ± 0.66	6.35 ± 0.06	7.82 ± 0.19	1.06 ± 0.04	4925
211940736	179.21 ± 1.07	14.11 ± 0.07	4.74 ± 0.09	1.2 ± 0.04	4883
211942783	95.2 ± 0.72	9.21 ± 0.14	6.04 ± 0.18	1.03 ± 0.05	4790
211944175	130.09 ± 1.29	10.7 ± 0.05	6.1 ± 0.13	1.45 ± 0.05	5067
211946192	104.71 ± 0.26	9.03 ± 0.17	6.78 ± 0.21	1.43 ± 0.07	5146
211947009	167.1 ± 1.02	13.96 ± 0.06	4.63 ± 0.09	1.07 ± 0.04	4881
211948914	113.65 ± 0.9	10.32 ± 0.05	5.74 ± 0.12	1.12 ± 0.04	4998
211949149	117.01 ± 0.69	10.7 ± 0.09	5.45 ± 0.12	1.03 ± 0.04	4879
211950176	86.37 ± 0.74	8.24 ± 0.05	6.81 ± 0.14	1.19 ± 0.04	5058
211950307	76.04 ± 0.54	7.14 ± 0.05	7.82 ± 0.17	1.38 ± 0.05	4967
211951191	167.18 ± 1.18	13.31 ± 0.03	4.98 ± 0.1	1.23 ± 0.04	4893
211951502	100.54 ± 0.79	9.34 ± 0.04	5.96 ± 0.12	1.05 ± 0.04	4846
211952120	85.13 ± 0.48	8.09 ± 0.06	6.81 ± 0.15	1.17 ± 0.04	4800
211952899	155.18 ± 1.05	12.48 ± 0.28	5.44 ± 0.2	1.38 ± 0.08	5067
211955993	88.37 ± 0.98	8.39 ± 0.05	6.57 ± 0.15	1.13 ± 0.04	4925
211957162	161.75 ± 1.77	13.16 ± 0.12	5.01 ± 0.12	1.21 ± 0.05	5020
211958281	259.59 ± 2.12	18.66 ± 0.2	4.02 ± 0.1	1.26 ± 0.05	4926
211959469	111.87 ± 0.42	10.01 ± 0.04	5.91 ± 0.11	1.16 ± 0.04	4978
211959496	76.07 ± 0.77	7.79 ± 0.05	6.42 ± 0.14	0.92 ± 0.03	4809
211960077	149.59 ± 1.67	12.56 ± 0.12	4.91 ± 0.12	1.06 ± 0.04	4825
211960133	79.29 ± 0.43	7.86 ± 0.05	6.92 ± 0.14	1.13 ± 0.04	4961
211960292	217.45 ± 3.32	16.74 ± 0.07	4.11 ± 0.1	1.09 ± 0.04	5029
211963891	108.26 ± 1.51	9.72 ± 0.1	6.32 ± 0.17	1.31 ± 0.06	5197
211965425	159.83 ± 1.89	13.82 ± 0.06	4.66 ± 0.1	1.05 ± 0.04	5032
211965863	86.27 ± 0.76	8.63 ± 0.03	6.49 ± 0.13	1.1 ± 0.04	5063
211966704	180.94 ± 1.28	13.92 ± 0.04	4.8 ± 0.09	1.22 ± 0.04	4843
211966907	127.31 ± 1.5	11.11 ± 0.11	5.64 ± 0.14	1.21 ± 0.05	5097
211968472	151.05 ± 1.68	13.64 ± 0.14	4.53 ± 0.11	0.93 ± 0.04	5069
211968713	196.8 ± 2.49	15.62 ± 0.04	4.47 ± 0.1	1.19 ± 0.04	5083

Continued on next page

Table A.1 – continued from previous page

EPIC ID	$\nu_{\max}$ (μHz)	$\Delta\nu$ (μHz)	Radius ($R_\odot$)	Mass ($M_\odot$)	$T_{\rm eff}$ (K)
211970899	77.67 ± 0.86	7.35 ± 0.07	7.16 ± 0.18	1.15 ± 0.05	4723
211971185	279.9 ± 4.62	20.96 ± 0.07	3.54 ± 0.09	1.06 ± 0.04	5184
211973150	115.68 ± 1.23	10.31 ± 0.05	5.67 ± 0.12	1.1 ± 0.04	4713
211973251	61.4 ± 0.47	6.22 ± 0.07	7.86 ± 0.2	1.1 ± 0.04	4782
211973295	186.57 ± 1.02	15.59 ± 0.03	4.2 ± 0.08	0.98 ± 0.03	4946
211974782	209.96 ± 1.63	16.34 ± 0.04	4.17 ± 0.08	1.08 ± 0.04	5019
211976283	248.65 ± 4.94	18.06 ± 0.37	4.1 ± 0.16	1.25 ± 0.08	4989
211976420	138.0 ± 1.09	10.92 ± 0.03	6.36 ± 0.12	1.69 ± 0.06	5186
211976553	149.27 ± 1.07	12.36 ± 0.05	5.19 ± 0.1	1.19 ± 0.04	4936
211977001	195.05 ± 1.06	14.97 ± 0.04	4.53 ± 0.09	1.18 ± 0.04	4878
211977620	170.91 ± 1.0	14.11 ± 0.22	4.79 ± 0.14	1.19 ± 0.05	5230
211978005	268.92 ± 10.55	18.48 ± 0.08	4.3 ± 0.19	1.5 ± 0.11	5145
211979615	70.55 ± 0.95	6.92 ± 0.08	7.75 ± 0.21	1.26 ± 0.06	4983
211980584	76.91 ± 0.75	7.24 ± 0.12	7.44 ± 0.23	1.24 ± 0.06	4817
211980975	145.25 ± 1.18	12.76 ± 0.05	4.77 ± 0.09	0.98 ± 0.03	5013
211982711	120.73 ± 0.84	10.52 ± 0.05	5.93 ± 0.12	1.28 ± 0.04	5079
211983454	162.82 ± 1.8	14.01 ± 0.07	4.6 ± 0.1	1.04 ± 0.04	5122
211987214	154.2 ± 1.37	12.65 ± 0.04	5.09 ± 0.1	1.18 ± 0.04	4969
211987744	239.41 ± 2.77	17.26 ± 0.09	4.55 ± 0.1	1.52 ± 0.06	5207
211987853	98.48 ± 0.65	8.87 ± 0.11	6.8 ± 0.18	1.37 ± 0.06	4963
211989221	182.86 ± 1.52	15.25 ± 0.04	4.36 ± 0.08	1.04 ± 0.03	5077
211990802	135.06 ± 0.97	11.86 ± 0.04	5.35 ± 0.1	1.17 ± 0.04	5089
211991869	139.65 ± 4.9	11.86 ± 0.15	5.54 ± 0.24	1.3 ± 0.09	5053
211993594	182.26 ± 0.96	14.37 ± 0.09	4.66 ± 0.09	1.18 ± 0.04	4939
211993851	235.05 ± 1.18	17.25 ± 0.05	4.1 ± 0.08	1.16 ± 0.04	4955
211993967	91.95 ± 0.48	8.78 ± 0.11	6.45 ± 0.16	1.14 ± 0.05	4924
211994035	197.14 ± 1.42	14.84 ± 0.04	4.79 ± 0.09	1.35 ± 0.04	4963
211994196	190.58 ± 1.24	14.88 ± 0.03	4.68 ± 0.09	1.25 ± 0.04	5126
211994208	189.07 ± 1.25	14.86 ± 0.08	4.74 ± 0.09	1.28 ± 0.04	5106
211994369	152.29 ± 1.68	12.99 ± 0.11	5.15 ± 0.12	1.24 ± 0.05	5204
211994631	170.54 ± 2.0	13.97 ± 0.08	4.64 ± 0.1	1.09 ± 0.04	5009
211996201	138.64 ± 2.06	11.45 ± 0.05	5.63 ± 0.13	1.31 ± 0.05	4949
211996770	188.33 ± 1.21	15.46 ± 0.05	4.38 ± 0.08	1.09 ± 0.03	5222
211998264	124.95 ± 1.54	10.04 ± 0.04	6.39 ± 0.14	1.5 ± 0.06	4939
211998917	167.05 ± 3.18	13.4 ± 0.02	5.08 ± 0.13	1.3 ± 0.06	5101
211999235	104.93 ± 1.09	9.94 ± 0.22	6.22 ± 0.23	1.26 ± 0.07	4839
211999644	115.98 ± 0.63	10.62 ± 0.04	5.67 ± 0.11	1.12 ± 0.04	4953
212000542	64.56 ± 0.48	6.47 ± 0.05	7.86 ± 0.17	1.17 ± 0.04	4798
212000944	201.85 ± 1.44	15.52 ± 0.06	4.48 ± 0.09	1.21 ± 0.04	4957
212002052	91.81 ± 1.19	8.02 ± 0.1	7.61 ± 0.22	1.59 ± 0.07	4893
212002576	114.97 ± 1.12	10.76 ± 0.05	5.48 ± 0.11	1.03 ± 0.04	5115
212004033	184.81 ± 1.41	15.17 ± 0.03	4.45 ± 0.09	1.1 ± 0.04	5001
212004573	212.35 ± 1.3	16.63 ± 0.16	4.18 ± 0.09	1.11 ± 0.04	5001
212005141	149.47 ± 1.96	12.34 ± 0.11	5.43 ± 0.14	1.33 ± 0.06	5085
212006515	156.34 ± 1.07	13.12 ± 0.05	4.76 ± 0.09	1.04 ± 0.03	4967
212006835	154.34 ± 1.01	13.27 ± 0.09	4.7 ± 0.1	1.01 ± 0.04	4986
212007729	213.45 ± 2.12	15.96 ± 0.07	4.63 ± 0.09	1.39 ± 0.05	5156
212008123	90.4 ± 0.92	8.52 ± 0.04	6.72 ± 0.14	1.22 ± 0.04	5231
212009016	217.39 ± 1.26	17.05 ± 0.16	4.15 ± 0.09	1.13 ± 0.04	5094
212010612	180.94 ± 1.6	14.69 ± 0.04	4.66 ± 0.09	1.19 ± 0.04	4987
212015317	155.46 ± 1.12	12.06 ± 0.05	5.83 ± 0.11	1.6 ± 0.05	5111
212015412	129.7 ± 0.65	11.59 ± 0.06	5.17 ± 0.1	1.03 ± 0.03	4928
212016980	167.15 ± 0.59	13.47 ± 0.03	5.04 ± 0.09	1.28 ± 0.04	5065
212017013	161.38 ± 3.04	14.59 ± 0.17	4.31 ± 0.13	0.91 ± 0.04	5322
212018779	127.88 ± 0.85	11.29 ± 0.13	5.47 ± 0.13	1.15 ± 0.04	5125
212018792	72.73 ± 0.9	7.01 ± 0.08	7.8 ± 0.21	1.31 ± 0.06	4790
212019569	137.16 ± 2.25	11.62 ± 0.18	5.57 ± 0.18	1.28 ± 0.07	5144
212019604	219.58 ± 1.93	15.83 ± 0.44	4.75 ± 0.21	1.49 ± 0.1	5190
212020639	186.07 ± 1.13	15.06 ± 0.06	4.4 ± 0.08	1.07 ± 0.04	4946
212022005	213.67 ± 2.12	15.59 ± 0.03	4.57 ± 0.09	1.31 ± 0.05	4859
212023032	156.85 ± 1.98	13.41 ± 0.02	4.68 ± 0.1	1.02 ± 0.04	4964

Continued on next page

Table A.1 – continued from previous page

EPIC ID	$\nu_{\max}$ (μHz)	$\Delta\nu$ (μHz)	Radius ($R_{\odot}$)	Mass ($M_{\odot}$)	$T_{\rm eff}$ (K)
212023390	85.48 ± 0.89	8.26 ± 0.05	6.51 ± 0.15	1.07 ± 0.04	4916
212023681	212.51 ± 1.77	16.04 ± 0.05	4.28 ± 0.09	1.15 ± 0.04	4844
212025635	144.1 ± 0.99	11.64 ± 0.05	5.72 ± 0.11	1.41 ± 0.05	5014
212028009	121.63 ± 1.06	10.7 ± 0.04	5.55 ± 0.11	1.11 ± 0.04	4889
212028523	278.77 ± 1.11	19.71 ± 0.04	3.83 ± 0.07	1.22 ± 0.04	4913
212030008	142.97 ± 2.03	12.08 ± 0.03	5.08 ± 0.12	1.09 ± 0.04	4873
212030053	97.76 ± 1.05	8.84 ± 0.06	6.55 ± 0.15	1.24 ± 0.05	4827
212030541	149.95 ± 0.99	12.11 ± 0.05	5.27 ± 0.11	1.23 ± 0.04	4843
212031767	70.21 ± 0.56	6.93 ± 0.08	7.61 ± 0.19	1.2 ± 0.05	4807
212033069	213.25 ± 1.45	14.7 ± 0.16	5.34 ± 0.13	1.83 ± 0.07	5059
212033294	103.03 ± 2.09	9.59 ± 0.08	6.16 ± 0.18	1.17 ± 0.06	5090
212033418	88.49 ± 0.78	8.33 ± 0.05	6.69 ± 0.14	1.17 ± 0.04	4995
212034935	160.89 ± 1.4	13.37 ± 0.03	4.88 ± 0.1	1.14 ± 0.04	5090
212035029	122.43 ± 1.0	10.13 ± 0.11	6.48 ± 0.16	1.55 ± 0.06	5105
212068701	205.47 ± 2.13	16.64 ± 0.09	4.12 ± 0.09	1.05 ± 0.04	5063
212068923	274.86 ± 2.0	19.5 ± 0.52	3.87 ± 0.16	1.23 ± 0.08	5100
212071890	228.75 ± 9.32	18.51 ± 0.2	3.82 ± 0.18	1.02 ± 0.08	5175
212072069	148.72 ± 1.17	12.46 ± 0.1	5.05 ± 0.11	1.12 ± 0.04	4948
212074488	149.14 ± 1.6	11.77 ± 0.16	5.55 ± 0.16	1.35 ± 0.06	4929
212077970	188.29 ± 2.58	14.42 ± 0.15	4.89 ± 0.13	1.35 ± 0.06	5133
212079021	85.03 ± 0.52	8.27 ± 0.04	6.73 ± 0.13	1.15 ± 0.04	5013
212079141	177.13 ± 1.62	13.39 ± 0.06	5.31 ± 0.11	1.5 ± 0.05	5090
212081257	81.1 ± 0.83	7.51 ± 0.07	7.41 ± 0.18	1.31 ± 0.05	4928
212086134	219.19 ± 0.86	17.45 ± 0.03	3.91 ± 0.07	1.0 ± 0.03	4893
212088815	78.38 ± 0.85	8.01 ± 0.05	6.57 ± 0.15	1.0 ± 0.04	5066
212089781	164.82 ± 2.67	13.34 ± 0.06	4.96 ± 0.12	1.21 ± 0.05	5011
212090108	73.26 ± 1.0	7.36 ± 0.06	7.43 ± 0.19	1.22 ± 0.05	5154
212091821	81.52 ± 1.14	7.84 ± 0.04	6.95 ± 0.17	1.16 ± 0.05	4892
212092964	63.48 ± 2.76	6.75 ± 0.04	7.63 ± 0.36	1.11 ± 0.09	5167
212093142	85.21 ± 0.87	7.61 ± 0.15	7.78 ± 0.27	1.54 ± 0.08	4976
212095108	130.14 ± 0.93	11.1 ± 0.17	5.8 ± 0.16	1.32 ± 0.06	5106
212095585	129.24 ± 1.27	10.96 ± 0.11	5.75 ± 0.14	1.28 ± 0.05	4991
212095879	193.09 ± 4.01	16.23 ± 0.09	4.0 ± 0.11	0.92 ± 0.04	4954
212096224	160.15 ± 2.33	12.19 ± 0.1	5.85 ± 0.15	1.65 ± 0.07	4969
212097988	194.62 ± 1.57	14.65 ± 0.05	4.8 ± 0.09	1.33 ± 0.04	5010
212102471	131.76 ± 2.81	12.11 ± 0.06	4.72 ± 0.14	0.86 ± 0.04	4841
212103088	190.17 ± 5.05	15.56 ± 0.11	4.41 ± 0.15	1.12 ± 0.06	5229
212104491	248.03 ± 3.9	18.03 ± 0.05	4.27 ± 0.1	1.38 ± 0.06	5204
212105410	269.54 ± 8.82	19.21 ± 0.05	3.91 ± 0.15	1.23 ± 0.08	5063
212106017	186.64 ± 1.51	15.11 ± 0.03	4.42 ± 0.09	1.09 ± 0.04	4973
212106947	86.32 ± 0.6	8.17 ± 0.11	6.96 ± 0.19	1.25 ± 0.05	4935
212107012	54.23 ± 0.41	6.12 ± 0.06	7.64 ± 0.18	0.93 ± 0.04	4738
212107041	174.69 ± 0.89	14.01 ± 0.08	4.55 ± 0.09	1.06 ± 0.04	4799
212107343	257.76 ± 1.73	18.48 ± 0.19	3.98 ± 0.1	1.21 ± 0.05	4897
212107729	234.34 ± 5.38	17.46 ± 0.25	4.14 ± 0.14	1.2 ± 0.07	4979
212109772	79.72 ± 0.51	7.76 ± 0.09	6.83 ± 0.17	1.09 ± 0.04	4673
212110146	180.91 ± 0.6	14.71 ± 0.07	4.61 ± 0.09	1.16 ± 0.04	5171
212110370	194.51 ± 0.96	15.46 ± 0.07	4.47 ± 0.08	1.17 ± 0.04	5187
212113212	101.99 ± 1.21	9.44 ± 0.07	6.39 ± 0.15	1.26 ± 0.05	5232
212119372	105.74 ± 0.66	9.72 ± 0.06	5.95 ± 0.12	1.11 ± 0.04	4925
212120235	111.31 ± 0.49	10.09 ± 0.05	5.65 ± 0.11	1.04 ± 0.03	4846
212120904	102.83 ± 0.75	9.01 ± 0.17	6.54 ± 0.21	1.3 ± 0.06	4925
212121127	91.47 ± 1.35	8.38 ± 0.06	6.81 ± 0.17	1.25 ± 0.05	4846
212126323	248.49 ± 2.21	18.74 ± 0.2	3.78 ± 0.09	1.06 ± 0.04	5079
212126418	108.77 ± 0.94	10.17 ± 0.18	5.69 ± 0.18	1.05 ± 0.05	4876
212127095	131.99 ± 0.83	11.14 ± 0.09	5.61 ± 0.12	1.23 ± 0.04	4982
212131927	187.94 ± 1.76	14.2 ± 0.04	5.0 ± 0.1	1.4 ± 0.05	5089
212132267	120.01 ± 0.59	10.66 ± 0.07	5.68 ± 0.11	1.16 ± 0.04	5085
212136331	280.0 ± 0.27	19.78 ± 0.06	3.88 ± 0.07	1.26 ± 0.04	5024
212137133	59.49 ± 1.54	6.63 ± 0.13	7.55 ± 0.32	1.02 ± 0.07	4951
212137284	232.86 ± 1.98	18.76 ± 0.18	3.76 ± 0.09	1.0 ± 0.04	5127

Continued on next page

Table A.1 – continued from previous page

EPIC ID	$\nu_{\max}$ (μHz)	$\Delta\nu$ (μHz)	Radius ($R_\odot$)	Mass ($M_\odot$)	$T_{\rm eff}$ (K)
212138434	94.25 ± 1.37	8.82 ± 0.08	6.76 ± 0.18	1.31 ± 0.06	5221
212138991	182.51 ± 0.96	14.52 ± 0.15	4.79 ± 0.11	1.27 ± 0.05	5185
212139014	192.54 ± 1.4	15.15 ± 0.11	4.72 ± 0.1	1.31 ± 0.05	5141
212139873	132.38 ± 0.73	11.28 ± 0.06	5.62 ± 0.11	1.25 ± 0.04	5102
212140399	287.02 ± 1.34	20.15 ± 0.12	3.8 ± 0.07	1.24 ± 0.04	5076
212140579	128.05 ± 1.41	11.01 ± 0.08	5.69 ± 0.13	1.24 ± 0.05	5079
212140966	190.45 ± 1.91	14.73 ± 0.08	4.86 ± 0.1	1.36 ± 0.05	5167
212141417	130.8 ± 0.86	10.79 ± 0.1	5.77 ± 0.13	1.28 ± 0.05	4845
212141886	222.33 ± 3.07	16.8 ± 0.09	4.24 ± 0.1	1.19 ± 0.05	5040
212142295	213.41 ± 1.93	17.2 ± 0.05	4.04 ± 0.08	1.05 ± 0.04	5167
212143876	253.45 ± 5.25	17.77 ± 0.04	4.25 ± 0.12	1.36 ± 0.06	4954
212144599	166.02 ± 1.09	13.92 ± 0.05	4.78 ± 0.09	1.14 ± 0.04	5009
212146773	111.91 ± 0.76	10.2 ± 0.04	5.8 ± 0.11	1.12 ± 0.04	4986
212147744	143.81 ± 1.02	11.91 ± 0.05	5.64 ± 0.11	1.39 ± 0.05	5219
212148160	146.23 ± 1.04	12.27 ± 0.1	5.23 ± 0.12	1.2 ± 0.04	4992
212152070	217.42 ± 2.35	16.86 ± 0.08	4.01 ± 0.09	1.03 ± 0.04	4765
212154588	226.82 ± 2.13	17.57 ± 0.13	4.08 ± 0.09	1.14 ± 0.04	5042
212155226	76.04 ± 0.9	7.49 ± 0.08	7.09 ± 0.18	1.13 ± 0.05	4908
212155719	64.37 ± 0.38	6.63 ± 0.05	7.75 ± 0.17	1.15 ± 0.04	4858
212156938	120.04 ± 2.12	10.4 ± 0.06	5.87 ± 0.15	1.23 ± 0.05	4916
212157482	148.85 ± 1.25	10.72 ± 0.31	7.17 ± 0.32	2.31 ± 0.15	5274
212157989	181.68 ± 2.39	13.6 ± 0.11	5.23 ± 0.13	1.48 ± 0.06	5010
212158048	131.69 ± 0.77	11.26 ± 0.06	5.4 ± 0.11	1.13 ± 0.04	4848
212158216	156.47 ± 2.94	12.56 ± 0.1	5.42 ± 0.15	1.39 ± 0.07	5028
212159064	170.35 ± 1.25	13.33 ± 0.08	4.91 ± 0.1	1.2 ± 0.04	4834
212160539	123.1 ± 1.21	9.62 ± 0.2	7.08 ± 0.25	1.84 ± 0.1	4910
212161576	170.34 ± 1.21	14.29 ± 0.09	4.61 ± 0.09	1.09 ± 0.04	5008
212164688	175.51 ± 1.26	14.07 ± 0.08	4.58 ± 0.09	1.08 ± 0.04	4771
212167144	165.5 ± 1.25	13.43 ± 0.09	5.01 ± 0.11	1.25 ± 0.04	5055
212167180	183.44 ± 1.85	14.42 ± 0.09	4.81 ± 0.1	1.28 ± 0.05	5128
212168223	131.26 ± 0.78	11.29 ± 0.03	5.38 ± 0.1	1.12 ± 0.04	4892
212168259	145.81 ± 1.17	12.61 ± 0.12	5.04 ± 0.12	1.11 ± 0.04	5022
212168382	200.11 ± 2.42	16.77 ± 0.17	4.08 ± 0.1	1.02 ± 0.04	5050
212168511	68.06 ± 0.74	6.69 ± 0.04	7.75 ± 0.18	1.2 ± 0.05	4780
212169504	211.19 ± 0.89	16.07 ± 0.27	4.3 ± 0.13	1.15 ± 0.05	4945
212172027	73.0 ± 1.06	7.48 ± 0.1	7.23 ± 0.21	1.15 ± 0.05	5024
212172991	90.05 ± 0.42	8.84 ± 0.03	6.33 ± 0.12	1.08 ± 0.03	5002
212176995	190.23 ± 2.22	15.53 ± 0.08	4.23 ± 0.09	1.01 ± 0.04	4979
212178825	268.95 ± 0.0	19.18 ± 0.13	3.89 ± 0.08	1.21 ± 0.04	5012
212179600	138.18 ± 4.42	11.79 ± 0.14	5.3 ± 0.21	1.15 ± 0.08	5045
212274652	151.95 ± 0.79	12.74 ± 0.03	5.2 ± 0.1	1.24 ± 0.04	4803
212278055	101.29 ± 0.8	9.22 ± 0.27	6.36 ± 0.29	1.22 ± 0.08	4834
212279035	151.23 ± 0.8	13.06 ± 0.04	4.94 ± 0.09	1.12 ± 0.04	4952
212294653	90.5 ± 0.36	8.63 ± 0.16	6.59 ± 0.21	1.18 ± 0.06	4925
212295397	208.74 ± 1.97	16.51 ± 0.06	4.01 ± 0.08	0.99 ± 0.04	4793
212295651	223.98 ± 1.36	15.57 ± 0.04	4.84 ± 0.09	1.56 ± 0.05	4911
212297049	217.07 ± 1.29	17.0 ± 0.03	4.05 ± 0.07	1.06 ± 0.03	5040
212301092	251.65 ± 2.55	17.42 ± 0.35	4.26 ± 0.15	1.34 ± 0.07	4754
212301192	122.14 ± 0.61	10.15 ± 0.04	6.18 ± 0.12	1.38 ± 0.04	4911
212301917	203.31 ± 1.2	16.19 ± 0.05	4.25 ± 0.08	1.1 ± 0.04	5038
212302366	153.04 ± 0.64	12.97 ± 0.05	4.83 ± 0.09	1.06 ± 0.03	4941
212303202	69.63 ± 1.07	6.92 ± 0.05	7.86 ± 0.2	1.29 ± 0.06	4984
212307389	82.53 ± 0.95	7.93 ± 0.06	6.99 ± 0.16	1.2 ± 0.05	4889
212312393	78.98 ± 0.49	8.04 ± 0.12	6.51 ± 0.18	0.99 ± 0.04	4823
212314902	64.86 ± 0.69	6.72 ± 0.03	7.85 ± 0.17	1.2 ± 0.04	4866
212315444	122.84 ± 1.19	11.13 ± 0.1	5.37 ± 0.13	1.05 ± 0.04	4970
212317251	83.46 ± 0.59	7.65 ± 0.05	7.52 ± 0.16	1.4 ± 0.05	4884
212317267	96.89 ± 1.39	9.34 ± 0.09	5.9 ± 0.16	1.0 ± 0.04	4989
212319712	71.41 ± 0.34	7.23 ± 0.06	7.16 ± 0.15	1.08 ± 0.04	4965
212320620	162.31 ± 1.2	13.97 ± 0.09	4.61 ± 0.1	1.04 ± 0.04	4922
212324691	74.84 ± 0.94	7.26 ± 0.08	7.72 ± 0.2	1.34 ± 0.06	5000

Continued on next page

Table A.1 – continued from previous page

EPIC ID	$\nu_{\max}$ (μHz)	$\Delta\nu$ (μHz)	Radius ($R_\odot$)	Mass ($M_\odot$)	$T_{\rm eff}$ (K)
212324974	248.08 ± 1.43	17.77 ± 0.23	4.09 ± 0.11	1.23 ± 0.05	4971
212329497	158.64 ± 0.72	12.96 ± 0.05	5.16 ± 0.1	1.27 ± 0.04	4999
212330226	138.6 ± 2.12	11.93 ± 0.04	5.08 ± 0.12	1.05 ± 0.04	4864
212330427	81.54 ± 0.82	7.78 ± 0.1	7.02 ± 0.19	1.19 ± 0.05	5021
212330940	126.27 ± 2.46	10.93 ± 0.01	5.66 ± 0.15	1.21 ± 0.05	4918
212331780	110.08 ± 0.73	9.71 ± 0.07	5.94 ± 0.13	1.13 ± 0.04	4958
212332022	148.97 ± 0.76	12.21 ± 0.03	5.09 ± 0.1	1.13 ± 0.04	4834
212333981	116.26 ± 0.53	9.62 ± 0.04	7.65 ± 0.14	2.22 ± 0.07	5183
212339009	129.57 ± 0.78	11.47 ± 0.03	5.3 ± 0.1	1.08 ± 0.04	4867
212341963	144.64 ± 0.77	11.94 ± 0.02	5.28 ± 0.1	1.19 ± 0.04	4723
212342578	112.02 ± 0.52	9.98 ± 0.03	5.83 ± 0.11	1.12 ± 0.04	4855
212344901	144.42 ± 2.26	12.27 ± 0.04	5.26 ± 0.13	1.2 ± 0.05	4918
212346679	168.18 ± 0.91	13.68 ± 0.05	4.89 ± 0.09	1.21 ± 0.04	4985
212348913	279.36 ± 2.34	18.94 ± 0.16	3.61 ± 0.08	1.0 ± 0.04	5152
212354794	129.3 ± 0.73	11.23 ± 0.04	5.28 ± 0.1	1.06 ± 0.03	4945
212357017	111.72 ± 1.02	9.33 ± 0.04	6.65 ± 0.14	1.46 ± 0.05	4932
212362900	66.83 ± 0.6	6.75 ± 0.04	7.67 ± 0.17	1.16 ± 0.04	4805
212364408	206.4 ± 1.21	16.48 ± 0.17	4.08 ± 0.1	1.02 ± 0.04	4837
212364586	73.61 ± 0.52	7.32 ± 0.05	7.34 ± 0.16	1.18 ± 0.04	4725
212365392	161.47 ± 1.03	13.29 ± 0.15	4.76 ± 0.12	1.08 ± 0.04	4798
212365490	134.8 ± 1.42	11.52 ± 0.04	5.36 ± 0.11	1.15 ± 0.04	4796
212371042	130.42 ± 1.01	11.4 ± 0.03	5.39 ± 0.1	1.13 ± 0.04	4940
212377434	73.77 ± 0.4	7.33 ± 0.04	7.11 ± 0.14	1.09 ± 0.04	4831
212381160	233.53 ± 1.46	18.05 ± 0.06	3.95 ± 0.08	1.09 ± 0.04	5038
212381326	108.02 ± 0.84	10.06 ± 0.07	5.71 ± 0.12	1.05 ± 0.04	4906
212391225	104.41 ± 0.6	9.44 ± 0.05	6.08 ± 0.12	1.14 ± 0.04	4850
212392830	171.93 ± 1.01	13.62 ± 0.05	5.03 ± 0.1	1.3 ± 0.04	4982
212394715	131.24 ± 0.7	11.48 ± 0.12	5.32 ± 0.13	1.1 ± 0.04	4831
212396190	100.41 ± 1.12	9.66 ± 0.11	5.8 ± 0.15	1.0 ± 0.04	4857
212402298	71.68 ± 0.81	7.37 ± 0.04	7.31 ± 0.16	1.15 ± 0.04	4994
212405476	88.96 ± 0.76	8.4 ± 0.09	6.7 ± 0.17	1.19 ± 0.05	4792
212406696	96.95 ± 0.9	9.04 ± 0.1	6.27 ± 0.16	1.13 ± 0.05	4871
212406865	99.26 ± 0.95	9.64 ± 0.07	5.87 ± 0.13	1.03 ± 0.04	4917
212407479	82.53 ± 0.54	7.79 ± 0.04	7.25 ± 0.15	1.29 ± 0.04	4903
212409863	107.93 ± 1.47	10.2 ± 0.13	5.56 ± 0.16	0.99 ± 0.05	4848
212411913	207.92 ± 1.32	16.66 ± 0.1	4.06 ± 0.08	1.02 ± 0.03	4942
212413766	202.61 ± 2.43	16.12 ± 0.08	4.19 ± 0.09	1.06 ± 0.04	4930
212414143	148.18 ± 2.18	11.98 ± 0.18	5.57 ± 0.18	1.38 ± 0.07	4969
212416240	115.04 ± 0.66	9.9 ± 0.14	6.11 ± 0.17	1.27 ± 0.05	5038
212416500	150.9 ± 1.53	12.58 ± 0.21	5.04 ± 0.16	1.14 ± 0.06	4844
212418105	139.46 ± 2.26	12.37 ± 0.12	5.01 ± 0.14	1.05 ± 0.05	4844
212420108	66.77 ± 1.19	6.89 ± 0.08	7.64 ± 0.22	1.17 ± 0.06	5186
212421926	207.82 ± 1.62	16.53 ± 0.09	4.19 ± 0.09	1.1 ± 0.04	5057
212422485	113.81 ± 1.05	10.29 ± 0.04	5.87 ± 0.12	1.18 ± 0.04	4948
212422971	155.95 ± 0.74	12.76 ± 0.04	5.01 ± 0.09	1.16 ± 0.04	4904
212423102	198.86 ± 2.49	15.18 ± 0.14	4.75 ± 0.12	1.36 ± 0.06	5133
212423582	113.66 ± 0.91	10.47 ± 0.1	5.62 ± 0.13	1.07 ± 0.04	4960
212423781	160.29 ± 1.3	13.28 ± 0.04	5.05 ± 0.1	1.24 ± 0.04	4974
212424187	131.27 ± 2.48	10.77 ± 0.18	6.42 ± 0.22	1.66 ± 0.09	5050
212426865	184.81 ± 0.91	14.28 ± 0.04	4.81 ± 0.09	1.27 ± 0.04	4820
212431715	208.31 ± 1.13	16.38 ± 0.05	4.27 ± 0.08	1.14 ± 0.04	4971
212434736	116.14 ± 1.07	10.24 ± 0.2	5.85 ± 0.2	1.18 ± 0.06	4787
212440723	86.76 ± 2.78	8.53 ± 0.05	6.33 ± 0.24	1.03 ± 0.07	4937
212444038	74.68 ± 0.95	7.35 ± 0.03	7.02 ± 0.16	1.07 ± 0.04	4795
212448768	143.91 ± 0.76	12.12 ± 0.03	5.23 ± 0.1	1.17 ± 0.04	4813
212453810	217.95 ± 1.64	15.48 ± 0.08	4.82 ± 0.1	1.51 ± 0.05	4970
212454757	126.87 ± 0.37	11.34 ± 0.06	5.43 ± 0.1	1.12 ± 0.04	4935
212456213	230.26 ± 1.77	16.57 ± 0.05	4.29 ± 0.09	1.24 ± 0.04	4792
212457945	166.49 ± 0.9	13.53 ± 0.02	4.74 ± 0.09	1.1 ± 0.04	4779
212461372	116.45 ± 1.28	10.37 ± 0.02	5.79 ± 0.12	1.16 ± 0.04	4924
212462271	208.8 ± 1.25	16.37 ± 0.06	4.12 ± 0.08	1.05 ± 0.03	4876

Continued on next page

Table A.1 – continued from previous page

EPIC ID	$\nu_{\max}$ (μHz)	$\Delta\nu$ (μHz)	Radius ($R_\odot$)	Mass ($M_\odot$)	$T_{\rm eff}$ (K)
212465262	66.22 ± 0.4	6.68 ± 0.04	7.84 ± 0.16	1.21 ± 0.04	4804
212467134	166.06 ± 0.74	13.45 ± 0.03	4.86 ± 0.09	1.16 ± 0.04	4866
212467922	203.49 ± 1.42	15.37 ± 0.04	4.48 ± 0.09	1.2 ± 0.04	4870
212469827	116.93 ± 1.18	10.45 ± 0.02	5.69 ± 0.12	1.13 ± 0.04	4721
212470043	197.65 ± 0.89	15.27 ± 0.03	4.42 ± 0.08	1.14 ± 0.04	4667
212477236	187.49 ± 1.34	15.29 ± 0.12	4.46 ± 0.1	1.13 ± 0.04	5018
212478724	95.5 ± 0.84	8.95 ± 0.09	6.37 ± 0.15	1.16 ± 0.05	4955
212479153	78.98 ± 0.58	7.78 ± 0.07	6.96 ± 0.16	1.14 ± 0.04	4875
212479761	194.33 ± 3.66	15.79 ± 0.09	4.36 ± 0.12	1.11 ± 0.05	5062
212481465	206.79 ± 1.33	16.4 ± 0.04	4.16 ± 0.08	1.07 ± 0.04	4869
212481725	163.04 ± 0.74	13.46 ± 0.06	4.84 ± 0.09	1.14 ± 0.04	4956
212483607	170.02 ± 1.32	14.06 ± 0.11	4.74 ± 0.1	1.15 ± 0.04	4981
212486823	144.07 ± 0.74	12.3 ± 0.06	5.14 ± 0.1	1.14 ± 0.04	4877
212487900	193.03 ± 3.3	14.89 ± 0.09	4.76 ± 0.12	1.31 ± 0.06	4918
212490222	229.23 ± 0.83	16.99 ± 0.05	4.13 ± 0.08	1.15 ± 0.04	4877
212496254	120.03 ± 0.94	10.37 ± 0.03	5.75 ± 0.12	1.17 ± 0.04	4803
212496557	80.89 ± 0.41	7.77 ± 0.05	7.0 ± 0.14	1.17 ± 0.04	4780
212497160	54.93 ± 0.46	6.28 ± 0.1	8.0 ± 0.23	1.08 ± 0.05	5357
212497454	63.09 ± 0.52	6.5 ± 0.04	7.94 ± 0.17	1.18 ± 0.04	5069
212497705	122.51 ± 1.25	10.83 ± 0.03	5.64 ± 0.12	1.17 ± 0.04	4884
212497825	62.44 ± 0.66	6.53 ± 0.05	7.83 ± 0.18	1.14 ± 0.04	4845
212498037	138.03 ± 1.35	12.03 ± 0.06	5.22 ± 0.11	1.13 ± 0.04	5066
212498207	176.06 ± 2.26	13.97 ± 0.1	4.96 ± 0.12	1.31 ± 0.05	5081
212498250	68.05 ± 0.66	6.78 ± 0.05	7.84 ± 0.18	1.24 ± 0.05	4905
212499125	109.38 ± 0.75	9.99 ± 0.05	5.95 ± 0.12	1.16 ± 0.04	4996
212501900	128.69 ± 1.78	11.32 ± 0.26	5.38 ± 0.21	1.11 ± 0.07	4966
212502915	68.5 ± 1.06	6.95 ± 0.06	7.48 ± 0.2	1.14 ± 0.05	4869
212508433	174.55 ± 1.58	14.45 ± 0.1	4.62 ± 0.1	1.12 ± 0.04	5015
212509108	83.61 ± 0.53	8.28 ± 0.03	6.55 ± 0.13	1.07 ± 0.04	4886
212510298	145.37 ± 0.94	12.44 ± 0.12	5.25 ± 0.12	1.21 ± 0.05	4957
212510857	223.71 ± 2.11	17.6 ± 0.12	3.95 ± 0.09	1.05 ± 0.04	4865
212511051	228.99 ± 2.45	17.62 ± 0.11	4.13 ± 0.09	1.18 ± 0.04	5178
212512569	99.86 ± 1.05	9.38 ± 0.23	6.34 ± 0.25	1.21 ± 0.07	5080
212513783	118.75 ± 1.04	9.59 ± 0.1	7.16 ± 0.17	1.85 ± 0.07	5156
212515202	75.8 ± 0.94	7.68 ± 0.03	7.11 ± 0.16	1.15 ± 0.04	4921
212518402	63.45 ± 0.96	6.76 ± 0.07	7.46 ± 0.2	1.05 ± 0.05	4873
212521191	79.15 ± 0.76	8.04 ± 0.03	6.66 ± 0.14	1.05 ± 0.04	5002
212522065	137.89 ± 1.25	12.84 ± 0.26	4.76 ± 0.16	0.95 ± 0.05	5291
212526482	123.97 ± 1.03	10.35 ± 0.05	6.28 ± 0.13	1.47 ± 0.05	4932
212526571	61.85 ± 0.98	6.56 ± 0.05	7.61 ± 0.2	1.06 ± 0.05	4882
212527968	140.99 ± 0.89	11.99 ± 0.05	5.26 ± 0.1	1.16 ± 0.04	4851
212528607	117.11 ± 0.77	10.73 ± 0.21	5.58 ± 0.18	1.09 ± 0.05	4962
212529275	98.66 ± 0.44	8.96 ± 0.05	6.5 ± 0.13	1.24 ± 0.04	4907
212530208	147.97 ± 0.6	12.11 ± 0.03	5.25 ± 0.1	1.2 ± 0.04	4851
212530719	151.29 ± 2.14	11.96 ± 0.18	5.74 ± 0.18	1.5 ± 0.07	4854
212533129	160.16 ± 0.87	13.65 ± 0.03	4.84 ± 0.09	1.14 ± 0.04	4879
212536051	144.89 ± 0.67	12.48 ± 0.12	5.18 ± 0.11	1.17 ± 0.04	5105
212538830	199.61 ± 3.62	15.74 ± 0.1	4.61 ± 0.12	1.3 ± 0.06	5126
212539817	77.22 ± 0.71	7.71 ± 0.06	7.07 ± 0.16	1.16 ± 0.04	4899
212542543	250.69 ± 1.36	18.17 ± 0.44	4.29 ± 0.17	1.41 ± 0.08	4984
212545537	86.71 ± 0.94	8.28 ± 0.13	6.96 ± 0.21	1.27 ± 0.06	4994
212546716	138.72 ± 0.54	11.8 ± 0.08	5.39 ± 0.11	1.2 ± 0.04	4899
212547195	96.5 ± 0.74	8.57 ± 0.15	7.19 ± 0.22	1.51 ± 0.07	5017
212548516	92.17 ± 0.51	8.62 ± 0.08	6.56 ± 0.15	1.18 ± 0.04	4967
212548704	114.54 ± 0.85	10.52 ± 0.08	5.72 ± 0.13	1.13 ± 0.04	5086
212550462	50.14 ± 1.31	5.89 ± 0.08	8.0 ± 0.29	0.96 ± 0.06	5123
212551902	167.96 ± 0.88	14.09 ± 0.06	4.7 ± 0.09	1.12 ± 0.04	5138
212552129	91.68 ± 0.66	8.63 ± 0.07	6.48 ± 0.15	1.14 ± 0.04	4821
212552329	72.96 ± 1.02	7.45 ± 0.07	7.31 ± 0.19	1.18 ± 0.05	4912
212554367	118.54 ± 0.84	10.56 ± 0.18	5.61 ± 0.17	1.1 ± 0.05	4796
212554814	81.62 ± 1.28	8.03 ± 0.04	6.58 ± 0.16	1.04 ± 0.04	4824

Continued on next page

Table A.1 – continued from previous page

EPIC ID	$\nu_{\max}$ (μHz)	$\Delta\nu$ (μHz)	Radius ($R_\odot$)	Mass ($M_\odot$)	T_{eff} (K)
212555250	245.41 ± 1.14	17.67 ± 0.08	4.39 ± 0.08	1.44 ± 0.05	5001
212556229	173.88 ± 1.16	14.1 ± 0.15	4.71 ± 0.11	1.15 ± 0.04	4930
212557162	128.55 ± 1.93	10.15 ± 0.13	6.94 ± 0.2	1.88 ± 0.09	5106
212557715	127.45 ± 1.84	11.22 ± 0.08	5.71 ± 0.14	1.26 ± 0.05	4984
212559650	152.67 ± 1.64	12.67 ± 0.1	5.0 ± 0.12	1.13 ± 0.04	4746
212562020	184.13 ± 1.1	15.09 ± 0.03	4.45 ± 0.08	1.1 ± 0.04	4864
212565520	112.9 ± 0.5	10.18 ± 0.05	5.95 ± 0.11	1.2 ± 0.04	5034
212566197	130.01 ± 2.06	10.4 ± 0.21	6.44 ± 0.24	1.62 ± 0.09	4979
212566230	119.52 ± 0.61	10.85 ± 0.1	5.46 ± 0.12	1.06 ± 0.04	4841
212567485	177.42 ± 1.31	13.99 ± 0.06	4.88 ± 0.1	1.26 ± 0.04	4966
212569083	97.5 ± 0.78	9.25 ± 0.04	6.23 ± 0.13	1.14 ± 0.04	4881
212569687	146.06 ± 6.47	12.94 ± 0.09	4.99 ± 0.24	1.11 ± 0.09	5001
212570575	159.76 ± 1.08	13.21 ± 0.06	5.11 ± 0.1	1.26 ± 0.04	5259
212571207	243.68 ± 6.95	17.71 ± 0.09	4.14 ± 0.14	1.24 ± 0.07	4717
212571648	85.23 ± 0.71	8.29 ± 0.05	6.59 ± 0.14	1.1 ± 0.04	4859
212572414	196.32 ± 2.35	14.66 ± 0.06	4.96 ± 0.11	1.45 ± 0.05	5222
212572608	128.36 ± 2.84	10.42 ± 0.06	6.38 ± 0.19	1.57 ± 0.08	5089
212572805	70.32 ± 0.47	6.96 ± 0.06	7.59 ± 0.17	1.2 ± 0.04	4888
212573348	132.15 ± 0.63	11.32 ± 0.04	5.47 ± 0.11	1.17 ± 0.04	4613
212574108	106.08 ± 0.78	8.97 ± 0.09	7.29 ± 0.17	1.71 ± 0.07	5183
212574314	109.05 ± 0.87	9.99 ± 0.07	5.87 ± 0.13	1.12 ± 0.04	4921
212576935	236.05 ± 2.43	17.64 ± 0.04	4.06 ± 0.08	1.16 ± 0.04	4946
212578979	223.44 ± 5.17	16.76 ± 0.29	4.58 ± 0.17	1.45 ± 0.09	5328
212579177	235.43 ± 1.99	18.45 ± 0.09	3.76 ± 0.08	0.99 ± 0.03	5130
212579721	187.04 ± 1.08	14.84 ± 0.07	4.58 ± 0.09	1.17 ± 0.04	4935
212580414	142.65 ± 1.57	12.13 ± 0.05	5.34 ± 0.11	1.22 ± 0.04	4991
212583634	205.45 ± 1.53	15.22 ± 0.16	4.78 ± 0.12	1.41 ± 0.06	4835
212585386	162.43 ± 0.99	13.01 ± 0.03	5.07 ± 0.1	1.24 ± 0.04	4899
212586147	277.95 ± 3.3	20.21 ± 0.34	3.75 ± 0.12	1.17 ± 0.06	5023
212589423	153.06 ± 1.88	13.05 ± 0.07	4.85 ± 0.11	1.07 ± 0.04	4851
212591315	201.31 ± 1.31	16.13 ± 0.04	4.28 ± 0.08	1.11 ± 0.04	5012
212591347	162.15 ± 0.54	13.21 ± 0.04	4.91 ± 0.09	1.16 ± 0.04	4929
212593719	158.64 ± 2.26	11.99 ± 0.06	5.72 ± 0.14	1.53 ± 0.06	5028
212594782	73.04 ± 0.72	7.34 ± 0.06	7.33 ± 0.17	1.17 ± 0.05	4948
212595290	65.47 ± 0.7	6.71 ± 0.08	7.83 ± 0.21	1.2 ± 0.05	5028
212595534	76.94 ± 0.81	7.09 ± 0.03	7.74 ± 0.17	1.34 ± 0.05	4614
212596377	81.29 ± 0.71	8.32 ± 0.1	6.57 ± 0.17	1.06 ± 0.04	5039
212599558	84.86 ± 0.3	7.93 ± 0.06	6.84 ± 0.14	1.16 ± 0.04	4849
212600319	103.02 ± 1.1	9.67 ± 0.04	5.83 ± 0.13	1.04 ± 0.04	4851
212600478	166.79 ± 1.57	12.46 ± 0.07	5.9 ± 0.12	1.76 ± 0.06	5171
212600508	232.29 ± 1.22	17.83 ± 0.05	4.03 ± 0.07	1.13 ± 0.04	5100
212600636	135.59 ± 0.74	11.76 ± 0.06	5.37 ± 0.11	1.17 ± 0.04	4886
212601036	67.0 ± 0.86	6.85 ± 0.1	7.56 ± 0.23	1.14 ± 0.05	4902
212604856	179.69 ± 1.06	14.4 ± 0.14	4.81 ± 0.11	1.26 ± 0.05	5116
212605959	193.66 ± 1.4	14.55 ± 0.13	4.92 ± 0.11	1.41 ± 0.05	5054
212606189	106.0 ± 0.74	9.54 ± 0.13	6.18 ± 0.16	1.2 ± 0.05	4842
212606903	182.24 ± 1.45	14.82 ± 0.04	4.43 ± 0.09	1.06 ± 0.04	4876
212607392	99.81 ± 1.16	8.78 ± 0.13	6.55 ± 0.2	1.25 ± 0.06	4933
212607796	186.07 ± 0.96	14.76 ± 0.04	4.66 ± 0.09	1.21 ± 0.04	5049
212608806	110.57 ± 0.63	9.86 ± 0.05	5.89 ± 0.12	1.13 ± 0.04	4929
212611849	90.5 ± 0.76	8.27 ± 0.06	6.84 ± 0.15	1.25 ± 0.05	4873
212612522	210.61 ± 1.05	16.25 ± 0.13	4.22 ± 0.09	1.11 ± 0.04	4957
212616900	203.05 ± 0.81	16.6 ± 0.05	4.01 ± 0.07	0.97 ± 0.03	5111
212618050	127.21 ± 0.79	10.21 ± 0.08	6.65 ± 0.14	1.7 ± 0.06	5115
212619755	62.25 ± 0.93	6.83 ± 0.04	7.34 ± 0.18	1.0 ± 0.04	4984
212621705	174.54 ± 1.49	13.72 ± 0.05	4.82 ± 0.1	1.2 ± 0.04	4975
212622100	111.62 ± 0.78	10.46 ± 0.04	5.61 ± 0.11	1.05 ± 0.03	5076
212623385	101.05 ± 0.58	9.36 ± 0.06	6.16 ± 0.13	1.14 ± 0.04	4894
212624344	78.35 ± 0.69	7.67 ± 0.08	7.29 ± 0.17	1.25 ± 0.05	4951
212624591	79.6 ± 1.31	7.95 ± 0.08	6.67 ± 0.19	1.05 ± 0.05	4801
212624988	76.77 ± 0.63	8.0 ± 0.11	6.45 ± 0.17	0.95 ± 0.04	4904

Continued on next page

Table A.1 – continued from previous page

EPIC ID	$\nu_{\max}$ (μHz)	$\Delta\nu$ (μHz)	Radius (R$_\odot$)	Mass (M$_\odot$)	$T_{\rm eff}$ (K)
212626314	152.26 ± 1.8	13.18 ± 0.04	4.91 ± 0.11	1.11 ± 0.04	4964
212626855	142.71 ± 0.69	12.73 ± 0.06	5.13 ± 0.1	1.16 ± 0.04	5159
212627232	148.24 ± 1.02	12.67 ± 0.06	5.06 ± 0.1	1.14 ± 0.04	4963
212627690	58.56 ± 0.58	6.15 ± 0.03	7.95 ± 0.17	1.08 ± 0.04	4896
212629242	177.38 ± 0.83	13.77 ± 0.08	4.8 ± 0.1	1.2 ± 0.04	4835
212631920	183.45 ± 0.84	15.16 ± 0.05	4.57 ± 0.08	1.17 ± 0.04	5152
212633100	153.16 ± 0.88	13.08 ± 0.12	4.91 ± 0.11	1.11 ± 0.04	5019
212634125	133.78 ± 2.1	11.73 ± 0.06	5.29 ± 0.13	1.12 ± 0.05	4960
212637642	112.08 ± 0.97	10.6 ± 0.05	5.54 ± 0.11	1.04 ± 0.04	4993
212638061	111.99 ± 0.93	10.15 ± 0.13	5.92 ± 0.16	1.17 ± 0.05	5018
212638862	136.03 ± 1.54	11.56 ± 0.09	5.53 ± 0.13	1.25 ± 0.05	4912
212641219	113.11 ± 0.7	10.22 ± 0.05	5.74 ± 0.11	1.1 ± 0.04	4918
212642408	166.2 ± 2.72	13.9 ± 0.06	4.79 ± 0.12	1.15 ± 0.05	5225
212642532	65.04 ± 1.26	6.75 ± 0.04	7.55 ± 0.21	1.1 ± 0.05	4929
212643371	120.18 ± 0.47	10.85 ± 0.07	5.5 ± 0.11	1.09 ± 0.04	4963
212643448	215.39 ± 1.36	16.74 ± 0.22	4.17 ± 0.11	1.12 ± 0.05	4865
212643613	130.36 ± 1.07	11.37 ± 0.2	5.59 ± 0.18	1.23 ± 0.06	5100
212643750	199.55 ± 1.39	15.69 ± 0.1	4.44 ± 0.09	1.18 ± 0.04	5065
212643873	131.69 ± 0.59	11.12 ± 0.06	5.67 ± 0.11	1.26 ± 0.04	4988
212644310	146.21 ± 0.6	12.54 ± 0.05	5.07 ± 0.09	1.13 ± 0.04	5006
212645082	201.36 ± 1.55	16.51 ± 0.22	4.19 ± 0.11	1.07 ± 0.04	5202
212646229	98.62 ± 0.71	9.08 ± 0.05	6.44 ± 0.13	1.22 ± 0.04	4925
212647785	197.76 ± 1.81	15.39 ± 0.04	4.52 ± 0.09	1.21 ± 0.04	4992
212648235	120.44 ± 0.68	10.35 ± 0.05	5.72 ± 0.11	1.15 ± 0.04	4731
212649511	74.37 ± 2.91	8.28 ± 0.01	6.03 ± 0.26	0.8 ± 0.06	4953
212650234	105.26 ± 0.51	9.49 ± 0.08	5.99 ± 0.13	1.11 ± 0.04	4802
212656715	107.62 ± 0.82	10.08 ± 0.06	5.84 ± 0.12	1.1 ± 0.04	4984
212658455	102.12 ± 0.96	9.27 ± 0.03	6.27 ± 0.13	1.19 ± 0.04	4905
212658955	88.31 ± 0.97	8.53 ± 0.06	6.51 ± 0.15	1.11 ± 0.04	4957
212660503	74.77 ± 0.86	7.39 ± 0.04	7.13 ± 0.16	1.12 ± 0.04	4863
212660907	94.47 ± 0.71	9.05 ± 0.08	6.49 ± 0.15	1.21 ± 0.04	4997
212663573	162.79 ± 0.85	13.51 ± 0.04	4.52 ± 0.08	0.97 ± 0.03	4973
212665000	132.21 ± 0.64	10.46 ± 0.1	6.44 ± 0.15	1.64 ± 0.06	4897
212669168	76.82 ± 0.33	7.57 ± 0.08	7.36 ± 0.18	1.25 ± 0.05	4959
212670258	102.77 ± 0.53	9.51 ± 0.12	5.96 ± 0.15	1.08 ± 0.04	4858
212673547	138.51 ± 3.89	12.3 ± 0.07	5.1 ± 0.17	1.09 ± 0.06	4957
212673978	116.14 ± 0.89	10.57 ± 0.03	5.77 ± 0.11	1.17 ± 0.04	4899
212674537	142.85 ± 0.86	12.56 ± 0.12	5.0 ± 0.11	1.07 ± 0.04	5091
212675193	79.99 ± 0.63	8.37 ± 0.13	6.49 ± 0.18	1.03 ± 0.05	5131
212680658	170.7 ± 1.91	13.37 ± 0.03	4.96 ± 0.1	1.24 ± 0.04	4967
212681389	210.37 ± 1.08	16.13 ± 0.08	4.44 ± 0.09	1.25 ± 0.04	5090
212681448	178.0 ± 2.37	14.38 ± 0.06	4.79 ± 0.11	1.24 ± 0.05	5092
212682720	145.39 ± 1.36	12.54 ± 0.04	5.14 ± 0.1	1.16 ± 0.04	5262
212682773	261.93 ± 2.59	19.06 ± 0.05	3.9 ± 0.08	1.19 ± 0.04	5088
212684857	148.22 ± 1.36	12.09 ± 0.13	5.26 ± 0.13	1.21 ± 0.05	4875
212685061	143.2 ± 1.9	13.17 ± 0.04	4.76 ± 0.11	0.99 ± 0.04	5033
212685771	129.94 ± 0.72	11.03 ± 0.05	5.55 ± 0.11	1.18 ± 0.04	4961
212686303	97.96 ± 0.62	8.69 ± 0.07	6.98 ± 0.15	1.43 ± 0.05	5039
212686431	58.93 ± 1.43	6.46 ± 0.11	7.45 ± 0.29	0.97 ± 0.06	4690
212687303	125.57 ± 0.85	11.05 ± 0.04	5.53 ± 0.11	1.15 ± 0.04	4988
212687403	72.77 ± 0.44	7.2 ± 0.05	7.33 ± 0.15	1.15 ± 0.04	4835
212687849	70.32 ± 0.51	7.06 ± 0.04	7.62 ± 0.16	1.22 ± 0.04	4905
212689886	147.25 ± 1.13	12.34 ± 0.04	5.13 ± 0.1	1.15 ± 0.04	4932
212695660	108.63 ± 0.46	9.84 ± 0.05	6.09 ± 0.12	1.21 ± 0.04	4925
212697502	143.02 ± 1.16	12.4 ± 0.06	5.03 ± 0.1	1.08 ± 0.04	4928
212699714	132.07 ± 0.76	11.21 ± 0.18	5.44 ± 0.16	1.15 ± 0.05	4889
212702456	97.59 ± 0.72	9.05 ± 0.07	6.31 ± 0.14	1.15 ± 0.04	4933
212702625	103.8 ± 0.81	9.0 ± 0.25	7.47 ± 0.33	1.8 ± 0.12	5396
212702847	95.5 ± 0.57	8.65 ± 0.13	6.71 ± 0.19	1.27 ± 0.06	4923
212703382	171.02 ± 0.81	13.4 ± 0.06	5.07 ± 0.1	1.31 ± 0.04	4937
212703924	191.64 ± 2.9	15.26 ± 0.09	4.29 ± 0.11	1.04 ± 0.04	4844

Continued on next page

Table A.1 – continued from previous page

EPIC ID	$\nu_{\rm max}$ (μHz)	$\Delta\nu$ (μHz)	Radius (R$_\odot$)	Mass (M$_\odot$)	$T_{\rm eff}$ (K)
212704542	117.15 ± 0.86	10.07 ± 0.05	6.07 ± 0.12	1.28 ± 0.04	4829
212706291	139.16 ± 0.86	11.63 ± 0.05	5.41 ± 0.1	1.21 ± 0.04	5048
212706376	146.68 ± 1.52	12.86 ± 0.05	4.89 ± 0.1	1.05 ± 0.04	5191
212708555	119.12 ± 0.65	10.53 ± 0.06	5.72 ± 0.11	1.16 ± 0.04	4903
212708825	143.42 ± 0.98	11.69 ± 0.05	5.81 ± 0.11	1.47 ± 0.05	5087
212709542	134.06 ± 1.09	11.44 ± 0.03	5.68 ± 0.11	1.31 ± 0.04	4989
212709723	164.7 ± 1.12	13.73 ± 0.06	4.75 ± 0.09	1.11 ± 0.04	4951
212710941	125.61 ± 0.57	11.2 ± 0.05	5.69 ± 0.11	1.24 ± 0.04	5108
212711147	140.77 ± 1.15	11.94 ± 0.12	5.58 ± 0.13	1.34 ± 0.05	5244
212711618	149.28 ± 0.95	12.58 ± 0.09	5.15 ± 0.11	1.19 ± 0.04	4974
212711911	82.13 ± 0.3	7.73 ± 0.15	7.46 ± 0.24	1.38 ± 0.07	4948
212715267	229.62 ± 1.56	17.53 ± 0.04	4.07 ± 0.08	1.14 ± 0.04	4951
212715936	107.36 ± 1.74	9.89 ± 0.06	5.88 ± 0.15	1.11 ± 0.05	4952
212717529	232.38 ± 1.12	18.1 ± 0.04	4.06 ± 0.07	1.17 ± 0.04	5297
212719814	88.96 ± 0.53	8.62 ± 0.11	6.68 ± 0.17	1.2 ± 0.05	5133
212724763	103.33 ± 1.08	9.59 ± 0.04	6.01 ± 0.13	1.11 ± 0.04	4969
212725025	113.86 ± 0.53	10.88 ± 0.31	5.35 ± 0.23	0.98 ± 0.06	5024
212725648	78.52 ± 0.51	7.52 ± 0.05	7.23 ± 0.15	1.21 ± 0.04	4870
212726717	114.69 ± 1.34	10.59 ± 0.04	5.75 ± 0.12	1.15 ± 0.04	5135
212728042	200.04 ± 0.83	15.12 ± 0.08	4.67 ± 0.09	1.3 ± 0.04	4987
212731330	136.52 ± 0.75	11.52 ± 0.05	5.2 ± 0.1	1.07 ± 0.04	4903
212732293	211.83 ± 1.57	17.18 ± 0.05	3.9 ± 0.08	0.96 ± 0.03	4963
212733290	205.83 ± 1.55	16.49 ± 0.03	4.11 ± 0.08	1.04 ± 0.03	4975
212734971	80.25 ± 1.4	7.5 ± 0.03	7.42 ± 0.19	1.3 ± 0.06	4839
212736216	218.13 ± 1.23	17.3 ± 0.06	4.01 ± 0.08	1.05 ± 0.03	5114
212760680	57.57 ± 1.99	6.16 ± 0.08	7.78 ± 0.34	1.02 ± 0.07	4706
212766797	98.32 ± 0.66	9.03 ± 0.11	6.17 ± 0.16	1.1 ± 0.04	4735
212767652	130.96 ± 0.78	11.38 ± 0.06	5.3 ± 0.11	1.09 ± 0.04	4998
212781976	173.6 ± 0.77	14.46 ± 0.12	4.76 ± 0.1	1.21 ± 0.04	5399
212786057	170.83 ± 1.04	14.09 ± 0.08	4.8 ± 0.1	1.19 ± 0.04	5102
212788951	143.85 ± 0.59	11.85 ± 0.03	5.26 ± 0.1	1.17 ± 0.04	4778
212796298	102.47 ± 0.58	9.4 ± 0.04	6.14 ± 0.12	1.15 ± 0.04	4974
212796425	69.54 ± 0.65	6.83 ± 0.05	7.64 ± 0.17	1.19 ± 0.04	4828
212798759	165.18 ± 1.16	13.94 ± 0.07	4.64 ± 0.09	1.06 ± 0.04	4927
212798866	203.53 ± 1.6	15.56 ± 0.04	4.43 ± 0.09	1.18 ± 0.04	4896
212807400	214.1 ± 1.34	16.04 ± 0.08	4.52 ± 0.09	1.31 ± 0.04	4913
212809205	264.13 ± 0.75	18.91 ± 0.17	3.98 ± 0.08	1.25 ± 0.04	5277
212812593	211.09 ± 6.93	13.44 ± 0.1	6.23 ± 0.24	2.43 ± 0.16	5065
212813809	113.64 ± 0.54	10.18 ± 0.16	6.07 ± 0.17	1.26 ± 0.06	5012
212818050	72.59 ± 2.26	7.2 ± 0.07	7.47 ± 0.28	1.2 ± 0.08	4949
212818978	100.65 ± 0.76	9.43 ± 0.03	6.18 ± 0.12	1.15 ± 0.04	4902
212822092	207.16 ± 1.64	16.55 ± 0.09	4.12 ± 0.09	1.05 ± 0.04	4910
212822692	91.94 ± 1.07	8.94 ± 0.07	6.07 ± 0.15	1.0 ± 0.04	4857
212822937	109.38 ± 0.96	10.68 ± 0.04	5.44 ± 0.11	0.98 ± 0.03	5120
212830012	161.84 ± 1.06	12.89 ± 0.07	5.21 ± 0.1	1.31 ± 0.04	5058
213432065	201.61 ± 1.57	15.21 ± 0.06	4.54 ± 0.09	1.23 ± 0.04	4836
213497176	86.13 ± 0.63	8.08 ± 0.09	6.97 ± 0.17	1.24 ± 0.05	4782
213523476	147.28 ± 2.84	11.81 ± 0.05	5.52 ± 0.15	1.33 ± 0.06	4777
213533540	108.99 ± 1.03	10.02 ± 0.09	5.99 ± 0.14	1.18 ± 0.05	4848
213628417	209.84 ± 4.08	16.17 ± 0.12	4.11 ± 0.12	1.04 ± 0.05	4729
213638949	193.9 ± 3.4	15.13 ± 0.06	4.62 ± 0.12	1.25 ± 0.05	4788
213649499	141.88 ± 0.79	12.02 ± 0.15	5.28 ± 0.14	1.18 ± 0.05	4818
213670870	160.44 ± 1.59	12.51 ± 0.04	5.34 ± 0.11	1.35 ± 0.05	4888
213698261	78.81 ± 0.65	7.78 ± 0.03	6.9 ± 0.14	1.11 ± 0.04	4913
213707868	183.69 ± 2.28	13.67 ± 0.34	5.25 ± 0.21	1.51 ± 0.09	4822
213716898	193.17 ± 1.34	14.72 ± 0.05	4.67 ± 0.09	1.25 ± 0.04	4910
213736396	133.41 ± 1.49	11.15 ± 0.08	5.69 ± 0.13	1.29 ± 0.05	4938
213809000	229.2 ± 1.92	17.52 ± 0.01	4.0 ± 0.08	1.09 ± 0.04	4817
213828212	121.84 ± 0.47	10.77 ± 0.05	5.79 ± 0.11	1.23 ± 0.04	4858
214794287	105.42 ± 0.79	9.32 ± 0.05	6.28 ± 0.13	1.22 ± 0.04	4862
215745876	207.71 ± 1.78	15.9 ± 0.14	4.45 ± 0.1	1.23 ± 0.05	4872

Continued on next page

Table A.1 – continued from previous page

EPIC ID	$\nu_{\max}$ (μHz)	$\Delta\nu$ (μHz)	Radius ($R_\odot$)	Mass ($M_\odot$)	$T_{\rm eff}$ (K)
216824878	75.92 ± 0.82	7.3 ± 0.06	7.63 ± 0.18	1.32 ± 0.05	4838
219245901	120.12 ± 2.98	10.11 ± 0.05	6.38 ± 0.2	1.47 ± 0.08	4863
219265626	135.82 ± 0.53	11.88 ± 0.03	5.22 ± 0.1	1.1 ± 0.04	4766
219541572	51.16 ± 1.92	6.02 ± 0.07	7.66 ± 0.34	0.89 ± 0.07	4933
219664066	111.98 ± 4.3	10.63 ± 0.07	5.45 ± 0.24	0.99 ± 0.07	4837
219675588	92.86 ± 0.82	8.53 ± 0.05	6.66 ± 0.15	1.22 ± 0.04	4749
220145271	229.5 ± 0.94	17.06 ± 0.07	4.14 ± 0.08	1.17 ± 0.04	4854
220153795	167.98 ± 1.64	13.57 ± 0.16	4.84 ± 0.13	1.17 ± 0.05	4903
220168079	129.83 ± 3.45	10.35 ± 0.05	6.58 ± 0.21	1.69 ± 0.09	5132
220168763	99.89 ± 1.14	9.54 ± 0.05	5.94 ± 0.13	1.05 ± 0.04	4963
220172066	64.17 ± 0.29	6.51 ± 0.05	7.96 ± 0.17	1.2 ± 0.04	4964
220172318	197.28 ± 1.8	15.97 ± 0.05	4.14 ± 0.08	1.0 ± 0.03	4952
220172462	124.47 ± 1.16	10.58 ± 0.03	5.85 ± 0.12	1.26 ± 0.04	4842
220180335	196.47 ± 1.35	15.6 ± 0.06	4.29 ± 0.08	1.07 ± 0.04	4896
220182172	174.28 ± 2.43	14.17 ± 0.18	4.56 ± 0.13	1.07 ± 0.05	4883
220184973	149.21 ± 0.78	12.58 ± 0.04	5.14 ± 0.1	1.18 ± 0.04	4897
220186908	117.29 ± 1.11	10.85 ± 0.05	5.53 ± 0.11	1.08 ± 0.04	5005
220187433	154.95 ± 1.12	13.11 ± 0.05	4.83 ± 0.09	1.08 ± 0.04	4927
220190310	233.09 ± 1.13	17.07 ± 0.05	4.26 ± 0.08	1.26 ± 0.04	4955
220195617	156.3 ± 1.53	11.85 ± 0.02	5.94 ± 0.12	1.65 ± 0.06	4914
220198130	70.03 ± 0.66	7.13 ± 0.04	7.24 ± 0.16	1.08 ± 0.04	4728
220201651	99.34 ± 0.71	9.17 ± 0.09	6.19 ± 0.14	1.12 ± 0.04	4887
220203192	78.37 ± 0.49	7.88 ± 0.04	6.77 ± 0.13	1.07 ± 0.04	4913
220205428	76.37 ± 1.3	7.33 ± 0.09	7.28 ± 0.22	1.19 ± 0.06	4578
220205992	145.63 ± 0.92	12.2 ± 0.1	5.37 ± 0.12	1.27 ± 0.05	5068
220206625	130.98 ± 1.03	11.62 ± 0.02	5.34 ± 0.1	1.12 ± 0.04	5071
220211230	259.89 ± 2.39	18.46 ± 0.09	4.07 ± 0.09	1.28 ± 0.05	4919
220213120	172.87 ± 1.49	13.65 ± 0.03	4.87 ± 0.1	1.22 ± 0.04	4867
220214945	105.9 ± 0.74	9.05 ± 0.11	6.6 ± 0.17	1.35 ± 0.05	4738
220216322	93.89 ± 0.79	8.73 ± 0.09	6.41 ± 0.16	1.14 ± 0.05	4737
220222356	212.69 ± 0.91	16.04 ± 0.1	4.41 ± 0.09	1.24 ± 0.04	4732
220223398	76.25 ± 0.48	7.15 ± 0.04	7.43 ± 0.15	1.22 ± 0.04	4787
220224794	167.51 ± 0.96	13.33 ± 0.03	5.18 ± 0.09	1.36 ± 0.04	5115
220231449	134.51 ± 1.13	11.83 ± 0.15	5.38 ± 0.14	1.18 ± 0.05	5067
220235178	163.19 ± 1.21	13.17 ± 0.03	5.04 ± 0.1	1.24 ± 0.04	4948
220236156	143.18 ± 0.93	12.47 ± 0.18	4.99 ± 0.14	1.06 ± 0.05	5053
220236502	166.21 ± 1.18	13.87 ± 0.19	4.64 ± 0.13	1.06 ± 0.05	5062
220237706	120.76 ± 0.87	10.57 ± 0.04	5.62 ± 0.11	1.13 ± 0.04	4750
220242839	94.51 ± 1.2	9.43 ± 0.09	6.0 ± 0.15	1.03 ± 0.04	5044
220245148	101.81 ± 0.82	9.81 ± 0.06	5.7 ± 0.12	0.98 ± 0.03	4959
220251380	125.43 ± 0.97	11.26 ± 0.08	5.4 ± 0.11	1.09 ± 0.04	5032
220262410	56.37 ± 0.8	6.35 ± 0.04	7.33 ± 0.18	0.89 ± 0.04	4903
220265167	176.38 ± 0.74	14.36 ± 0.07	4.64 ± 0.09	1.14 ± 0.04	5065
220266494	101.62 ± 0.96	9.31 ± 0.04	6.19 ± 0.13	1.15 ± 0.04	4957
220269908	83.83 ± 0.63	8.34 ± 0.06	6.69 ± 0.15	1.13 ± 0.04	5017
220271051	168.07 ± 1.33	13.62 ± 0.03	4.83 ± 0.09	1.17 ± 0.04	4949
220272140	105.62 ± 0.88	9.41 ± 0.07	6.51 ± 0.15	1.35 ± 0.05	4763
220272443	187.4 ± 1.74	15.86 ± 0.06	4.14 ± 0.08	0.96 ± 0.03	5041
220272657	209.79 ± 1.73	17.36 ± 0.17	3.99 ± 0.09	1.02 ± 0.04	5105
220273371	232.29 ± 0.94	17.54 ± 0.09	4.02 ± 0.08	1.12 ± 0.04	4907
220287156	171.06 ± 0.58	13.58 ± 0.1	4.86 ± 0.1	1.19 ± 0.04	4817
220295194	91.61 ± 0.48	7.95 ± 0.14	7.66 ± 0.24	1.6 ± 0.08	5033
220301224	182.19 ± 1.92	14.67 ± 0.05	4.6 ± 0.1	1.15 ± 0.04	5072
220304159	107.69 ± 0.5	9.61 ± 0.04	6.27 ± 0.12	1.27 ± 0.04	4923
220304376	138.09 ± 0.47	11.95 ± 0.04	4.81 ± 0.09	0.93 ± 0.03	4905
220309349	156.35 ± 0.95	13.34 ± 0.06	4.82 ± 0.09	1.09 ± 0.04	4917
220316390	89.86 ± 1.34	8.05 ± 0.05	7.09 ± 0.18	1.32 ± 0.06	4647
220318037	179.68 ± 0.75	14.64 ± 0.04	4.51 ± 0.08	1.09 ± 0.03	4885
220319932	74.3 ± 0.72	6.85 ± 0.04	7.98 ± 0.17	1.37 ± 0.05	4718
220321339	80.72 ± 0.89	7.58 ± 0.05	7.48 ± 0.17	1.35 ± 0.05	4897
220321666	144.78 ± 1.21	12.15 ± 0.03	5.12 ± 0.1	1.12 ± 0.04	4792

Continued on next page

Table A.1 – continued from previous page

EPIC ID	$\nu_{\max}$ (μHz)	$\Delta\nu$ (μHz)	Radius ($R_\odot$)	Mass ($M_\odot$)	T_{eff} (K)
220323488	197.14 ± 1.71	15.89 ± 0.04	4.28 ± 0.08	1.08 ± 0.04	5081
220329169	129.17 ± 0.7	10.97 ± 0.06	5.68 ± 0.11	1.24 ± 0.04	4739
220329319	108.87 ± 0.53	9.77 ± 0.04	6.15 ± 0.12	1.23 ± 0.04	4939
220331762	110.45 ± 1.03	9.9 ± 0.04	5.95 ± 0.12	1.16 ± 0.04	4911
220336129	239.87 ± 1.65	17.53 ± 0.03	4.05 ± 0.08	1.16 ± 0.04	4908
220339926	102.37 ± 1.14	9.2 ± 0.27	5.97 ± 0.28	1.05 ± 0.07	4775
220346242	131.58 ± 1.06	11.14 ± 0.06	5.62 ± 0.12	1.24 ± 0.04	4908
220346323	178.58 ± 1.1	14.27 ± 0.04	4.71 ± 0.09	1.18 ± 0.04	4989
220352975	124.08 ± 1.35	11.04 ± 0.06	5.65 ± 0.12	1.19 ± 0.04	5087
220354307	221.42 ± 0.99	16.48 ± 0.05	4.61 ± 0.08	1.44 ± 0.04	5199
220355423	162.61 ± 0.73	13.69 ± 0.03	4.78 ± 0.09	1.11 ± 0.03	5079
220360170	108.62 ± 0.56	10.25 ± 0.09	5.58 ± 0.12	1.01 ± 0.04	4956
220360503	236.77 ± 1.05	17.91 ± 0.03	4.07 ± 0.07	1.18 ± 0.04	5005
220361086	178.29 ± 1.0	14.64 ± 0.05	4.5 ± 0.09	1.08 ± 0.03	4924
220362185	225.85 ± 1.79	17.52 ± 0.02	3.99 ± 0.08	1.08 ± 0.04	4974
220362416	142.18 ± 0.97	11.99 ± 0.07	5.29 ± 0.11	1.19 ± 0.04	5067
220363283	167.03 ± 1.23	14.16 ± 0.05	4.57 ± 0.09	1.04 ± 0.03	5012
220365733	100.82 ± 2.69	9.68 ± 0.05	5.75 ± 0.19	0.99 ± 0.06	5000
220371178	135.22 ± 0.63	12.08 ± 0.05	4.97 ± 0.09	0.99 ± 0.03	5028
220378396	171.35 ± 1.29	13.88 ± 0.15	4.88 ± 0.12	1.23 ± 0.05	5020
220382480	84.37 ± 0.44	8.69 ± 0.1	6.26 ± 0.15	1.0 ± 0.04	5119
220382767	157.59 ± 0.94	12.59 ± 0.11	5.39 ± 0.12	1.37 ± 0.05	5205
220388590	214.55 ± 0.99	15.83 ± 0.04	4.55 ± 0.08	1.32 ± 0.04	5049
220390069	230.18 ± 1.61	18.22 ± 0.08	3.8 ± 0.08	0.99 ± 0.03	4974
220391088	172.96 ± 1.01	13.65 ± 0.17	5.0 ± 0.13	1.3 ± 0.05	5006
220393476	182.44 ± 1.42	14.55 ± 0.07	4.59 ± 0.09	1.15 ± 0.04	4952
220409518	96.83 ± 0.43	8.85 ± 0.09	6.72 ± 0.16	1.32 ± 0.05	5087
220409539	103.2 ± 1.19	8.92 ± 0.05	6.76 ± 0.16	1.39 ± 0.05	4593
220415082	164.23 ± 1.31	13.26 ± 0.03	4.96 ± 0.1	1.2 ± 0.04	4890
220416796	109.95 ± 0.78	9.08 ± 0.12	7.07 ± 0.19	1.64 ± 0.07	4788
220426655	169.09 ± 1.25	14.12 ± 0.07	4.66 ± 0.09	1.1 ± 0.04	4990
220428840	160.04 ± 0.97	12.99 ± 0.05	5.0 ± 0.1	1.19 ± 0.04	4874
220435457	126.14 ± 0.72	10.51 ± 0.08	6.08 ± 0.13	1.39 ± 0.05	4860
220442308	92.28 ± 0.47	8.33 ± 0.06	7.31 ± 0.15	1.49 ± 0.05	5039
220457518	185.67 ± 1.02	13.66 ± 0.1	5.21 ± 0.11	1.5 ± 0.05	4929
220464501	73.77 ± 0.57	7.05 ± 0.06	7.84 ± 0.18	1.35 ± 0.05	4960
220464772	175.17 ± 1.21	14.62 ± 0.1	4.66 ± 0.1	1.16 ± 0.04	5203
220468554	116.24 ± 0.93	10.65 ± 0.03	5.31 ± 0.11	0.96 ± 0.03	4890
220470556	76.03 ± 0.66	7.43 ± 0.04	7.16 ± 0.15	1.15 ± 0.04	4783
220470763	117.94 ± 0.72	10.47 ± 0.09	5.55 ± 0.13	1.07 ± 0.04	4764
220471410	159.79 ± 0.92	13.45 ± 0.07	4.69 ± 0.09	1.04 ± 0.04	4877
220472462	117.1 ± 0.81	10.13 ± 0.13	6.09 ± 0.16	1.29 ± 0.05	4992
220472863	143.82 ± 1.52	12.09 ± 0.04	5.3 ± 0.11	1.21 ± 0.04	5018
220492152	96.0 ± 0.46	8.66 ± 0.16	6.77 ± 0.22	1.31 ± 0.06	4897
220494336	62.57 ± 0.54	6.39 ± 0.04	7.54 ± 0.17	1.02 ± 0.04	4745
220494500	93.64 ± 0.56	8.79 ± 0.1	6.23 ± 0.15	1.07 ± 0.04	4841
220496855	207.71 ± 1.89	15.41 ± 0.06	4.77 ± 0.09	1.42 ± 0.05	5177
220498033	111.07 ± 0.9	10.18 ± 0.04	5.6 ± 0.11	1.03 ± 0.03	4965
220501588	206.44 ± 1.19	16.03 ± 0.2	4.45 ± 0.11	1.23 ± 0.05	5084
220501668	125.13 ± 0.79	11.4 ± 0.04	5.28 ± 0.1	1.04 ± 0.03	4962
220508609	120.05 ± 0.84	10.88 ± 0.08	5.36 ± 0.12	1.02 ± 0.04	4649
220513748	214.63 ± 1.4	16.81 ± 0.03	4.02 ± 0.08	1.03 ± 0.03	4883
220522361	201.95 ± 0.95	16.49 ± 0.05	4.16 ± 0.08	1.05 ± 0.03	4859
220524755	231.3 ± 2.25	17.44 ± 0.03	4.05 ± 0.08	1.13 ± 0.04	4926
220525477	274.76 ± 1.61	19.49 ± 0.04	3.81 ± 0.07	1.18 ± 0.04	4960
220526037	219.6 ± 1.2	18.01 ± 0.06	3.7 ± 0.07	0.89 ± 0.03	4901
220527876	88.52 ± 0.44	8.58 ± 0.03	6.41 ± 0.12	1.08 ± 0.04	4900
220531146	229.01 ± 2.37	19.1 ± 0.24	3.31 ± 0.09	0.73 ± 0.03	4933
220537239	278.18 ± 3.5	18.95 ± 0.14	4.18 ± 0.1	1.46 ± 0.06	5073
220538008	212.46 ± 1.26	16.96 ± 0.02	3.97 ± 0.07	0.99 ± 0.03	4943
220539225	74.55 ± 0.91	7.1 ± 0.06	7.85 ± 0.19	1.37 ± 0.06	5025

Continued on next page

Table A.1 – continued from previous page

EPIC ID	$\nu_{\max}$ (μHz)	$\Delta\nu$ (μHz)	Radius ($R_\odot$)	Mass ($M_\odot$)	T_{eff} (K)
220541482	128.58 ± 1.83	10.96 ± 0.03	5.56 ± 0.13	1.17 ± 0.05	4972
220543175	81.99 ± 1.17	7.91 ± 0.12	6.89 ± 0.22	1.15 ± 0.06	4935
220545742	110.23 ± 0.59	10.11 ± 0.06	5.88 ± 0.12	1.14 ± 0.04	5070
220548055	201.4 ± 1.42	15.57 ± 0.1	4.73 ± 0.1	1.38 ± 0.05	4993
220557296	150.71 ± 0.79	12.81 ± 0.03	4.84 ± 0.09	1.05 ± 0.03	4840
220562375	88.45 ± 0.61	8.01 ± 0.03	6.84 ± 0.14	1.19 ± 0.04	4623
220563581	138.83 ± 0.82	11.73 ± 0.06	5.32 ± 0.11	1.16 ± 0.04	4947
220568814	90.14 ± 0.95	8.2 ± 0.07	7.86 ± 0.19	1.74 ± 0.07	4586
220569010	113.36 ± 1.22	9.87 ± 0.04	6.04 ± 0.13	1.22 ± 0.05	4733
220574095	124.72 ± 0.93	11.07 ± 0.04	5.4 ± 0.11	1.08 ± 0.04	4862
220574134	120.95 ± 0.85	10.3 ± 0.02	6.21 ± 0.12	1.41 ± 0.05	5080
220580254	242.53 ± 1.44	17.01 ± 0.09	4.36 ± 0.09	1.36 ± 0.05	4979
220583285	156.29 ± 1.19	12.14 ± 0.06	6.03 ± 0.12	1.75 ± 0.06	4809
220608428	148.47 ± 2.55	11.26 ± 0.05	6.3 ± 0.16	1.77 ± 0.08	5115
220610745	80.67 ± 0.68	7.68 ± 0.08	7.24 ± 0.17	1.25 ± 0.05	4948
220613966	142.84 ± 1.22	11.6 ± 0.05	5.57 ± 0.11	1.31 ± 0.05	4842
220628328	165.05 ± 1.23	12.64 ± 0.05	5.4 ± 0.11	1.43 ± 0.05	4937
220632312	231.61 ± 3.57	17.84 ± 0.11	4.06 ± 0.1	1.15 ± 0.05	5062
220638639	242.64 ± 2.45	18.49 ± 0.12	3.81 ± 0.08	1.05 ± 0.04	4956
220643264	200.36 ± 1.66	16.15 ± 0.27	4.17 ± 0.13	1.04 ± 0.05	4913
220649490	191.03 ± 1.77	14.49 ± 0.06	4.71 ± 0.1	1.25 ± 0.04	4936
220653241	84.34 ± 1.42	7.91 ± 0.03	6.85 ± 0.18	1.16 ± 0.05	4659
220692210	95.68 ± 0.72	8.85 ± 0.05	6.31 ± 0.13	1.12 ± 0.04	4766
220699696	176.63 ± 1.72	14.55 ± 0.07	4.68 ± 0.1	1.18 ± 0.04	5096
220705541	78.38 ± 1.18	7.45 ± 0.08	7.43 ± 0.2	1.28 ± 0.06	4999
220721747	207.43 ± 2.09	16.49 ± 0.39	4.18 ± 0.16	1.08 ± 0.06	5046
220750649	93.78 ± 1.0	8.81 ± 0.07	6.5 ± 0.15	1.18 ± 0.05	5016
222930532	156.37 ± 1.54	13.05 ± 0.02	4.85 ± 0.1	1.09 ± 0.04	4592
223153645	121.3 ± 1.1	10.06 ± 0.16	6.22 ± 0.19	1.39 ± 0.07	4334
223233532	68.89 ± 1.3	7.09 ± 0.18	7.21 ± 0.32	1.06 ± 0.07	4647
223252098	98.96 ± 0.83	8.78 ± 0.06	6.6 ± 0.15	1.26 ± 0.05	4550
225989687	234.46 ± 3.79	17.77 ± 0.04	3.93 ± 0.1	1.08 ± 0.05	4605
227348805	114.68 ± 1.03	9.67 ± 0.06	6.35 ± 0.14	1.36 ± 0.05	4657
227840890	100.35 ± 1.81	8.65 ± 0.15	6.94 ± 0.25	1.42 ± 0.08	4450
228711577	145.91 ± 1.51	12.76 ± 0.1	4.88 ± 0.11	1.04 ± 0.04	5020
228714709	99.15 ± 0.6	8.44 ± 0.09	7.24 ± 0.18	1.53 ± 0.06	4618
228715469	131.79 ± 1.01	12.1 ± 0.18	3.85 ± 0.11	0.52 ± 0.02	4985
228717379	132.84 ± 1.25	11.63 ± 0.06	5.4 ± 0.11	1.16 ± 0.04	4972
228717636	106.1 ± 1.05	9.89 ± 0.19	5.95 ± 0.2	1.13 ± 0.06	4973
228720455	118.93 ± 1.37	10.53 ± 0.06	5.88 ± 0.13	1.24 ± 0.05	4942
228721941	184.02 ± 1.23	14.33 ± 0.04	4.7 ± 0.09	1.2 ± 0.04	4894
228722897	168.21 ± 2.22	13.98 ± 0.14	4.64 ± 0.12	1.08 ± 0.05	4936
228725318	151.36 ± 1.2	12.22 ± 0.27	5.51 ± 0.2	1.39 ± 0.08	4918
228726144	99.18 ± 0.57	8.66 ± 0.11	6.93 ± 0.18	1.41 ± 0.06	4733
228734058	174.15 ± 1.02	14.38 ± 0.17	4.48 ± 0.11	1.04 ± 0.04	4946
228735434	96.14 ± 0.97	8.63 ± 0.09	6.71 ± 0.17	1.28 ± 0.05	4880
228739714	153.96 ± 2.34	12.36 ± 0.04	5.35 ± 0.13	1.31 ± 0.05	4873
228741749	77.48 ± 0.62	7.92 ± 0.06	6.58 ± 0.14	0.99 ± 0.04	4835
228742659	189.82 ± 0.59	15.47 ± 0.11	4.08 ± 0.08	0.92 ± 0.03	4811
228743122	141.75 ± 0.72	12.34 ± 0.05	5.0 ± 0.1	1.05 ± 0.03	4852
228743475	167.85 ± 1.48	14.08 ± 0.13	4.76 ± 0.11	1.16 ± 0.04	4972
228747669	127.66 ± 0.89	10.85 ± 0.09	5.53 ± 0.12	1.14 ± 0.04	4890
228748428	103.78 ± 0.67	9.38 ± 0.21	6.2 ± 0.23	1.18 ± 0.07	4906
228749746	134.26 ± 0.62	11.97 ± 0.04	5.16 ± 0.1	1.07 ± 0.03	4935
228750765	225.59 ± 1.86	16.92 ± 0.07	4.35 ± 0.09	1.29 ± 0.04	5122
228750838	284.19 ± 1.55	20.0 ± 0.05	3.76 ± 0.07	1.19 ± 0.04	4839
228752254	94.71 ± 1.09	9.09 ± 0.08	6.13 ± 0.15	1.06 ± 0.04	4947
228753015	79.36 ± 0.69	8.01 ± 0.08	6.76 ± 0.16	1.09 ± 0.04	4930
228754001	249.35 ± 1.72	18.55 ± 0.13	3.87 ± 0.08	1.11 ± 0.04	4908
228755001	155.91 ± 5.67	12.99 ± 0.15	5.05 ± 0.22	1.2 ± 0.09	5039
228758590	196.12 ± 1.46	14.83 ± 0.06	4.75 ± 0.09	1.32 ± 0.04	4865

Continued on next page

Table A.1 – continued from previous page

EPIC ID	$\nu_{\max}$ (μHz)	$\Delta\nu$ (μHz)	Radius ($R_\odot$)	Mass ($M_\odot$)	$T_{\rm eff}$ (K)
228758894	149.24 ± 0.65	12.22 ± 0.07	5.2 ± 0.1	1.19 ± 0.04	4783
228759949	125.74 ± 0.71	10.7 ± 0.06	5.81 ± 0.12	1.26 ± 0.04	5073
228760817	146.07 ± 0.97	12.26 ± 0.11	5.03 ± 0.11	1.09 ± 0.04	5028
228760954	109.69 ± 0.71	9.95 ± 0.16	6.17 ± 0.18	1.26 ± 0.06	4912
228763718	129.24 ± 1.07	10.88 ± 0.11	5.76 ± 0.14	1.27 ± 0.05	4893
228768295	235.3 ± 1.94	17.48 ± 0.05	3.97 ± 0.08	1.09 ± 0.04	4939
228770416	238.49 ± 2.45	17.84 ± 0.17	3.96 ± 0.1	1.11 ± 0.04	4889
228771173	260.2 ± 2.4	18.59 ± 0.11	4.01 ± 0.09	1.24 ± 0.04	5077
228772190	101.81 ± 0.58	9.46 ± 0.05	6.29 ± 0.12	1.21 ± 0.04	5026
228774437	86.76 ± 0.73	7.61 ± 0.07	7.4 ± 0.17	1.36 ± 0.05	5029
228776066	70.48 ± 0.47	6.86 ± 0.07	7.56 ± 0.18	1.17 ± 0.05	4815
228776599	143.81 ± 0.81	11.77 ± 0.13	5.58 ± 0.13	1.34 ± 0.05	5138
228776603	109.53 ± 0.83	9.49 ± 0.06	6.17 ± 0.13	1.22 ± 0.04	4705
228777563	121.84 ± 1.1	10.66 ± 0.08	5.7 ± 0.13	1.18 ± 0.04	4897
228779057	81.47 ± 0.66	7.99 ± 0.1	6.89 ± 0.18	1.16 ± 0.05	5021
228781647	93.51 ± 1.1	8.86 ± 0.06	6.22 ± 0.14	1.07 ± 0.04	4886
228782420	156.9 ± 1.01	14.08 ± 0.08	4.43 ± 0.09	0.92 ± 0.03	4968
228783907	196.61 ± 1.19	15.38 ± 0.08	4.32 ± 0.09	1.08 ± 0.04	4827
228786508	82.51 ± 0.29	8.09 ± 0.08	6.86 ± 0.15	1.16 ± 0.04	5051
228787269	78.47 ± 0.73	7.47 ± 0.09	7.59 ± 0.2	1.36 ± 0.06	4827
228788464	98.0 ± 0.39	8.63 ± 0.09	7.14 ± 0.16	1.51 ± 0.06	5105
228788585	173.95 ± 0.94	14.47 ± 0.09	4.5 ± 0.09	1.05 ± 0.04	5105
228789698	123.57 ± 2.31	10.7 ± 0.07	5.69 ± 0.16	1.19 ± 0.05	4903
228790729	65.68 ± 0.65	6.97 ± 0.09	7.38 ± 0.2	1.07 ± 0.05	4792
228791859	160.1 ± 0.8	12.96 ± 0.07	4.99 ± 0.1	1.18 ± 0.04	4977
228792955	209.15 ± 1.27	15.14 ± 0.15	4.77 ± 0.11	1.41 ± 0.05	4908
228794783	184.14 ± 1.85	14.66 ± 0.1	4.67 ± 0.1	1.2 ± 0.04	5200
228795694	69.0 ± 0.27	6.75 ± 0.05	7.82 ± 0.17	1.24 ± 0.04	4910
228796389	245.65 ± 2.12	18.6 ± 0.08	3.96 ± 0.08	1.17 ± 0.04	5107
228799099	159.17 ± 0.81	12.26 ± 0.06	5.67 ± 0.11	1.53 ± 0.05	5092
228799450	194.7 ± 2.95	15.71 ± 0.17	4.21 ± 0.12	1.02 ± 0.05	4766
228801006	105.13 ± 0.53	9.47 ± 0.06	6.29 ± 0.13	1.24 ± 0.04	5011
228801092	256.12 ± 2.17	19.3 ± 0.36	3.84 ± 0.12	1.14 ± 0.06	5426
228808510	148.55 ± 1.49	13.53 ± 0.4	4.61 ± 0.21	0.96 ± 0.07	5134
228809268	250.77 ± 2.05	18.48 ± 0.15	3.92 ± 0.09	1.15 ± 0.04	4895
228813422	69.85 ± 0.84	6.75 ± 0.08	7.93 ± 0.21	1.29 ± 0.06	5011
228813972	175.16 ± 0.77	14.09 ± 0.06	4.76 ± 0.09	1.19 ± 0.04	4961
228814071	101.61 ± 0.56	9.49 ± 0.06	6.15 ± 0.12	1.15 ± 0.04	5159
228816314	98.07 ± 0.43	9.47 ± 0.15	5.76 ± 0.16	0.96 ± 0.04	4889
228817956	147.5 ± 1.99	11.45 ± 0.13	5.88 ± 0.16	1.51 ± 0.07	4791
228822439	102.26 ± 0.62	9.57 ± 0.05	6.1 ± 0.12	1.14 ± 0.04	4874
228825731	124.5 ± 0.51	10.88 ± 0.04	5.63 ± 0.1	1.18 ± 0.04	5001
228830315	90.53 ± 0.88	8.9 ± 0.18	6.35 ± 0.22	1.1 ± 0.06	5219
228830786	150.66 ± 1.26	12.1 ± 0.12	5.52 ± 0.13	1.38 ± 0.05	4933
228833025	66.35 ± 0.84	6.93 ± 0.07	7.4 ± 0.19	1.08 ± 0.05	5009
228833740	192.45 ± 1.53	15.89 ± 0.07	4.32 ± 0.08	1.09 ± 0.04	5409
228834206	132.07 ± 0.86	10.64 ± 0.12	6.29 ± 0.16	1.57 ± 0.06	4907
228838826	126.73 ± 0.56	11.32 ± 0.08	5.48 ± 0.11	1.15 ± 0.04	5319
228839832	219.43 ± 1.4	16.88 ± 0.03	4.2 ± 0.08	1.16 ± 0.04	5043
228845816	63.96 ± 0.39	6.51 ± 0.09	7.65 ± 0.21	1.09 ± 0.05	4629
228845944	79.19 ± 0.41	7.69 ± 0.08	7.08 ± 0.17	1.18 ± 0.05	4840
228846546	129.62 ± 1.04	11.35 ± 0.06	5.53 ± 0.11	1.19 ± 0.04	5049
228847288	204.46 ± 0.78	15.12 ± 0.16	4.79 ± 0.11	1.4 ± 0.05	4924
228848482	120.8 ± 1.49	11.27 ± 0.08	5.27 ± 0.12	1.01 ± 0.04	5112
228848988	96.59 ± 0.57	9.14 ± 0.09	6.22 ± 0.14	1.12 ± 0.04	4913
228853371	110.77 ± 0.96	10.36 ± 0.2	5.81 ± 0.19	1.14 ± 0.06	5202
228857099	176.67 ± 1.33	14.28 ± 0.07	4.62 ± 0.09	1.12 ± 0.04	4895
228857125	192.03 ± 0.91	15.79 ± 0.04	4.33 ± 0.08	1.09 ± 0.03	5314
228858437	108.35 ± 2.2	9.39 ± 0.12	6.55 ± 0.21	1.39 ± 0.07	5025
228859153	221.44 ± 2.45	17.42 ± 0.35	3.78 ± 0.13	0.93 ± 0.05	4881
228859569	182.33 ± 0.75	14.31 ± 0.08	4.57 ± 0.09	1.12 ± 0.04	4751

Continued on next page

Table A.1 – continued from previous page

EPIC ID	$\nu_{\rm max}$ (μHz)	$\Delta\nu$ (μHz)	Radius ($R_\odot$)	Mass ($M_\odot$)	$T_{\rm eff}$ (K)
228860224	127.09 ± 0.87	11.51 ± 0.06	5.18 ± 0.1	1.01 ± 0.03	4936
228860670	66.99 ± 0.37	6.71 ± 0.06	7.87 ± 0.18	1.23 ± 0.05	4850
228865380	261.84 ± 9.7	18.79 ± 0.05	4.09 ± 0.17	1.33 ± 0.09	4991
228866283	149.94 ± 1.36	12.81 ± 0.05	4.93 ± 0.1	1.08 ± 0.04	4934
228866634	85.11 ± 2.47	7.53 ± 0.11	7.72 ± 0.31	1.49 ± 0.1	4677
228871871	115.72 ± 0.84	10.12 ± 0.07	6.06 ± 0.13	1.27 ± 0.04	5033
228872454	106.41 ± 0.68	9.03 ± 0.2	6.98 ± 0.25	1.55 ± 0.08	4887
228873333	149.76 ± 1.9	12.64 ± 0.09	5.05 ± 0.12	1.14 ± 0.05	5018
228875623	229.74 ± 1.26	17.58 ± 0.05	4.12 ± 0.08	1.17 ± 0.04	4998
228876370	164.31 ± 0.91	13.62 ± 0.04	4.96 ± 0.09	1.22 ± 0.04	4833
228879483	266.27 ± 0.61	20.31 ± 0.2	3.52 ± 0.08	0.98 ± 0.04	4898
228882446	239.95 ± 2.23	17.83 ± 0.05	3.99 ± 0.08	1.13 ± 0.04	5054
228909656	250.16 ± 1.56	18.71 ± 0.09	3.8 ± 0.07	1.07 ± 0.04	5169
228921656	194.72 ± 0.3	14.98 ± 0.5	5.03 ± 0.25	1.53 ± 0.11	5492
228931059	103.99 ± 2.22	9.19 ± 0.09	6.48 ± 0.2	1.29 ± 0.07	4923
228955892	199.82 ± 0.97	16.45 ± 0.05	4.1 ± 0.07	1.01 ± 0.03	5091
228957921	220.99 ± 1.57	16.7 ± 0.04	4.21 ± 0.08	1.17 ± 0.04	4993
228967892	156.45 ± 1.37	13.76 ± 0.4	4.72 ± 0.22	1.06 ± 0.07	5123
228974313	131.88 ± 0.94	11.99 ± 0.08	4.9 ± 0.1	0.94 ± 0.03	5007
228974563	176.47 ± 1.07	13.49 ± 0.2	5.32 ± 0.15	1.51 ± 0.06	5153
228979945	233.78 ± 1.82	17.71 ± 0.05	3.95 ± 0.08	1.08 ± 0.04	5085
229005585	86.18 ± 0.5	8.49 ± 0.04	6.52 ± 0.13	1.09 ± 0.04	4923
229026541	119.38 ± 2.14	10.96 ± 0.04	5.55 ± 0.14	1.11 ± 0.05	5080
229029325	229.08 ± 1.8	15.71 ± 0.26	4.93 ± 0.15	1.66 ± 0.08	4864
229030405	96.0 ± 0.59	8.62 ± 0.19	6.94 ± 0.25	1.39 ± 0.08	4986
229032783	91.78 ± 0.81	8.22 ± 0.06	6.87 ± 0.16	1.26 ± 0.05	4845
229033193	92.13 ± 0.63	8.78 ± 0.07	6.42 ± 0.14	1.13 ± 0.04	5231
229048445	231.99 ± 3.75	17.42 ± 0.12	4.23 ± 0.11	1.26 ± 0.05	5041
229055549	190.99 ± 2.15	15.02 ± 0.13	4.55 ± 0.11	1.18 ± 0.05	4945
229056060	222.06 ± 0.82	16.87 ± 0.04	4.21 ± 0.08	1.18 ± 0.04	4914
229071342	88.54 ± 0.67	8.22 ± 0.07	7.1 ± 0.16	1.34 ± 0.05	5056
229091595	99.32 ± 0.68	8.61 ± 0.09	7.35 ± 0.17	1.63 ± 0.06	5064
229091997	174.53 ± 1.54	14.18 ± 0.15	4.71 ± 0.12	1.16 ± 0.05	4946
229095441	94.91 ± 1.08	9.08 ± 0.09	6.32 ± 0.16	1.14 ± 0.05	5068
229095965	56.11 ± 0.38	6.25 ± 0.05	7.82 ± 0.17	1.02 ± 0.04	4750
229097029	101.81 ± 1.05	9.62 ± 0.17	5.97 ± 0.19	1.08 ± 0.05	4987
229100348	142.93 ± 0.92	12.31 ± 0.09	5.24 ± 0.11	1.18 ± 0.04	4995
229100657	166.09 ± 0.5	13.22 ± 0.24	5.06 ± 0.16	1.27 ± 0.06	5036
229107489	192.94 ± 4.11	16.33 ± 0.09	4.14 ± 0.12	1.01 ± 0.05	5136
229109624	102.54 ± 0.68	9.02 ± 0.18	7.09 ± 0.24	1.57 ± 0.08	4824
229110707	82.07 ± 1.02	7.69 ± 0.05	7.61 ± 0.18	1.43 ± 0.06	4954
229114792	88.56 ± 0.59	8.85 ± 0.13	6.17 ± 0.17	1.0 ± 0.04	5100
229114973	158.89 ± 1.17	11.36 ± 0.07	6.48 ± 0.13	1.98 ± 0.07	5013
229122401	74.7 ± 0.92	7.35 ± 0.15	7.66 ± 0.27	1.33 ± 0.07	5107
229123875	81.58 ± 0.64	8.22 ± 0.1	6.64 ± 0.17	1.08 ± 0.04	4993
229135416	118.07 ± 2.8	9.63 ± 0.08	6.86 ± 0.22	1.67 ± 0.09	5093
229141080	163.25 ± 2.14	13.01 ± 0.05	5.1 ± 0.12	1.26 ± 0.05	4774
229144264	206.66 ± 2.36	16.11 ± 0.06	4.16 ± 0.09	1.05 ± 0.04	4860
229150764	79.39 ± 0.54	7.85 ± 0.12	7.15 ± 0.2	1.23 ± 0.05	5056
229155461	157.09 ± 0.85	13.9 ± 0.28	4.53 ± 0.15	0.97 ± 0.05	5004
229156449	224.75 ± 3.34	17.71 ± 0.35	4.03 ± 0.15	1.11 ± 0.06	5049
229163252	78.54 ± 2.68	7.51 ± 0.11	7.5 ± 0.33	1.32 ± 0.1	4972
229175729	122.99 ± 0.85	10.46 ± 0.13	6.02 ± 0.16	1.33 ± 0.05	4828
229442148	74.86 ± 1.89	7.02 ± 0.09	7.71 ± 0.28	1.3 ± 0.08	4628
229460578	114.81 ± 1.22	9.59 ± 0.12	6.61 ± 0.18	1.49 ± 0.07	4727
229461478	90.8 ± 1.88	7.86 ± 0.19	7.72 ± 0.34	1.61 ± 0.11	4666
230199318	200.1 ± 2.43	16.13 ± 0.4	4.21 ± 0.17	1.06 ± 0.07	4735
230506262	103.68 ± 0.48	9.17 ± 0.04	6.37 ± 0.13	1.24 ± 0.04	4402
230521077	175.43 ± 1.64	14.09 ± 0.05	4.87 ± 0.1	1.26 ± 0.05	4599
230527654	90.81 ± 0.32	8.01 ± 0.08	7.39 ± 0.17	1.47 ± 0.06	4614
230591161	178.84 ± 6.45	14.0 ± 0.05	5.14 ± 0.21	1.44 ± 0.1	4643

Continued on next page

Table A.1 – continued from previous page

EPIC ID	$\nu_{\max}$ (μHz)	$\Delta\nu$ (μHz)	Radius ($R_\odot$)	Mass ($M_\odot$)	$T_{\rm eff}$ (K)
230610385	61.87 ± 0.65	6.68 ± 0.08	7.05 ± 0.19	0.89 ± 0.04	4678
230615572	180.7 ± 1.11	14.44 ± 0.07	5.08 ± 0.1	1.46 ± 0.05	4758
230618520	132.3 ± 0.89	10.27 ± 0.08	7.35 ± 0.16	2.22 ± 0.08	4684
230619863	71.98 ± 1.01	7.13 ± 0.05	7.53 ± 0.19	1.22 ± 0.05	4666
230623420	90.6 ± 0.61	8.25 ± 0.07	7.25 ± 0.16	1.43 ± 0.05	4633
230626784	183.66 ± 0.98	14.47 ± 0.09	4.86 ± 0.1	1.31 ± 0.05	4619
230711939	88.95 ± 0.77	8.43 ± 0.04	6.78 ± 0.14	1.23 ± 0.04	4685
230718263	107.23 ± 0.82	9.3 ± 0.04	7.15 ± 0.15	1.69 ± 0.06	4625
230727711	119.68 ± 0.7	10.76 ± 0.05	5.56 ± 0.11	1.1 ± 0.04	4657
230731829	81.19 ± 1.35	7.58 ± 0.04	7.54 ± 0.2	1.38 ± 0.06	4601
230732244	149.41 ± 1.93	12.46 ± 0.14	5.1 ± 0.14	1.16 ± 0.05	4705
230738543	169.93 ± 2.15	12.94 ± 0.06	5.53 ± 0.13	1.57 ± 0.06	4713
230739609	86.12 ± 0.05	8.17 ± 0.13	6.88 ± 0.2	1.21 ± 0.05	4666
230751800	106.67 ± 1.03	8.59 ± 0.1	7.6 ± 0.2	1.83 ± 0.08	4589
230763211	103.48 ± 0.78	9.39 ± 0.08	6.05 ± 0.14	1.11 ± 0.04	4571
230771958	225.6 ± 2.69	18.27 ± 0.25	3.73 ± 0.11	0.94 ± 0.04	4724
230800710	180.62 ± 3.1	13.32 ± 0.11	5.43 ± 0.15	1.59 ± 0.07	4787
230819723	170.01 ± 0.74	14.04 ± 0.16	4.75 ± 0.12	1.15 ± 0.05	4619
230826795	171.53 ± 3.42	14.35 ± 0.11	4.81 ± 0.14	1.22 ± 0.06	4741
230854219	92.38 ± 0.57	7.8 ± 0.23	7.84 ± 0.35	1.67 ± 0.11	4580
230868883	180.59 ± 1.69	13.8 ± 0.1	5.16 ± 0.12	1.45 ± 0.06	4722
230892316	135.83 ± 1.2	11.63 ± 0.05	5.43 ± 0.11	1.2 ± 0.04	4651
230944393	115.39 ± 0.51	10.49 ± 0.05	5.42 ± 0.11	1.0 ± 0.03	4568
230952945	146.39 ± 0.71	12.14 ± 0.08	5.2 ± 0.11	1.17 ± 0.04	4712
231027349	196.51 ± 1.58	14.81 ± 0.17	4.69 ± 0.12	1.28 ± 0.05	4667
231099350	72.18 ± 0.85	7.99 ± 0.11	6.15 ± 0.18	0.8 ± 0.04	4731
231106339	196.85 ± 1.59	15.42 ± 0.07	4.47 ± 0.09	1.18 ± 0.04	4682
231109894	172.28 ± 2.17	13.18 ± 0.17	5.09 ± 0.14	1.31 ± 0.06	4698
231165317	88.62 ± 0.91	7.9 ± 0.07	7.95 ± 0.19	1.71 ± 0.07	4704
231186027	174.42 ± 1.18	13.85 ± 0.13	4.81 ± 0.11	1.2 ± 0.05	4663
231198724	134.97 ± 1.19	11.27 ± 0.09	5.55 ± 0.13	1.23 ± 0.05	4633
231220187	131.68 ± 1.27	11.17 ± 0.04	5.63 ± 0.12	1.25 ± 0.05	4668
231235326	74.24 ± 1.82	7.08 ± 0.17	7.62 ± 0.34	1.27 ± 0.09	4690
231258174	83.34 ± 0.59	7.83 ± 0.08	7.44 ± 0.18	1.39 ± 0.05	4671
231265573	105.52 ± 1.4	8.99 ± 0.08	6.87 ± 0.18	1.48 ± 0.06	4722
231267707	159.86 ± 0.88	12.48 ± 0.1	5.29 ± 0.12	1.31 ± 0.05	4615
231272282	141.69 ± 2.19	11.51 ± 0.04	5.51 ± 0.14	1.27 ± 0.05	4586
231423485	168.48 ± 1.24	12.56 ± 0.23	5.54 ± 0.18	1.53 ± 0.08	4589
231477865	200.2 ± 3.61	15.15 ± 0.13	4.8 ± 0.14	1.4 ± 0.07	4603
231535046	171.72 ± 2.61	13.67 ± 0.11	5.42 ± 0.14	1.58 ± 0.07	4595
231686381	171.52 ± 2.37	13.08 ± 0.2	5.4 ± 0.17	1.5 ± 0.08	4598
231796165	213.41 ± 2.44	16.25 ± 0.18	4.22 ± 0.11	1.12 ± 0.05	4581
231840743	126.74 ± 2.87	10.37 ± 0.22	6.18 ± 0.26	1.43 ± 0.1	4661
231876812	83.6 ± 0.53	7.78 ± 0.05	7.19 ± 0.16	1.28 ± 0.05	4590
231888373	192.07 ± 1.26	14.83 ± 0.06	4.61 ± 0.09	1.21 ± 0.04	4644
231889300	111.58 ± 3.64	9.57 ± 0.12	6.33 ± 0.26	1.32 ± 0.09	4641
231911215	186.63 ± 1.48	14.54 ± 0.16	4.71 ± 0.12	1.23 ± 0.05	4644
231935373	125.78 ± 1.24	11.3 ± 0.05	5.5 ± 0.12	1.15 ± 0.04	4749
231960058	101.34 ± 0.53	8.87 ± 0.05	6.75 ± 0.14	1.37 ± 0.05	4609
231963227	129.86 ± 0.8	11.43 ± 0.04	5.25 ± 0.11	1.06 ± 0.04	4562
231980039	100.12 ± 0.58	9.12 ± 0.09	6.54 ± 0.15	1.28 ± 0.05	4661
232008804	107.86 ± 0.49	9.6 ± 0.13	6.26 ± 0.16	1.26 ± 0.05	4705
232042100	161.69 ± 1.21	13.2 ± 0.04	5.06 ± 0.1	1.25 ± 0.04	4648
232136212	84.93 ± 1.1	7.78 ± 0.06	7.47 ± 0.19	1.42 ± 0.06	4606
232136841	120.64 ± 1.38	10.01 ± 0.04	6.38 ± 0.14	1.46 ± 0.06	4596
232151786	77.53 ± 0.62	7.7 ± 0.04	7.47 ± 0.16	1.33 ± 0.05	4697
232166636	113.69 ± 1.1	8.94 ± 0.09	7.98 ± 0.19	2.21 ± 0.09	4785
232235988	155.89 ± 6.22	12.11 ± 0.03	6.26 ± 0.28	1.91 ± 0.15	4730
232238597	87.28 ± 1.09	7.9 ± 0.08	7.41 ± 0.2	1.43 ± 0.06	4605
232241604	100.55 ± 0.83	9.12 ± 0.1	6.56 ± 0.16	1.3 ± 0.05	4703
232268287	95.31 ± 0.95	8.9 ± 0.11	6.79 ± 0.19	1.34 ± 0.06	4641

Continued on next page

Table A.1 – continued from previous page

EPIC ID	$\nu_{\max}$ (μHz)	$\Delta\nu$ (μHz)	Radius ($R_\odot$)	Mass ($M_\odot$)	$T_{\rm eff}$ (K)
232299542	106.84 ± 0.63	10.08 ± 0.09	5.8 ± 0.13	1.08 ± 0.04	4737
232309563	123.74 ± 1.12	10.23 ± 0.04	6.52 ± 0.14	1.6 ± 0.06	4711
232312095	172.27 ± 1.17	13.24 ± 0.04	5.43 ± 0.11	1.54 ± 0.05	4658
232326739	64.45 ± 0.35	6.48 ± 0.04	7.99 ± 0.17	1.21 ± 0.04	4663
233171174	199.54 ± 1.24	14.97 ± 0.21	4.76 ± 0.13	1.35 ± 0.06	4572
233403827	242.84 ± 2.4	18.33 ± 0.11	3.83 ± 0.09	1.06 ± 0.04	4592
233434080	119.98 ± 0.76	10.65 ± 0.06	6.01 ± 0.12	1.33 ± 0.05	4670
233443231	83.76 ± 0.9	7.7 ± 0.1	7.28 ± 0.21	1.31 ± 0.06	4631
233444135	194.48 ± 0.81	15.58 ± 0.02	4.4 ± 0.08	1.13 ± 0.04	4649
233452452	108.52 ± 2.66	9.67 ± 0.07	6.12 ± 0.2	1.21 ± 0.07	4612
233453207	112.27 ± 1.59	9.41 ± 0.26	6.66 ± 0.31	1.48 ± 0.1	4633
233454418	131.28 ± 0.82	11.18 ± 0.04	5.56 ± 0.11	1.2 ± 0.04	4611
233456959	202.11 ± 1.52	16.4 ± 0.07	4.2 ± 0.09	1.07 ± 0.04	4739
233466593	113.36 ± 1.54	9.63 ± 0.09	6.39 ± 0.17	1.37 ± 0.06	4642
233467346	76.65 ± 0.93	7.69 ± 0.08	6.83 ± 0.18	1.06 ± 0.05	4594
233471953	211.6 ± 2.57	16.6 ± 0.06	4.41 ± 0.1	1.26 ± 0.05	4677
233478079	191.64 ± 1.66	15.72 ± 0.07	4.5 ± 0.1	1.2 ± 0.04	4693
233479382	146.96 ± 1.74	12.57 ± 0.09	4.74 ± 0.12	0.96 ± 0.04	4553
233493072	108.32 ± 0.82	9.57 ± 0.25	6.49 ± 0.27	1.38 ± 0.09	4594
233510715	63.96 ± 0.52	6.38 ± 0.1	7.98 ± 0.24	1.19 ± 0.06	4645
233524145	98.15 ± 0.43	8.77 ± 0.18	6.52 ± 0.23	1.22 ± 0.06	4645
234192198	232.26 ± 1.18	18.27 ± 0.14	3.72 ± 0.08	0.95 ± 0.03	4679
234233751	94.15 ± 1.0	7.82 ± 0.06	7.87 ± 0.19	1.71 ± 0.07	4636
234241530	139.45 ± 3.64	10.96 ± 0.21	5.98 ± 0.25	1.46 ± 0.1	4699
234292072	149.14 ± 2.1	11.89 ± 0.16	5.95 ± 0.18	1.62 ± 0.08	4691
234469630	152.36 ± 1.5	12.53 ± 0.09	5.32 ± 0.12	1.3 ± 0.05	4637
234482049	130.07 ± 0.59	10.57 ± 0.15	6.52 ± 0.18	1.69 ± 0.07	4651
234499351	172.41 ± 1.04	14.13 ± 0.05	4.65 ± 0.09	1.11 ± 0.04	4569
234500395	175.69 ± 6.74	14.56 ± 0.13	4.42 ± 0.2	1.02 ± 0.08	4625
234517876	234.43 ± 2.3	16.98 ± 0.09	4.37 ± 0.1	1.34 ± 0.05	4610
234526692	86.22 ± 1.93	7.64 ± 0.12	7.67 ± 0.28	1.5 ± 0.09	4630
234541050	140.9 ± 0.99	12.02 ± 0.06	5.0 ± 0.1	1.03 ± 0.04	4587
234577836	170.7 ± 2.25	13.37 ± 0.08	5.02 ± 0.12	1.27 ± 0.05	4552
234664196	55.21 ± 1.05	6.06 ± 0.12	7.48 ± 0.29	0.89 ± 0.05	4641
234740724	161.87 ± 0.95	12.78 ± 0.06	5.09 ± 0.1	1.23 ± 0.04	4669
234812139	100.15 ± 0.24	9.01 ± 0.06	6.3 ± 0.13	1.16 ± 0.04	4549
234970161	109.97 ± 1.19	9.98 ± 0.16	5.75 ± 0.19	1.07 ± 0.05	3947
235167688	209.53 ± 1.5	16.46 ± 0.06	4.6 ± 0.09	1.39 ± 0.05	4772
235372401	171.92 ± 1.26	14.17 ± 0.07	4.58 ± 0.1	1.07 ± 0.04	4648
235854622	71.53 ± 0.49	6.9 ± 0.06	7.7 ± 0.18	1.24 ± 0.05	4537
235998421	217.79 ± 1.76	17.73 ± 0.09	3.86 ± 0.08	0.97 ± 0.04	4557
236048293	253.92 ± 2.16	18.13 ± 0.36	4.14 ± 0.14	1.3 ± 0.07	5059
236681684	120.31 ± 0.95	10.64 ± 0.12	6.25 ± 0.16	1.47 ± 0.06	4738
236702393	202.68 ± 1.59	15.28 ± 0.17	4.81 ± 0.12	1.42 ± 0.06	4673
236704015	156.78 ± 4.88	12.77 ± 0.19	4.89 ± 0.2	1.1 ± 0.08	4597
238181374	147.76 ± 1.19	12.44 ± 0.09	5.22 ± 0.12	1.21 ± 0.05	4641
238257378	114.61 ± 2.37	9.95 ± 0.29	6.16 ± 0.31	1.3 ± 0.1	4793
240375839	69.33 ± 1.6	7.17 ± 0.18	7.15 ± 0.33	1.05 ± 0.08	4645
240609398	167.85 ± 1.72	13.12 ± 0.06	5.06 ± 0.11	1.27 ± 0.05	4634
242049262	186.34 ± 1.74	15.11 ± 0.13	4.23 ± 0.1	0.98 ± 0.04	4593
242126298	252.36 ± 2.34	17.59 ± 0.14	4.37 ± 0.1	1.44 ± 0.06	4624
242217985	178.14 ± 3.7	13.77 ± 0.2	4.79 ± 0.17	1.2 ± 0.07	4549
245924645	72.2 ± 1.03	7.09 ± 0.04	7.6 ± 0.18	1.24 ± 0.05	4835
245930757	183.9 ± 2.98	14.77 ± 0.09	4.72 ± 0.12	1.24 ± 0.05	4890
245931953	60.87 ± 1.23	6.67 ± 0.07	7.66 ± 0.23	1.08 ± 0.05	5076
245932976	101.9 ± 0.55	9.09 ± 0.04	6.6 ± 0.12	1.33 ± 0.04	5098
245942467	142.87 ± 0.95	12.17 ± 0.07	5.17 ± 0.1	1.14 ± 0.04	4951
245946860	224.83 ± 1.55	17.41 ± 0.39	4.08 ± 0.15	1.13 ± 0.06	5112
245948147	266.89 ± 6.82	19.67 ± 0.19	3.78 ± 0.13	1.15 ± 0.06	5070
245948290	99.56 ± 0.97	9.38 ± 0.05	6.3 ± 0.13	1.2 ± 0.04	4889
245955781	116.03 ± 1.3	10.26 ± 0.1	5.95 ± 0.15	1.23 ± 0.05	5060

Continued on next page

Table A.1 – continued from previous page

EPIC ID	$\nu_{\max}$ (μHz)	$\Delta\nu$ (μHz)	Radius ($R_\odot$)	Mass ($M_\odot$)	$T_{\rm eff}$ (K)
245968102	104.15 ± 0.46	9.35 ± 0.05	6.31 ± 0.12	1.23 ± 0.04	4808
245968556	166.02 ± 1.14	14.16 ± 0.03	4.51 ± 0.09	1.01 ± 0.03	4965
245970149	279.94 ± 2.79	19.48 ± 0.08	4.03 ± 0.08	1.37 ± 0.05	5125
245970884	137.94 ± 2.67	12.69 ± 0.06	4.8 ± 0.13	0.96 ± 0.04	5061
245975499	74.65 ± 1.04	7.25 ± 0.05	7.5 ± 0.19	1.25 ± 0.05	4793
245984830	136.7 ± 0.94	11.89 ± 0.04	5.45 ± 0.11	1.23 ± 0.04	4893
245986504	111.35 ± 0.75	9.9 ± 0.06	6.17 ± 0.13	1.27 ± 0.04	4995
245991772	93.73 ± 0.8	8.76 ± 0.04	6.5 ± 0.14	1.18 ± 0.04	4815
245993571	185.72 ± 1.58	14.8 ± 0.09	4.69 ± 0.1	1.23 ± 0.04	5056
245999894	93.43 ± 0.73	9.03 ± 0.05	6.35 ± 0.13	1.13 ± 0.04	4980
246009840	162.8 ± 0.68	12.82 ± 0.06	5.25 ± 0.1	1.34 ± 0.04	5090
246015285	106.22 ± 0.58	9.32 ± 0.04	6.39 ± 0.12	1.28 ± 0.04	4855
246018877	100.78 ± 0.88	9.18 ± 0.07	6.25 ± 0.14	1.16 ± 0.04	4717
246025392	178.59 ± 1.25	14.55 ± 0.12	4.77 ± 0.1	1.24 ± 0.04	5085
246030494	151.43 ± 0.74	12.53 ± 0.12	5.3 ± 0.12	1.28 ± 0.05	5015
246031188	241.84 ± 1.97	18.98 ± 0.22	3.84 ± 0.1	1.09 ± 0.04	5097
246034572	97.38 ± 2.56	9.39 ± 0.06	6.25 ± 0.2	1.16 ± 0.06	5126
246036955	154.09 ± 2.05	13.18 ± 0.04	4.82 ± 0.11	1.07 ± 0.04	5106
246037628	88.44 ± 2.42	8.55 ± 0.06	6.75 ± 0.23	1.22 ± 0.07	5052
246044428	112.44 ± 1.64	10.72 ± 0.06	5.49 ± 0.13	1.02 ± 0.04	5074
246045334	85.02 ± 0.65	7.92 ± 0.05	7.26 ± 0.15	1.34 ± 0.05	4836
246049442	233.68 ± 0.88	17.04 ± 0.07	4.43 ± 0.08	1.38 ± 0.04	5003
246051485	160.41 ± 3.93	13.36 ± 0.09	4.77 ± 0.15	1.08 ± 0.06	4903
246052621	217.93 ± 3.7	15.79 ± 0.12	4.75 ± 0.12	1.48 ± 0.07	5166
246054082	125.29 ± 1.28	11.15 ± 0.09	5.58 ± 0.13	1.18 ± 0.04	5041
246059957	125.26 ± 0.83	11.52 ± 0.06	5.2 ± 0.1	1.02 ± 0.03	5052
246061278	107.13 ± 0.71	9.95 ± 0.09	5.73 ± 0.13	1.04 ± 0.04	4878
246061897	170.5 ± 0.8	13.19 ± 0.07	5.2 ± 0.1	1.37 ± 0.05	4790
246065324	129.88 ± 0.79	11.76 ± 0.05	4.83 ± 0.09	0.89 ± 0.03	5066
246066505	231.03 ± 2.21	16.78 ± 0.11	4.56 ± 0.1	1.46 ± 0.05	5101
246066965	295.14 ± 9.77	20.59 ± 0.07	3.63 ± 0.14	1.15 ± 0.08	4816
246070817	185.2 ± 0.72	14.7 ± 0.04	4.55 ± 0.08	1.14 ± 0.04	4903
246074288	179.63 ± 1.13	13.33 ± 0.08	5.58 ± 0.11	1.7 ± 0.06	5051
246075387	170.75 ± 1.11	13.55 ± 0.05	4.81 ± 0.09	1.16 ± 0.04	4841
246079566	191.92 ± 1.24	15.67 ± 0.03	4.37 ± 0.08	1.11 ± 0.04	4941
246082198	232.24 ± 4.98	16.97 ± 0.42	4.31 ± 0.19	1.28 ± 0.09	4868
246086500	118.67 ± 1.12	10.95 ± 0.07	5.49 ± 0.12	1.07 ± 0.04	5147
246089278	135.75 ± 1.26	10.98 ± 0.08	6.03 ± 0.13	1.48 ± 0.05	5038
246093660	111.26 ± 0.92	10.22 ± 0.04	5.68 ± 0.11	1.07 ± 0.04	4987
246105812	82.83 ± 0.88	8.35 ± 0.04	6.61 ± 0.14	1.09 ± 0.04	5193
246106685	285.18 ± 2.19	20.05 ± 0.13	3.88 ± 0.08	1.3 ± 0.05	5024
246110350	113.05 ± 1.28	9.61 ± 0.03	6.72 ± 0.14	1.55 ± 0.06	5175
246111183	99.17 ± 0.53	9.61 ± 0.06	5.92 ± 0.12	1.04 ± 0.04	5055
246112343	157.43 ± 1.15	13.81 ± 0.04	4.35 ± 0.08	0.87 ± 0.03	5120
246115215	127.36 ± 0.84	11.09 ± 0.19	5.36 ± 0.16	1.08 ± 0.05	4841
246116964	105.28 ± 1.02	9.77 ± 0.05	6.19 ± 0.13	1.23 ± 0.04	5071
246123960	252.45 ± 2.16	16.11 ± 0.15	5.61 ± 0.13	2.45 ± 0.09	5069
246125264	156.26 ± 1.12	12.2 ± 0.06	5.55 ± 0.11	1.43 ± 0.05	5001
246136239	281.63 ± 7.7	19.86 ± 0.2	4.03 ± 0.14	1.39 ± 0.08	5081
246141302	250.74 ± 2.89	19.75 ± 0.06	3.48 ± 0.07	0.9 ± 0.03	4991
246142259	94.08 ± 0.39	8.72 ± 0.06	6.6 ± 0.14	1.22 ± 0.04	5037
246143798	246.36 ± 1.36	18.88 ± 0.1	3.82 ± 0.07	1.08 ± 0.04	5003
246144190	208.69 ± 7.31	16.54 ± 0.08	3.94 ± 0.16	0.95 ± 0.06	5042
246154489	194.62 ± 3.96	14.38 ± 0.04	4.92 ± 0.13	1.4 ± 0.07	4816
246156371	102.97 ± 0.63	9.56 ± 0.04	5.98 ± 0.11	1.09 ± 0.04	4983
246166528	154.43 ± 0.93	12.36 ± 0.16	5.29 ± 0.13	1.28 ± 0.05	5122
246172781	105.58 ± 0.41	9.63 ± 0.03	5.77 ± 0.11	1.03 ± 0.03	4725
246178430	104.0 ± 0.52	9.03 ± 0.07	6.58 ± 0.14	1.33 ± 0.05	4754
246178907	107.16 ± 0.49	9.76 ± 0.04	6.08 ± 0.12	1.18 ± 0.04	4792
246184564	151.54 ± 1.1	11.77 ± 0.04	5.57 ± 0.11	1.37 ± 0.05	4836
246185964	137.3 ± 2.81	11.16 ± 0.04	6.03 ± 0.16	1.51 ± 0.07	4974

Continued on next page

Table A.1 – continued from previous page

EPIC ID	$\nu_{\max}$ (μHz)	$\Delta\nu$ (μHz)	Radius ($R_\odot$)	Mass ($M_\odot$)	$T_{\rm eff}$ (K)
246192065	163.03 ± 0.82	14.14 ± 0.05	4.5 ± 0.08	0.99 ± 0.03	5049
246195110	165.01 ± 1.67	13.32 ± 0.03	4.96 ± 0.1	1.21 ± 0.04	4728
246196888	131.99 ± 2.44	10.41 ± 0.29	6.81 ± 0.32	1.87 ± 0.13	5220
246197428	165.02 ± 1.78	14.02 ± 0.2	4.54 ± 0.13	1.01 ± 0.05	5064
246201252	174.42 ± 1.54	13.94 ± 0.04	5.17 ± 0.1	1.44 ± 0.05	4931
246210478	260.88 ± 3.74	18.94 ± 0.08	3.91 ± 0.09	1.19 ± 0.05	4888
246217241	285.79 ± 0.4	20.09 ± 0.16	3.87 ± 0.08	1.29 ± 0.04	4953
246217553	283.71 ± 0.0	19.98 ± 0.08	4.03 ± 0.07	1.41 ± 0.04	5081
246249492	223.82 ± 1.7	17.59 ± 0.07	3.78 ± 0.07	0.94 ± 0.03	5103
246261330	225.89 ± 2.14	16.21 ± 0.19	4.57 ± 0.12	1.41 ± 0.06	5160
246264787	239.41 ± 1.07	18.25 ± 0.1	3.77 ± 0.07	1.0 ± 0.03	4845
246275313	177.25 ± 1.92	15.53 ± 0.18	4.0 ± 0.1	0.84 ± 0.04	5044
246277916	250.6 ± 2.38	18.42 ± 0.06	3.89 ± 0.08	1.12 ± 0.04	4937
246279724	158.33 ± 0.65	12.86 ± 0.05	4.97 ± 0.09	1.15 ± 0.04	4880
246281612	180.79 ± 0.78	14.88 ± 0.04	4.37 ± 0.08	1.02 ± 0.03	5004
246284189	160.37 ± 1.8	12.39 ± 0.03	5.4 ± 0.11	1.38 ± 0.05	4946
246284449	62.39 ± 0.92	6.62 ± 0.06	7.76 ± 0.2	1.13 ± 0.05	4907
246284507	174.03 ± 0.87	13.85 ± 0.07	4.9 ± 0.1	1.25 ± 0.04	4957
246291096	193.24 ± 1.09	15.64 ± 0.04	4.3 ± 0.08	1.07 ± 0.03	5083
246294209	192.57 ± 1.63	15.73 ± 0.05	4.27 ± 0.08	1.05 ± 0.04	5062
246297126	122.71 ± 0.79	10.41 ± 0.06	6.34 ± 0.13	1.51 ± 0.05	4925
246304467	255.7 ± 4.74	18.46 ± 0.07	4.11 ± 0.11	1.3 ± 0.06	5104
246307595	237.62 ± 1.76	17.47 ± 0.26	4.23 ± 0.12	1.27 ± 0.06	5044
246311919	111.32 ± 0.86	9.99 ± 0.04	5.97 ± 0.12	1.18 ± 0.04	5116
246315422	142.67 ± 0.78	11.89 ± 0.05	5.35 ± 0.1	1.21 ± 0.04	4992
246319339	240.99 ± 1.91	18.12 ± 0.04	3.97 ± 0.08	1.13 ± 0.04	4908
246320742	84.46 ± 0.68	8.2 ± 0.14	7.13 ± 0.22	1.31 ± 0.06	5096
246321326	190.05 ± 1.84	15.35 ± 0.07	4.49 ± 0.09	1.16 ± 0.04	5037
246329533	241.63 ± 1.87	18.54 ± 0.05	3.84 ± 0.08	1.06 ± 0.04	4816
246333432	104.3 ± 0.45	9.34 ± 0.03	6.22 ± 0.12	1.19 ± 0.04	4739
246341907	222.37 ± 1.78	15.13 ± 0.09	5.16 ± 0.11	1.76 ± 0.06	4873
246344886	91.27 ± 0.39	8.81 ± 0.06	6.39 ± 0.13	1.11 ± 0.04	5027
246356654	67.2 ± 0.5	6.7 ± 0.06	7.9 ± 0.18	1.24 ± 0.05	4867
246361654	238.54 ± 4.19	17.07 ± 0.14	4.51 ± 0.12	1.47 ± 0.07	5129
246362029	173.56 ± 1.2	13.61 ± 0.04	5.14 ± 0.1	1.38 ± 0.05	4966
246362431	257.54 ± 2.35	18.96 ± 0.09	3.85 ± 0.08	1.14 ± 0.04	4876
246366435	130.04 ± 0.31	11.47 ± 0.03	5.21 ± 0.09	1.04 ± 0.03	4884
246366549	94.64 ± 0.65	9.0 ± 0.26	6.33 ± 0.28	1.13 ± 0.07	5163
246376068	208.79 ± 2.03	16.66 ± 0.11	4.08 ± 0.09	1.04 ± 0.04	5055
246377577	88.36 ± 0.9	8.65 ± 0.17	6.25 ± 0.22	1.02 ± 0.05	4963
246383694	132.16 ± 1.06	11.38 ± 0.04	5.5 ± 0.11	1.19 ± 0.04	4951
246389006	153.21 ± 0.73	13.12 ± 0.07	4.73 ± 0.09	1.01 ± 0.03	4891
246394868	88.56 ± 0.99	7.62 ± 0.04	7.92 ± 0.18	1.64 ± 0.06	4849
246399436	173.92 ± 0.95	14.27 ± 0.09	4.58 ± 0.09	1.08 ± 0.04	4991
246400855	243.31 ± 6.18	20.37 ± 0.32	3.29 ± 0.12	0.79 ± 0.05	4933
246403570	126.14 ± 0.84	10.81 ± 0.05	5.69 ± 0.11	1.21 ± 0.04	4816
246404736	237.62 ± 1.57	17.56 ± 0.11	4.09 ± 0.08	1.18 ± 0.04	5058
246404865	116.76 ± 1.14	9.6 ± 0.05	6.58 ± 0.14	1.49 ± 0.05	5063
246405082	196.6 ± 3.25	13.96 ± 0.11	5.21 ± 0.14	1.57 ± 0.07	4759
246416108	150.53 ± 2.41	12.48 ± 0.2	5.17 ± 0.17	1.2 ± 0.06	4917
246419226	68.2 ± 0.38	6.98 ± 0.05	7.24 ± 0.15	1.05 ± 0.04	4961
246420761	95.76 ± 1.35	8.73 ± 0.06	6.89 ± 0.17	1.37 ± 0.06	5050
246424715	240.9 ± 1.64	17.53 ± 0.06	4.21 ± 0.08	1.27 ± 0.04	4956
246425779	99.96 ± 0.85	8.58 ± 0.03	6.82 ± 0.14	1.35 ± 0.05	4556
246428198	184.96 ± 1.84	15.2 ± 0.05	4.37 ± 0.09	1.06 ± 0.04	4935
246436559	183.91 ± 1.23	14.77 ± 0.06	4.58 ± 0.09	1.15 ± 0.04	4920
246439574	237.86 ± 1.53	18.1 ± 0.04	4.0 ± 0.08	1.15 ± 0.04	4963
246442058	264.61 ± 2.13	18.94 ± 0.07	3.92 ± 0.08	1.21 ± 0.04	4857
246444091	108.43 ± 0.61	9.11 ± 0.06	6.73 ± 0.14	1.45 ± 0.05	4895
246444771	134.65 ± 1.01	11.79 ± 0.06	5.29 ± 0.11	1.13 ± 0.04	4886
246445649	86.56 ± 0.67	8.22 ± 0.07	6.84 ± 0.16	1.21 ± 0.05	4915

Continued on next page

Table A.1 – continued from previous page

EPIC ID	$\nu_{\rm max}$ (μHz)	$\Delta\nu$ (μHz)	Radius ($R_\odot$)	Mass ($M_\odot$)	$T_{\rm eff}$ (K)
246447414	126.15 ± 0.85	9.95 ± 0.22	6.73 ± 0.25	1.7 ± 0.09	4856
246452407	126.54 ± 0.7	10.86 ± 0.09	5.45 ± 0.12	1.09 ± 0.04	4721
246452427	146.62 ± 2.06	12.35 ± 0.23	5.32 ± 0.18	1.26 ± 0.07	5123
246456604	91.86 ± 0.58	8.78 ± 0.08	6.31 ± 0.14	1.09 ± 0.04	5077
246459581	290.49 ± 0.0	20.34 ± 0.1	3.83 ± 0.07	1.28 ± 0.04	4897
246464786	161.57 ± 1.04	13.66 ± 0.05	4.7 ± 0.09	1.07 ± 0.03	5076
246466173	237.11 ± 3.94	16.34 ± 0.41	4.88 ± 0.21	1.71 ± 0.11	5108
246471750	141.56 ± 1.01	12.38 ± 0.03	4.83 ± 0.09	0.97 ± 0.03	4886
246472224	100.2 ± 1.56	8.45 ± 0.07	7.32 ± 0.19	1.59 ± 0.07	5123
246486082	200.42 ± 1.0	15.3 ± 0.07	4.57 ± 0.09	1.25 ± 0.04	4889
246486268	197.61 ± 2.21	15.98 ± 0.05	4.28 ± 0.09	1.09 ± 0.04	5009
246495646	72.47 ± 0.41	7.26 ± 0.06	7.22 ± 0.15	1.12 ± 0.04	4932
246498789	92.22 ± 0.77	8.47 ± 0.06	6.7 ± 0.15	1.22 ± 0.04	4775
246499024	78.18 ± 0.55	7.03 ± 0.05	7.9 ± 0.18	1.41 ± 0.05	4488
246506368	153.73 ± 0.49	12.82 ± 0.04	4.91 ± 0.09	1.09 ± 0.03	4838
246641098	97.57 ± 1.15	8.27 ± 0.04	7.51 ± 0.17	1.63 ± 0.06	4553
246650102	103.85 ± 2.18	8.65 ± 0.1	7.49 ± 0.24	1.76 ± 0.09	4798
246690095	90.8 ± 0.6	8.87 ± 0.04	6.26 ± 0.13	1.06 ± 0.04	4565
246699952	85.79 ± 0.74	7.54 ± 0.09	7.98 ± 0.22	1.63 ± 0.07	4210
246720935	59.65 ± 0.7	6.4 ± 0.12	7.82 ± 0.27	1.09 ± 0.06	4587
246752514	155.72 ± 1.56	12.37 ± 0.03	5.58 ± 0.12	1.46 ± 0.05	4668
246758668	251.41 ± 4.31	17.41 ± 0.08	4.43 ± 0.11	1.47 ± 0.07	4559
246768362	98.74 ± 1.32	8.65 ± 0.16	7.29 ± 0.26	1.59 ± 0.09	4588
246770054	173.53 ± 0.91	13.09 ± 0.17	5.43 ± 0.14	1.53 ± 0.06	4664
246782570	272.57 ± 8.11	17.25 ± 0.19	4.75 ± 0.19	1.81 ± 0.12	3908
246786926	138.65 ± 4.17	11.58 ± 0.03	5.44 ± 0.19	1.21 ± 0.07	4634
246796597	91.26 ± 0.95	8.84 ± 0.15	6.47 ± 0.21	1.15 ± 0.06	4636
246799215	94.72 ± 0.77	8.25 ± 0.26	7.33 ± 0.36	1.51 ± 0.11	4443
246801120	244.13 ± 0.34	17.81 ± 0.29	4.19 ± 0.12	1.29 ± 0.06	4635
246803474	220.16 ± 1.26	16.35 ± 0.17	4.55 ± 0.11	1.38 ± 0.06	4507
246805921	122.74 ± 0.58	10.28 ± 0.06	6.21 ± 0.13	1.42 ± 0.05	4566
246824109	110.78 ± 1.47	9.2 ± 0.15	6.93 ± 0.22	1.58 ± 0.08	4743
246827184	159.58 ± 1.17	13.01 ± 0.06	5.19 ± 0.11	1.3 ± 0.05	4704
246843098	177.67 ± 1.53	13.92 ± 0.02	4.96 ± 0.1	1.31 ± 0.05	4539
246848070	107.11 ± 1.18	9.02 ± 0.04	7.14 ± 0.16	1.65 ± 0.06	4678
246872409	99.69 ± 2.03	8.96 ± 0.07	6.88 ± 0.2	1.43 ± 0.07	4626
246889637	197.44 ± 1.48	14.58 ± 0.11	5.08 ± 0.11	1.54 ± 0.06	4659
246895511	191.26 ± 1.93	14.77 ± 0.09	4.66 ± 0.11	1.23 ± 0.05	4298
246899913	165.89 ± 1.58	12.92 ± 0.28	5.5 ± 0.2	1.52 ± 0.09	4781
246906927	82.86 ± 0.71	7.96 ± 0.04	6.82 ± 0.15	1.13 ± 0.04	4608
246913131	145.51 ± 1.04	12.45 ± 0.08	5.17 ± 0.11	1.17 ± 0.04	4675
246918781	105.61 ± 1.46	9.05 ± 0.08	6.83 ± 0.18	1.47 ± 0.06	4578
246922913	53.19 ± 2.05	6.34 ± 0.11	7.4 ± 0.36	0.87 ± 0.07	4575
246934631	87.63 ± 3.19	8.82 ± 0.04	6.38 ± 0.26	1.08 ± 0.08	4665
246939509	76.67 ± 0.9	7.22 ± 0.07	7.78 ± 0.2	1.38 ± 0.06	4584
246949207	83.87 ± 0.75	7.78 ± 0.04	7.6 ± 0.16	1.47 ± 0.05	4653
246957690	65.47 ± 0.87	6.67 ± 0.04	7.57 ± 0.18	1.1 ± 0.05	4430
246966703	194.03 ± 2.72	14.55 ± 0.03	4.82 ± 0.11	1.34 ± 0.05	4578
246966983	202.36 ± 1.57	15.66 ± 0.2	4.56 ± 0.12	1.27 ± 0.05	4591
246972382	190.45 ± 1.29	14.86 ± 0.04	4.85 ± 0.09	1.37 ± 0.05	4903
246974789	121.76 ± 1.0	10.99 ± 0.01	5.52 ± 0.11	1.11 ± 0.04	4641
246980430	123.49 ± 0.62	11.38 ± 0.03	5.28 ± 0.1	1.03 ± 0.03	4576
246985477	101.57 ± 0.72	9.0 ± 0.06	6.7 ± 0.15	1.36 ± 0.05	4552
246990428	222.97 ± 3.67	15.05 ± 0.08	5.24 ± 0.14	1.83 ± 0.08	4532
247003167	232.18 ± 4.79	17.34 ± 0.08	4.16 ± 0.12	1.2 ± 0.06	4443
247004138	106.84 ± 2.71	9.7 ± 0.07	6.31 ± 0.21	1.29 ± 0.07	4522
247006562	188.0 ± 2.72	13.79 ± 0.13	5.36 ± 0.14	1.63 ± 0.07	4669
247007140	75.82 ± 1.4	7.34 ± 0.05	7.53 ± 0.21	1.28 ± 0.06	4410
247008412	132.79 ± 1.02	11.57 ± 0.05	5.2 ± 0.11	1.06 ± 0.04	4464
247010448	222.28 ± 2.58	15.37 ± 0.06	5.37 ± 0.12	1.97 ± 0.07	4689
247015179	153.02 ± 0.69	12.33 ± 0.07	5.44 ± 0.11	1.36 ± 0.05	4627

Continued on next page

Table A.1 – continued from previous page

EPIC ID	$\nu_{\max}$ (μHz)	$\Delta\nu$ (μHz)	Radius ($R_\odot$)	Mass ($M_\odot$)	$T_{\rm eff}$ (K)
247019978	83.85 ± 1.47	7.79 ± 0.1	7.51 ± 0.23	1.42 ± 0.07	4726
247040177	146.66 ± 1.11	12.12 ± 0.07	5.39 ± 0.12	1.28 ± 0.05	4554
247040958	168.57 ± 1.28	14.3 ± 0.19	4.55 ± 0.13	1.05 ± 0.05	4615
247043893	76.31 ± 1.44	7.41 ± 0.04	7.49 ± 0.2	1.28 ± 0.06	4627
247059356	148.25 ± 3.85	12.22 ± 0.02	5.31 ± 0.17	1.25 ± 0.07	4571
247068016	83.79 ± 0.53	7.87 ± 0.06	7.3 ± 0.16	1.34 ± 0.05	4492
247075061	122.41 ± 0.75	10.65 ± 0.08	5.79 ± 0.13	1.22 ± 0.05	4428
247089169	110.19 ± 1.04	9.69 ± 0.09	6.2 ± 0.15	1.26 ± 0.05	4307
247093797	223.78 ± 1.27	17.28 ± 0.11	4.21 ± 0.09	1.21 ± 0.04	4649
247095174	77.14 ± 1.47	7.36 ± 0.06	7.28 ± 0.22	1.2 ± 0.06	4235
247099258	95.03 ± 2.05	8.27 ± 0.13	7.54 ± 0.27	1.63 ± 0.1	4632
247100949	114.01 ± 1.63	9.95 ± 0.06	6.05 ± 0.15	1.23 ± 0.05	4354
247115997	144.62 ± 1.1	11.21 ± 0.08	6.3 ± 0.14	1.74 ± 0.07	4610
247116221	140.03 ± 3.19	11.36 ± 0.31	5.65 ± 0.27	1.32 ± 0.1	4414
247118472	96.25 ± 0.85	8.81 ± 0.1	6.47 ± 0.17	1.19 ± 0.05	4471
247128155	113.92 ± 1.11	9.97 ± 0.07	6.19 ± 0.15	1.31 ± 0.05	4342
247135742	293.85 ± 0.01	20.52 ± 0.35	3.97 ± 0.12	1.42 ± 0.07	4706
247136595	66.24 ± 2.24	6.59 ± 0.04	7.71 ± 0.31	1.15 ± 0.08	4335
247141445	88.96 ± 0.68	8.51 ± 0.09	6.74 ± 0.17	1.21 ± 0.05	4623
247163383	94.34 ± 0.75	8.8 ± 0.04	5.96 ± 0.13	0.96 ± 0.04	4199
247167112	91.56 ± 2.18	8.09 ± 0.05	7.37 ± 0.23	1.47 ± 0.08	4578
247175605	229.7 ± 0.89	16.99 ± 0.06	4.22 ± 0.08	1.21 ± 0.04	4580
247180268	191.64 ± 1.94	16.34 ± 0.2	3.82 ± 0.11	0.82 ± 0.04	4252
247180947	174.62 ± 1.12	13.52 ± 0.03	5.17 ± 0.1	1.4 ± 0.05	4660
247192492	132.84 ± 1.15	11.11 ± 0.15	5.81 ± 0.16	1.34 ± 0.06	4650
247201938	86.13 ± 0.54	7.78 ± 0.16	7.53 ± 0.27	1.45 ± 0.08	4322
247209797	108.48 ± 1.21	10.53 ± 0.12	5.57 ± 0.15	1.03 ± 0.04	4620
247217911	97.45 ± 1.71	8.6 ± 0.03	7.24 ± 0.19	1.55 ± 0.07	4651
247218943	263.25 ± 9.78	18.67 ± 0.08	4.1 ± 0.17	1.33 ± 0.1	4510
247239983	127.17 ± 1.1	10.74 ± 0.11	5.84 ± 0.14	1.29 ± 0.05	4597
247242128	110.69 ± 0.78	9.95 ± 0.07	5.92 ± 0.13	1.15 ± 0.04	4482
247245851	115.27 ± 0.59	9.79 ± 0.04	6.45 ± 0.13	1.44 ± 0.05	4428
247246929	98.64 ± 0.93	9.18 ± 0.08	6.41 ± 0.15	1.22 ± 0.05	4720
247248503	82.65 ± 0.67	7.53 ± 0.05	7.47 ± 0.17	1.35 ± 0.05	4378
247254143	81.08 ± 1.03	7.57 ± 0.07	7.55 ± 0.2	1.38 ± 0.06	4605
247255785	157.01 ± 1.83	13.09 ± 0.11	4.99 ± 0.12	1.17 ± 0.05	4554
247271841	223.57 ± 2.48	16.32 ± 0.12	4.47 ± 0.11	1.33 ± 0.05	4532
247274252	163.81 ± 0.68	12.88 ± 0.06	5.19 ± 0.1	1.31 ± 0.04	4487
247276476	175.08 ± 0.95	14.06 ± 0.05	4.65 ± 0.09	1.12 ± 0.04	4567
247279992	199.6 ± 0.8	15.25 ± 0.05	4.53 ± 0.09	1.22 ± 0.04	4492
247281934	90.68 ± 0.99	7.89 ± 0.14	7.39 ± 0.25	1.45 ± 0.08	4180
247284142	142.02 ± 1.96	12.09 ± 0.06	5.31 ± 0.13	1.2 ± 0.05	4642
247288610	124.45 ± 3.47	10.76 ± 0.07	5.69 ± 0.2	1.19 ± 0.07	4182
247288794	165.61 ± 1.28	13.11 ± 0.11	5.22 ± 0.12	1.36 ± 0.05	4615
247292412	175.55 ± 3.48	13.85 ± 0.14	4.71 ± 0.14	1.14 ± 0.06	4424
247297022	98.37 ± 2.94	8.32 ± 0.1	7.62 ± 0.3	1.71 ± 0.11	4563
247298530	195.16 ± 0.87	15.73 ± 0.03	4.22 ± 0.08	1.03 ± 0.03	4574
247299829	98.26 ± 0.57	8.06 ± 0.25	7.7 ± 0.37	1.7 ± 0.12	4318
247305721	155.1 ± 0.67	12.76 ± 0.07	4.99 ± 0.1	1.14 ± 0.04	4375
247317220	147.94 ± 2.05	11.94 ± 0.09	5.46 ± 0.14	1.31 ± 0.06	4450
247318560	211.08 ± 1.26	16.19 ± 0.02	4.42 ± 0.09	1.24 ± 0.04	4551
247323387	139.99 ± 0.66	11.67 ± 0.06	5.41 ± 0.11	1.21 ± 0.04	4402
247323825	167.88 ± 1.62	14.48 ± 0.32	4.41 ± 0.17	0.98 ± 0.06	4589
247330913	212.74 ± 3.38	17.41 ± 0.14	3.93 ± 0.1	0.99 ± 0.04	4705
247339112	94.07 ± 0.44	8.57 ± 0.11	6.63 ± 0.17	1.22 ± 0.05	4494
247341848	181.85 ± 1.25	14.65 ± 0.05	4.55 ± 0.09	1.12 ± 0.04	4587
247342198	90.89 ± 2.25	8.84 ± 0.13	6.35 ± 0.24	1.1 ± 0.07	4669
247343283	87.25 ± 1.37	8.6 ± 0.1	6.35 ± 0.18	1.05 ± 0.05	4736
247346861	148.31 ± 1.18	12.32 ± 0.06	5.3 ± 0.11	1.25 ± 0.04	4634
247350482	140.06 ± 0.89	11.78 ± 0.06	5.52 ± 0.11	1.28 ± 0.04	4660
247359442	159.54 ± 2.6	13.96 ± 0.07	4.45 ± 0.11	0.94 ± 0.04	4680

Continued on next page

Table A.1 – continued from previous page

EPIC ID	$\nu_{\max}$ (μHz)	$\Delta\nu$ (μHz)	Radius ($R_{\odot}$)	Mass ($M_{\odot}$)	T_{eff} (K)
247361101	183.44 ± 2.34	13.95 ± 0.09	5.05 ± 0.12	1.4 ± 0.06	4625
247361205	84.71 ± 0.82	7.53 ± 0.1	7.88 ± 0.22	1.57 ± 0.07	4583
247369087	225.39 ± 1.43	17.49 ± 0.07	4.14 ± 0.08	1.17 ± 0.04	4670
247371917	177.89 ± 1.33	14.19 ± 0.05	4.83 ± 0.1	1.25 ± 0.04	4633
247374445	110.43 ± 3.65	9.82 ± 0.1	6.33 ± 0.26	1.34 ± 0.09	4680
247376509	152.46 ± 1.39	12.59 ± 0.13	5.22 ± 0.13	1.25 ± 0.05	4793
247380881	92.33 ± 1.22	8.64 ± 0.11	6.55 ± 0.19	1.18 ± 0.06	4451
247380893	137.41 ± 0.85	12.13 ± 0.17	5.1 ± 0.14	1.07 ± 0.05	4565
247385070	104.29 ± 0.86	8.74 ± 0.04	7.03 ± 0.15	1.51 ± 0.06	4456
247387736	156.4 ± 0.97	12.93 ± 0.06	5.18 ± 0.11	1.27 ± 0.04	4670
247388198	97.18 ± 1.59	8.07 ± 0.09	7.94 ± 0.23	1.83 ± 0.09	4642
247389389	189.85 ± 1.15	14.69 ± 0.11	4.66 ± 0.1	1.22 ± 0.05	4484
247389792	117.06 ± 1.53	9.72 ± 0.04	6.55 ± 0.15	1.49 ± 0.06	4633
247392167	78.68 ± 3.19	7.83 ± 0.04	6.8 ± 0.31	1.08 ± 0.08	4613
247393160	192.22 ± 0.97	15.56 ± 0.03	4.34 ± 0.08	1.09 ± 0.04	4483
247393369	155.77 ± 1.43	12.75 ± 0.05	5.2 ± 0.11	1.26 ± 0.05	4640
247395250	96.37 ± 0.72	8.76 ± 0.08	6.72 ± 0.16	1.3 ± 0.05	4600
247410176	68.52 ± 1.23	6.79 ± 0.05	7.79 ± 0.22	1.23 ± 0.06	4314
247411298	107.31 ± 3.43	10.74 ± 0.1	5.1 ± 0.2	0.83 ± 0.06	4607
247411547	74.12 ± 0.58	8.03 ± 0.06	6.71 ± 0.15	1.03 ± 0.04	4876
247417014	76.64 ± 1.8	8.14 ± 0.06	6.14 ± 0.2	0.85 ± 0.05	4224
247417990	152.18 ± 1.86	12.87 ± 0.07	5.07 ± 0.12	1.18 ± 0.05	4575
247419145	125.2 ± 1.58	10.02 ± 0.03	6.51 ± 0.15	1.57 ± 0.06	4544
247423298	112.91 ± 0.81	9.83 ± 0.04	6.09 ± 0.13	1.24 ± 0.04	4477
247424257	85.51 ± 0.6	8.31 ± 0.06	6.3 ± 0.15	0.99 ± 0.04	4325
247427333	106.0 ± 1.17	9.89 ± 0.04	5.8 ± 0.13	1.06 ± 0.04	4626
247429960	100.61 ± 0.61	9.15 ± 0.04	6.64 ± 0.14	1.34 ± 0.05	4609
247436029	119.6 ± 1.16	9.17 ± 0.18	7.68 ± 0.26	2.12 ± 0.11	4719
247440090	146.28 ± 0.74	11.97 ± 0.09	5.48 ± 0.12	1.31 ± 0.05	4575
247442148	116.67 ± 1.24	10.09 ± 0.06	6.18 ± 0.14	1.33 ± 0.05	4672
247442949	95.74 ± 1.35	8.66 ± 0.07	6.78 ± 0.18	1.31 ± 0.06	4425
247444231	210.84 ± 0.91	16.66 ± 0.03	4.05 ± 0.08	1.03 ± 0.03	4397
247448965	119.99 ± 0.72	9.58 ± 0.05	6.95 ± 0.15	1.73 ± 0.06	4521
247449486	85.34 ± 1.18	8.29 ± 0.11	6.91 ± 0.2	1.23 ± 0.06	4561
247451928	91.53 ± 1.11	7.94 ± 0.08	7.71 ± 0.2	1.62 ± 0.07	4451
247455983	70.12 ± 0.52	6.87 ± 0.09	7.83 ± 0.22	1.28 ± 0.06	4461
247459595	112.52 ± 2.08	9.57 ± 0.11	6.58 ± 0.2	1.46 ± 0.07	4630
247462972	93.35 ± 0.94	8.21 ± 0.09	7.26 ± 0.19	1.46 ± 0.06	4485
247463581	104.32 ± 0.85	9.65 ± 0.14	6.09 ± 0.17	1.16 ± 0.05	4703
247464087	206.38 ± 2.37	18.03 ± 0.54	3.54 ± 0.17	0.77 ± 0.05	4643
247466416	175.4 ± 0.93	13.67 ± 0.02	4.86 ± 0.09	1.22 ± 0.04	4561
247472807	107.88 ± 0.41	9.52 ± 0.05	6.36 ± 0.13	1.3 ± 0.05	4426
247473339	159.88 ± 1.13	12.75 ± 0.15	5.36 ± 0.14	1.38 ± 0.06	4723
247479337	122.83 ± 1.22	10.39 ± 0.03	5.93 ± 0.13	1.28 ± 0.05	4438
247483410	154.55 ± 0.91	12.68 ± 0.15	5.05 ± 0.13	1.17 ± 0.05	4430
247496832	167.36 ± 1.26	12.78 ± 0.13	5.51 ± 0.13	1.52 ± 0.06	4580
247498070	168.88 ± 4.78	12.9 ± 0.1	5.31 ± 0.19	1.41 ± 0.09	4627
247501164	170.5 ± 2.79	13.38 ± 0.03	5.13 ± 0.13	1.34 ± 0.06	4681
247505420	118.08 ± 0.71	10.23 ± 0.04	5.92 ± 0.12	1.23 ± 0.04	4559
247514730	119.28 ± 1.65	10.35 ± 0.09	5.92 ± 0.16	1.24 ± 0.05	4597
247515124	81.29 ± 0.73	7.47 ± 0.17	7.72 ± 0.29	1.44 ± 0.08	4607
247515418	113.77 ± 4.21	9.12 ± 0.12	7.26 ± 0.33	1.79 ± 0.14	4668
247519710	81.79 ± 1.4	7.36 ± 0.2	7.78 ± 0.36	1.46 ± 0.1	4417
247521922	78.07 ± 2.11	8.19 ± 0.05	6.38 ± 0.21	0.95 ± 0.05	4660
247525461	147.84 ± 1.02	12.93 ± 0.06	4.74 ± 0.1	0.99 ± 0.03	4603
247527328	224.5 ± 4.76	17.21 ± 0.03	4.1 ± 0.12	1.13 ± 0.05	4650
247527442	160.12 ± 0.66	12.96 ± 0.04	5.11 ± 0.1	1.25 ± 0.04	4530
247533030	235.8 ± 1.66	17.71 ± 0.06	3.96 ± 0.08	1.09 ± 0.04	4477
247533516	138.86 ± 1.07	10.98 ± 0.13	6.06 ± 0.16	1.51 ± 0.06	4592
247535124	100.37 ± 0.7	9.02 ± 0.23	6.55 ± 0.27	1.28 ± 0.08	4636
247537267	139.9 ± 1.2	12.37 ± 0.08	4.73 ± 0.11	0.92 ± 0.04	4410

Continued on next page

Table A.1 – continued from previous page

EPIC ID	$\nu_{\max}$ (μHz)	$\Delta\nu$ (μHz)	Radius ($R_\odot$)	Mass ($M_\odot$)	$T_{\rm eff}$ (K)
247537467	102.83 ± 1.04	9.48 ± 0.13	6.09 ± 0.18	1.13 ± 0.05	4460
247539580	98.95 ± 0.78	8.46 ± 0.05	7.38 ± 0.16	1.61 ± 0.06	4590
247556419	171.99 ± 1.64	12.76 ± 0.13	5.57 ± 0.14	1.59 ± 0.06	4653
247562160	192.52 ± 3.89	14.17 ± 0.21	5.07 ± 0.18	1.47 ± 0.08	4526
247567964	120.89 ± 1.18	10.92 ± 0.08	5.61 ± 0.13	1.14 ± 0.04	4551
247569216	189.32 ± 1.69	14.45 ± 0.07	4.95 ± 0.11	1.4 ± 0.05	4690
247573825	75.41 ± 0.52	7.75 ± 0.06	6.61 ± 0.15	0.97 ± 0.04	4343
247575807	91.25 ± 0.89	8.29 ± 0.1	7.06 ± 0.19	1.35 ± 0.06	4488
247577539	145.59 ± 1.95	11.86 ± 0.09	5.47 ± 0.14	1.29 ± 0.06	4464
247580222	150.97 ± 1.1	12.81 ± 0.21	4.96 ± 0.15	1.11 ± 0.05	4364
247580322	96.4 ± 0.81	8.45 ± 0.04	7.32 ± 0.16	1.56 ± 0.06	4667
247589424	100.86 ± 1.35	8.4 ± 0.09	7.46 ± 0.21	1.66 ± 0.08	4298
247592428	151.63 ± 1.96	12.24 ± 0.04	5.57 ± 0.13	1.42 ± 0.06	4625
247595727	211.7 ± 1.6	16.21 ± 0.05	4.33 ± 0.09	1.19 ± 0.04	4243
247596240	104.38 ± 0.79	8.95 ± 0.04	6.72 ± 0.15	1.39 ± 0.05	4211
247598582	162.12 ± 1.73	13.46 ± 0.14	4.88 ± 0.13	1.16 ± 0.05	4670
247602703	62.74 ± 1.84	6.65 ± 0.09	7.39 ± 0.3	1.01 ± 0.07	4129
247603722	224.37 ± 2.33	16.7 ± 0.19	4.23 ± 0.11	1.19 ± 0.05	4440
247608059	180.63 ± 2.11	14.85 ± 0.07	4.54 ± 0.1	1.12 ± 0.04	4595
247608114	59.68 ± 0.67	6.49 ± 0.14	7.33 ± 0.28	0.94 ± 0.06	4297
247620503	103.22 ± 0.82	9.57 ± 0.09	5.98 ± 0.15	1.1 ± 0.04	4417
247621044	60.98 ± 1.0	6.35 ± 0.04	7.77 ± 0.21	1.08 ± 0.05	4415
247624784	170.36 ± 2.57	14.66 ± 0.18	4.27 ± 0.13	0.92 ± 0.04	4453
247634667	103.61 ± 0.74	9.86 ± 0.05	5.8 ± 0.12	1.04 ± 0.04	4320
247635562	78.95 ± 0.98	7.3 ± 0.05	7.75 ± 0.19	1.4 ± 0.06	4412
247640159	147.34 ± 0.67	12.06 ± 0.05	5.43 ± 0.11	1.3 ± 0.04	4605
247646821	200.93 ± 2.8	15.84 ± 0.26	4.3 ± 0.14	1.11 ± 0.06	4435
247650391	153.33 ± 1.66	12.73 ± 0.09	4.99 ± 0.12	1.13 ± 0.05	4421
247679306	155.8 ± 1.76	12.6 ± 0.07	5.29 ± 0.12	1.31 ± 0.05	4491
247681348	107.25 ± 1.58	9.75 ± 0.08	6.2 ± 0.16	1.24 ± 0.05	4701
247691951	117.21 ± 1.82	9.78 ± 0.27	6.49 ± 0.3	1.47 ± 0.1	4566
247692813	126.0 ± 1.91	10.6 ± 0.07	5.88 ± 0.15	1.29 ± 0.06	4364
247704345	192.97 ± 3.45	15.11 ± 0.12	4.65 ± 0.13	1.26 ± 0.06	4338
247711273	193.24 ± 2.81	15.2 ± 0.16	4.6 ± 0.13	1.23 ± 0.06	4536
247714886	96.73 ± 2.99	8.4 ± 0.08	7.31 ± 0.28	1.54 ± 0.1	4413
247718788	170.48 ± 2.14	13.06 ± 0.06	5.35 ± 0.12	1.46 ± 0.06	4572
247728107	186.49 ± 2.41	15.33 ± 0.03	4.23 ± 0.1	0.99 ± 0.04	4226
247744588	109.47 ± 3.64	9.48 ± 0.11	6.49 ± 0.27	1.38 ± 0.1	4686
247756950	195.22 ± 5.71	14.54 ± 0.05	5.0 ± 0.17	1.47 ± 0.09	4682
247775793	97.96 ± 1.2	9.41 ± 0.07	6.21 ± 0.15	1.14 ± 0.05	4435
247778889	231.71 ± 3.02	18.09 ± 0.26	3.81 ± 0.12	1.0 ± 0.05	4347
247781341	100.46 ± 1.33	8.8 ± 0.16	6.94 ± 0.24	1.44 ± 0.08	4299
247794883	80.41 ± 1.05	7.48 ± 0.23	7.52 ± 0.37	1.35 ± 0.1	4254
247799074	155.89 ± 1.23	12.86 ± 0.11	4.97 ± 0.12	1.14 ± 0.05	4299
247799320	126.1 ± 0.7	11.38 ± 0.04	5.36 ± 0.11	1.08 ± 0.04	4290
247808229	104.23 ± 1.73	10.59 ± 0.16	5.1 ± 0.17	0.8 ± 0.04	4404
247809121	194.29 ± 5.79	15.7 ± 0.35	4.29 ± 0.2	1.07 ± 0.08	4616
247814069	131.18 ± 2.19	10.34 ± 0.24	6.49 ± 0.27	1.64 ± 0.1	4484
247830259	121.1 ± 0.89	10.42 ± 0.05	6.15 ± 0.13	1.38 ± 0.05	4528
247843831	100.4 ± 0.86	9.22 ± 0.06	6.24 ± 0.14	1.16 ± 0.04	4380
247845521	93.26 ± 1.04	7.91 ± 0.08	7.34 ± 0.21	1.43 ± 0.07	3686
247846189	100.86 ± 1.12	8.24 ± 0.06	7.89 ± 0.19	1.87 ± 0.07	4604
247848504	97.62 ± 0.8	9.19 ± 0.05	6.2 ± 0.14	1.12 ± 0.04	4329
247855982	63.91 ± 1.24	6.97 ± 0.02	7.24 ± 0.2	1.0 ± 0.05	4551
247874568	108.03 ± 1.1	9.34 ± 0.04	6.41 ± 0.14	1.31 ± 0.05	4383
247883248	88.21 ± 2.25	8.45 ± 0.13	6.44 ± 0.25	1.08 ± 0.07	4252
247903271	111.56 ± 2.45	10.03 ± 0.09	6.09 ± 0.19	1.25 ± 0.07	4668
247920055	172.54 ± 1.97	13.47 ± 0.06	4.9 ± 0.11	1.22 ± 0.05	4333
247926656	190.38 ± 3.86	14.74 ± 0.05	4.69 ± 0.13	1.25 ± 0.06	4415
247963975	98.2 ± 2.3	8.38 ± 0.09	7.41 ± 0.26	1.61 ± 0.09	3819
247973513	111.05 ± 1.83	9.05 ± 0.14	7.24 ± 0.25	1.74 ± 0.1	4039

Continued on next page

Table A.1 – continued from previous page

EPIC ID	ν_{max} (μHz)	$\Delta\nu$ (μHz)	Radius ($R_{\odot}$)	Mass ($M_{\odot}$)	T_{eff} (K)
247976157	100.98 ± 0.95	8.17 ± 0.06	7.91 ± 0.18	1.87 ± 0.07	4462
248062465	194.89 ± 3.48	14.31 ± 0.07	5.2 ± 0.14	1.59 ± 0.07	4314
248075236	66.44 ± 1.44	6.9 ± 0.07	7.57 ± 0.25	1.14 ± 0.06	4355
248081953	76.17 ± 0.65	7.2 ± 0.11	7.74 ± 0.23	1.35 ± 0.06	4346
248087689	77.05 ± 0.78	7.23 ± 0.13	7.42 ± 0.25	1.23 ± 0.07	4114
248104041	79.3 ± 0.81	7.36 ± 0.08	7.46 ± 0.2	1.29 ± 0.06	4256
248108837	99.27 ± 1.13	8.91 ± 0.07	6.58 ± 0.16	1.27 ± 0.05	4411
248295571	210.39 ± 3.42	16.91 ± 0.08	3.94 ± 0.1	0.97 ± 0.04	4479

References

Aguilera-Gómez, C., Chanamé, J., Pinsonneault, M. H., & Carlberg, J. K. 2016a, ApJ, 829, 127

—. 2016b, ApJ, 833, L24

Aigrain, S., Parviainen, H., & Pope, B. J. S. 2016, MNRAS, 459, 2408

Akeson, R. L., Chen, X., Ciardi, D., et al. 2013, PASP, 125, 989

Allard, F., Homeier, D., & Freytag, B. 2011, in Astronomical Society of the Pacific Conference Series, Vol. 448, 16th Cambridge Workshop on Cool Stars, Stellar Systems, and the Sun, ed. C. Johns-Krull, M. K. Browning, & A. A. West, 91

Allard, F., Homeier, D., Freytag, B., et al. 2013, Memorie della Societa Astronomica Italiana Supplementi, 24, 128

Andrews, S. M., Rosenfeld, K. A., Kraus, A. L., & Wilner, D. J. 2013, ApJ, 771, 129

Anglada-Escudé, G., Amado, P. J., Barnes, J., et al. 2016, Nature, 536, 437

Arentoft, T., Grundahl, F., White, T. R., et al. 2019, A&A, 622, A190

Auvergne, M., Bodin, P., Boisnard, L., et al. 2009, A&A, 506, 411

Baraffe, I., Chabrier, G., Fortney, J., & Sotin, C. 2014, Protostars and Planets VI, 763

Barclay, T. 2015, ktransit 0.2.2, Zenodo, doi:10.5281/zenodo.35265. `http://dx.doi.org/10.5281/zenodo.35265`

Barclay, T., Endl, M., Huber, D., et al. 2015, ApJ, 800, 46

Barclay, T., Pepper, J., & Quintana, E. V. 2018, ApJS, 239, 2

Bashi, D., Helled, R., Zucker, S., & Mordasini, C. 2017, A&A, 604, A83

Bastien, F. A., Stassun, K. G., Pepper, J., et al. 2014, AJ, 147, 29

Batalha, N. M., Borucki, W. J., Koch, D. G., et al. 2010, ApJ, 713, L109

Batygin, K., & Stevenson, D. J. 2010, ApJ, 714, L238

Batygin, K., Stevenson, D. J., & Bodenheimer, P. H. 2011, ApJ, 738, 1

Bedding, T. R., Huber, D., Stello, D., et al. 2010, ApJ, 713, L176

Bodenheimer, P., Lin, D. N. C., & Mardling, R. A. 2001, ApJ, 548, 466

Boltzmann, L. 1884, Annalen der Physik, 258, 291

Borucki, W. J., Koch, D., Basri, G., et al. 2010, Science, 327, 977

Bovy, J., Rix, H.-W., Green, G. M., Schlafly, E. F., & Finkbeiner, D. P. 2016, ApJ, 818, 130

Bowler, B. P., Johnson, J. A., Marcy, G. W., et al. 2010, ApJ, 709, 396

Boyajian, T. S., van Belle, G., & von Braun, K. 2014, AJ, 147, 47

Bressan, A., Marigo, P., Girardi, L., et al. 2012, MNRAS, 427, 127

Brewer, B. J., & Stello, D. 2009, MNRAS, 395, 2226

Brown, T. M., Gilliland, R. L., Noyes, R. W., & Ramsey, L. W. 1991a, ApJ, 368, 599

—. 1991b, ApJ, 368, 599

Bryan, M. L., Knutson, H. A., Howard, A. W., et al. 2016, ApJ, 821, 89

Buchhave, L. A., Latham, D. W., Johansen, A., et al. 2012, Nature, 486, 375

Burke, C. J. 2008, ApJ, 679, 1566

Burrows, A., Guillot, T., Hubbard, W. B., et al. 2000, ApJ, 534, L97

Burrows, A., Marley, M., Hubbard, W. B., et al. 1997, ApJ, 491, 856

Burt, J., Vogt, S. S., Butler, R. P., et al. 2014, ApJ, 789, 114

Butler, R. P., Marcy, G. W., Williams, E., et al. 1996, PASP, 108, 500

Campante, T. L., Barclay, T., Swift, J. J., et al. 2015, ApJ, 799, 170

Campante, T. L., Schofield, M., Kuszlewicz, J. S., et al. 2016, ApJ, 830, 138

Carlberg, J. K., Majewski, S. R., & Arras, P. 2009, ApJ, 700, 832

Carter, J. A., & Winn, J. N. 2009, ApJ, 704, 51

Casagrande, L., Silva Aguirre, V., Schlesinger, K. J., et al. 2016, MNRAS, 455, 987

Chabrier, G., & Baraffe, I. 2007, ApJ, 661, L81

Chaplin, W. J., & Miglio, A. 2013, ARA&A, 51, 353

Chaplin, W. J., Basu, S., Huber, D., et al. 2014, ApJS, 210, 1

Charbonneau, D., Brown, T. M., Latham, D. W., & Mayor, M. 2000, ApJ, 529, L45

Chen, J., & Kipping, D. 2017, ApJ, 834, 17

Choi, J., Dotter, A., Conroy, C., et al. 2016, ArXiv e-prints, arXiv:1604.08592

Christensen-Dalsgaard, J., & Frandsen, S. 1983, Sol. Phys., 82, 469

Christensen-Dalsgaard, J., Kjeldsen, H., Brown, T. M., et al. 2010, ApJ, 713, L164

Christiansen, J. L., Clarke, B. D., Burke, C. J., et al. 2015, ApJ, 810, 95

Ciceri, S., Lillo-Box, J., Southworth, J., et al. 2015, A&A, 573, L5

Claret, A., & Bloemen, S. 2011, A&A, 529, A75

Coelho, P., Barbuy, B., Meléndez, J., Schiavon, R. P., & Castilho, B. V. 2005, A&A, 443, 735

Coelho, P. R. T. 2014, MNRAS, 440, 1027

Cohen, M., Wheaton, W. A., & Megeath, S. T. 2003, AJ, 126, 1090

Collier Cameron, A., Horne, K., Penny, A., & James, D. 1999, Nature, 402, 751

Collier Cameron, A., Mortier, A., Phillips, D., et al. 2019, MNRAS, 487, 1082

Corsaro, E., Stello, D., Huber, D., et al. 2012, ApJ, 757, 190

Cui, X.-Q., Zhao, Y.-H., Chu, Y.-Q., et al. 2012, Research in Astronomy and Astrophysics, 12, 1197

Cumming, A., Butler, R. P., Marcy, G. W., et al. 2008, PASP, 120, 531

Dawson, R. I., & Johnson, J. A. 2018, ARA&A, 56, 175

Dawson, R. I., Johnson, J. A., Fabrycky, D. C., et al. 2014, ApJ, 791, 89

Delgado Mena, E., Lovis, C., Santos, N. C., et al. 2018, A&A, 619, A2

Demory, B.-O., & Seager, S. 2011, ApJS, 197, 12

Dobbs-Dixon, I., Lin, D. N. C., & Mardling, R. A. 2004, ApJ, 610, 464

Dressing, C. D., & Charbonneau, D. 2015, ApJ, 807, 45

Driscoll, P. E., & Barnes, R. 2015, Astrobiology, 15, 739

Dumusque, X. 2016, A&A, 593, A5

Dziembowski, W. A., Gough, D. O., Houdek, G., & Sienkiewicz, R. 2001, MNRAS, 328, 601

Eastman, J., Gaudi, B. S., & Agol, E. 2012, EXOFAST: Fast transit and/or RV fitter for single exoplanet, Astrophysics Source Code Library, , , ascl:1207.001

—. 2013, PASP, 125, 83

Essick, R., & Weinberg, N. N. 2016, ApJ, 816, 18

Everett, M. E., Barclay, T., Ciardi, D. R., et al. 2015, AJ, 149, 55

Fitzpatrick, E. L. 1999, PASP, 111, 63

Foreman-Mackey, D., Agol, E., Angus, R., & Ambikasaran, S. 2017, ArXiv e-prints, arXiv:1703.09710

Foreman-Mackey, D., Hogg, D. W., Lang, D., & Goodman, J. 2013, PASP, 125, 306

Fortney, J. J., Marley, M. S., & Barnes, J. W. 2007, ApJ, 659, 1661

Fressin, F., Torres, G., Charbonneau, D., et al. 2013, ApJ, 766, 81

Fuller, J. 2017, MNRAS, 472, 1538

Fulton, B., & Petigura, E. 2017, radvel 0.9.1, Zenodo, doi:10.5281/zenodo.580821. `http://dx.doi.org/10.5281/zenodo.580821`

Fulton, B. J., Petigura, E. A., Blunt, S., & Sinukoff, E. 2018a, ArXiv e-prints, arXiv:1801.01947

—. 2018b, PASP, 130, 044504

Fulton, B. J., Howard, A. W., Winn, J. N., et al. 2013, ApJ, 772, 80

Fulton, B. J., Weiss, L. M., Sinukoff, E., et al. 2015, ApJ, 805, 175

Fulton, B. J., Petigura, E. A., Howard, A. W., et al. 2017, ArXiv e-prints, arXiv:1703.10375

Gaia Collaboration, Brown, A. G. A., Vallenari, A., et al. 2018, ArXiv e-prints, arXiv:1804.09365

Gaidos, E., Fischer, D. A., Mann, A. W., & Howard, A. W. 2013, ApJ, 771, 18

Gaidos, E., Mann, A. W., & Ansdell, M. 2016, ApJ, 817, 50

Gallet, F., Bolmont, E., Mathis, S., Charbonnel, C., & Amard, L. 2017, ArXiv e-prints, arXiv:1705.10164

Gaudi, B. S., Seager, S., & Mallen-Ornelas, G. 2005, ApJ, 623, 472

Gaudi, B. S., Stassun, K. G., Collins, K. A., et al. 2017, Nature, 546, 514

Gelman, A., & Rubin, D. B. 1992, Statistical Science, 7, 457

Ghezzi, L., & Johnson, J. A. 2015, ApJ, 812, 96

Ghezzi, L., Montet, B. T., & Johnson, J. A. 2018, ApJ, 860, 109

Gibson, N. P., Aigrain, S., Pont, F., et al. 2012, MNRAS, 422, 753

Gilliland, R. L., Chaplin, W. J., Dunham, E. W., et al. 2011, ApJS, 197, 6

Ginzburg, S., & Sari, R. 2016, ApJ, 819, 116

Goldreich, P., & Soter, S. 1966, , 5, 375

González Hernández, J. I., & Bonifacio, P. 2009, A&A, 497, 497

Graczyk, D., Pietrzyński, G., Thompson, I. B., et al. 2018, ApJ, 860, 1

Grunblatt, S. K., Howard, A. W., & Haywood, R. D. 2015, ApJ, 808, 127

Grunblatt, S. K., Huber, D., Gaidos, E. J., et al. 2016, AJ, 152, 185

Grunblatt, S. K., Huber, D., Gaidos, E., et al. 2017, AJ, 154, 254

—. 2018, ApJ, 861, L5

Gu, P.-G., Lin, D. N. C., & Bodenheimer, P. H. 2003, The Astrophysical Journal, 588, 509. http://stacks.iop.org/0004-637X/588/i=1/a=509

Guillot, T., Burrows, A., Hubbard, W. B., Lunine, J. I., & Saumon, D. 1996, ApJ, 459, L35

Guillot, T., & Gautier, D. 2014, ArXiv e-prints, arXiv:1405.3752

Guillot, T., & Showman, A. P. 2002, A&A, 385, 156

Han, E., Wang, S. X., Wright, J. T., et al. 2014, PASP, 126, 827

Harvey, J. 1985a, in ESA Special Publication, Vol. 235, Future Missions in Solar, Heliospheric & Space Plasma Physics, ed. E. Rolfe & B. Battrick, 199–208

Harvey, J. 1985b, in ESA Special Publication, Vol. 235, Future Missions in Solar, Heliospheric & Space Plasma Physics, ed. E. Rolfe & B. Battrick

Hatzes, A. P., Cochran, W. D., McArthur, B., et al. 2000, ApJ, 544, L145

Haywood, R. D., Collier Cameron, A., Queloz, D., et al. 2014, MNRAS, 443, 2517

Hebb, L., Collier-Cameron, A., Loeillet, B., et al. 2009, ApJ, 693, 1920

Hellier, C., Anderson, D. R., Collier Cameron, A., et al. 2012, MNRAS, 426, 739

Henden, A. A., Levine, S. E., Terrell, D., Smith, T. C., & Welch, D. 2012, Journal of the American Association of Variable Star Observers (JAAVSO), 40, 430

Henry, G. W., Marcy, G. W., Butler, R. P., & Vogt, S. S. 2000, ApJ, 529, L41

Herbrich, R., Lawrence, N. D., & Seeger, M. 2003, in Advances in Neural Information Processing Systems 15, ed. S. Becker, S. Thrun, & K. Obermayer (MIT Press), 625–632. http://papers.nips.cc/paper/2240-fast-sparse-gaussian-process-methods-the-informative-vector-machine.pdf

Hirano, T., Suto, Y., Winn, J. N., et al. 2011, ApJ, 742, 69

Hon, M., Stello, D., & Yu, J. 2018, MNRAS, 476, 3233

Houdek, G., Balmforth, N. J., Christensen-Dalsgaard, J., & Gough, D. O. 1999, A&A, 351, 582

Howard, A. W., Marcy, G. W., Bryson, S. T., et al. 2012, ApJS, 201, 15

Howell, S. B., Sobeck, C., Haas, M., et al. 2014, PASP, 126, 398

Hsu, D. C., Ford, E. B., Ragozzine, D., & Morehead, R. C. 2018, AJ, 155, 205

Huber, D. 2016, IAU Focus Meeting, 29, 620

Huber, D., Bryson, S. T., Haas, M. R., et al. 2015, ArXiv e-prints, arXiv:1512.02643

Huber, D., Stello, D., Bedding, T. R., et al. 2009a, Communications in Asteroseismology, 160, 74

—. 2009b, Communications in Asteroseismology, 160, 74

Huber, D., Bedding, T. R., Stello, D., et al. 2010, ApJ, 723, 1607

—. 2011a, ApJ, 743, 143

Huber, D., Bedding, T. R., Arentoft, T., et al. 2011b, ApJ, 731, 94

Huber, D., Chaplin, W. J., Christensen-Dalsgaard, J., et al. 2013a, ApJ, 767, 127

Huber, D., Carter, J. A., Barbieri, M., et al. 2013b, Science, 342, 331

Huber, D., Bryson, S. T., Haas, M. R., et al. 2016, ApJS, 224, 2

Huber, D., Zinn, J., Bojsen-Hansen, M., et al. 2017, ApJ, 844, 102

Huber, D., Chaplin, W. J., Chontos, A., et al. 2019, arXiv e-prints, arXiv:1901.01643

Hut, P. 1981, A&A, 99, 126

Jackson, B., Arras, P., Penev, K., Peacock, S., & Marchant, P. 2017, ApJ, 835, 145

Jarrett, T. H., Cohen, M., Masci, F., et al. 2011, ApJ, 735, 112

Jenkins, J. M., Caldwell, D. A., Chandrasekaran, H., et al. 2010, ApJ, 713, L87

Johnson, J. A., Aller, K. M., Howard, A. W., & Crepp, J. R. 2010a, PASP, 122, 905

Johnson, J. A., & Apps, K. 2009, ApJ, 699, 933

Johnson, J. A., Butler, R. P., Marcy, G. W., et al. 2007a, ApJ, 670, 833

Johnson, J. A., Morton, T. D., & Wright, J. T. 2013, ApJ, 763, 53

Johnson, J. A., Fischer, D. A., Marcy, G. W., et al. 2007b, ApJ, 665, 785

—. 2007c, ApJ, 665, 785

Johnson, J. A., Bowler, B. P., Howard, A. W., et al. 2010b, ApJ, 721, L153

Johnson, J. A., Huber, D., Boyajian, T., et al. 2014, ApJ, 794, 15

Johnson, J. A., Petigura, E. A., Fulton, B. J., et al. 2017, ArXiv e-prints, arXiv:1703.10402

Jones, M. I., Jenkins, J. S., Brahm, R., et al. 2016, A&A, 590, A38

Jones, M. I., Brahm, R., Espinoza, N., et al. 2017, ArXiv e-prints, arXiv:1707.00779

Kallinger, T., De Ridder, J., Hekker, S., et al. 2014, A&A, 570, A41

Kervella, P., & Fouqué, P. 2008, A&A, 491, 855

Kjeldsen, H., & Bedding, T. R. 1995a, A&A, 293, astro-ph/9403015

—. 1995b, A&A, 293, 87

Kovács, G., Zucker, S., & Mazeh, T. 2002, A&A, 391, 369

Kudritzki, R.-P., Urbaneja, M. A., Bresolin, F., Hosek, Jr., M. W., & Przybilla, N. 2014, ApJ, 788, 56

Kunder, A., Kordopatis, G., Steinmetz, M., et al. 2017, AJ, 153, 75

Kunitomo, M., Ikoma, M., Sato, B., Katsuta, Y., & Ida, S. 2011, ApJ, 737, 66

Lantz, B., Aldering, G., Antilogus, P., et al. 2004, in Proc. SPIE, Vol. 5249, Optical Design and Engineering, ed. L. Mazuray, P. J. Rogers, & R. Wartmann, 146–155

Latham, D. W., Mazeh, T., Stefanik, R. P., Mayor, M., & Burki, G. 1989, Nature, 339, 38

Laughlin, G., Crismani, M., & Adams, F. C. 2011, ApJ, 729, L7

Lillo-Box, J., Barrado, D., & Correia, A. C. M. 2016, A&A, 589, A124

Lillo-Box, J., Barrado, D., Henning, T., et al. 2014, A&A, 568, L1

Lloyd, J. P. 2011, ApJ, 739, L49

—. 2013, ApJ, 774, L2

Lopez, E. D., & Fortney, J. J. 2016, ApJ, 818, 4

Lundkvist, M. S., Kjeldsen, H., Albrecht, S., et al. 2016, Nature Communications, 7, 11201

MacLeod, M., Cantiello, M., & Soares-Furtado, M. 2018, ApJ, 853, L1

Majewski, S. R., Schiavon, R. P., Frinchaboy, P. M., et al. 2017, AJ, 154, 94

Malmquist, K. G. 1922, Meddelanden fran Lunds Astronomiska Observatorium Serie I, 100, 1

Mandel, K., & Agol, E. 2002, ApJ, 580, L171

Mann, A. W., Feiden, G. A., Gaidos, E., Boyajian, T., & von Braun, K. 2015, ApJ, 804, 64

Mann, A. W., & von Braun, K. 2015, PASP, 127, 102

Mann, A. W., Dupuy, T., Muirhead, P. S., et al. 2017, AJ, 153, 267

Marcy, G., Butler, R. P., Fischer, D., et al. 2005, Progress of Theoretical Physics Supplement, 158, 24

Marcy, G. W., & Butler, R. P. 1996, ApJ, 464, L147

Marois, C., Macintosh, B., Barman, T., et al. 2008, Science, 322, 1348

Mathur, S., Metcalfe, T. S., Woitaszek, M., et al. 2012, ApJ, 749, 152

Mayo, A. W., Vanderburg, A., Latham, D. W., et al. 2018, AJ, 155, 136

Mayor, M., & Queloz, D. 1995, Nature, 378, 355

Mayor, M., Marmier, M., Lovis, C., et al. 2011, arXiv e-prints, arXiv:1109.2497

Metchev, S. A., & Hillenbrand, L. A. 2009, ApJS, 181, 62

Miller, N., & Fortney, J. J. 2011, ApJ, 736, L29

Miller, N., Fortney, J. J., & Jackson, B. 2009, ApJ, 702, 1413

Montalbán, J., Miglio, A., Noels, A., Scuflaire, R., & Ventura, P. 2010, ApJ, 721, L182

Morton, T. D., Bryson, S. T., Coughlin, J. L., et al. 2016, ApJ, 822, 86

Neal, R. M. 1997, arXiv preprint physics/9701026

Niedzielski, A., Villaver, E., Nowak, G., et al. 2016, A&A, 589, L1

North, T. S. H., Campante, T. L., Miglio, A., et al. 2017, ArXiv e-prints, arXiv:1708.00716

Ogilvie, G. I., & Lin, D. N. C. 2004, ApJ, 610, 477

Owen, J. E., & Wu, Y. 2017, ApJ, 847, 29

Patra, K. C., Winn, J. N., Holman, M. J., et al. 2017, ArXiv e-prints, arXiv:1703.06582

Perryman, M. A. C., Lindegren, L., Kovalevsky, J., et al. 1997a, A&A, 323, L49

—. 1997b, A&A, 323, L49

Petigura, E. A. 2015, PhD thesis, University of California, Berkeley

Petigura, E. A., Howard, A. W., & Marcy, G. W. 2013, Proceedings of the National Academy of Science, 110, 19273

Petigura, E. A., Howard, A. W., Marcy, G. W., et al. 2017a, ArXiv e-prints, arXiv:1703.10400

Petigura, E. A., Sinukoff, E., Lopez, E. D., et al. 2017b, AJ, 153, 142

Pinsonneault, M. H., Elsworth, Y., Epstein, C., et al. 2014, ApJS, 215, 19

Pollacco, D. L., Skillen, I., Collier Cameron, A., et al. 2006, PASP, 118, 1407

Pols, O. R., Schröder, K.-P., Hurley, J. R., Tout, C. A., & Eggleton, P. P. 1998, MNRAS, 298, 525

Pope, B. J. S., Parviainen, H., & Aigrain, S. 2016, MNRAS, arXiv:1606.01264

Privitera, G., Meynet, G., Eggenberger, P., et al. 2016a, A&A, 593, A128

—. 2016b, A&A, 593, L15

Quinn, S. N., White, T. R., Latham, D. W., et al. 2015, ApJ, 803, 49

Quiñonero-Candela, J., & Rasmussen, C. E. 2005, The Journal of Machine Learning Research, 6, 1939

Rappaport, S., Sanchis-Ojeda, R., Rogers, L. A., Levine, A., & Winn, J. N. 2013, ApJ, 773, L15

Rasmussen, C. E. 2006

Rauer, H., Catala, C., Aerts, C., et al. 2014, Experimental Astronomy, 38, 249

Rayner, J. T., Toomey, D. W., Onaka, P. M., et al. 2003, PASP, 115, 362

Reffert, S., Bergmann, C., Quirrenbach, A., Trifonov, T., & Künstler, A. 2015, A&A, 574, A116

Refsdal, S., & Weigert, A. 1970, A&A, 6, 426

Ricker, G. R., Winn, J. N., Vanderspek, R., et al. 2014, in Society of Photo-Optical Instrumentation Engineers (SPIE) Conference Series, Vol. 9143, Society of Photo-Optical Instrumentation Engineers (SPIE) Conference Series, 914320

Santerne, A., Moutou, C., Tsantaki, M., et al. 2016, A&A, 587, A64

Sato, B., Kambe, E., Takeda, Y., et al. 2005, PASJ, 57, 97

Schlafly, E. F., & Finkbeiner, D. P. 2011, ApJ, 737, 103

Schlaufman, K. C., & Winn, J. N. 2013, ApJ, 772, 143

Sharma, S., Stello, D., Bland-Hawthorn, J., Huber, D., & Bedding, T. R. 2016, ApJ, 822, 15

Silva Aguirre, V., Davies, G. R., Basu, S., et al. 2015, MNRAS, 452, 2127

Simpson, P. B. 1951, The Annals of Mathematical Statistics, 22, 476

Skrutskie, M. F., Cutri, R. M., Stiening, R., et al. 2006, AJ, 131, 1163

Sliski, D. H., & Kipping, D. M. 2014, ApJ, 788, 148

Smith, J. C., Stumpe, M. C., Van Cleve, J. E., et al. 2012, PASP, 124, 1000

Stefan, J. 1879, Über die Beziehung zwischen der Wärmestrahlung und der Temperatur (Aus der kk Hof-und Staatsdruckerei)

Stello, D., Cantiello, M., Fuller, J., Garcia, R. A., & Huber, D. 2016, PASA, 33, e011

Stello, D., Chaplin, W. J., Basu, S., Elsworth, Y., & Bedding, T. R. 2009, MNRAS, 400, L80

Stello, D., Huber, D., Bedding, T. R., et al. 2013, ApJ, 765, L41

Stello, D., Huber, D., Sharma, S., et al. 2015, ApJ, 809, L3

Stello, D., Zinn, J., Elsworth, Y., et al. 2017, ApJ, 835, 83

Stephens, M. A. 1974, Journal of the American statistical Association, 69, 730

Storch, N. I., Anderson, K. R., & Lai, D. 2014, Science, 345, 1317

Struve, O. 1952, The Observatory, 72, 199

Stumpe, M. C., Smith, J. C., Van Cleve, J. E., et al. 2012, PASP, 124, 985

Sullivan, P. W., Winn, J. N., Berta-Thompson, Z. K., et al. 2015, ApJ, 809, 77

Takarada, T., Sato, B., Omiya, M., et al. 2018, PASJ, 70, 59

Tayar, J., Stassun, K. G., & Corsaro, E. 2018, arXiv e-prints, arXiv:1812.04010

Thorngren, D. P., Fortney, J. J., & Lopez, E. D. 2015, ArXiv e-prints, arXiv:1511.07854

Tremblin, P., Chabrier, G., Mayne, N. J., et al. 2017, ArXiv e-prints, arXiv:1704.05440

Ulrich, R. K. 1986, ApJ, 306, L37

Valenti, J. A., & Fischer, D. A. 2005, ApJS, 159, 141

Van Eylen, V., Agentoft, C., Lundkvist, M. S., et al. 2018, MNRAS, 479, 4786

Van Eylen, V., & Albrecht, S. 2015, ApJ, 808, 126

Van Eylen, V., Albrecht, S., Gandolfi, D., et al. 2016, ArXiv e-prints, arXiv:1605.09180

van Sluijs, L., & Van Eylen, V. 2018, MNRAS, 474, 4603

Vanderburg, A., & Johnson, J. A. 2014, PASP, 126, 948

Vanderburg, A., Latham, D. W., Buchhave, L. A., et al. 2015, ArXiv e-prints, arXiv:1511.07820

—. 2016, ApJS, 222, 14

Vanhollebeke, E., Groenewegen, M. A. T., & Girardi, L. 2009, A&A, 498, 95

Veras, D. 2016, Royal Society Open Science, 3, 150571

Villaver, E., & Livio, M. 2009, ApJ, 705, L81

Villaver, E., Livio, M., Mustill, A. J., & Siess, L. 2014, ApJ, 794, 3

Vogt, S. S., Allen, S. L., Bigelow, B. C., et al. 1994, in Proc. SPIE, Vol. 2198, Instrumentation in Astronomy VIII, ed. D. L. Crawford & E. R. Craine, 362

Wang, J. M., Fleet, D. J., & Hertzmann, A. 2008, Pattern Analysis and Machine Intelligence, IEEE Transactions on, 30, 283

White, T. R., Bedding, T. R., Stello, D., et al. 2011, ApJ, 743, 161

Wolszczan, A., & Frail, D. A. 1992, Nature, 355, 145

Wright, E. L., Eisenhardt, P. R. M., Mainzer, A. K., et al. 2010, AJ, 140, 1868

Wu, Y. 2005, ApJ, 635, 688

Wu, Y., & Lithwick, Y. 2013, ApJ, 763, 13

Xie, J.-W., Dong, S., Zhu, Z., et al. 2016, Proceedings of the National Academy of Science, 113, 11431

Yu, J., Huber, D., Bedding, T. R., et al. 2018, ApJS, 236, 42

—. 2016, MNRAS, 463, 1297

Zahn, J.-P. 1977, A&A, 57, 383